CHARACTERISATION OF SURFACES MODIFIED THROUGH SELF-ASSEMBLED MONOLAYERS AND CLICK CHEMISTRY

A thesis submitted in fulfilment of the requirements for the degree of

DOCTOR OF PHILOSOPHY

of

RHODES UNIVERSITY

by

MEGAN COATES

Supervisor: Prof T Nyokong

January 2013

ABSTRACT

Different approaches to surface modification were investigated in this work on gold, glassy carbon, multi-walled carbon nanotube paper and on single-walled carbon nanotubes adsorbed on glassy carbon. These approaches include electrochemical grafting, electropolymerisation, click chemistry, axial ligation, adsorption and self-assembled monolayers. The modified surfaces were characterised using a variety of techniques; predominantly electrochemistry, scanning electrochemical microscopy and X-ray photoelectron spectroscopy.

For the formation of self-assembled monolayers on gold, four new manganese(III) phthalocyanines (**1a–d**), octa-substituted at the peripheral position with pentylthio, decylthio, benzylthio, and phenylthio groups were synthesized and characterised. X-ray photoelectron spectroscopy was used to show the formation of a sulphur-gold bond. A number of approaches using 4-azidoaniline (**2a**) combined with azide-alkyne click chemistry and electrochemistry were also used to anchor ferrocene and pyridine moieties on to the carbon surfaces, including direct *in situ* diazotation and grafting, electropolymerisation, and the synthesis of the diazonium salt followed by grafting. Iron phthalocyanine was linked to the pyridine-clicked surfaces through axial ligation, where the strong axial bond formed by the interaction between the central metal and the lone pair of the nitrogen in the pyridine group resulted in stable modified electrodes. The potential of these surfaces for the detection of analytes such as thiocyanate, hydrazine and sulphite are briefly shown as well.

This work also describes for the first time the possibility of performing local micro-electrochemical grafting of a gold substrate by 4-azidobenzenediazonium (**2b**) using scanning electrochemical microscopy in a single and simple one step approach, without complications from adsorption.

ACKNOWLEDGEMENTS

Firstly, I would like to thank my supervisor, Professor Nyokong, for the wonderful years I have had working in your lab for my entire postgraduate studies. For the experience of travelling overseas to work in Paris, for the conference trips, presentations, posters, publications, and all of the opportunities you have given me to grow as a scientist and person: I cannot thank you enough. I appreciate all of the support, encouragement and confidence you have given me. I hope you keep touching lives for many years to come!

I would like to thank Dr Edith Antunes for all of the pep-talks, chats, and the unwavering support you give to all of the students. To Ms Gail Cobus as well: thank you for everything you have done to enable all of these trips and travels, and also for the talks and fun times. To my lab S22, past and current: you guys are the best! And thanks also to the Rhodes University Chemistry Department for such a welcoming environment.

Thank you to Dr Fethi Bedioui and Dr Sophie Griveau for your hospitality while I worked in your lab in Paris, and for introducing me to click chemistry and SECM. It was a truly inspirational experience.

A big thank you to my friends for keeping me going, and just being awesome. Particularly Sarah, Roxann and Mary who have been with me since first year: you guys are next!

To my aunt and uncle, Eve and Jim Cambray, thank you for giving me a second home in Grahamstown. I appreciate your support more than I can say.

I am very grateful to Mrs Liezel Strydom and Mr John Gillam in the Rhodes Financial Aid office for all of their help.

I would like to acknowledge the financial contribution of the Rhodes University Prestigious Henderson Scholarship, and the Department of Science and Technology (DST) National Research Foundation (NRF) Innovations Doctoral Scholarship towards this work, and for the support throughout my studies. I also thank the PROTEA project 25828RE (France–South Africa), and the DST/Mintek Nanotechnology Innovation Centre (NIC). This work was supported by the DST/NRF South African Research Chairs Initiative for Professor of Medicinal Chemistry and Nanotechnology as well as Rhodes University.

Finally, thank you to all of my family, and especially my parents Tony and Debbie Coates, for always believing in me. I love you all so much.

Mom and Dad – this is thanks to you. There are just no words.

CONTENTS

LIST OF ABBREVIATIONS

ACN	Acetonitrile
AFM	Atomic Force Microscopy
a.u.	Arbitrary unit
AuE	Gold electrode
bp	Boiling point
CA	Chronoamperometry
CE	Counter electrode
Click chemistry	Sharpless copper(I) catalyzed azide-alkyne cycloaddition reaction
CNT	Carbon nanotube
CPE	Constant phase element
CT	Charge-transfer
CV	Cyclic voltammetry/voltammogram
DCM	Dichloromethane
DMF	N,N-dimethylformamide
DMSO	Dimethylsulphoxide
DPV	Differential pulse voltammetry
EDTA	Ethylenediaminetetraacetic acid
EIS	Electrochemical Impedance Spectroscopy
Fc	Ferrocene
GCE	Glassy carbon electrode
GC/SWCNT	GCE with adsorbed SWCNTs
HOMO	Highest occupied molecular orbital
^{1}H NMR	Proton nuclear magnetic resonance

IR	Infrared
LoD	Limit of detection
LUMO	Lowest unoccupied molecular orbital
MALDI-TOF	Matrix Assisted Laser Desorption/Ionisation – Time of Flight
MPc	Metallophthalocyanine
MWCNT(s)	Multi-walled carbon nanotube(s)
OTE	Optically transparent electrode
OTTLE	Optically transparent thin layer electrode
PANI	Polyaniline
PBS	Phosphate buffer solution
Pc	Phthalocyanine
PEDOT	Poly(3,4-(1-azidomethylethylene)dioxythiophene)
PtE	Platinum electrode
RDS	Rate determining step
RE	Reference electrode
Redox	Reduction/oxidation
SAM(s)	Self assembled monolayer(s)
SECM	Scanning electrochemical microscopy
SEM	Scanning electron microscopy
SWCNT(s)	Single-walled carbon nanotube(s)
SWCNT-BDA	1,4-Benzenediammine functionalised SWCNTs
SWCNT-COOH	Carboxylic acid functionalised SWCNTs
SWV	Square wave voltammetry
TAPc	Tetraaminophthalocyanine
$TBABF_4$	Tetrabutylammonium tetrafluoroborate

THF	Tetrahydrofuran
TEM	Transmission electron microscopy
UME	Ultramicroelectrode
UV-vis	Ultraviolet-visible
WE	Working electrode
XPS	X-ray photoelectron spectroscopy

LIST OF SYMBOLS

α	Peripheral position
β	Non-peripheral position
ε	Extinction coefficient
θ	Phase shift
Γ	Surface coverage
λ_Q	Wavelength of the maximum absorbance of the Q band
A	Absorbance/real area of electrode
a	Radius
C	Concentration/capacitance
C_{ADS}	Adsorbed species capacitance
C_{DL}	Diffusion layer capacitance
D	Diffusion coefficient
d	Distance
e^-	Electron
ΔE	Peak to peak potential separation
E_p	Peak potential
E_{app}	Applied potential
E_{tip}	Applied potential to SECM probe
$E_{p1/2}$	Half-wave potential
F	Faraday's constant
I	Current
I_{lim}	Limiting current
I_p	Peak current

M	Molar concentration
n	Number of electrons transferred
Q	Charge/constant phase element capacitance
R	Universal gas constant
R_{ADS}	Adsorbed species resistance
R_{CT}	Charge transfer resistance
R_S	Solution resistance
T	Temperature
ν	Scan rate
V	Volts
Z'	Real impedance component
Z''	Imaginary impedance component

LIST OF FIGURES

LIST OF SCHEMES

LIST OF TABLES

CHAPTER 1

INTRODUCTION

1.1. Surface modification of electrodes

1.1.1. Overview

Surface modification is a necessary area of research in the production of smart textiles and solar cells, in corrosion science, and in the development of electrochemical sensors. Although the focus of this work is on the modification of electrodes, several of the techniques described here can be applied to these other areas as well. Many different modification approaches can be taken, depending on the type of surface or electrode used, the molecule/complex to undergo attachment, and the desired application of the electrode or surface. For example, electrodes required for biological sensing need to be nontoxic, and in many cases reproducibility, stability and sensitivity are very important factors. Frequently, a step-wise approach to attachment is best, as it allows the use of easily-synthesized linkers to bind useful molecules to the electrode surface.

This introduction will cover first the types of molecules, complexes and materials that have been attached to electrodes in this work, discussing their applications and properties, and follow with the attachment approaches that have been taken with a final explanation of the characterisation techniques that have been used.

1.1.2. Ferrocene (Fc)

The electrochemical behaviour of ferrocene has been well studied in solution [1–3]. Because of its good electrochemical activity it can be used as a redox probe when modifying electrodes, as well as an important electron mediator and catalyst [4,5]. Ferrocene has been attached to electrode surfaces through covalent and non-covalent methods, including grafting and electropolymerisation as popular techniques [6–15]. Ferrocene is also commonly used as a mediator for enzyme reactions, particularly with glucose oxidase [16–18]. Table 1.1 shows a selection of the attachment approaches that have been used with ferrocene. The aims of using ferrocene in this work were, firstly, to make use of this complex as a redox probe to ensure that the attachment approaches were successful, and secondly to show the potential of the surface for electrocatalysis.

Table 1.1. Selection of literature examples of attachment methods used to confine ferrocene on different electrode surfaces.

Ferrocene Functional Group	Substrate	Attachment	Analyte	Reference
COOH	PtE	amide	-	[6]
SH	AuE	SAM	-	[7]
NH_2	MWCNT array	amide	DNA	[11]
C≡CH	AuE	click chemistry [a]	-	[12]
C≡CH	PGE/GCE	click chemistry [b]	-	[14]
N_3	PGE/GCE	click chemistry [c]	-	[14]
-	GCE	nafion	glucose	[16]
bis-Amide	PtE, GCE	electropolymerisation	Li^+	[4]
Chitosan	GCE/MWCNT	adsorption	sulphite	[5]

[a] With SAM of azido-thiol; [b] with grafted 4-azidobenzenediazonium salt; [c] with grafted ethynylbenzenediazonium salt; abbreviations: SAM = self-assembled monolayer, PtE = platinum electrode, AuE = gold electrode, GCE = glassy carbon electrode, MWCNT = multi-walled carbon nanotubes, PGE = pyrolytic graphite edge electrode, click chemistry = Sharpless copper(I) catalyzed azide-alkyne cycloaddition reaction.

As seen in Table 1.1, ferrocene has been attached to pyrolytic graphite edge (PGE) and glassy carbon (GCE) electrodes through the grafting of 4-azidobenzenediazonium salt, and the click chemistry reaction between the alkyne group of ethynylferrocene and the

surface azide groups [14]. The latter method of attachment shows a great deal of potential for applications in surface chemistry. However, studies are still scarce on the alkyne/azide method for attaching ferrocene. This work thus investigates the use of the C≡CH functional group of ethynylferrocene to attach this complex to different surfaces – adsorbed single-walled carbon nanotubes on glassy carbon (GC/SWCNT) and multi-walled carbon nanotube paper (MWCNT-paper), compared to attachment on the GCE – through a combination of grafting, electropolymerisation and click chemistry. Nanomaterials have in many cases caused significant improvement in the behaviour of electrodes [19–21], and make this a particularly interesting approach. These new, ferrocene-modified surfaces are used in order to show the potential of this attachment method for many applications. The ferrocene-modified electrode is employed for the detection of sulphite as a test molecule.

1.1.3. Metallophthalocyanines (MPcs)

1.1.3.1. General properties and applications

Metallophthalocyanines (MPcs) are macrocyclic 18π-electron systems and a variety of substituents can be positioned at four different points on each isoiminoindoline ring, resulting in a large range of products with a common central structure (Fig. 1.1). They have been widely studied because of their diversity. Their properties and characteristics can be simply tailored by changing the central metal and/or the nature of the substituents on the ring [22–31].

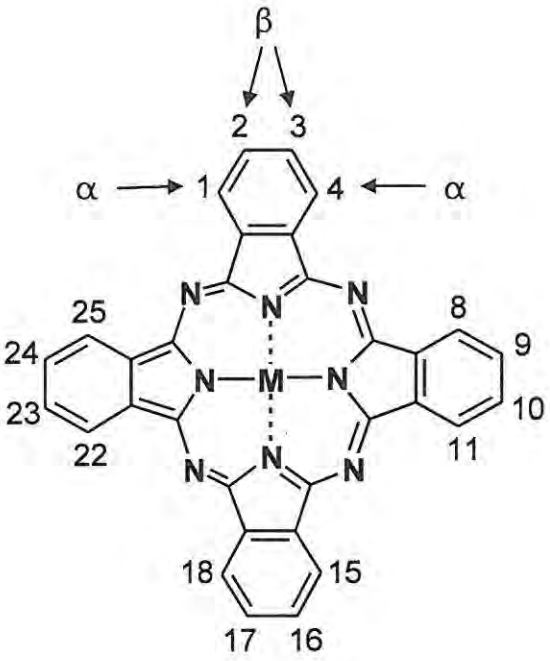

Figure 1.1. General structure of MPcs showing the α (non-peripheral) and β (peripheral) positions and the conventional numbering system.

Depending on the central metal that is used, MPcs have found applications in optics [24], imaging, pigments, photodynamic therapy of cancer [23], and electrochemistry [22]. For electrochemistry purposes, the d-group metals manganese, iron, cobalt and nickel are electroactive. MPcs containing these metals can be easily oxidised and reduced at the central metal, allowing them to act as electron transfer mediators [22]. The substituents introduced on the Pc ring are important not only for the introduction of linking groups, but also for their impact on the solubility of the complex.

This work investigates a common method in which MPcs can be modified in order to facilitate attachment to electrode surfaces through self-assembly, as well as use of the link through axial bonds which has rarely been exploited for surface modification.

1.1.3.2. MPcs as electrode modifiers

Electrodes modified with MPcs have been widely used to facilitate electrocatalysis of many analytes that are otherwise difficult to detect, as MPcs immobilised on electrode surfaces can act as electron relays for redox reaction activation [22]. The substituents on the Pc ring can also be used to link the MPcs to an electrode, in order to make a reproducible, stable and uniform modified surface.

MPcs have been used to form self-assembled monolayers (SAMs) on gold [31–35], they have been deposited on alumina and silica by thermal evaporation under vacuum [36,37], adsorbed or electrodeposited on graphite and glassy carbon electrodes [38–42], adsorbed on semiconductors [37], bound to a SAM of mercaptopyridine on gold through axial ligation [43] and covalently linked to a carbon surface using a combination of grafting and chemical linking [44], among other techniques. However, new and better methods for linking MPcs to surfaces are constantly being investigated, in order to find a method that can be applied to many different surfaces and that would provide a more stable means of attachment and improved electrocatalytic behaviour.

1.1.3.3. Synthetic methods of Pcs

The general synthesis of phthalocyanines can be outlined as seen in Scheme 1.1, using an unsubstituted phthalonitrile as the starting material [45]. However, phthalic anhydride, 1,3-diiminoisoindoline, phthalimide or phthalic acid can also be used as starting materials. For MPc synthesis, the starting material generally needs to be refluxed in a suitable solvent with reagents like a metal salt (if a metallated Pc is desired), a base and a catalyst. Substituted Pcs can be synthesized in a similar way, using the appropriately substituted starting material [45].

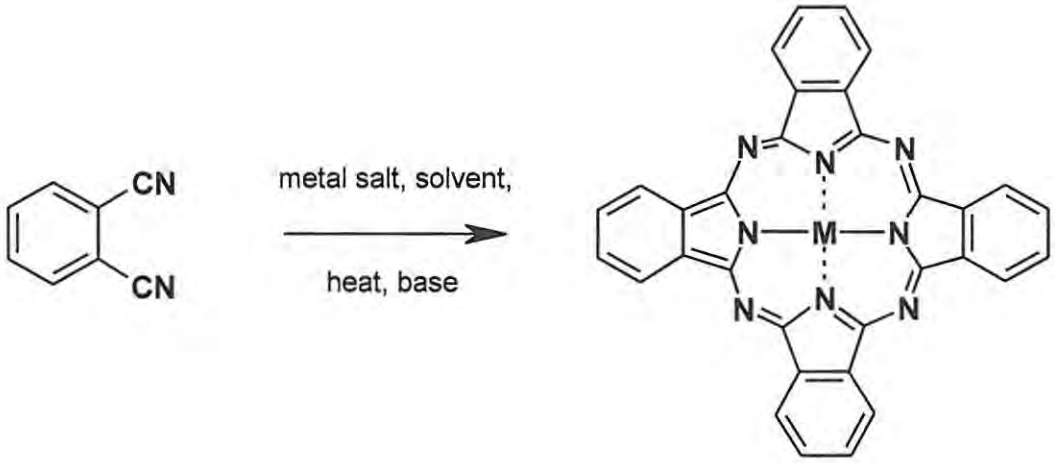

Scheme 1.1. General synthesis route for MPcs using phthalonitrile as the starting material.

The peripheral rings of the Pc can be substituted at the α (non-peripheral) or β (peripheral) positions, and they are commonly tetra- or octa-substituted. An illustration of these positions and the numbering of the Pc substituents is shown in Fig. 1.1. Although tetra-substitution is more common, octa-substitution has an advantage due to isomeric purity, which makes purification and characterisation simpler. Of interest in this work are the octa-substituted thio-Pcs, and the general synthesis is shown in Scheme 1.2 [46].

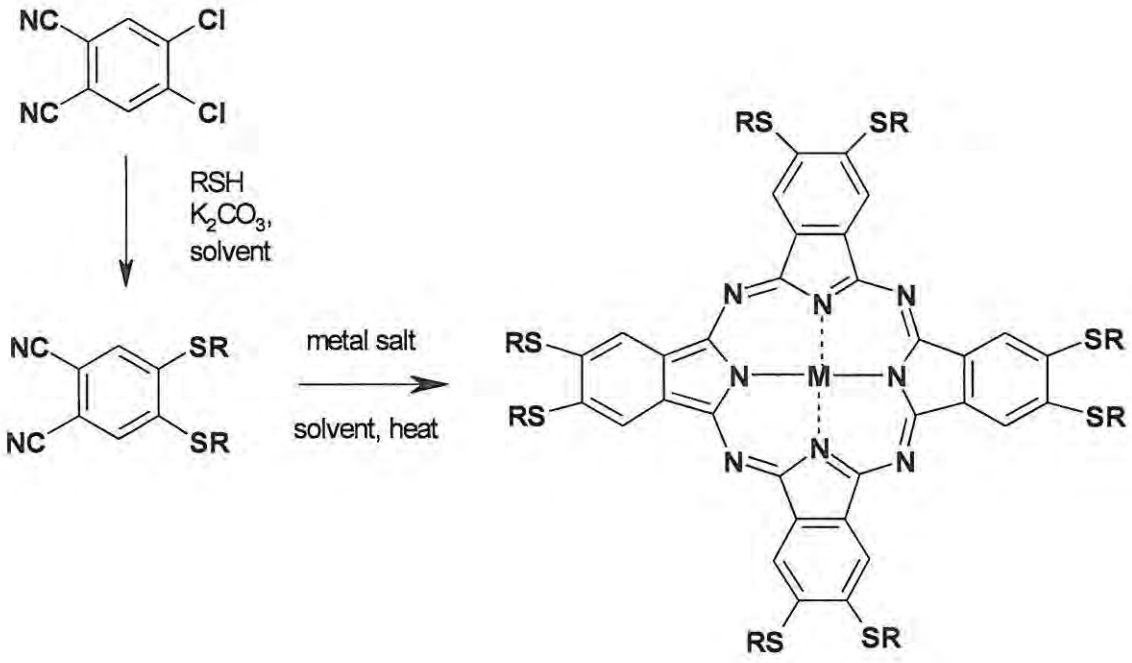

Scheme 1.2. Synthesis route for MPcs octa-substituted at the peripheral position with sulphur groups.

1.1.3.4. Characterisation of MPcs

MPcs can be characterised by both spectroscopic and electrochemical techniques. Pcs have two characteristic absorbance bands (Q and Soret/B band) due to the electronic transitions following Gouterman's model [25,26]. The B band absorbs in the blue region between 300 and 450 nm, and the more intense Q band absorbs in the red region between 600 and 800 nm, as shown in Fig. 1.2(a) [47] with the electronic levels shown in Fig. 1.2(b) [26]. These highest occupied molecular orbital-lowest occupied molecular orbital (HOMO-LUMO) transitions from a_{1u} to e_g of the Q band can be varied by the introduction of electron withdrawing or donating groups on the ring, increasing or decreasing the HOMO-LUMO gap and causing a blue or red shift in the Q band, respectively [26]. Other factors that also affect the Q band are the oxidation state of the metal, the position of the substituents (non-peripheral vs peripheral), and the solvent [26].

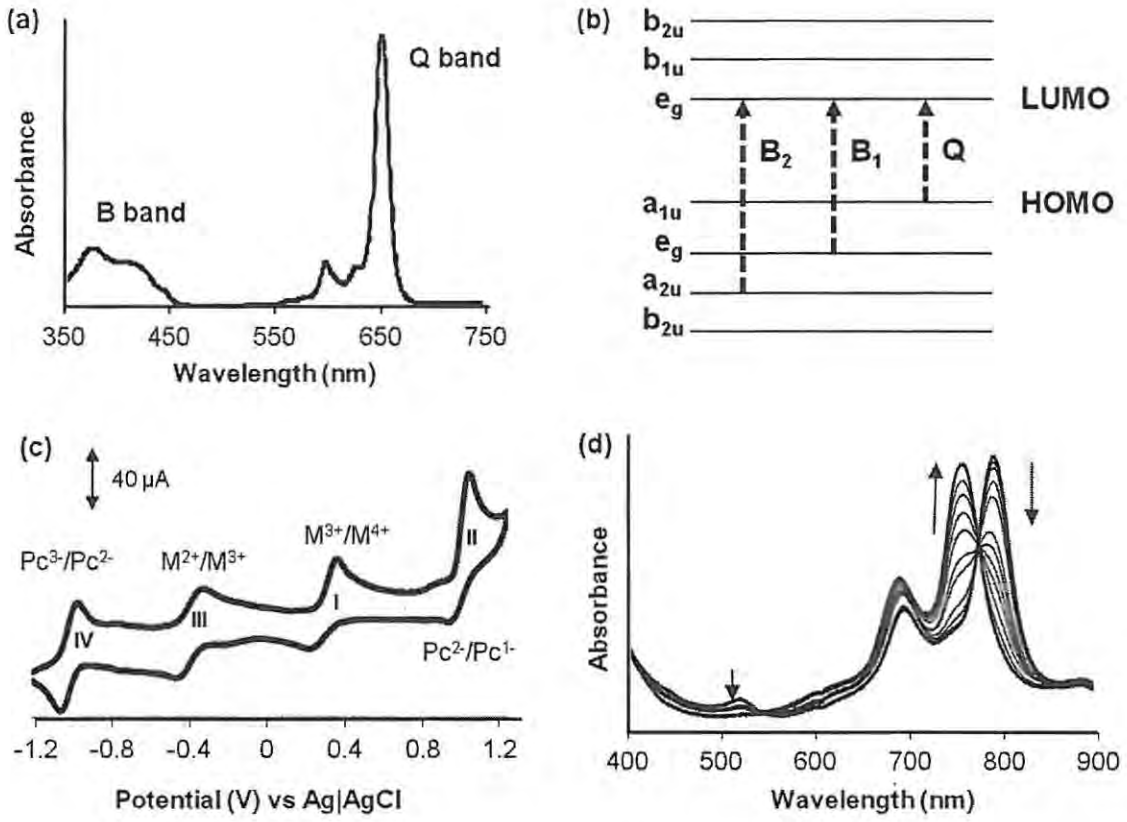

Figure 1.2. (a) Absorbance spectrum of a MPc, (b) Gouterman's orbital model of MPc electronic transitions, (c) typical cyclic voltammogram of a MPc showing common ring and metal redox processes and (d) spectroelectrochemistry absorbance spectrum showing absorbance changes upon reduction of the central metal from M^{3+} to M^{2+} charge state [47].

Electrochemical characterisation of Pcs can be used to elucidate the redox processes occurring because of the electron-rich ring and the variable oxidation state of the central metal. At its neutral ground state, the Pc ring is a dianion with a charge of 2- [45]. The Pc^{2-} can undergo successive oxidation or reduction reactions, losing electrons to form the Pc^{1-} and Pc^{0} π-cations, or gaining electrons to form reduced Pc^{3-}, Pc^{4-}, Pc^{5-} and Pc^{6-} π-

anions [48]. For the M(II)Pc complexes where the central metal orbitals lie between the HOMO and LUMO of the ring, the first oxidation occurs at the metal, e.g. for Co(II) and Fe(II), while with Cu(II) and Zn(II), for example, ring oxidation generally occurs first, depending on the solvent [45]. The typical cyclic voltammogram (CV) of a metallated Pc is shown in Fig. 1.2(c) [47].

Spectroelectrochemistry involves the combination of optical and electrochemical analyses. Common electrochemical cells used are either an optically transparent electrode (OTE) or an optically transparent thin-layer electrode (OTTLE), and electrolysis is particularly fast and efficient in the latter system [49–51]. For basic spectroelectrochemistry, a beam of light is passed through the cell and the absorbance changes upon oxidation/reduction are monitored. For MPcs, the Q band in the absorbance spectra can be used to characterise the complex [26]. Oxidation or reduction of the Pc can occur at the ring or at the metal, and the species produced upon oxidation/reduction have different absorbance spectra that can be used to determine where the oxidation/reduction occurs [26,48]. If it occurs at the central metal, this results in a shift in the Q band without much change in intensity [26,30,31,52]. If at the ring, this results in a collapse of the Q band, and the formation of new bands between 400 and 600 nm [48]. Spectroelectrochemistry can thus be used to show these oxidation and reduction processes, and also to show where in the complex it occurs, making it a particularly useful technique for analysing MPcs and for confirming the electrochemical assignments of redox processes. A typical spectroelectrochemistry result for MPc oxidation and reduction is shown in Fig. 1.2(d).

1.1.4. Carbon Nanotubes (CNTs)

Carbon nanotubes (CNTs) are visualised as hollow tubes made up of rolled graphene sheets of sp^2 carbons, Fig. 1.3. They are also called "buckytubes" or "fullerene pipes", because they are in the same structural family as buckminsterfullerene, or buckyballs, which are nano-sized in three dimensions, while the CNTs are nano-sized in two dimensions only [53,54]. CNTs were first discovered as hollow tubular carbon filaments in 1952 by Radushkevich and Lukyanovich [55], and were first grown by chemical vapour deposition in 1976 by Oberlin et al. [56]. They only gained real popularity, however, after the publication in Nature in 1991 by Iijima [57]. The types of CNTs most commonly used are the single-walled CNTs (SWCNTs), or the multi-walled CNTs (MWCNTs). SWCNTs were first recorded in 1993 by Iijima and Ichihashi [58] and Bethune et al. [59]. Their nano-size affords these materials unique properties, such as mechanical strength, good electrical conductivity, chemical stability and a large surface area to volume ratio [54,60,61]. The electronic properties of CNTs can range in behaviour from metallic and semi-metallic to semi-conductive, depending on the structure and helicity – with the MWCNTs having more complex behaviour, while the SWCNTs in general have excellent electron transport properties [54].

Figure 1.3. Structure of single-walled carbon nanotubes (SWCNTs).

Typically the diameter of SWCNTs ranges from 0.4 – 2 nm [54,58,59], while the MWCNTs have diameters up to 20 nm [62,63]. CNTs can be functionalised with carboxylic acid groups through oxidation with concentrated acid, which also serves to shorten and purify the tubes [53]. CNTs generally have poor solubility and show strong aggregation in many solvents due to oxidation occurring primarily at the ends of the tubes. However, this can also be beneficial in preventing leaching from surfaces where the CNTs are merely adsorbed [21].

Particularly interesting for electrochemical applications are the many cases in which CNTs have been shown to improve the behaviour of electrodes and sensors [19–21]. CNTs have been shown to improve electron transfer rates when used on electrodes, and have even exhibited some electrocatalytic properties, although this is attributed to the more reactive open ends of the tubes [54,60]. CNTs can cause reduction in overpotentials and surface fouling on electrodes as well as an increase in the voltammetric signals [64–66]. These nanomaterials have been investigated for their applications in the development of

electrochemical sensors and for surface modification purposes, where improvements in sensitivity and lowering of detection limits is important in the analysis of analytes found in very low concentrations. CNTs can be immobilized on electrodes (most commonly carbon electrodes) by a number of different methods, including dry drop (on GCEs), screen-printing, self-assembly or abrasive immobilization (on basal plane PGEs) among others [21,64–68]. Dry drop immobilisation on GCEs is one of the fastest and simplest examples, and relies on the $\pi - \pi$ interactions between the CNTs and the GCE surface [21,65]. Both MWCNTs and SWCNTs have been shown to increase the electrocatalytic activity of modified electrodes in a number of cases, including the reduction of oxygen in buffer solution (MWCNTs) and nitrite (SWCNTs) as specific examples [21]. CNTs can be oriented (vertically aligned) or non-oriented (random mixture) on the electrode surface, each with a potentially different effect on the sensor [69].

CNTs can also be modified through methods other than oxidation in acidic media, in order to attach other catalysts or complexes. Direct covalent modification of CNTs, either adsorbed on an electrode or in a paper form (bucky paper) with both ferrocene and iron phthalocyanine (FePc), has been investigated in this work through electrochemical grafting and click chemistry, which will be discussed in more detail in the next section.

1.1.5. Modification approaches

As mentioned in each section describing species that can be attached to electrodes, there are numerous ways in which surfaces can undergo modification. Electrochemistry is used

for electrografting and electropolymerisation directly on electrodes. Self assembly, adsorption (drop dry) and chemical modification techniques were used in this work as well. These are systematically described with examples below.

1.1.5.1. Self assembled monolayers (SAMs)

Gold and platinum are the two most commonly used metal electrodes [49]. The high conductivity of metal electrodes means that they have a low background current, they are easily polished, and there are a number of ways in which they can be modified [50]. However, they can easily undergo passivation and gold has a limited potential range [49,50]. Despite its disadvantages, a particularly useful property of gold is that sulphur binds to it strongly and spontaneously, and so a self-assembled monolayer (SAM) of thiol-terminating compounds, or compounds containing sulphur, can be formed on gold [22,51,70].

Strong adsorption of sulphur-containing compounds on gold in the form of SAMs provides a useful method of modification, as the monolayer is often uniform and quite stable [70], although often not thermally stable [71]. Many compounds can be attached to the surface in this way, such as phthalocyanines and long-chain alkyl groups among others [22,27,51,70]. The SAM on gold does not require a terminating –SH group, and has been seen to form with disulphides and di-substituted sulphides while leaving the C-S bond intact [70,72–74].

Fig. 1.4 shows a few examples of the types of compounds that can be bound to gold, as well as a representation of thiols and RS on gold. This also illustrates the different orientations SAMs can have on gold.

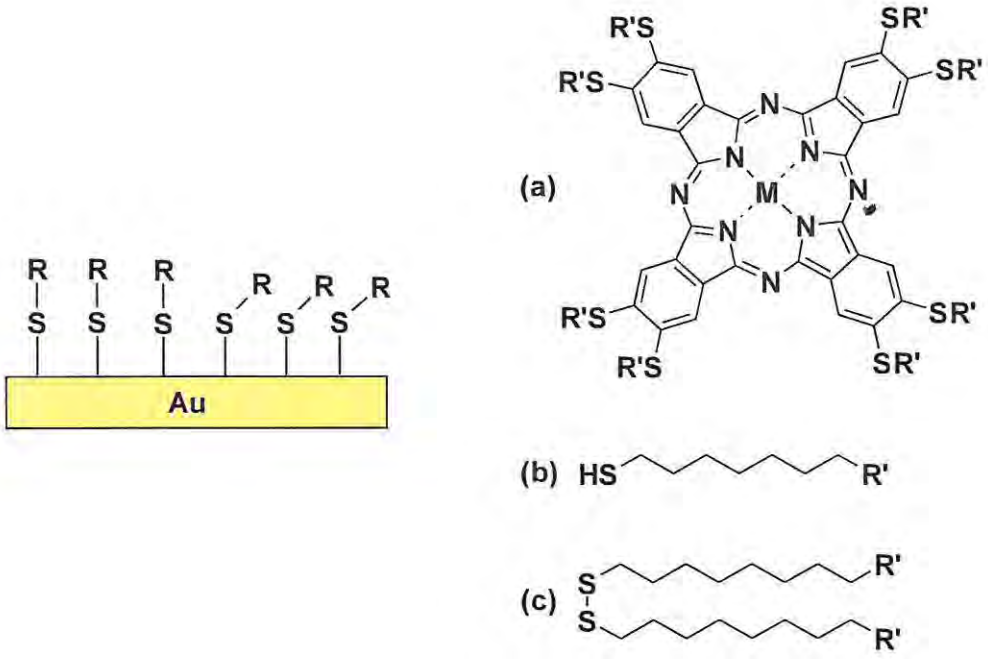

Figure 1.4. A schematic representation of a long-chain thiol bonded to gold as a multi-directional SAM and examples of (a) peripherally octa-substituted MPc with sulphur-containing substituents, (b) thiol and (c) disulphide, all of which can be used to form SAMs on gold [70–74].

While many MPcs have been studied for SAM formation on gold, manganese phthalocyanines (MnPcs) have not been extensively explored, due to their relatively low electroactive behaviour compared to metals such as iron [75]. However, manganese has

good biocompatibility, and MnPcs are believed to have potential as superoxide dismutase mimics [76,77].

Table 1.2 shows the MnPcs which have been used to form SAMs on gold through this S-Au bond, as well as some details of the surface coverage (Γ) of the MnPcs on gold and the analytes these electrodes have been used to detect with the limit of detection (LoD), if applicable [27,31,47,78–85].

Table 1.2. Manganese phthalocyanines used to form self-assembled monolayers on gold.

MnPc	Γ [a] (10^{10} mol.cm^{-2})	Analyte	LoD (μM)	Reference
β-MnTBTPc	0.69	nitrite, sulphite	-	[31,78,79]
β-MnTDdTPc	0.78	nitrite, sulphite	-	[31,78,79]
α-MnTPhTPc	1.06	nitrite, l-cysteine	0.29, 0.29	[27,80]
α-MnOHTPc	0.77	H_2O_2	0.10	[47]
β -MnOHTPc	1.74	H_2O_2	0.24	[47]
α-MnTPyTPc	1.73	nitrite, l-cysteine	0.27, 0.31	[80]
α-Mn-Q-TPyTPc	2.77	nitrite, l-cysteine	0.18, 0.28	[80]
β -MnTPyTPc	2.80	nitrite, l-cysteine	0.30, 0.31	[80]
β -Mn-Q-TPyTPc	2.67	nitrite, l-cysteine	0.27, 0.29	[80]
α-MnOPTPc	1.10	l-cysteine	0.75	[52,81]
α-MnTBTPc	0.69	carbofuran	-	[82]
α-MnTDEAETPc	2.69	carbofuran	-	[83]
β -MnOPyTPc	2.40	nitrite	0.29	[84]
β -Mn-Q-OPyTPc	1.14	nitrite	0.20	[84]
β -MnOOTPc	-	-	-	[85]
β -MnODdTPc	-	-	-	[85]

[a] Surface coverage determined by electrochemistry; abbreviations: LoD = limit of detection, β = peripheral substitution, α = non-peripheral substitution, TBT = tetra(benzylthio), TDdT = tetra(dodecylthio), TPhT = tetra(phenylthio), OPT =

octa(pentylthio), TPyT = tetra(2-mercaptopyridine), Q = quarternized, ODT = octa(decylthio), OBT = octa(benzylthio), OPhT = octa(phenylthio), TDEAET = tetra(diethylaminoethanethiol), OHT = octa(hexylthio), OPyT = octa(2-mercaptopyridine), OOT = octa(octylthio), ODdT = octa(dodecylthio).

Table 1.2 shows that a variety of MnPc complexes have been employed for SAMs, but only two complexes were compared for the effects of the position of substitution (α vs β), and only one set of tetra-substituted MnPcs were compared for the effect of alkyl- vs arylthio substituents. Also, the fate of the R-S bond for alkyl and arylthio substituents following SAM formation has not been adequately discussed for these complexes, and particularly the impact these substituents have on attachment to the gold surface.

For the SAM studies in this work, manganese phthalocyanine octa-substituted at the peripheral position with aryl- and alkylthio groups were used. Four new MnPcs were synthesised following a similar procedure to that reported in literature [52], and these are shown in Fig. 1.5. The comparison of SAM formation and electrochemical behaviour of the aryl *vs* alkyl substituents was of interest, and they could be compared to their tetra or non-peripheral counterparts and similar complexes shown in Table 1.2. X-ray photoelectron spectroscopy characterisation was also useful in confirming the formation of the Au-S bond, the fate of the R-S bond, and in giving some insight into reasons for the different surface coverage values for the different substituents. Finally, the SAM of complex **1d** was used to detect thiocyanate as a test analyte for the potential of this surface for electrocatalysis.

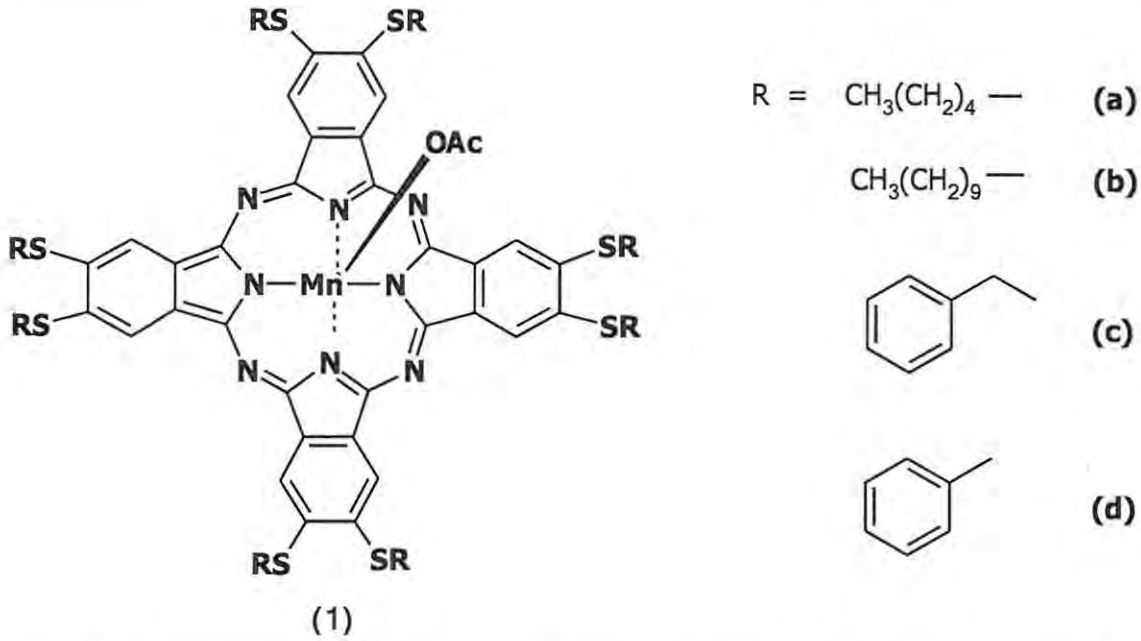

(1)

Figure 1.5. Structures of the MnPc complexes produced in this work. Complex **1a**, manganese(III) octa(pentylthio)phthalocyanine, (OAc)MnPc$^{\beta}${S(CH$_2$)$_4$CH$_3$}$_8$ (MnOPTPc). Complex **1b**, manganese(III) octa(decylthio)phthalocyanine, (OAc)MnPc$^{\beta}${(SCH$_2$)$_9$CH$_3$}$_8$ (MnODTPc). Complex **1c**, manganese(III) octa(benzylthio) phthalocyanine, (OAc)MnPc$^{\beta}$(SCH$_2$Ph)$_8$ (MnOBTPc). Complex **1d**, manganese(III) octa(phenylthio)phthalocyanine, (OAc)MnPc$^{\beta}$(SPh)$_8$ (MnOPhTPc).

1.1.5.2. Grafting of diazonium salts

Grafting is the term given to the covalent linkage of diazonium salts to a conductive surface by electrochemical or chemical reduction, and although this modification has been done mostly on carbon, almost any conductive or semi-conductive surface can be modified using this technique, making it one of the most versatile surface chemistry reactions [86–92]. It is also a relatively new technique, with grafting of diazonium salts

through electrochemical reduction of a carbon surface first shown in 1992 by Delamar et al. [86]. Grafting proceeds by the reaction shown in Scheme 1.3 on glassy carbon as an example, with nitrogen as the by-product [86–88]. This is a simplified diagram as multilayer formation is most common, unless bulky R groups are used, due to the highly reactive nature of the radical [93]. This method has been used to attach a variety of different diazonium salts on surfaces, and these layers require mechanical abrasion before they can be removed – again confirming that the linkage is through a covalent bond [14,87,88,94–98]. The density of the layer can be controlled by varying parameters like the concentration of the diazonium salt, the number of reduction cycles, and the scan rate [87,99]. Grafting of certain diazonium salts has also been shown to have a blocking effect on the electrode, particularly when the layer is well-packed [88]. This blocking effect can thus be used to determine whether the layer is pinhole free, or if there are any defects in the coverage [88].

MPcs bearing amino [100] and carboxyl [44] substituents have been attached to 4-nitrobenzenediazonium grafted surfaces, following reduction of the nitro group to an amino group, through (i) attachment to benzene-1,4-dicarbaldehyde activated 4-aminobenzenediazonium via Schiff-base reaction on screen printed gold electrodes [100] and (ii) amide linkage to grafted 4-aminobenzenediazonium on glassy carbon [44], respectively.

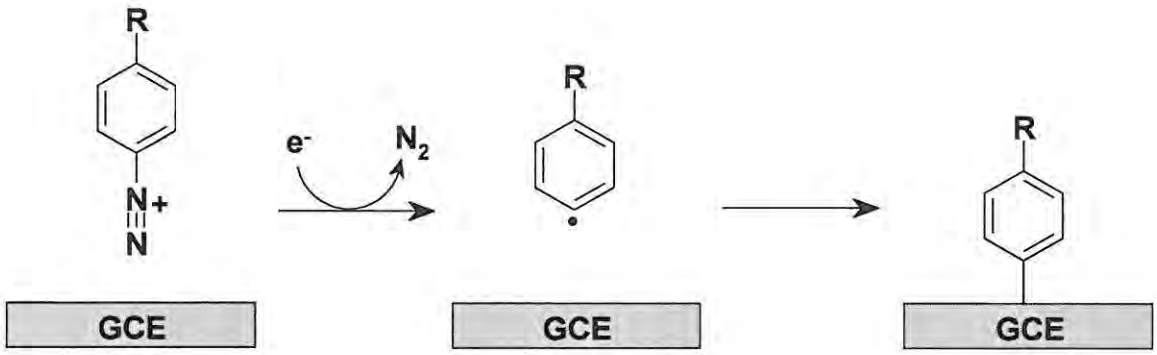

Scheme 1.3. Schematic representation of a diazonium salt grafting on to a GCE upon electrochemical reduction.

Although many different diazonium salts show good possibilities for providing linking groups on electrode surfaces, this work focuses on 4-azidobenzenediazonium tetrafluoroborate grafting primarily on GCEs. The precursor 4-azidoaniline is labelled **2a** and the 4-azidobenzenediazonium salt **2b** in this work. This diazonium salt has two major advantages afforded by the azide substituent: (i) the kinetics of adsorption is slower than the commonly used diazonium salts [14] and (ii) it offers an attractive and efficient way of further chemical functionalisation of the electrografted surface through the well known Sharpless copper(I) catalyzed azide-alkyne cycloaddition reaction, which is referred to simply as the "click chemistry" reaction in this work [14]. Table 1.3 shows some of the molecules that have been linked to electrode surfaces through the use of the electrochemically grafted diazonium salts bearing azide or alkyne groups and click chemistry, from ferrocene [14,101] and biomolecules [14] to polymers [102], as well as some examples of chemical grafting of these diazonium salts on SWCNTs for attachment of MPcs [103], porphyrins [104], ferrocene [105] and polystyrene [106].

Table 1.3. Selection of (bio)molecules that have been attached to surfaces through linking to electrochemically and chemically grafted azide/alkyne-bearing diazonium salts.

Grafting Method	Substrate	(Bio)molecule	Diazonium Functional Group	Reference
Electrochemical	PGE/GCE	ferrocene-C≡CH	N_3 (**2b**)	[14]
	PGE/GCE	ferrocene-CH_3N_3	C≡CH	[14]
	PGE	biotin-C≡CH	N_3 (**2b**)	[14]
	GCE	ferrocene-CH_3N_3	C≡C-Si($CH(CH_3)_2$)$_3$	[101]
	AuE	OEG	CH_3N_3 (from CH_3Br)	[102]
	AuE	FEG	CH_3N_3 (from CH_3Br)	[102]
Chemical	SWCNT	ZnPc-N_3	C≡C-Si(CH_3)$_3$	[103]
	SWCNT	ZnPy-N_3	C≡C-Si(CH_3)$_3$	[104]
	SWCNT	ferrocene-C≡CH	N_3 (**2b**)	[105]
	SWCNT	polystyrene-N_3	OCH_3C≡CH	[106]

Abbreviations: AuE = gold electrode, GCE = glassy carbon electrode, SWCNT = single-walled carbon nanotubes, PGE = pyrolytic graphite edge electrode, OEG = 4,7,10,13,16-pentaoxanonadeca-1,18-diyne (n = 4), FEG = 7,7,8,8,9,9,10,10,11,11,12,12, 13,13,14,14,14-heptadecafluoro-4-oxatetradeca-1-yne, ZnPc = zinc phthalocyanine, ZnPy = zinc porphyrin.

As Table 1.3 shows, electrochemical grafting of **2b** on bare glassy carbon has been done, however this work presents the first investigation into grafting of this salt for attachment

of ferrocene on MWCNT-paper and adsorbed SWCNTs on a GCE, as well as click chemistry with 4-ethynylpyridine for axial ligation to FePc. Chemical grafting of many different types of diazonium salts on SWCNTs has been reported thoroughly by Tour and co-workers [107–110], but for the case of the **2b** species of interest in this work, there is only one very recent report of attachment of ferrocene through click chemistry [105]. However, electrochemical grafting of SWCNT-paper was shown to be possible by Bahr et. al [89], and is a new and relatively unexplored area of interest in materials science. Chemical grafting on MWCNTs has also been scarcely reported, due to its lower reactivity and the lower degree of functionalisation [109,111].

Grafting of **2b** on GC/SWCNT as well as on branched MWCNT-paper for the attachment of ferrocene is thus reported here for the first time, and the click chemistry reaction was also used for attachment of pyridine, followed by axial ligation to FePc, on the GCE and GC/SWCNT surface. Click chemistry is discussed in more detail in Section 1.1.5.4, and axial ligation in Section 1.1.5.5.

GCEs are often used because of their chemical inertness, wide potential range, good mechanical and electrochemical properties and their good performance [49]. These electrodes require pre-treatment by polishing with an alumina slurry or diamond paste to improve their electron-transfer rates by removing surface contaminants [49,50]. Carbon's high surface reactivity means that it can form bonds with hydrogen, hydroxyl, carboxyl and quinone groups [50,112]. This makes the electrode susceptible to poisoning (passivation), but also means that it can be easily modified [50]. It is often necessary to modify GCEs to improve their detection limits and efficiency [44]. Glassy carbon is the

most widely used of the carbon electrodes, which also include carbon paste and graphite [50]. Very high temperatures and pressures are required to produce this hard isotrope of carbon [50]. Because glassy carbon is partly amorphous, its structure is not completely uniform [50]. GCEs have been modified by covalent immobilisation of reactive groups as early as the 1970's [113,114]. Porphyrins were one of the early class of compounds covalently attached to the surface of the electrode, and their potential as electron-transfer mediators in electrocatalysis was mentioned [113]. Phthalocyanines are currently being widely studied for their abilities to act as electrocatalysts and are from the same family of compounds as porphyrins.

Grafting of more complex derivatives of diazonium salts has also been investigated as an approach for introducing redox-active species directly on to the electrode surface. These include porphyrins, osmium and ruthenium complexes [115–117]. As a comparison to the graft-then-click chemistry approach, direct grafting of the pre-clicked complex 4-(4-ferrocenyl-1H-1,2,3-triazol-1-yl)aniline (**2c**) through *in situ* diazotation (to the diazonium salt **2d**) and electrochemical grafting is reported in this work for the first time, and was compared to electropolymerisation of the aniline derivatives which are discussed in more detail in the next section. The structure of complex **2c** is shown in Fig. 1.6.

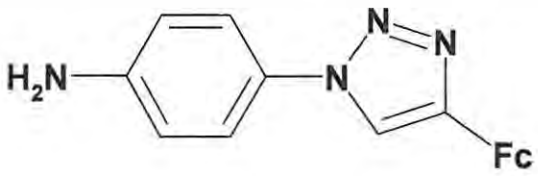

Figure 1.6. Structure of 4-(4-ferrocenyl-1H-1,2,3-triazol-1-yl)aniline (2c).

As well as a "global" modification through electrochemical grafting, another point of interest is in micropatterning of surfaces (or "local" modification) using this reaction in combination with scanning electrochemical microscopy (SECM). For this purpose, gold plate electrodes were used due to the availability of an SECM setup where the gold substrate could be given an electrochemical bias as well as the SECM probe. Although grafting is a useful process for modifying surfaces, several studies have also shown the spontaneous adsorption of diazonium species on carbon, gold and copper surfaces from acetonitrile and aqueous solutions [94,118–123], which may prevent the precise control of further electrochemical grafting. Thus, the use of diazonium salts for the microstructuring of surfaces by ultramicrotechniques such as SECM is restricted due to the spontaneous derivatization of exposed surfaces. An example was recently reported on direct electrochemical patterning of a diazonium salt via a one-pot sequential reaction for local electrogeneration of the diazonium salt, followed by its electrografting on the substrate [124], and although this approach avoided the spontaneous adsorption of the diazonium salt on the substrate, the technical protocol needed precise control of the multi-step procedure. The efficiency of the strategy strongly depended on the kinetics of the diazotization reaction and the electroreduction of the obtained diazonium salt can

also occur at the SECM tip and block the micro-grafting process. Besides this approach, one can cite the drawing of patterns of a thin passivating layer on a gold electrode surface by electrochemical reduction of an aryliodonium salt at very negative potential values by SECM [125]. The slow kinetics of **2b** made it an ideal candidate for micropatterning, and this work shows for the first time the microelectrochemical patterning of gold surfaces by application of SECM in a three-electrode configuration using **2b** with a very simple approach. An example of this technique is shown in Scheme 1.4 below.

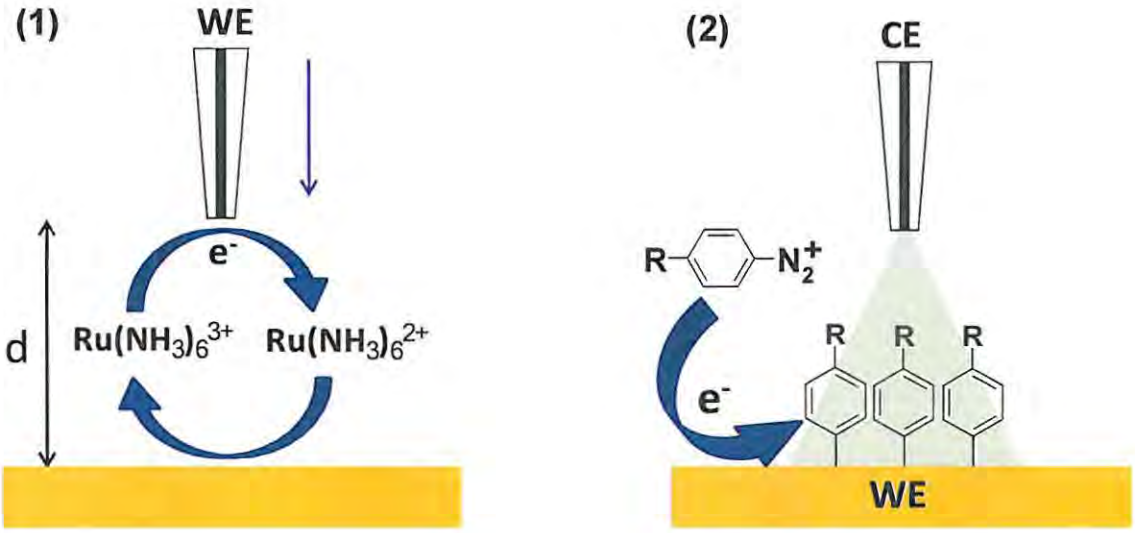

Scheme 1.4. SECM local grafting of a gold substrate by (1) approaching the substrate using the SECM probe and reduction of $[Ru(NH_3)_6]Cl_3$ as a redox mediator to a desired distance *d* from the surface and (2) using the SECM probe as the counter electrode and the substrate as the working electrode while reducing the diazonium salt.

1.1.5.3. Electropolymerisation of aniline

Electropolymerisation of aniline to form polyaniline (PANI) is a well-known and well-used electrochemical process, and in a few cases substituted aniline has also been electropolymerised [51,126–131]. When dealing with *para*-substituted aniline, as is the interest in this work, polymerisation can occur through branching at either the *ortho*- or *para*-position, Scheme 1.5, resulting in retention or elimination of the substituted group respectively [126]. It is believed that oxidation through a potential step method, as opposed to a potential sweep method, can increase the rate of *ortho*-coupling [132]. However, *ortho*-position coupling is not sterically favourable for the formation of a fully conjugated system, and this has been mentioned as a cause for a drop in conductivity of the polymer of 4-nitroaniline [131].

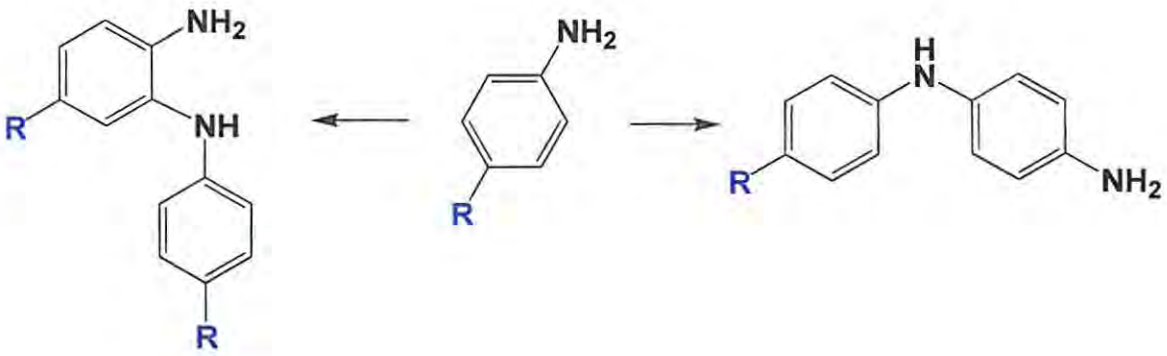

Scheme 1.5. Electropolymerisation routes of *para*-substituted aniline, through either the *ortho* (left) or *para* (right) positions.

It is also likely that the electron-donating/withdrawing nature of substituents would play a role in the ease of polymerisation of these anilines, with strong electron withdrawing groups likely having a negative effect on polymer formation [131]. These layers, depending on their composition, can be expected to have pH-dependent behaviour [131].

Electropolymerised layers are useful for surface modification as they can greatly enhance the electrochemically active area of the electrode, resulting in more sensitive sensors [131]. Although electropolymerisation of *para*-substituted anilines is slower than for the *ortho*- or *meta*-substituted derivatives [129], it is possible to use this technique to introduce interesting linking groups into the electropolymerised layer, for further modification by click chemistry in this case.

This work compares electropolymerisation of 4-azidoaniline (**2a**) with electrografting of the diazonium salt **2b** for the attachment of ferrocene to a glassy carbon electrode through click chemistry. This is the first investigation of this *para*-substituted aniline for electropolymerisation purposes, and also for electropolymerisation of 4-(4-ferrocenyl-1H-1,2,3-triazol-1-yl)aniline (**2c**), Fig. 1.6. This work also makes a comparison of the electropolymerisation of complex **2c** with the polymerise-then-click chemistry strategy.

1.1.5.4. Click chemistry

The usefulness of grafting and electropolymerisation can be further expanded by combining these methods with a click chemistry reaction. The Sharpless "click" reaction term was first used in 2001 [133]. For a reaction to qualify under the "click chemistry"

title, it must conform to a number of criteria. These include high yields with inoffensive by-products that are easily removed, simple product isolation and reaction conditions, and the product should be stable [133]. A very good example of a click chemistry reaction is the Huisgen 1,3-dipolar cycloaddition of azides and alkynes to give triazole linkages [133,134]. This reaction has been used in the synthesis of organic compounds [133–138], and more recently in the functionalisation of many different surfaces (gold, silica and glassy carbon) [12,14,71,73,102,135,139–141]. The general scheme for click chemistry on a **2b**-grafted layer is shown in Scheme 1.6.

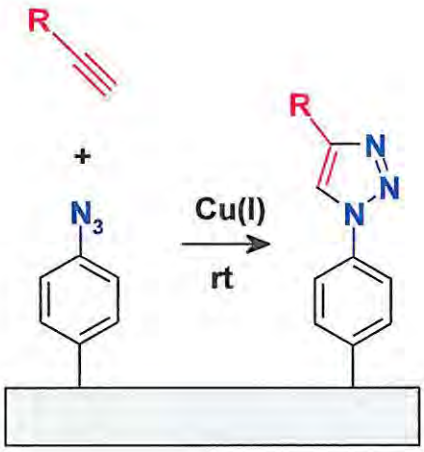

Scheme 1.6. A schematic representation of the Sharpless click chemistry reaction using the Huisgen 1,3-dipolar cycloaddition of a substituted alkyne with a **2b**-grafted layer on a substrate.

Recent studies have reported on electropolymerisation of pyrrole synthesized with terminal azide or alkyne groups and on the use of poly(3,4-(1-

azidomethylethylene)dioxythiophene) (PEDOT) bearing azide groups for interfacial click chemistry [15,142,143]. There are an increasing number of reports of other polymers making use of the click chemistry reaction as well [144–148]. But, to our knowledge, this work presents the first case of electropolymerisation of aniline-based derivatives such as **2a** for use in click chemistry attachment of ferrocene. Research on ferrocene-based polymers has many applications, such as the fabrication of biosensors [149]. We also investigate here the use of 4-ethynylpyridine click chemistry to a **2b**-grafted surface for the axial ligation of FePc to the modified electrode.

1.1.5.5. Axial ligation to pyridine

Comprehensive studies on coordination of MPcs to bases containing nitrogen have been done, and FePc in particular has been shown to form strong axial bonds to pyridine [150–154]. FePc forms a 1:1 five-coordinate complex with pyridine immediately in solution, but a 1:2 complex can also form after time, with the pyridine molecular planes perpendicular to the phthalocyanine plane [151,153]. Unsubstituted FePc with pyridine adducts is thermally stable up to 175 °C [154], making this coordinate link potentially useful for surface modification purposes. Despite the possibility of linking MPcs to bound pyridine groups, this has only been briefly explored for adsorption of a cobalt phthalocyanine and cobalt porphyrin complex to a SAM of 4-mercaptopyridine on gold [155], and the electrocatalytic ability of these surfaces was studied in greater detail for iron, manganese and cobalt phthalocyanine [43,156]. This is a very useful approach to

attaching Pcs without extensive modification of the ring, and showed good stability over time [43,156]. Scheme 1.7 shows the axial ligation of MPcs to these mercaptopyridine SAMs. However, because of the limitations of these Au-S SAMs to gold electrodes, axial ligation to pyridine has not been explored for modification of carbon electrodes.

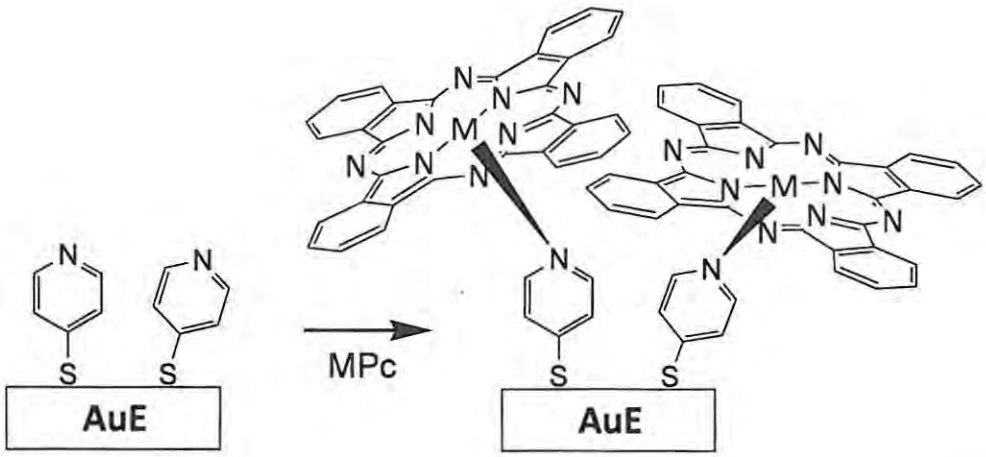

Scheme 1.7. Attachment of MPc through axial ligation to 4-mercaptopyridine SAMs on gold electrodes.

This work presents the first case of utilising grafting of diazonium salts, click chemistry, and axial ligation for attachment of FePc to carbon surfaces, and has potential for application to many other conductive substrates.

1.1.5.6. Adsorption (drop dry)

Adsorption (drop dry, casting, or thermal annealing) is a non-covalent method of modification, where simple intermolecular forces such as electrostatic attraction and π-π interactions are used to hold a thin layer of modifying species on a surface. This technique is a particularly useful method of modifying carbon surfaces through the use of π-π interactions with CNTs and MPcs, which are electron rich.

Adsorption has been used to modify GCEs with Pcs and MPcs for the detection of nitric oxide [40,157], with SWCNTs and MPcs for the detection of hydrazine [66], and with MWCNTs for detection of nitric oxide and biomolecules [158,159] as a few examples. Although a simple form of modification, these layers were found to have good stability and activity for electrocatalysis [40,66,157]. Table 1.4 shows further examples of electrodes with adsorbed SWCNTs and MPcs for the detection of a range of analytes [65,66,160–165], with one example of MWCNTs [166]. The MPcs are either covalently linked to the CNTs, or a simple mixture of the two are adsorbed on the GCE.

Table 1.4. Selection of MPcs that have been linked to carbon nanotubes and adsorbed on glassy carbon electrodes.

MPc	Substrate	Attachment	Analyte(s)	Reference
CoPc	GC/SWCNT-COOH	adsorption	2-mercaptoethanol, nitric oxide	[65]
β-NiTSPc	GC/SWCNT-COOH	adsorption	2-mercaptoethanol, nitric oxide	[65]
CoPc	GC/SWCNT-COOH	adsorption	hydrazine	[66]
β-CoTCPc	GC/SWCNT-BDA	amide	diuron	[160]
β-CoTCPc	GC/SWCNT-BDA	adsorption	diuron	[160]
β-CoTAPc	GC/SWCNT-COOH	amide	2-mercaptoethanol	[161]
β-CoTAPc	GC/SWCNT-COOH	adsorption	2-mercaptoethanol	[161]
β-NiTAPc	GC/SWCNT-COOH	amide	2-mercaptoethanol	[162]
β-NiTAPc	GC/SWCNT-COOH	adsorption	2-mercaptoethanol	[162]
β-FeTAPc	GC/SWCNT-COOH	amide	amitrole, diuron	[163]
β-FeTAPc	GC/SWCNT-COOH	adsorption	amitrole, diuron	[163]
α-NiODPc	GC/SWCNT-COOH	adsorption	2,4-dichlorophenol	[164]
β-CoTOBPc	GC/SWCNT-COOH	amide	amitrole	[165]
β-CoTOBPc	GC/SWCNT-COOH	adsorption	amitrole	[165]
β-CoTSPc	GC/MWCNT-COOH	electro-deposition	epinephrine	[166]

Abbreviations: GC = glassy carbon electrode, SWCNT = single-walled carbon nanotubes, MWCNT = multi-walled carbon nanotubes, TA = tetraamino, TC = tetracarboxy, OD =

octadecyl, TS = tetrasulphonated, TOB = 1,4-tetra-(4-oxobenzamide), BDA = 1,4-benzene diamine

Despite these extensive studies into the improvement of GCEs by adsorption of CNTs for the electrocatalysis of many analytes, this work presents the first case of electrochemical grafting on adsorbed SWCNTs, and subsequent click chemistry reaction with ferrocene, or with ethynylpyridine for the axial ligation of FePc.

1.2. Surface characterisation methods

1.2.1. Overview

Modified electrodes can be characterised by electrochemical methods, and by methods like X-ray photoelectron spectroscopy, atomic force microscopy and scanning electron microscopy. These techniques combined give a good idea of the effectiveness of the modification, the properties of the layer and the integrity of the surface coverage, among other factors. It is important to do comprehensive analysis of the modification layer by layer, as this data can play a large role in explaining the behaviour of the electrode when it is used for electrocatalysis. Many techniques are difficult to use for these monolayers, because of the sensitivity required to detect such thin layers and because the size of the electrode makes many non-electrochemical techniques impractical as the electrode cannot be put directly in the sample holder. However, this problem can be circumvented by the use of gold-coated glass, used for non-electrochemical deposition of SAMs on gold in this work due to availability, and glassy carbon and gold plate electrodes which can be modified exactly like the conventional electrodes. These characterisation techniques will be described briefly to give an outline of their principles and their usefulness for this work.

1.2.2. *Cyclic Voltammetry (CV)*

CV is used extensively for the study of reaction mechanisms, adsorption processes and even for quantitative analysis [49]. CV can give a great deal of information on reaction pathways, the effect of chemical reaction steps on the redox process and reaction rates [49]. For adsorption processes, CV can be used to study the behaviour of adsorbed layers. Factors like the quantity of charge (Q) and current versus scan rate plots can be used to determine surface coverage (Γ) of the electrode by the adsorbed species, and even their orientation [49]. Adsorbed species can change the energetics of reactions, as there can be a difference in the ease of oxidation/reduction between the adsorbed and free species [51]. Where Nerstian behaviour is observed, equation 1.1 or 1.2 can be used to calculate surface coverage (Γ) [49]:

$$I_p = \frac{n^2F^2\Gamma A\nu}{4RT} \qquad 1.1$$

$$Q = n\mathrm{F}A\Gamma \qquad 1.2$$

where I_p = the peak current, n = number of electrons transferred, F = Faraday's constant, A = real surface area, ν = scan rate, R = Avogadro's constant, and T = temperature. The real surface area can be calculated using a redox active probe with a known diffusion constant (D) and the Randles-Sevcik equation 1.3 [49–51]:

$$I_p = (2.69 \times 10^5)\, n^{3/2}\mathrm{A}\mathrm{C}\mathrm{D}^{1/2}\nu^{1/2} \qquad 1.3$$

The behaviour of chemically modified electrodes can be studied in the same way using CV, as it has proved to be a useful tool for studying surface chemistry [49]. Monolayers,

particularly SAMs on gold, have been known to show blocking characteristics towards a number of well-studied redox probes. The efficiency of the layers at blocking redox probes is highly dependent on the structure of the molecules making up the layer, as this will determine the uniformity of the surface coverage, whether the layer is pinhole and defect free, and whether the layer is tightly packed as well as the orientation it will adopt [51]. Good redox probes include $[Fe(CN)_6]^{3+/4+}$, $CuSO_4$ and $Fe(NH_4)_2(SO_4)$.

There are numerous electrochemical experiments that can be used to determine different factors about the analytes, but the theory available is extensive and thorough, and methods will be discussed in subsequent chapters only so far as they relate to the modified electrodes in this work.

1.2.3. *Electrochemical impedance spectroscopy (EIS)*

Characterisation of solid-solid or solid-liquid interfaces is of great interest in electrochemistry and in materials science. EIS is a useful method for studying the properties at interfaces of electrodes, as the electrical response of the surface is dependent on the electrolyte, the structure and behaviour of the electrode, and the charged species in solution [51,167,168]. Impedance has applications in the characterisation of composite electrodes, solid state devices such as solid electrolyte chemical sensors and solar cells, the corrosion of materials and power sources such as batteries and fuel cells [169].

EIS involves the measurement of the impedance (Z) of the cell or electrode through application of a single-frequency voltage or current and determining the phase shift and

amplitude (or real and imaginary parts) of the current at that frequency using fast Fourier transform or analog circuit analysis [167]. Impedance is a complex quantity, and is composed of both real and imaginary parts. Most electrochemical systems, and their resulting impedance values, can be fitted to an equivalent circuit which can be used to analyse the system [167].

There are two plots which are commonly used to show impedance behaviour. These are the Nyquist and Bode complex-plane plots, which are shown in Fig. 1.7 [100]. The Nyquist figure plots the imaginary (Z'') versus real (Z') components of the impedance vector (Z) for a range of frequencies (ω), and is commonly used for characterisation of electrochemical systems [169], Fig. 1.7(a). Values such as the electrolyte resistance (R_e), charge transfer resistance (R_{CT}), double-layer capacitance (C_{DL}) and constant phase element (CPE) capacitance can be determined. A complimentary plot is the Bode plot, Fig. 1.7(b), where the overall impedance Z and the phase-angle (θ) are plotted against ω. The Bode plots have an advantage in that high and low frequency impedance behaviour is shown with equal weight along the plot [169]. In the Bode phase-angle plot, if θ tends to -90° at low frequency, this shows pure capacitive behaviour [169]. Fig. 1.7(c) shows the common Randles equivalent circuit fitting the data in the Nyquist plot, modelling the interfacial electrochemical reaction [169].

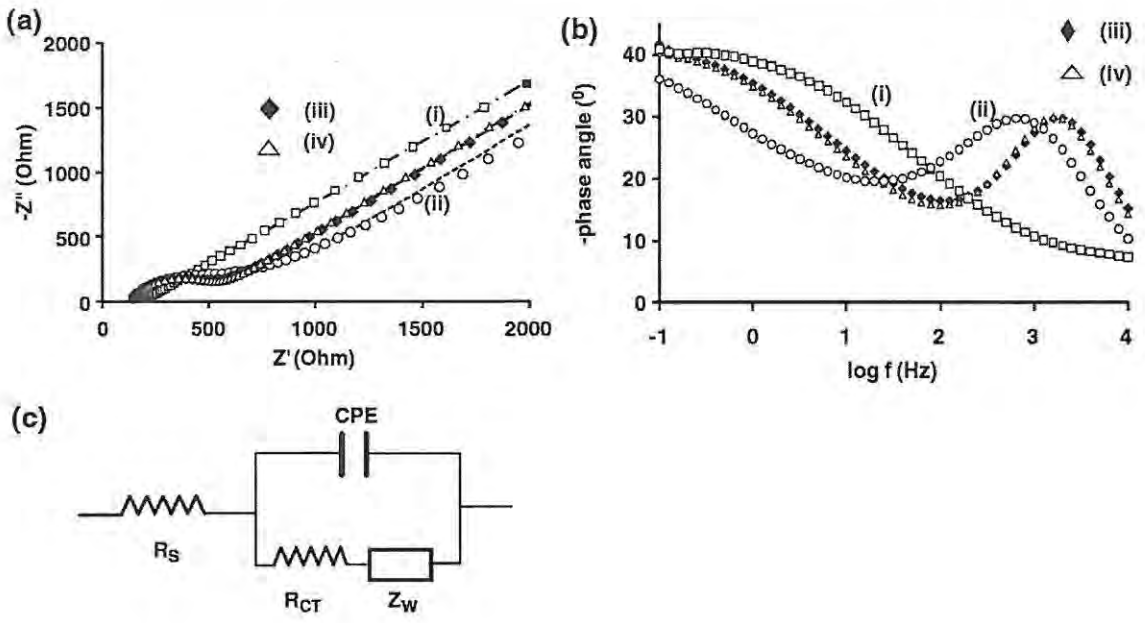

Figure 1.7. Examples of (a) Nyquist and (b) Bode plots of modified electrodes and (c) the Randles equivalent circuit for the Nyquist data fit. Adapted from [100].

1.2.4. Atomic force microscopy (AFM)

AFM is a technique that can be used to map both insulating and conducting surfaces, allowing nanoscopic resolution of surface topography [49–51]. Measurements are obtained by optically measuring deflections of a very small cantilever tip as it moves across a surface. These deflections are due to attractive or repulsive interactions between atoms on the tip and those on the surface [49–51]. This force interaction is monitored by a cantilever beam, and the image is created as the probe tip moves across the surface [49–51]. Two modes are constant height and constant force, but the latter is more frequently used as there is less chance of the probe crashing into the sample. AFM can be used to indicate clearly whether there is complete coverage by looking at the difference in the

height of the surface before and after modification, and it has been used to look at changes in the electrode surface after modification by, for example, adsorption, underpotential deposition and etching [39,51]. Aggregation is an important factor in the inhibition of SAM formation, as it can affect formation of a uniform layer on a surface [39,170,171] as well as the electrical properties [172] and reaction of the electrode with analytes. It could, for example, play a role in increasing or reducing passivation effects of the electrode, depending on the nature of the layer, and so AFM is an important technique needed to elucidate the properties of the layer.

A typical AFM image comparing a bare electrode to that modified with a SAM of thio-containing MPcs is shown in Fig. 1.8 [80].

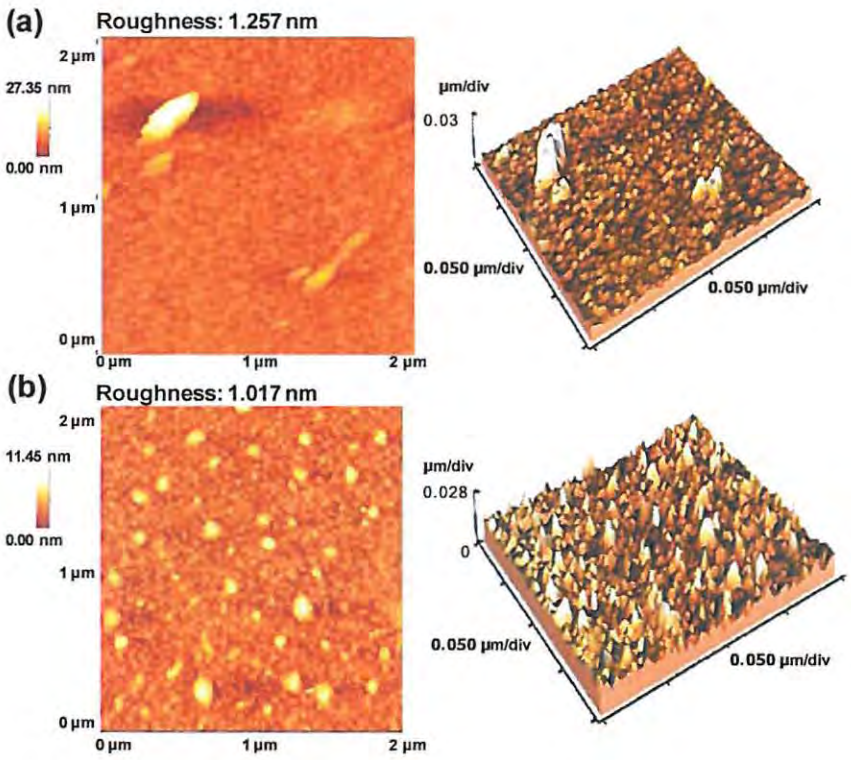

Figure 1.8. Example of an AFM image of a gold electrode before (a) and after (b) MPc-SAM formation. Adapted from [80].

1.2.5. *Scanning electron microscopy (SEM)*

SEM involves the analysis of surfaces under vacuum conditions, with a normal working range of between 50 nm and 10 µm [50]. A focused beam of monochromatic electrons is scanned across the sample, and the secondary products of the interaction between the electrons and the sample are detected [50]. The surface must be either conductive, or made conductive by spluttering with gold so that there is no build up of charge [50]. SEM can be used to look at the surface morphology of thin films formed at different

temperatures [173]. While this technique gives a broader view of the surface with regards to larger (micro-scale) aggregated clusters, like transmission electron microscopy (TEM) it does not give an indication of the height of the surface or aggregation on a smaller (nano) scale [170], unless high resolution SEM is used (HRSEM). Although detailed features are not visible in conventional SEM because the scale does not permit resolution of distinct molecules [50,172], the SEM images can indicate if there are areas with large clusters of aggregated molecules on the surface. Using SEM to compare the difference in topographies of surfaces is another method that can be used to confirm electrode modification.

Fig. 1.9 shows an example of SEM images of a gold electrode before and after MPc-SAM formation [100].

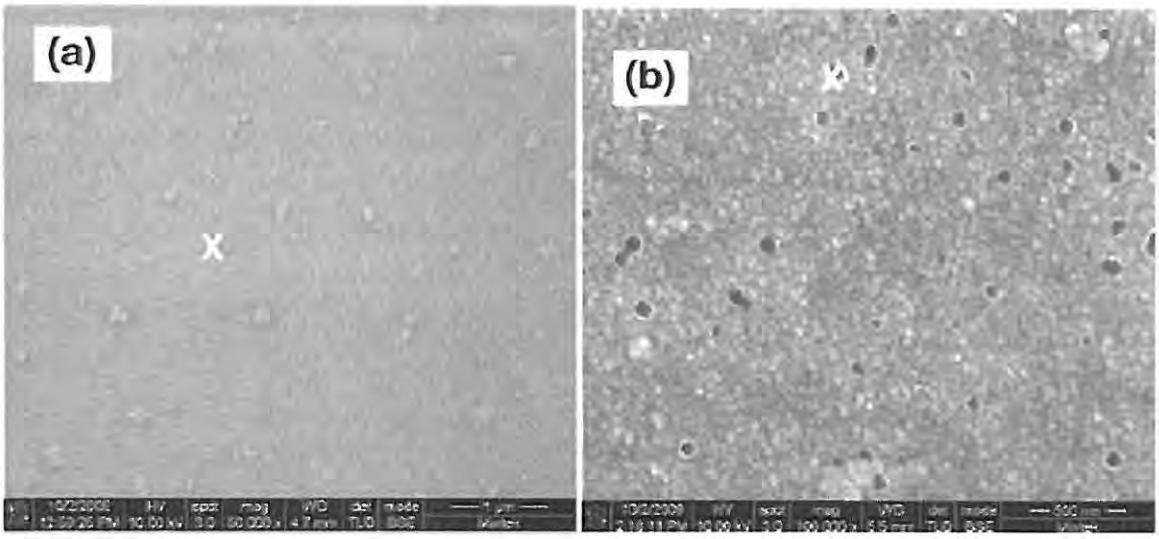

Figure 1.9. SEM images of gold electrodes before (a) and after (b) MPc-SAM formation. Adapted from [100].

1.2.6. *Scanning electrochemical microscopy (SECM)*

SECM is greatly useful in elucidating the chemical reactivity of a substrate, and has applications in corrosion science, fuel cells, biotechnology, and many others [174–176]. It gives kinetic information about reactions at the surface, and allows the creation of images or maps of the reactivity of the substrate in the form of chemical and electrochemical activity, as well as conductivity and surface topography [49–51,174–176]. In this work, the feedback mode of SECM was used to compare the different stages of modification.

In SECM, an ultramicroelectrode (UME) is used as the probe, instead of a cantilever tip as used in AFM, with a reference and counter electrode also being required. Here the tip current is monitored, and it is dependent on the electroactive redox probe in solution, the conductive nature of the substrate and on the tip-substrate distance [49]. When the tip is distant from the surface and a potential is applied to reduce/oxidise the species in solution, the UME has a steady state current that is dependent on the concentration and diffusion coefficient of the electroactive species and the radius of the UME [51]. The feedback mode is most common, and when in close proximity to an insulating surface the diffusion of electroactive material from the solution to the tip is blocked and the current decreases, while close proximity to a conducting surface results in regeneration of the electroactive species and thus increased current [49–51].

Fig. 1.10 shows a simplified example of the electroactive material moving freely towards the UME in bulk solution (a), the increase in current at a conductive surface (b), and the decrease in current at an insulating surface (c).

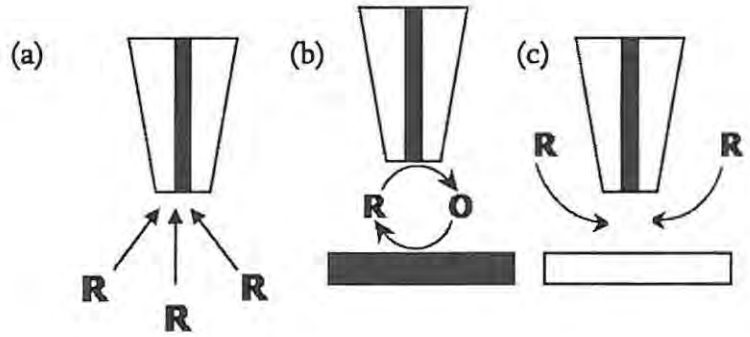

Figure 1.10. Simple representation of an SECM ultramicroelectrode (a) in bulk solution with free diffusion of electroactive material, (b) in close proximity to a conducting surface with a subsequent increase in current and (c) in close proximity to an insulating surface with a subsequent decrease in current.

Single approach curves can be done towards the surface from the bulk solution in order to get kinetic information, or the surface can be imaged by moving the tip across the sample [50,51,174]. Fig. 1.11 shows examples of (a) approach curves to both a conductive and insulating surface, (b) a side-view of an SECM image of an electrode that has had half of its surface modified and (c) the top view of the modified surface [122]. These images show very clearly that the modified part of the electrode was uniformly insulating, with currents below the limiting current (I_{lim}, current in bulk solution) showing negative feedback, while the bare electrode was conducting with currents showing a positive feedback response.

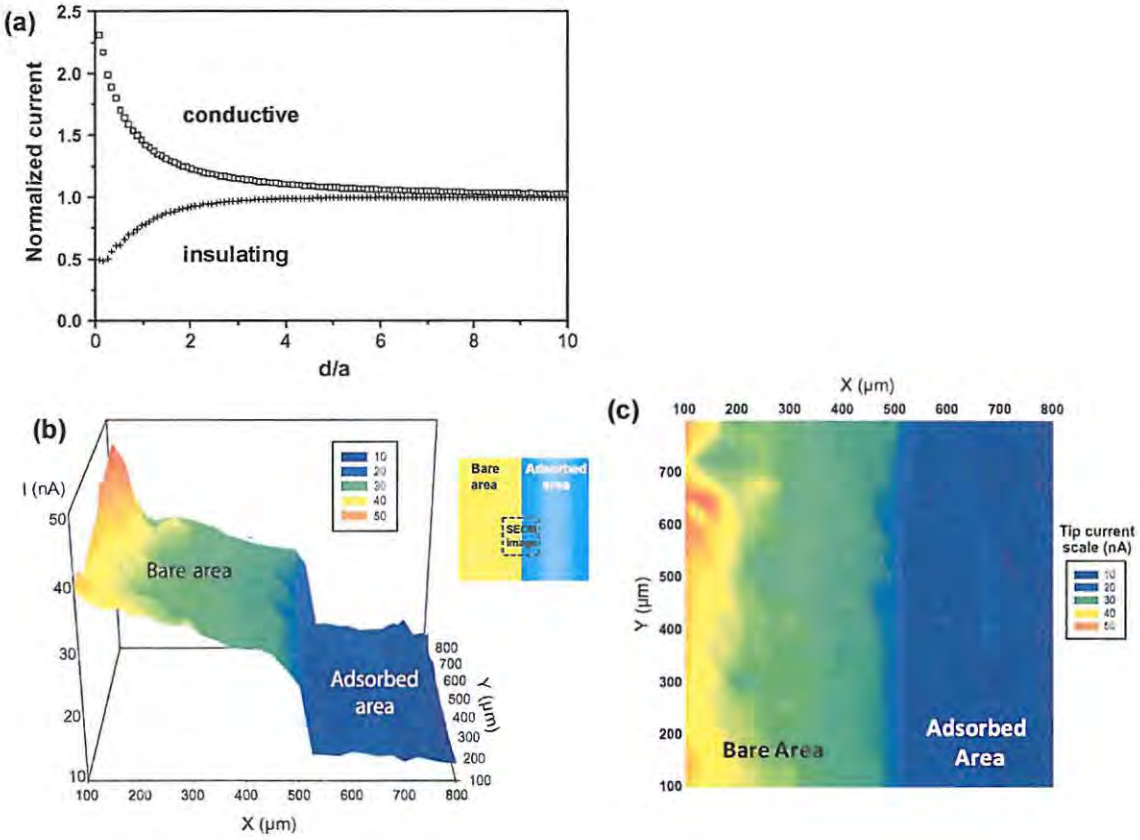

Figure 1.11. Examples of (a) approach curves to a conductive and insulating surface, (b) a side-view of an SECM image of an electrode that has had half of its surface modified and (c) the top view of the modified surface. Insert: schematic drawing of the area that was imaged. Adapted from [122].

SECM is useful not only as a technique for characterising localised surfaces and monitoring reaction kinetics, but it can also be used to modify surfaces for micropatterning purposes [124,125,176–179]. For micropatterning, the SECM probe is brought in close proximity to the substrate, and a potential bias is commonly applied to the probe (or in this case the substrate) to reduce or oxidise the species in solution that will locally modify the substrate surface, for example through corrosive etching [176] or

through locally generated diazonium grafting [124]. Because of the scarce research on local electrografting of diazonium salts, and in particular properties such as the distance to the substrate, size of the probe and the presence of an electrolyte, this was a very interesting area for investigation in this work, as illustrated in Scheme 1.4.

1.2.7. X-Ray photoelectron spectroscopy (XPS)

XPS is a surface analysis technique that has had many applications in materials science – particularly metallurgy, corrosion science, catalysis, polymer materials, microelectronics and semiconductor materials [180]. XPS involves photoemission where core level electrons are ejected by X-ray photons of energy, and when these electrons are excited and ejected without a loss of energy, they give peaks in the XPS spectrum with energies specific to the element from which they originate as well as the chemical state [180]. Some of the electrons undergo inelastic scattering, and these make up the background of the spectrum. As necessary for a surface technique, the analysis depth for XPS is a few nanometres [180]. XPS analysis is done under ultra-high vacuum, firstly because scattering of low energy electrons by gas molecules results in a loss of analytical signal and a corresponding increase in the background noise, and secondly because this technique is so sensitive that even surface-adsorbed gas molecules can be detected [180]. Choice of pass energy in XPS is important when looking for different chemical states by adjusting the resolution. However, with a lower pass energy and better resolution, there is also a decrease in transmission and a lower sensitivity and peak intensity [180]. XPS

peaks are usually split into two when the angular momentum quantum number is greater than 0, due to spin-orbit coupling [180]. This technique can be used for both qualitative and quantitative analysis.

XPS has been used to analyse thin films containing azide groups from as early as 1989 [181]. It was noted early in the study of metal azides that the nitrogen signal for an azide group is comprised of two peaks: one at higher energy from the central nitrogen which has a lower electron density, and an overlapped peak at lower energy from the adjacent two nitrogen atoms [181,182]. XPS has also been used to look at azide-bearing self-assembled monolayers on gold [8], and in both of these cases was used to monitor the reaction of these azides by studying the nitrogen signal and the disappearance (or appearance) of the nitrogen peak at higher energy which is considered to be particularly specific to this azide group [8,181]. More specifically, the disappearance of this higher energy peak has been used as proof of a successful click chemistry reaction and the formation of a triazole ring [12,13,143,183,184]. XPS is thus invaluable in monitoring layer-by-layer modification of surfaces, to ensure attachment and to monitor changes in the chemical states of the surface groups.

1.3. Electrocatalysis and analytes employed in this work

Accurate detection of analytes is particularly important when these targets are potentially harmful to the environment and health. Often these toxic compounds are present in very low concentrations, and accurate determination is vital because even small changes in concentration can be harmful. Electrocatalysis can be defined as the acceleration of electrochemical reactions in the presence of a catalyst – whether biological or chemical [50]. This is generally seen in cyclic voltammetry as a decrease in potential for oxidation of the analyte and/or an increase in current (and sensitivity), as seen in Fig. 1.12(a) [74].

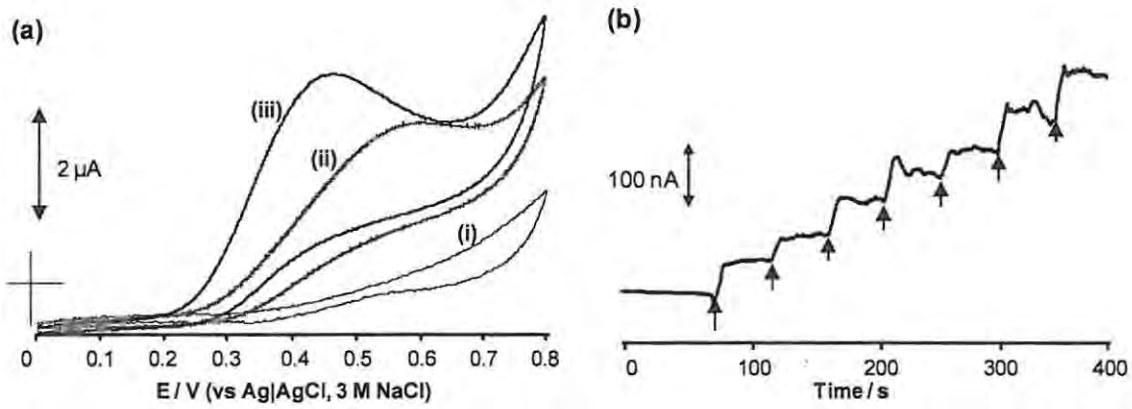

Figure 1.12. (a) Cyclic voltammogram showing electrocatalytic detection of an analyte by the modified electrodes (ii) and (iii), compared to the bare electrode (i). (b) Typical chronoamperometry result with sequential additions of an analyte to a modified electrode in a vigorously stirred solution. Adapted from [74].

Chronoamperometry, as seen in Fig. 1.12(b), can be used to determine the limit of detection (LoD) for an analyte, as well as the sensitivity of the electrode. For this technique, the electrode is immersed in a solution of the electrolyte which is vigorously stirred. The potential where the target analyte is reduced/oxidised is applied to the electrode, and the current is measured while aliquots of the analyte are added to the solution over time. From these results, a plot of current against concentration can be made to obtain the LoD and sensitivity values.

As mentioned, MPcs [22], CNTs [19–21] and ferrocene [4,5] have all shown electrocatalytic behaviour towards many analytes, and show good potential for detection of a range of environmentally important species. Although the focus of this work is on surface modification, one of the best methods to determine that successful attachment of electroactive species has occurred is to test the surface for electrocatalytic behaviour toward analytes in solution. For this purpose, most of the modified electrodes were used to detect analytes in solution. However, because of the different electrodes that were used and also the different complexes that were attached to the surfaces, they did not prove to be successful in electrocatalysis of the same analyte, making comparison difficult. Thus a number of different analytes were used – from hydrazine, thiocyanate, and sulphite – in order to show very briefly the success of the individual approaches for the attachment of electrocatalysts.

Thiocyanate is widely produced in the mining industry – often deliberately, as a less-toxic alternative to cyanide [185]. However, thiocyanate has high toxicity towards aquatic life, and detection of this analyte is important in monitoring effluent levels [185]. MPcs have

been used to detect thiocyanate in a number of cases, on both gold and glassy carbon electrodes [44,186–188]. This analyte was used to show the electrocatalytic ability of the MnPc-SAM surface.

Sulphites are commonly used as a preservative in many foods and drinks, due to their antimicrobial and antioxidant properties [189–191]. Toxicity of sulphite has been thoroughly tested in mammals, with high doses of sulphite showing inflammatory effects on the digestive system [190], some indications of co-carcinogenic behaviour [191] and intolerance and allergenic reactions in sensitive subjects [192]. Both MPcs and ferrocene have shown electrocatalytic detection of sulphite in solution [5,79], and it was used in this work to show the electrocatalytic behaviour of ferrocene covalently linked to the electrode through click chemistry.

Hydrazine is a highly toxic compound that can be easily absorbed through inhalation, ingestion and through the skin [193]. Even low doses of hydrazine can act as a central nervous system depressant, and high doses cause convulsions [193]. Studies have shown that this compound is also mutagenic and carcinogenic [194,195]. Hydrazine is mainly used in the formation of plastics, for water treatment, as a propellant, in fuel cells, and commonly as a pesticide [193]. MPcs have shown very good activity as electrocatalysts of hydrazine [75,196,197], making this a useful analyte to show successful attachment of FePc through axial ligation in this work.

1.4. Aims

The aims of this work were to explore different surface modification approaches for the attachment of redox-active species as potential electrocatalysts. These are as follows:

1) Investigation into self-assembled monolayers on gold, using new manganese phthalocyanine complexes bearing alkyl- and aryl-thio substituents.
2) Study into grafting of 4-azidobenzenediazonium and click chemistry with ferrocene on glassy carbon with and without adsorbed single-walled carbon nanotubes.
3) Comparison of the use of click chemistry before and after grafting of 4-azidobenzendiazonium and electropolymerisation of 4-azidoaniline, by analysis of the surface coverage of ferrocene.
4) Study into axial ligation of iron phthalocyanine to pyridine attached to GCEs by click chemistry with and without single-walled carbon nanotubes.
5) Investigation into the possibility of electrografting and click chemistry on resistive multi-walled carbon nanotube paper.
6) Applications of SECM for micro-grafting of 4-azidobenzenediazonium salt on gold plate electrodes.

CHAPTER 2

EXPERIMENTAL

2.1. Materials

The following chemicals were supplied by Aldrich: manganese (II) acetate, 1-pentanethiol, 1-decanethiol, thiophenol, tetrabutylammonium tetrafluoroborate ($TBABF_4$), ethylene glycol, iron phthalocyanine (FePc), 4-azidoaniline hydrochloride (**2a**), sodium nitrite, tetrafluoroboric acid, lithium aluminium hydride, potassium ferrocyanide, ferrous ammonium sulphate, ethynylferrocene (Fc-C≡CH), hexaammineruthenium(III) chloride, 4-ethynylpyridine hydrochloride, sodium dihydrogen phosphate, disodium hydrogen phosphate and potassium chloride. Merck supplied the following: dimethylsulphoxide (DMSO), dichloromethane (DCM), tetrahydrofuran (THF), dimethylformamide (DMF), chloroform, deuterated chloroform, methanol, ethanol, Bio-Beads S-X1 (200-400 mesh, Bio-Rad), silica gel 60 (0.04-0.063 mm), diethyl ether, acetone, perchloric acid and acetonitrile (ACN). Saarchem provided anhydrous potassium carbonate, copper sulphate, sodium sulphite, sodium acetate, acetic acid and pH 4 buffer tablets. Benzyl mercaptan was obtained from Fluka and Afrox supplied argon gas.

4,5-Dichlorophthalonitrile was synthesized according to a well-known procedure [198,199] starting from dichlorophthalic anhydride. 4-(4-Ferrocenyl-1H-1,2,3-triazol-1-yl)aniline (**2c**), Scheme 4.3, was synthesized according to previously reported procedures by the group of Dr Girard at the Unité de Pharmacologie Chimique et Génétique et Imagerie, Chimie ParisTech, France [200,201] and was donated for use in this work. Single-walled carbon nanotubes functionalized with carboxylic acid groups (SWCNT-

COOH, ≈1.5 nm in diameter and 1-5 μm in length, >95 % purity by thermal gravimetric analysis) and multi-walled carbon nanotube paper (MWCNT-paper, produced from 95 % purity bamboo structured MWCNTs with a diameter of 15 ± 5 nm and a length of 5 – 20 μm) were obtained from NanoLab (USA). Resistivity of the MWCNT-paper was measured by the manufacturer as 0.1 ohm-cm, with a density of 0.5 g/cm^3. Where necessary, ultra-pure water from a Milli-Q Water System (Millipore Corp., Bedford, MA, USA) was used. Solvents were dried and distilled before use, and all other chemicals and reagents were of analytical grade and were used as received.

2.2. Equipment

UV-visible spectra were recorded on a Cary 500 UV/Vis/NIR spectrophotometer. ^{1}H-nuclear magnetic resonance (NMR, 400 MHz) spectra were recorded using a Bruker AMX 400 MHz NMR spectrometer in $CDCl_3$ using standard 1D pulse programs. Elemental analysis of the purified Pcs was done using a Vario-Elementar Microcube ELIII. Spectroelectrochemical studies were done using a home-made optically transparent thin-layer electrochemical (OTTLE) cell connected to a Bioanalytical Systems (BAS) CV 27 voltammograph and using a Shimadzu Model UV-2550 UV-Vis Spectrophotometer. MALDI-TOF mass data was obtained in an α-cyano-4-hydroxycinnamic acid matrix, on a ABI Voyager DE-STR MALDI-TOF instrument in a positive ion mode, by the University of Stellenbosch in South Africa. AFM images were obtained in the non-contact mode in

air with a CP-11 Scanning Probe Microscope from Veeco Instruments (Carl Zeiss, South Africa) at a scan rate of 1 Hz. SEM images were recorded using a Tescan Digital Microscope model scanning electron microscope at the Rhodes University Electron Microscopy Unit. A Bruker Vertex 70 - Ram II spectrometer (equipped with a 1064 nm Nd:YAG laser and a liquid nitrogen cooled germanium detector) was used to collect the Raman spectral data. XPS analysis was done using an AXIS Ultra DLD, with Al (monochromatic) anode equipped with a charge neutraliser, supplied by Kratos Analytical. For wide XPS scans, the emission was 10 mA, the anode (HT) was 15 kV and the operating pressure was below 5 x 10^{-9} torr. A hybrid lens was used and the resolution to acquire the scans was at 160 eV pass energy in slot mode. The centre for the scans was at 520 eV with a width of 1205 eV, steps at 1 eV, and dwell time at 100 ms. High resolution scans were done using a resolution of 40 eV pass energy. The centre was at 399 eV with a width of 20 eV for the N(1s), and at 165 eV with a width of 14 eV for the S(2p), with 0.05 eV steps and dwell times of 500 ms. Analysis of the electrode surfaces was done using plate electrodes (glassy carbon and gold 1 cm x 1 cm from Goodfellow) which were modified in the same way as the conventional electrodes.

Cyclic (CV), square wave (SWV) and differential pulse (DPV) voltammetry as well as chronoamperometry (CA) data were obtained using a Bio-Analytical Systems (BAS) B/W 100 Electrochemical Workstation. A typical three-electrode system with a silver/silver chloride (Ag|AgCl) pseudo-reference, platinum auxiliary and glassy carbon (GCE) or gold (AuE) working electrode was used. A Ag|AgCl (3 M KCl) reference electrode was used in the aqueous solutions. The potential response of the Ag|AgCl pseudo-reference electrode

was less than the Ag|AgCl (3M KCl) by 0.015 ± 0.003V. The GCE and AuE working electrodes were cleaned by polishing on 1200 grit MicroCut® Discs (Beuhler) and then with 3 μm and 1 μm diamond paste (MetaDi® Supreme Polycrystalline Diamond Suspension, Beuhler) on a Beuhler felt pad before use. The concentration of the various MPcs in solution was in the millimolar (mM) range.

The SECM experiments were carried out using homemade 12.5, 25 and 50 μm Pt ultramicroelectrodes (UMEs) with Princeton Applied Research equipment (Uniscan Model 370), or with 12.5 μm Pt UMEs purchased from Uniscan. The homemade Pt UMEs were constructed by inserting the Pt wire of desired diameter into tapered glass capillaries, and melting the tapered glass around the wire. The connection was achieved using copper wire, the contact was made with silver glue and the probe was polished to expose the Pt wire. *RG* values of 40 and 20 for the tip of 12.5 μm diameter and 25 μm diameter, respectively, were evaluated before each experiment by optical microscopy (*RG* = a_{glass} / a with a = tip radius and a_{glass} = glass radius). The GCE or AuE plates were placed face-up in a Teflon® cell. Approach curves of the UME tip to the surface were carried out in either 5 mM $K_4[Fe(CN)_6]$ (oxidation at 0.5 V) or 5 mM $[Ru(NH_3)_6]Cl_3$ (reduction at –0.45 V) in 0.1 M KCl against Ag|AgCl. SECM images were obtained by maintaining the tip at a constant z position and scanning in the x-y plane over the desired area (constant-height mode of SECM) and monitoring changes in the steady-state current of $[Ru(NH_3)_6]Cl_3$ reduction at -0.45 V or $K_4[Fe(CN)_6]$ oxidation at 0.5 V *vs.* Ag|AgCl as the tip travels. Approach curves were performed using the Pt tip as the working electrode and

the Ag|AgCl wire as a pseudo-reference and counter electrode. The UME tip was cleaned following the same procedure as for the GCE.

2.3. Synthesis

The synthesis of the MPcs required for SAMs on gold and the 4-azidodiazonium tetrafluoroborate (**2b**) required for grafting are discussed below. As stated above, the synthesis of 4,5-dichlorophthalonitrile (**3**), Scheme 3.1, has been reported before [198,199] and so shall not be discussed here.

2.3.1. *Synthesis of MnPcs for SAMs*

The conversion to the required phthalonitriles followed by formation of the manganese phthalocyanines is illustrated in Scheme 3.1.

2.3.1.1. *4,5-Bis(pentylthio)phthalonitrile (4a)*

Compound **4a** was synthesized as reported in literature [52,202] with some modifications. Briefly, 1-pentanethiol (30.5 mmol) and **3** (2.0 g, 10.2 mmol) were dissolved in DMSO (15 ml) under argon. The mixture was stirred for 15 min and ground anhydrous potassium carbonate (5.1 g, 36.9 mmol) was added portion-wise over 2 h with stirring. The mixture

was stirred under an argon atmosphere for 12 h. Water (100 ml) was then added and the mixture stirred for 30 mins. The precipitate was filtered and washed with water, followed by recrystallisation from ethanol. Yield: 38%. IR (KBr): υ_{max}, cm^{-1} 3075, 2949, 2930, 2859, 2231 (C≡N), 1618, 1563, 1456, 1433, 1350, 1264, 1225, 1112, 929, 900, 869, 731, 682, 605, 527. ^1H NMR (400 MHz; $CDCl_3$; Me_4Si): δ, ppm 7.41 (2H, s, Ar-*H*), 3.01 (4H, t, S-C*H*$_2$), 1.76 (4H, m, -C*H*$_2$), 1.49 (4H, m, -C*H*$_2$), 1.39 (4H, m, -C*H*$_2$), 0.93 (6H, t, -C*H*$_3$).

2.3.1.2. *4,5-Bis(decylthio)phthalonitrile (4b)*

Compound **4b** was synthesized as described above for **4a**, using 1-decanethiol (30.5 mmol), DMSO (15 ml) under argon and **3** (2.0 g, 10.2 mmol). Yield: 56%. IR (KBr): υ_{max}, cm^{-1} 3071, 2943, 2921, 2852, 2359, 2340, 2230 (C≡N), 1692, 1614, 1580, 1457, 1343, 1224, 1186, 1108, 1004, 929, 899, 870, 831, 761, 735, 668, 609, 528. ^1H NMR (400 MHz; $CDCl_3$; Me_4Si): δ, ppm 7.41 (2H, s, Ar-*H*), 3.01 (4H, t, S-C*H*$_2$), 1.75 (4H, m, -C*H*$_2$), 1.49 (4H, m, -C*H*$_2$), 1.28 (24H, m, -C*H*$_2$), 0.89 (6H, t, -C*H*$_3$).

2.3.1.3. *4,5-Bis(benzylthio)phthalonitrile (4c)*

Compound **4c** was synthesized as described above for **4a**, using benzyl mercaptan (30.5 mmol), DMSO (15 ml) under argon and **3** (2.0 g, 10.2 mmol). Yield: 54%. IR (KBr): υ_{max}, cm^{-1} 3060, 3027, 2359, 2336, 2227 (C≡N), 1768, 1719, 1565, 1494, 1452, 1331, 1238, 1115,

1029, 933, 889, 873, 778, 712, 694, 633, 530, 483, 465. ^{1}H NMR (400 MHz; $CDCl_3$; Me_4Si): δ, ppm 7.40 (2H, s, Ar-*H*), 7.31 (10H, m, Ar-*H*), 4.20 (4H, s, S-C*H*$_2$).

2.3.1.4. *4,5-Bis(phenylthio)phthalonitrile (4d)*

Compound **4d** was synthesized as described above for **4a**, using thiophenol (30.5 mmol), DMSO (15 ml) under argon and **3** (2.0 g, 10.2 mmol). Yield: 75%. IR (KBr): υ_{max}, cm^{-1} 3075, 2959, 2921, 2850, 2229 (C≡N), 1768, 1714, 1653, 1564, 1473, 1453, 1437, 1384, 1349, 1331, 1259, 1218, 1108, 1022, 924, 883, 799, 758, 693, 528, 489. ^{1}H NMR (400 MHz; $CDCl_3$; Me_4Si): δ, ppm 7.53 (10H, m, Ar-*H*), 7.01 (2H, s, Ar-*H*).

2.3.1.5. *2,3,9,10,16,17,23,24-Octakis(pentylthio)phthalocyaninato-manganese(III)(Ac), (OAc)MnPc$^{\beta}${S(CH$_2$)$_4$CH$_3$}$_8$ (1a)*

Compound **4a** (0.9 g, 2.7 mmol), manganese (II) acetate (0.12 g, 0.71 mmol) and anhydrous ethylene glycol (6 ml) were mixed and refluxed for 4 h at 200 °C under argon. The mixture was allowed to cool before excess methanol was added to precipitate out the crude product, which was then purified using a Bio-Bead S-X1 column eluting with $CHCl_3$. Yield: 72%. UV-vis ($CHCl_3$): λ_{max}, nm (log ε) 405 (4.2), 465 (4.2), 530 (4.1), 768 (4.5). IR (KBr): υ_{max}, cm^{-1} 2955, 2925, 2856, 2360 (C-S), 2343, 1701, 1637, 1618, 1551, 1458, 1413, 1376, 1328, 1072, 959, 743, 669 (Mn-N), 618, 486. Anal. calcd. for

$C_{72}H_{96}N_8S_8Mn(Ac)$: C, 61.55; H, 6.91; N, 7.76; S, 17.76%. Found: C, 61.89; H, 7.05; N, 7.02; S, 17.35%. MS (MALDI-TOF): *m/z* 1384 (calcd. for $[M - Ac]^+$ 1385).

2.3.1.6. *2,3,9,10,16,17,23,24-Octakis(decylthio)phthalocyaninato-manganese(III)(Ac), (OAc)MnPc$^{\beta}${$(SCH_2)_9CH_3$}$_8$ (1b)*

Complex **1b** was synthesized as described above for **1a** using compound **4b** (1.0 g, 2.1 mmol), manganese (II) acetate (0.10 g, 0.55 mmol) and anhydrous ethylene glycol (6 ml). Yield: 32%. UV-vis ($CHCl_3$): λ_{max}, nm (log ε) 405 (4.2), 465 (4.3), 530 (4.2), 769 (4.6). IR (KBr): υ_{max}, cm^{-1} 2955, 2924, 2853, 2360 (C-S), 2342, 1701, 1654, 1592, 1458, 1414, 1377, 1328, 1073, 960, 782, 743, 669 (Mn-N), 597, 509. Anal. calcd. for $C_{112}H_{176}N_8S_8Mn(Ac)$ ($CHCl_3$): C, 65.01; H, 8.54; N, 5.28; S, 12.07%. Found: C, 64.61; H, 8.60; N, 4.59; S, 12.63%. MS (MALDI-TOF): *m/z* 1945 (calcd. for $[M - Ac]^+$ 1946).

2.3.1.7. *2,3,9,10,16,17,23,24-Octakis(benzylthio)phthalocyaninato-manganese(III)(Ac), (OAc)MnPc$^{\beta}$(SCH_2Ph)$_8$ (1c)*

Complex **1c** was synthesized as described above for **1a** using compound **4c** (1.3 g, 3.5 mmol), manganese (II) acetate (0.16 g, 0.92 mmol) and anhydrous ethylene glycol (6 ml). Yield: 74 %. UV-vis ($CHCl_3$): λ_{max}, nm (log ε) 407 (3.9), 472 (3.9), 530 (3.9), 770 (4.0). IR (KBr): υ_{max}, cm^{-1} 2924, 2853, 2360 (C-S), 2342, 1639, 1617, 1412, 1378, 1327, 1073, 958, 669 (Mn-N), 618, 486. Anal. calcd. for $C_{88}H_{64}N_8S_8Mn(Ac)$ ($CHCl_3$): C, 63.42; H, 3.98; N,

6.50; S, 14.88%. Found: C, 64.78; H, 3.73; N, 6.49; S, 15.08%. MS (MALDI-TOF): *m/z* 1544 (calcd. for [M - Ac]$^+$ 1545).

2.3.1.8. *2,3,9,10,16,17,23,24-Octakis(phenylthio)phthalocyaninato-manganese(III)(Ac), (OAc)MnPc$^{\beta}$(SPh)$_8$ (1d)*

Complex **1d** was synthesized as described above for **1a** using compound **4d** (1.0 g, 2.9 mmol), manganese (II) acetate (0.13 g, 0.76 mmol) and anhydrous ethylene glycol (6 ml). Yield: 55 %. UV-vis ($CHCl_3$): λ_{max}, nm (log ε) 462 (4.3), 530 (4.1), 694 (3.9), 773 (4.7). IR (KBr): υ_{max}, cm^{-1} 2923, 2852, 2361 (C-S), 2343, 1701, 1637, 1614, 1555, 1438, 1326, 1064, 955, 743, 669 (Mn-N), 618, 486. Anal. calcd. for $C_{80}H_{48}N_8S_8Mn(Ac)$ ($CHCl_3$): C, 61.87; H, 3.25; N, 6.96; S, 15.92%. Found: C, 62.72; H, 3.49; N, 6.65; S, 15.08%. MS (MALDI-TOF): *m/z* 1432 (calcd. for [M - Ac]$^+$ 1433).

2.3.2. *Synthesis of 4-azidobenzenediazonium tetrafluoroborate (2b)*

The synthesis of **2b** was carried out according to established procedure [14]. Briefly, a cold solution of $NaNO_2$ (155 mg, 2.25 mmol) in Milli-Q water (0.4 ml) was added dropwise to a cold solution of 4-azidoaniline hydrochloride (**2a**, 341 mg, 2 mmol) in HBF_4 (10 %, 2 ml) on ice while stirring. The mixture was stirred on ice for a further 1 h, before filtering off the product and rinsing with icy diethyl ether. The off-white product was purified by recrystallisation from acetonitrile and excess diethyl ether and kept at –30 °C

in the dark. Yield: 280 mg, 60 %. ^{1}H NMR ($CDCl_3$): δ, ppm 8.62 (2H, m, Ar-H), 7.64 (2H, m, Ar-H).

2.4. Electrode modification

2.4.1. *SAMs on a gold electrode*

For SAM studies, the clean gold electrode was rinsed with freshly distilled $CHCl_3$ and placed in de-aerated $CHCl_3$ containing the MnPc complex for 48 h. Gold-coated glass was used for surface characterization of the SAM films using AFM, SEM and Raman spectra, and gold plate electrodes were used for the XPS studies due to availability. The glass and gold plate samples were immersed in a solution of the desired complex in $CHCl_3$ for 10 days for the latter studies.

2.4.2. *SWCNT-adsorbed GC electrode (GC/SWCNT)*

The SWCNT suspension used contained 1.5 mg/ml of the SWCNT-COOH in DMF. The GCE was modified by placing 20 μl of the SWCNT solution (following sonication) on the electrode and then dried in the oven at 70 °C for 30 minutes. GCE modified with SWCNTs alone is denoted GC/SWCNT in the text. After the electrodes were modified and dried, they were rinsed several times with acetone, acetonitrile, ethanol and water to

remove weakly adsorbed components from the surface and conditioned by cycling in 0.1 M KPF_6.

2.4.3. *MWCNT-paper electrode*

The MWCNT-paper was cut into strips of 0.5 x 1.0 cm, with an approximate weight of 9-10 mg. The paper was rinsed thoroughly with acetone and water, and was modified using grafting and click chemistry as described below, by attaching one end to a silver-coated crocodile clip and immersing approximately half of the paper electrode in the electrolyte solution. Cyclic voltammetry results were corrected for weight of the MWCNT-paper.

2.4.4. *Grafting*

The clean electrode (GCE route B, GC/SWCNT route C, or MWCNT-paper route D) was grafted by scanning for five cycles between 0.47 and –0.8 V in 1 mM 4-azidobenzenediazonium tetrafluoroborate (**2b**) in 0.1 M $TBABF_4$ in de-aerated acetonitrile, Scheme 4.1. The successful blocking of the electrode by reductive electrodeposition of **2b** was confirmed by cyclic voltammetry and SECM imaging. The grafted electrode was then rinsed with Milli-Q water and acetone.

For comparison, *in situ* diazotation and grafting was also used to modify the GCE, and done as shown in Scheme 4.1, route A. Briefly, 1 mM of **2a** was prepared in 96:4 ACN/1 M HCl with 0.1 M $TBABF_4$. The deaerated solution was cooled to 0 °C for 15 min and 3

mM of $NaNO_2$ was added. After a further 15 min, the GC electrode was immersed in the solution (now containing **2b**) and grafted by two cycles at 50 mV/s from 0.5 to -0.7 V.

Scheme 4.3 shows the click chemistry-then graft approach, where the *in situ* diazotization of 4-(4-ferrocenyl-1H-1,2,3-triazol-1-yl)aniline (**2c**) was performed as follows: 1 mM of **2c** in 96:4 ACN/1 M HCl with 0.1 M $TBABF_4$ was deaerated with argon and cooled to 0 °C for 15 min before the addition of $NaNO_2$ (final concentration 3 mM). After 15 min of reaction, the *in situ* generated diazonium compound **2d** was electrografted on to the GCE by cycling the potential twice at 50 mV/s from 0.5 to -0.7 V. The electrochemical grafting of **2d** likely occurs as already reported for other diazonium salts, *via* the formation of an aryl radical followed by coupling between the radical and the electrode surface.

2.4.5. *Electropolymerisation*

Electropolymerisation of **2a** and of **2c** (Scheme 4.4) was done on the GCE as follows:

Electropolymerisation of 1 mM of **2a** was performed in a solution of 96:4 ACN/1 M HCl with 0.1 M $TBABF_4$. The potential was held at 0.8 V for 10 min. The electropolymerisation of 1 mM of **2c** was performed in ACN with 0.1 M $TBABF_4$ (the complex was not completely soluble even after ultrasonic agitation). The GCE was immersed in this solution, and the potential was held at 0.8 V for 10 min to form the electropolymerised layer.

2.4.6. *Click chemistry*

Click chemistry was used to attach both ferrocene and pyridine to the modified electrode layers. For click chemistry with ethynylferrocene, the grafted or electropolymerised electrode was immersed for 18 h in the dark in a solution of 2:1 EtOH/H_2O containing 1 mM ethynylferrocene, 5 mM $CuSO_4$ and 40 mM ascorbic acid. For reaction with 4-ethynylpyridine, the surface was clicked by immersion in 1 mM 4-ethynylpyridine, 5 mM $CuSO_4$ and 40 mM sodium ascorbate in water for 3 h and then rinsed thoroughly. This is shown in Scheme 4.2.

2.4.7. *Axial ligation*

For axial ligation of FePc, the electrode modification was carried out as shown in Scheme 4.2. Following grafting and click chemistry with pyridine as described above, the GCE or GC/SWCNT surface was immersed in a solution of 1 mM FePc in DMF for 3 h, and rinsed thoroughly.

2.4.8. *Micropatterning on a gold electrode*

Polycrystalline gold plates (Goodfellow, France) 1.5 x 1.5 cm and 2 mm thick were used as the substrate in the SECM experiments. Each substrate was manually polished before each experiment with diamond liquid (BioDiamant, Lamplan, France) of 1 μm and ¼ μm. The substrate was then thoroughly rinsed with ultra-pure water (Millipore System).

For local electrografting of **2b** by SECM, as shown in Scheme 1.4, the Pt tip (12.5 μm diameter) was positioned at a desired close distance from the gold substrate surface using conventional approach curve in feedback mode in aqueous 0.1 M KCl with 5 mM $[Ru(NH_3)_6]Cl_3$. After rinsing with Milli-Q water and then ACN, a solution of ACN containing 5 mM **2b** and 0.1 M $TBABF_4$ was introduced. The bare gold substrate was then polarized at -0.5 V while the SECM tip acted as a microanode (i.e. as a counter electrode in a three-electrode configuration). After reducing **2b** for 10 ms, the electrochemical set up was rinsed with ACN and Milli-Q water. SECM images were obtained as explained in Section 2.2.

RESULTS AND DISCUSSION

This section has been split into three chapters:

Chapter 3: Metallophthalocyanine synthesis and characterisation

Chapter 4: Electrode modification

Chapter 5: Electrocatalytic studies

PUBLICATIONS

Most of the work presented in the following chapters has been published in these articles:

1) Megan Coates, Edith Antunes & Tebello Nyokong. Electrochemical, spectroscopic and microscopic studies of new manganese phthalocyanine complexes in solution and as self-assembled monolayers on gold. *Journal of Porphyrins and Phthalocyanines* **14**, 568–581 (2010).

2) Megan Coates, Eva Cabet, Sophie Griveau, Tebello Nyokong & Fethi Bedioui. Microelectrochemical patterning of gold surfaces using 4-azidobenzenediazonium and scanning electrochemical microscopy. *Electrochemistry Communications* **13**, 150–153 (2010).

3) Megan Coates, Hichem Elamari, Christian Girard, Sophie Griveau, Tebello Nyokong & Fethi Bedioui. 4-Azidoaniline-based electropolymer as a building block for functionalisation of conductive surfaces, *Journal of Electroanalytical Chemistry* **670**, 79–84 (2012).

4) Megan Coates, Sophie Griveau, Fethi Bedioui & Tebello Nyokong. Layer by layer electrode surface functionalisation using carbon nanotubes, electrochemical grafting of azide-alkyne functions and click chemistry, *Electroanalysis* **24**, 1833–1838 (2012).

5) Megan Coates, Tebello Nyokong. Electrode modification using iron metallo-phthalocyanine through click chemistry and axial ligation with pyridine, *Journal of Electroanalytical Chemistry* **687**, 111–116 (2012).

6) Megan Coates, Tebello Nyokong. Characterization of glassy carbon electrodes modified with carbon nanotubes and iron phthalocyanine through grafting and click chemistry, *Electrochimica Acta, in press*

The following articles have been submitted for publication:

7) Megan Coates, Tebello Nyokong. X-ray photoelectron spectroscopy and scanning electrochemical microscopy of branched multi-walled carbon nanotube paper modified by electrochemical grafting and click chemistry, *submitted*

8) Megan Coates, Tebello Nyokong. X-ray photoelectron spectroscopy analysis of the effect of alkyl- and arylthio substituents on manganese phthalocyanine for self-assembled monolayer formation on gold, *submitted*

CHAPTER 3

METALLOPHTHALOCYANINE SYNTHESIS AND CHARACTERISATION

3.1. Synthesis

The syntheses of the aryl- and alkylthio substituted phthalonitriles were accomplished by reacting the appropriate thiol with 4,5-dichlorophthalonitrile in the presence of potassium carbonate, which facilitated a base-catalyzed nucleophilic aromatic displacement reaction, Scheme 3.1. The success of the phthalonitrile synthesis was confirmed by proton NMR analysis, and the clean spectra clearly showed the alkyl or aryl substituents bonded to the phthalonitrile through sulphur and resulting in a highly pure product. Sulphur caused deshielding of the adjacent CH_2 protons on the alkyl substituents, shifting them to 3.01 ppm. Integration of the proton peaks gave the expected values for the respective phthalonitriles.

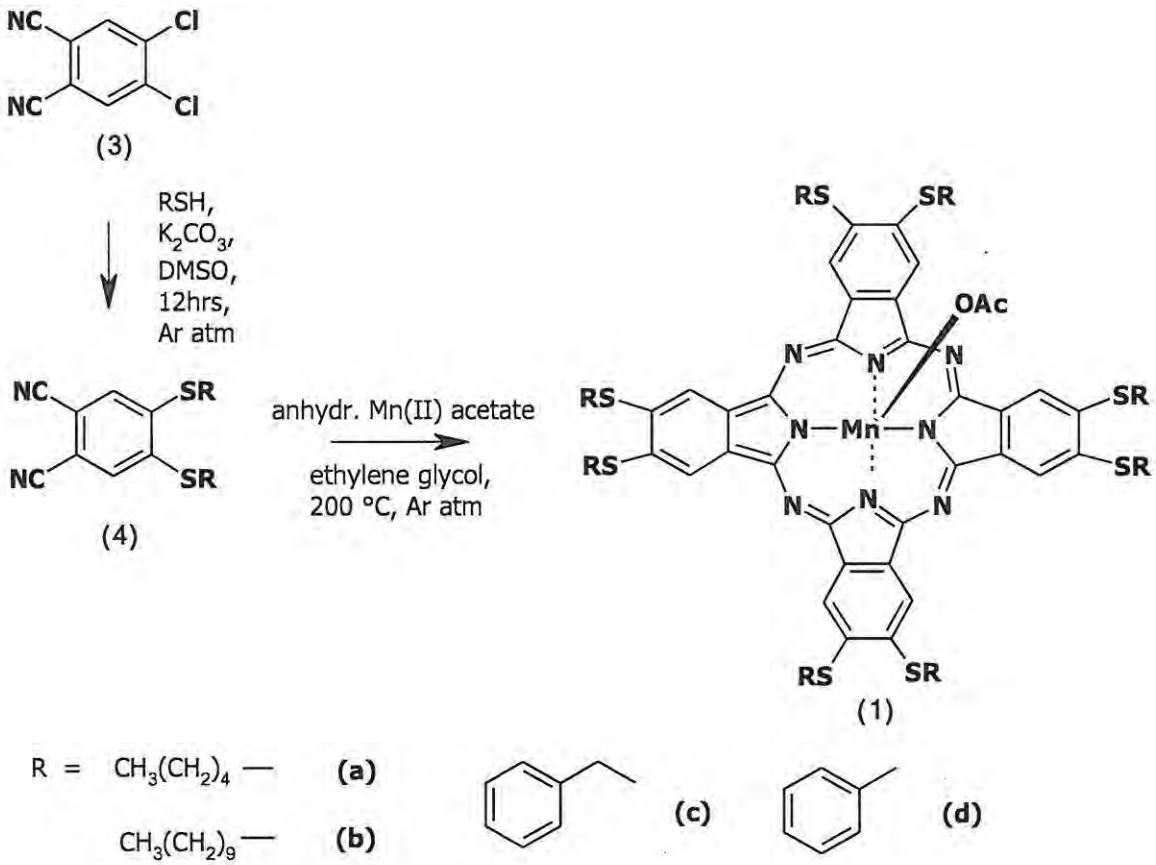

Scheme 3.1. Synthetic route for the produced thio-derivatised metallophthalocyanine complexes. Complex **1a**, manganese(III) octa(pentylthio)phthalocyanine, (OAc)MnPc$^{\beta}${$S(CH_2)_4CH_3$}$_8$. Complex **1b**, manganese(III) octa(decylthio)phthalocyanine, (OAc)MnPc$^{\beta}${$(SCH_2)_9CH_3$}$_8$. Complex **1c**, manganese(III) octa(benzylthio) phthalocyanine, (OAc)MnPc$^{\beta}$$(SCH_2Ph)_8$. Complex **1d**, manganese(III) octa(phenylthio)phthalocyanine, (OAc)MnPc$^{\beta}$$(SPh)_8$.

The aryl- and alkylthio phthalonitriles were then reacted with manganese(II) acetate by refluxing in ethylene glycol for 4 or 5 h. Yields of complexes **1a** to **1d** ranged from 32 to 74 %. The structure of these and similar complexes are shown in Fig. 3.1.

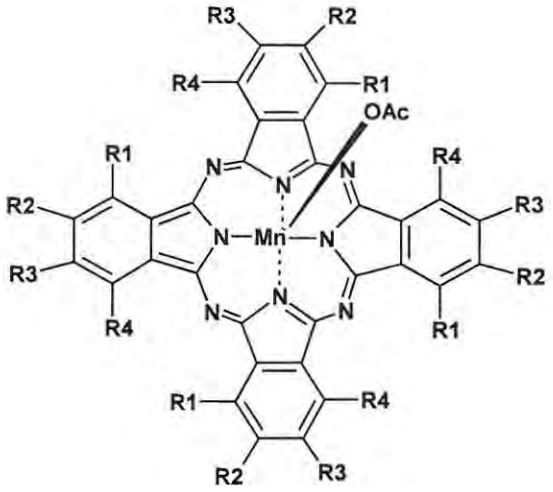

Complex number	Substituents	Abbreviation	Reference
1a	R1 = R4 =H; R2 = R3 = $S(CH_2)_4CH_3$	(OAc)$MnPc^{\beta}\{S(CH_2)_4CH_3\}_8$	This work
1b	R1 = R4 =H; R2 = R3 = $(SCH_2)_9CH_3$	(OAc)$MnPc^{\beta}\{(SCH_2)_9CH_3\}_8$	This work
1c	R1 = R4 =H; R2 = R3 = SCH_2Ph	(OAc)$MnPc^{\beta}(SCH_2Ph)_8$	This work
1d	R1 = R4 =H; R2 = R3 = SPh	(OAc)$MnPc^{\beta}(SPh)_8$	This work
5	R2 = R3 =H; R1 = R4 = $S(CH_2)_4CH_3$	(OAc)$MnPc^{\alpha}\{S(CH_2)_4CH_3\}_8$	[52]
6	R1 = R3 = R4 =H; R2 = $(SCH_2)_{11}CH_3$	(OAc)$MnPc^{\beta}\{(SCH_2)_{11}CH_3\}_4$	[31]
7	R1 = R3 = R4 =H; R2 = SCH_2Ph	(OAc)$MnPc^{\beta}(SCH_2Ph)_4$	[31]
8	R2 = R3 = R4 =H; R1 = SPh	(OH)$MnPc^{\alpha}(SPh)_4$	[27]

Figure 3.1. Molecular structures of the compared manganese phthalocyanine complexes.

The complexes were purified by column chromatography using Bio-Beads, which relies on size-exclusion. The use of a Bio-bead column instead of the commonly used silica column was much more effective and provided higher yields for the manganese complexes. The choice solvent for elution of the MnPcs was $CHCl_3$ as the use of THF as an eluting solvent resulted in the formation of μ-oxo MnPc species, as shown by its typical spectrum [26] in Fig. 3.2 with a peak at 650 nm.

μ-Oxo MnPc complexes absorb in the 630 to 650 nm region and hence are highly blue shifted compared to monomeric $Mn^{III}Pc$ complexes, which commonly have their Q band near 750 nm or above. The observed μ-oxo MnPc formation in THF could be a result of the different amounts of dissolved oxygen in this solvent compared to chloroform.

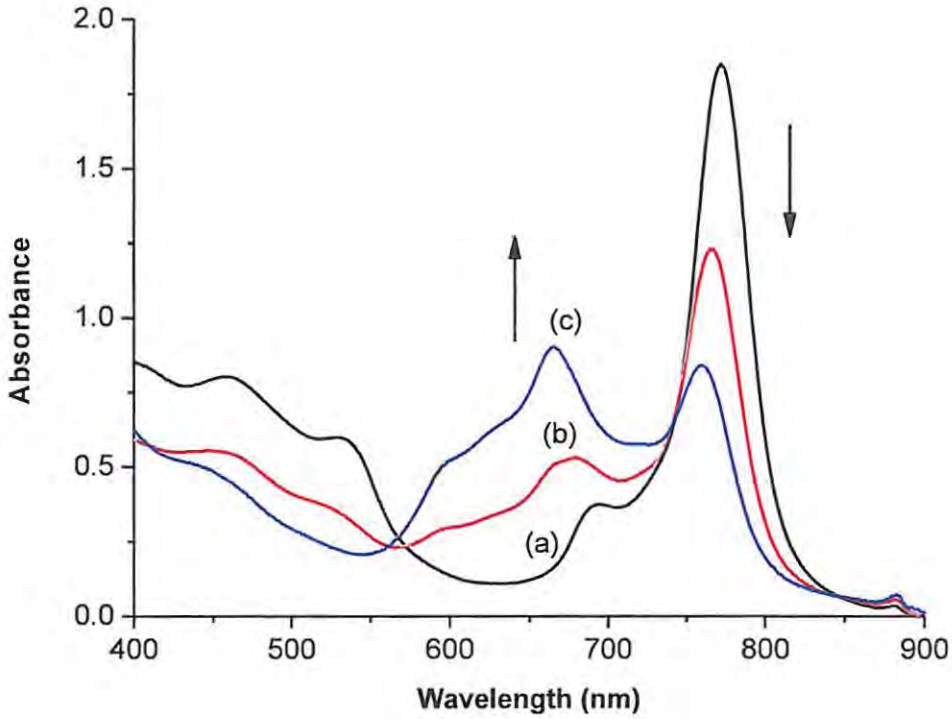

Figure 3.2. UV-visible spectra of **1d** showing spectral changes during elution from a Bio-bead column with DCM (a) followed by THF (b) and (c) in various subsequent fractions.

The mechanism for the formation of the μ-oxo dimer and Mn^{II} species was put forward by Lever et al. [203] and is as follows:

$PcMn^{II} + O_2 \leftrightarrows PcMn(O_2)$ 3.1

$PcMn(O_2) + PcMn^{II} \leftrightarrows PcMn^{III}–O_2–Mn^{III}Pc$ 3.2

$PcMn^{III}–O_2–Mn^{III}Pc \leftrightarrows 2PcMn^{IV}O$ 3.3

$2PcMn^{IV}O + 2PcMn^{II} \leftrightarrows 2PcMn^{III}–O–Mn^{III}Pc$ 3.4

Net: $4PcMn^{II} + O_2 \leftrightarrows 2PcMn^{III}–O–Mn^{III}Pc$ 3.5

Complexes **1c** and **1d** were soluble in $CHCl_3$, DCM, THF, DMF and DMSO, whereas **1a** and **1b** were insoluble in DMF and DMSO likely due to their more nonpolar alkyl substituents. Complexes **1a** and **1b** also showed good stability in the solvents over time, with little to no change in their spectra. However, complexes **1c** and **1d** exhibited unstable spectra in DMF and THF over time, with the formation of bands typical of the μ-oxo species, similar to that shown in Fig. 3.2, due to the effects of dissolved oxygen. It can be seen that the spectra and thus the colour of these Pcs changes depending on the solvent conditions, and care needs to be taken in their preparation.

The formation of the respective phthalocyanines was also confirmed by the disappearance of the distinctive C≡N band at 2230 cm^{-1} in the IR spectra (figures not shown). Also visible in the IR spectra was the very sharp Mn-N band at 669 cm^{-1}. This was present in all the spectra for the Pcs. Also useful for characterisation were the bands at 2923 and 2852 cm^{-1}, which are indicative of C-H stretches. These bands were more prominent in the alkylthio-Pcs, complexes **1a** and **1b**.

3.2. UV-vis spectroscopy

The UV-visible spectra of complexes **1a-d** are shown in Fig. 3.3 in chloroform. Because of the presence of manganese and the electron-donating properties of sulphur, the Q band is highly red-shifted and the complexes are dark red, brown, or dark brown in colour. This is typical of $Mn^{III}Pc$ complexes [31,52,204]. The synthesis used Mn(II) acetate, however as purification took place in aerobic conditions the $Mn^{III}Pc$ species was formed, and there was no indication of residual $Mn^{II}Pc$.

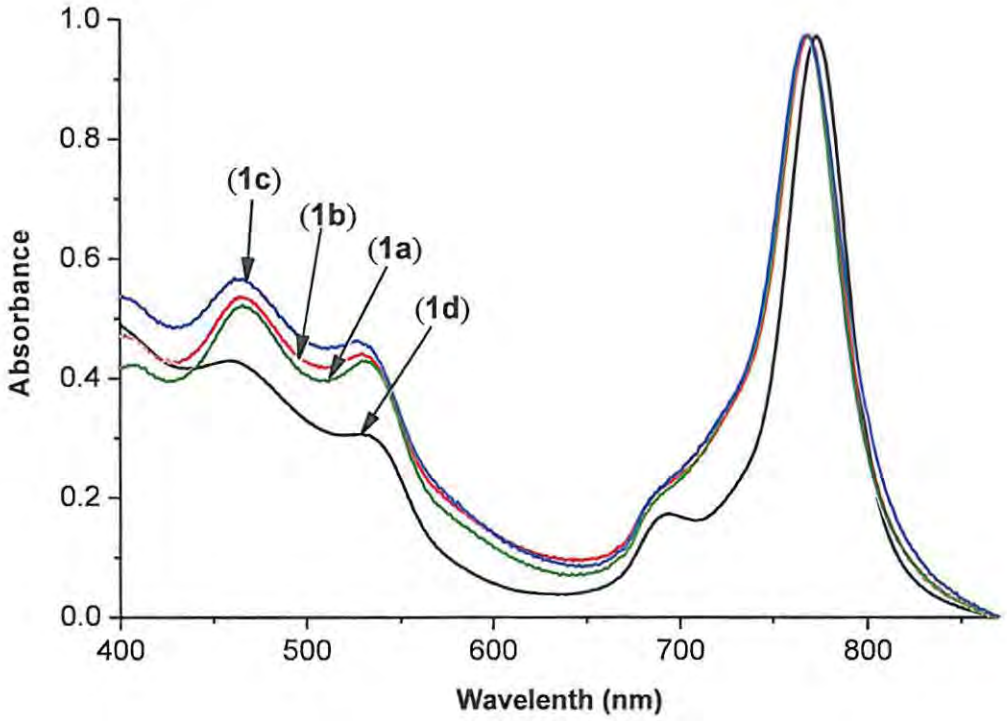

Figure 3.3. UV-visible spectra of **1a**, **1b**, **1c** and **1d** in $CHCl_3$.

Complex **1d** was slightly more red-shifted compared to the other Pcs, with a Q band at 773 nm, while the alkylthio-Pcs (**1a** and **1b**) had a Q band at 768 nm and for **1c** the Q band was at 767 nm in DCM, Table 3.1. The spectra in DCM were identical to that in $CHCl_3$. This correlates with previous work and confirms that the alkyl chain length in MPc complexes does not significantly affect the Q band position [204–206]. The spectral differences between the two arylthio-MnPcs could be attributed to the CH_2 group separating the sulphur and the ring for **1c**, and so making it behave more similarly to the alkyl substituents with regard to electron-donating ability. The electron-rich phenyl ring in complex **1d**, however, could directly contribute to the electron-donating properties of the substituents and shift the spectrum further to the red. This indicated that although alkyl chain length does not affect the electronic properties of the ring, aryl substituents can play a larger role.

The Pcs also had three bands near 405, 465 and 530 nm. The bands between 400 and 550 nm are due to charge-transfer between the metal and the Pc ring [26]. For both **1a** and **1b** the Q band spectra shifted to 755 nm in THF (data not shown). Fig. 3.3 shows that **1d** is less aggregated than the other Pcs, as judged by the narrower Q band. However, Beer's law was observed for all complexes at concentrations less than 9.0×10^{-6} M. Comparisons of Q band maxima (λ_Q) between similar complexes (peripherally tetra-substituted and non-peripherally octa-substituted, Fig. 3.1) are shown in Table 3.1.

Table 3.1. Q band wavelength of $Mn^{III}Pc$ derivatives in DCM, unless otherwise indicated.

MnPc complex	Q band wavelength (nm)	Reference
1a	768	This work
1b	768	This work
1c	767	This work
1d	773	This work
5	893	[52]
6	749	[31]
7	745	[31]
8	764 [a]	[27]

[a] In DMF

For compounds **1a** and **5** containing the same chain length but the latter non-peripherally substituted (structures are shown in Fig. 3.1), the Q band was observed at 768 nm and 893 nm [52] in DCM respectively (Table 3.1), showing that peripheral substitution caused an expected blue shift in the Q band compared to non-peripheral substitution [26].

Looking at the octa-substituted complex **1c** (λ_Q = 767) and comparing it to its tetra-substituted counterpart **7** (λ_Q = 745), the Q band was blue-shifted in the tetra complex [31]. These results show that the octa-substituted MnPcs exhibited greater electron-

donation by the substituents than the equivalent tetra MnPcs, which can be simply attributed to the greater number of substituents around the ring.

Comparing complexes **1d** (λ_Q = 773) and **8** (λ_Q = 764), one being the peripheral octa-substituted version (**1d**) and the other the tetra-substituted non-peripheral complex (**8**), the latter has a comparatively blue shifted Q band despite being non-peripherally substituted [27]. This indicates that the number of substituents plays a larger role on the electronic properties of the ring than the position of these substituents, although the solvent conditions were not the same in this case.

3.3. Electrochemistry

Fig. 3.4 shows the cyclic (CV) and differential pulse (DPV) voltammograms of all four of the new MnPc complexes. All electrochemical analyses were performed in de-aerated DCM using $TBABF_4$ as an electrolyte.

The half-wave potentials ($E_{p1/2}$) for **1a-d** and other similar compounds are shown in Table 3.2. Complexes **1a-d** displayed three main redox processes, with ΔE values from 93 to values greater than 200 mV. **1a** displayed redox processes at: $E_{p1/2}$ = +0.97 V (I), $E_{p1/2}$ = -0.35 V (II) and $E_{p1/2}$ = -1.07 V (III) versus Ag|AgCl with **1b** displaying redox processes at: $E_{p1/2}$ = +0.94 V (I), $E_{p1/2}$ = -0.46 V (II) and $E_{p1/2}$ = -1.08 V (III) versus Ag|AgCl. **1c** displayed redox processes at: $E_{p1/2}$ = +0.96 V (I), $E_{p1/2}$ = -0.26 V (II) and $E_{p1/2}$ = -0.94 V (III) versus Ag|AgCl while **1d** displayed redox processes at: $E_{p1/2}$ = +0.88 V (I), $E_{p1/2}$ = -0.34 V (II) and $E_{p1/2}$ = -1.15 V (III) versus Ag|AgCl. In some of the complexes, a weak process could be observed around -0.1 V. This process was attributed to aggregation of the compounds, as the peaks were observed to decrease with dilution, relative to the rest of the peaks.

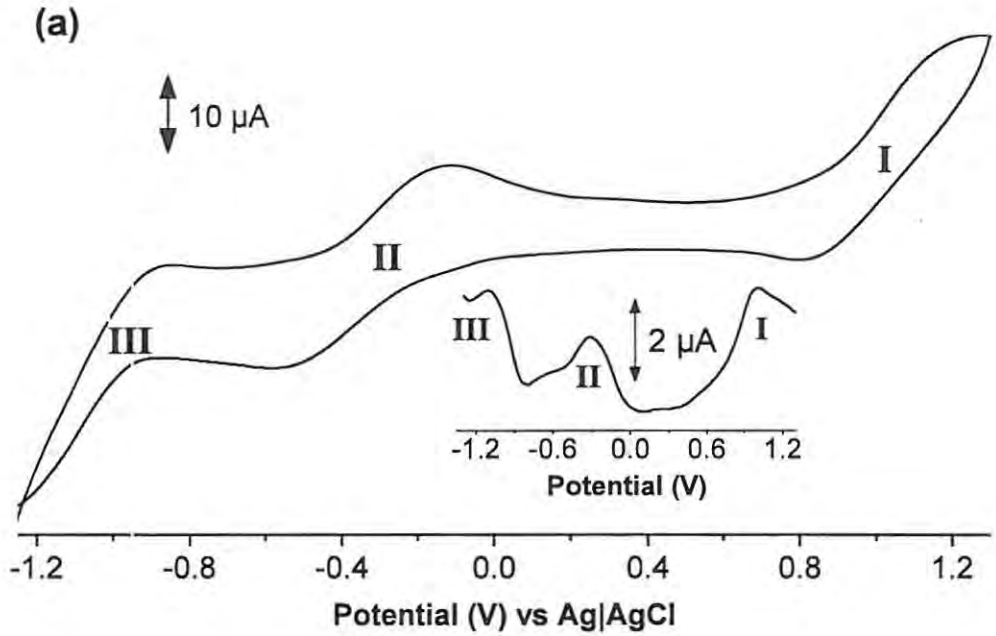
(a)
10 µA
I
II
III
III
II
2 µA
I
-1.2 -0.6 0.0 0.6 1.2
Potential (V)
-1.2 -0.8 -0.4 0.0 0.4 0.8 1.2
Potential (V) vs Ag|AgCl

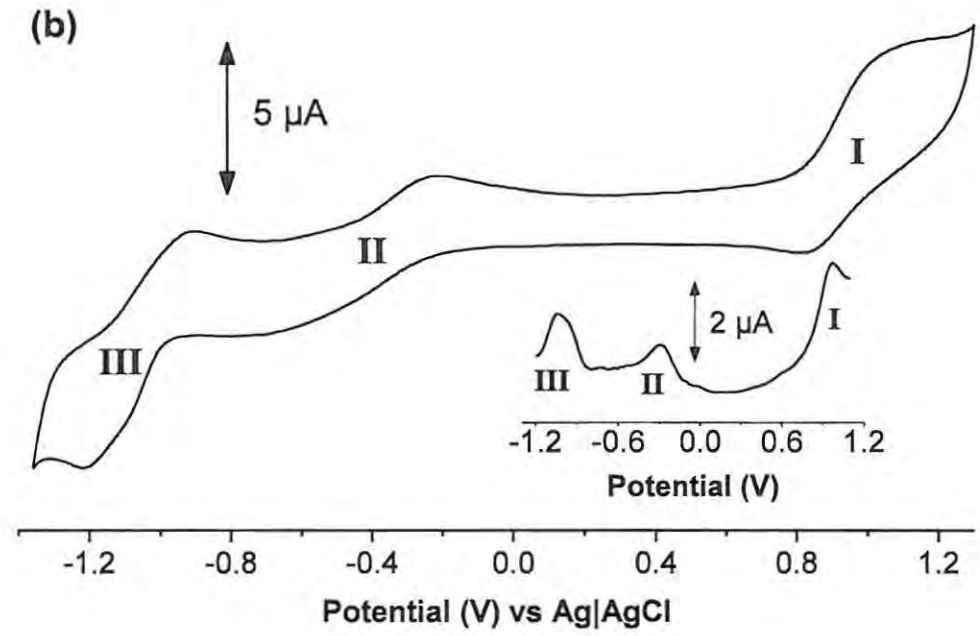
(b)
5 µA
I
II
III
III
II
2 µA
I
-1.2 -0.6 0.0 0.6 1.2
Potential (V)
-1.2 -0.8 -0.4 0.0 0.4 0.8 1.2
Potential (V) vs Ag|AgCl

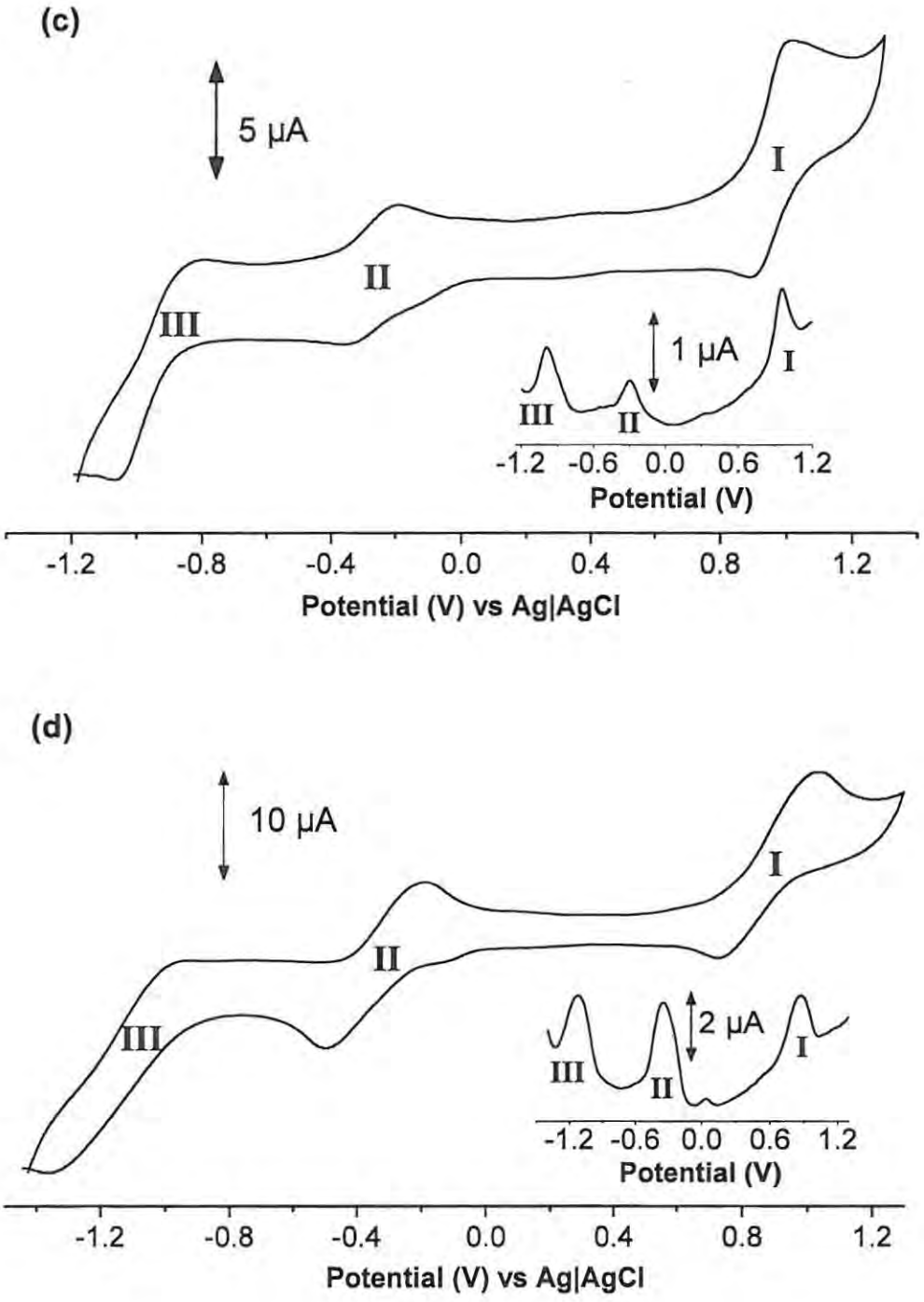

Figure 3.4. Cyclic voltammogram for (a) **1a**, (b) **1b**, (c) **1c** and (d) **1d** in DCM containing 0.1 M $TBABF_4$. Scan rate = 50 mV/s. Inset: DPV at 20 mV/s.

Plots of peak current (I_p) versus square root of the scan rate ($v^{1/2}$) were linear, suggesting diffusion control at the electrode surface for all of the complexes. Fig. 3.4 shows broad CV peaks, which are often observed in MnPc complexes, especially those containing long chain substituents [31]. This was also observed for the tetra-substituted complexes **6** and **7** (structures in Fig. 3.1) [31]. However, complex **5** octa-substituted with pentylthio groups at the non-peripheral positions showed reversible behaviour [52], most likely due to the prevention of aggregation by non-peripheral substitution. The assignments of these processes were confirmed with spectroelectrochemistry, as discussed below.

The $Mn^{III}Pc^{2-}/Mn^{II}Pc^{2-}$ process (**II**) could be clearly observed at similar potentials in all thio-derivatised MnPcs, Table 3.2 (except for **7**) [27,31,52]. Additionally, the DPV for the complexes show small oxidation peaks at 0.25 V for **1a**, 0.02 V for **1b**, 0.31 V for **1c** and 0.05 V for **1d**. This could not be conclusively assigned to the $Mn^{IV}Pc^{2-}/Mn^{III}Pc^{2-}$ process for the synthesized Pcs in this work, although the process has been observed before [31,52,204]. Process **III** has been assigned in similar complexes to either $Mn^{II}Pc^{2-}/Mn^{I}Pc^{2-}$ [28,30] or $Mn^{II}Pc^{2-}/Mn^{II}Pc^{3-}$ [30,31,42,52,204], although the latter has been reported more frequently. In this work, spectroelectrochemistry was used to assign this process to ring reduction. Process **I** could be attributed to ring oxidation, and it is in a similar range to that reported in literature [30,31,52]. Alkylthio- and arylthio-substituted complexes often decompose during ring oxidation, and this can contribute to the irreversibility of process **I** [30,31].

Table 3.2. Electrochemical data of thio-derivatised MnPcs. The compounds were analysed in DCM containing $TBABF_4$ and the half-wave potential ($E_{p1/2}$) as V against Ag|AgCl.

Complex	$Mn^{II}Pc^{2-}/Mn^{II}Pc^{3-}$ (III)	$Mn^{III}Pc^{2-}/Mn^{II}Pc^{2-}$ (II)	$Mn^{III}Pc^{1-}/Mn^{III}Pc^{2-}$ (I)	Reference
1a	-1.07	-0.35	0.97	This work
1b	-1.08	-0.46	0.94	This work
1c	-0.94	-0.26	0.96	This work
1d	-1.15	-0.34	0.88	This work
5	-1.24	-0.46	-	[52]
6	-0.98	-0.26	0.83	[31]
7	-0.84	-0.08	0.87	[31]

Ease of oxidation and reduction of complexes is related to the electron-donating or withdrawing effects of the substituents. Electron-donating substituents are expected to facilitate easier oxidation and harder reduction, as they should increase the electron density on the ring [207,208]. As aromatic rings are electron donors, **1d** should then be more electron-donating than **1c**, which would in turn be more electron-donating than **1a** followed by **1b**. This behaviour was partially confirmed by the absorbance spectra of the compounds (Fig. 3.3), which showed the Q band positions of **1a-c** at an approximately equivalent position, while **1d** was the most red-shifted as its phenyl substituents are the most electron-donating. As expected then, **1a-c** were harder to oxidize with regard to

process I when compared to complex **1d**. Looking at process III, **1d** was the hardest to reduce (as expected) with an $E_{p1/2}$ of –1.15 V, with **1a** and **1b** having similar values and **1c** being the easiest to reduce with an $E_{p1/2}$ of –0.94 V. The ease in reduction for **1c** could be attributed to the aromatic ring being separated from the Pc by a CH_2 group, as this has been observed before with complexes **6** and **7** [31]. No particular trend could be observed for process II except to note that again complex **1c** showed the greatest ease in reduction with an $E_{p1/2}$ of –0.26 V.

Looking at peripheral (**1a**) versus non-peripheral (**5**) substitution (with the same substituent), complex **1a** showed greater ease in reduction compared to complex **5** [52]. Pc ring oxidation of **5**, although attributed to $Mn^{IV}Pc^{-1}/Mn^{IV}Pc^{-2}$ rather than $Mn^{III}Pc^{-1}/Mn^{III}Pc^{-2}$ as in this work, showed that the non-peripheral complex was more easily oxidized with an $E_{p1/2}$ of 0.75 V [52]. Octa-substituted **1c** proved to be harder to oxidize compared to the tetra-substituted complex **7** containing the same substituent. The same was true of complex **1b** compared to the similar tetra-substituted compound **6** [31], although the chain lengths were slightly different.

3.4. Spectroelectrochemistry

Spectroelectrochemical studies allowed a confident assignment of the redox couples to be made. Fig. 3.5. shows the spectral changes that occurred for complex **1a**, which were similar to the spectral changes observed for the other complexes in this work. Oxidation at potentials of process I resulted in degradation of the complex as has been observed in literature during oxidation of thio-substituted MPc complexes [31]. Fig. 3.5(a) illustrates spectral changes observed on application of potentials more negative than process **II** (-0.65 V), clearly showing the reduction of Mn(III) to Mn(II) as there is a decrease in the Mn(III) Q band and a growing blue-shifted Q band that correlates to Mn(II) [26,27,31,52]. The Q band shifted from 768 nm for the Mn(III) complex to 720 nm for the Mn(II) complex and the colour of the complex in the OTTLE cell visibly changed from red-brown to green. There was also a decrease in intensity for the two charge transfer bands at 465 and 530 nm, with the former disappearing almost completely and the latter shifting to 540 nm. The spectra had three clear isosbestic points at 738, 614 and 407 nm and the value of n was calculated using $Q = nFCV$ to be approximately equal to 1.

Fig. 3.5(b) shows spectral changes observed on application of potentials more negative than process **III** (-1.3 V), with the decrease in the Q band and the formation of new features between 500 and 650 nm characteristic of ring-based reduction processes in Pcs [48], leading to the assignment of this as $Mn^{II}Pc^{2-}/Mn^{II}Pc^{3-}$. The spectral changes were similar to that reported elsewhere for this process [30,31,52].

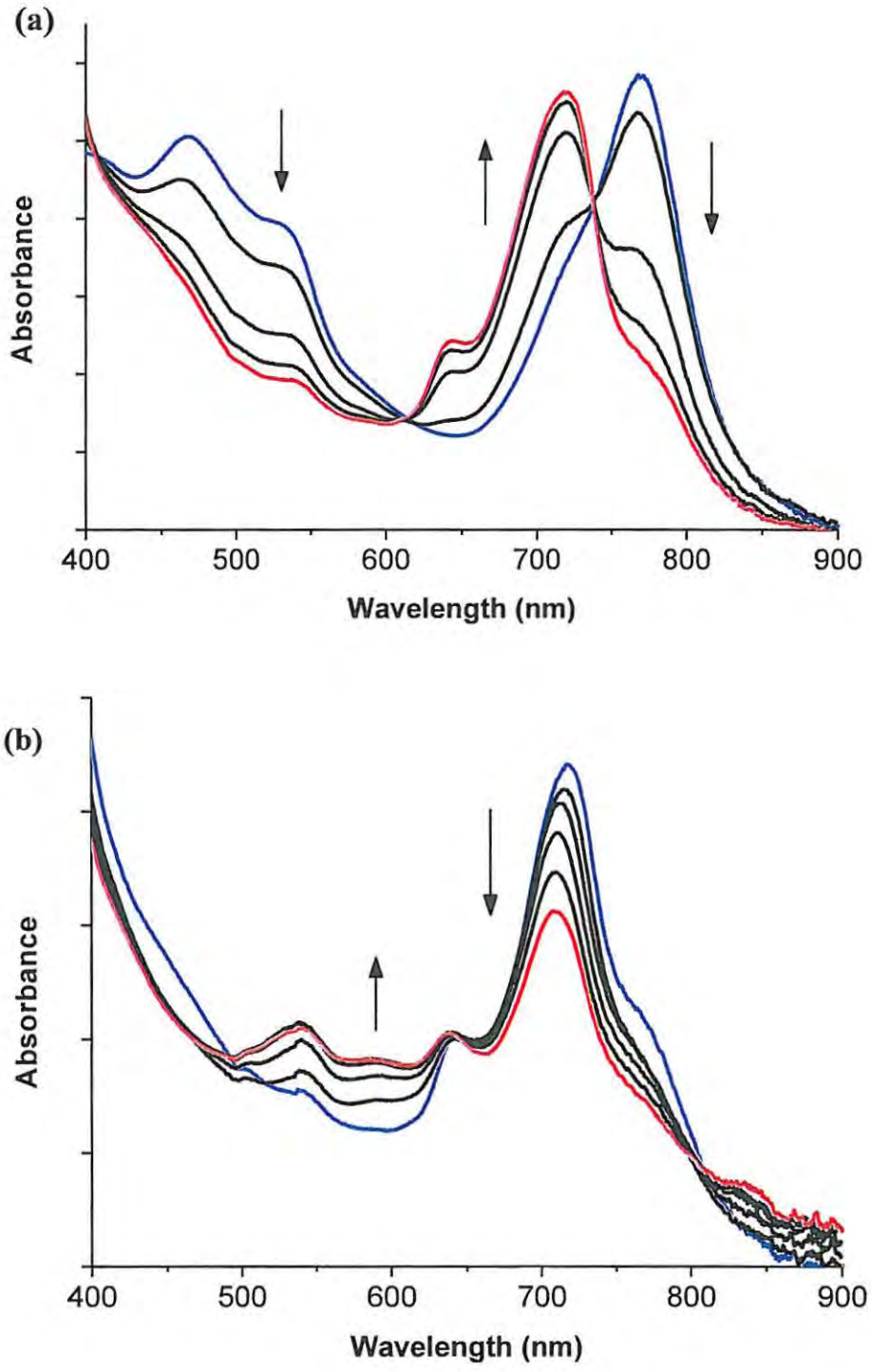

Figure 3.5. UV-Vis spectral changes for complex **1a** observed using controlled potential electrolysis at: (a) –0.65 V and (b) –1.3 V. Electrolyte = DCM with 0.1 M $TBABF_4$.

It has been shown that the nature of ring substituents are responsible for the formation of $Mn^{II}Pc^{3-}$ as opposed to $Mn^{I}Pc^{2-}$ [30] and there was no evidence of the broad Q band forming at around 550 nm that is characteristic of Mn^{I} [30], confirming process III as ring-based reduction. Based on these results, the processes could be assigned as follows:

$Mn^{III}Pc^{2-} \rightarrow Mn^{III}Pc^{1-} + e^-$ (process I) 3.6

$Mn^{III}Pc^{2-} + e^- \rightarrow Mn^{II}Pc^{2-}$ (process II) 3.7

$Mn^{II}Pc^{2-} + e^- \rightarrow Mn^{II}Pc^{3-}$ (process III) 3.8

CHAPTER 4

ELECTRODE MODIFICATION

4.1. Self assembled monolayers (SAMs)

SAMs of the new MnPcs were formed on gold in order to study the effect of alkyl- vs arylthio substituents on SAM formation, surface coverage values, blocking characteristics, and the fate of the alkyl and aryl groups following Au-S bond formation.

SAM films were formed by immersing the bare gold electrode in the desired complex for an average time of 48 h in each case. Formation of SAM films is facilitated by coordination of the sulphur group (using its lone pairs of electrons) with gold, with the C-S bond likely remaining intact as reported previously [72]. Electrochemistry, Raman spectroscopy, atomic force microscopy (AFM), scanning electron microscopy (SEM) and X-ray photoelectron spectroscopy (XPS) were used to characterize the modified gold electrodes and give further spectroscopic evidence of their formation. For the latter studies (Raman, AFM, SEM and XPS), only **1b** and **1d** were used to identify the effect of the different substituents on the SAM layer as both showed good blocking characteristics in the electrochemical studies. Gold-coated glass was immersed in the MnPc solution for 10 days for the Raman, AFM and SEM analyses, to ensure a fully-formed SAM and complete coverage, and gold plate electrodes were modified in the same way for the XPS analysis due to the availability of these plate electrodes which can be polished and reused.

4.1.1. Electrochemical characterisation

Electrochemical characterisation of SAMs can be used to show both the blocking behaviour of the surface towards commonly used redox probes and also to determine surface coverage of the MPcs on the surface.

4.1.1.1. Inhibition of faradaic processes

Electrochemical properties of the films are closely related to the extent to which they inhibit common faradaic processes associated with the bare gold surface. Fig. 4.1(a) shows the oxidation (at 0.21 V vs. Ag|AgCl) and reduction (gold oxide stripping peak, at 0.15 V vs. Ag|AgCl) of the bare gold surface in 1 M Na_2SO_4 in pH 4 buffer solution. As seen in this figure, there was appreciable passivation of this process in the presence of all the MPc-SAMs, although the **1c**-SAM was the least effective at blocking the electrode. Gold oxidation was considerably inhibited with a decrease in intensity of the gold oxide stripping peak, suggesting that the electrolyte was no longer accessible to the bare gold surface and confirming SAM formation.

Fig. 4.1(b) shows the cyclic voltammograms obtained for the bare AuE and the SAM-modified gold electrodes in 1 mM $Fe(NH_4)(SO_4)_2$ containing 1 M $HClO_4$. The clearly resolved quasi-reversible redox process ($[Fe(H_2O)_6]^{3+}/[Fe(H_2O)_6]^{2+}$) on the bare electrode was almost completely inhibited on SAMs of **1a** and **1b**, only slightly inhibited for the **1d**-SAM and almost completely uninhibited for the **1c**-SAM, where the oxidation process was better defined than for the bare electrode. The inhibition of this process on the SAM

modified gold electrodes suggests the isolation of the gold surface from the electrolyte, confirming defect-free SAM formation for **1a** and **1b**. For **1d**, the voltammograms were distorted, but more resolved for **1c**. It is possible that the bulky aryl substituents in **1c** and **1d** were less effective in blocking the redox process, as the SAMs they formed appeared to be more permeable to this analyte.

Fig. 4.1(c) shows the CVs of the bare AuE and the SAM-modified electrodes in 1 mM $CuSO_4$ in pH 4 buffer solution. The bulk deposition of Cu began at 133 mV (vs. Ag|AgCl on the negative scan) and the maximum of the large underpotential deposition stripping peak of the Cu occurred at 101 mV (vs. Ag|AgCl) on the bare AuE. This process was significantly inhibited on the SAM modified electrodes, indicating SAM formation for **1a**, **1b** and **1d**. The **1c**-SAM again showed the least inhibition of the redox process, indicating that it was not completely blocked.

Fig. 4.1(d) shows the CVs of the bare AuE and the SAM-modified electrodes in 1 mM solution of $[Fe(CN)_6]^{3-}$ containing 0.1 M KCl as the supporting electrolyte. Unlike the $[Fe(H_2O)_6]^{3+}/[Fe(H_2O)_6]^{2+}$ redox process in Fig 4.1(b), the $[Fe(CN)_6]^{3-/4-}$ redox couple was not inhibited on the SAM modified electrodes because of the fast nature of electron transfer for this process. This observation has been reported previously for adsorbed cobalt tetra-amino phthalocyanine films on a vitreous carbon electrode [209]. However, the cathodic to anodic peak potential separation (ΔE) for this process was larger for SAMs of **1a**, **1b** and **1d**, but the same for **1c**. The anodic and cathodic current intensities of the

$[Fe(CN)_6]^{3-/4-}$ redox couple on bare AuE are larger than that observed on the SAM-modified electrodes, confirming the formation of the SAM films.

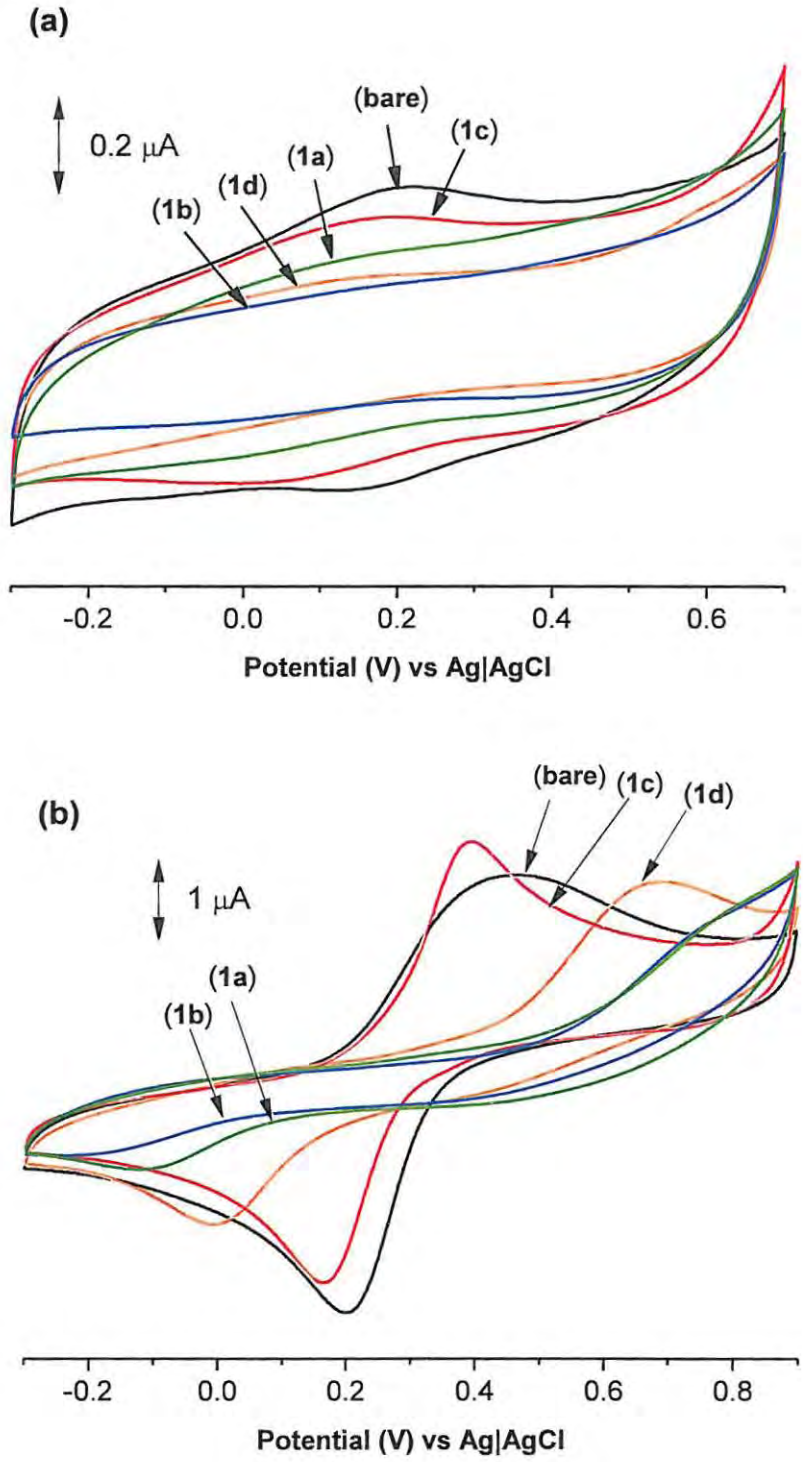

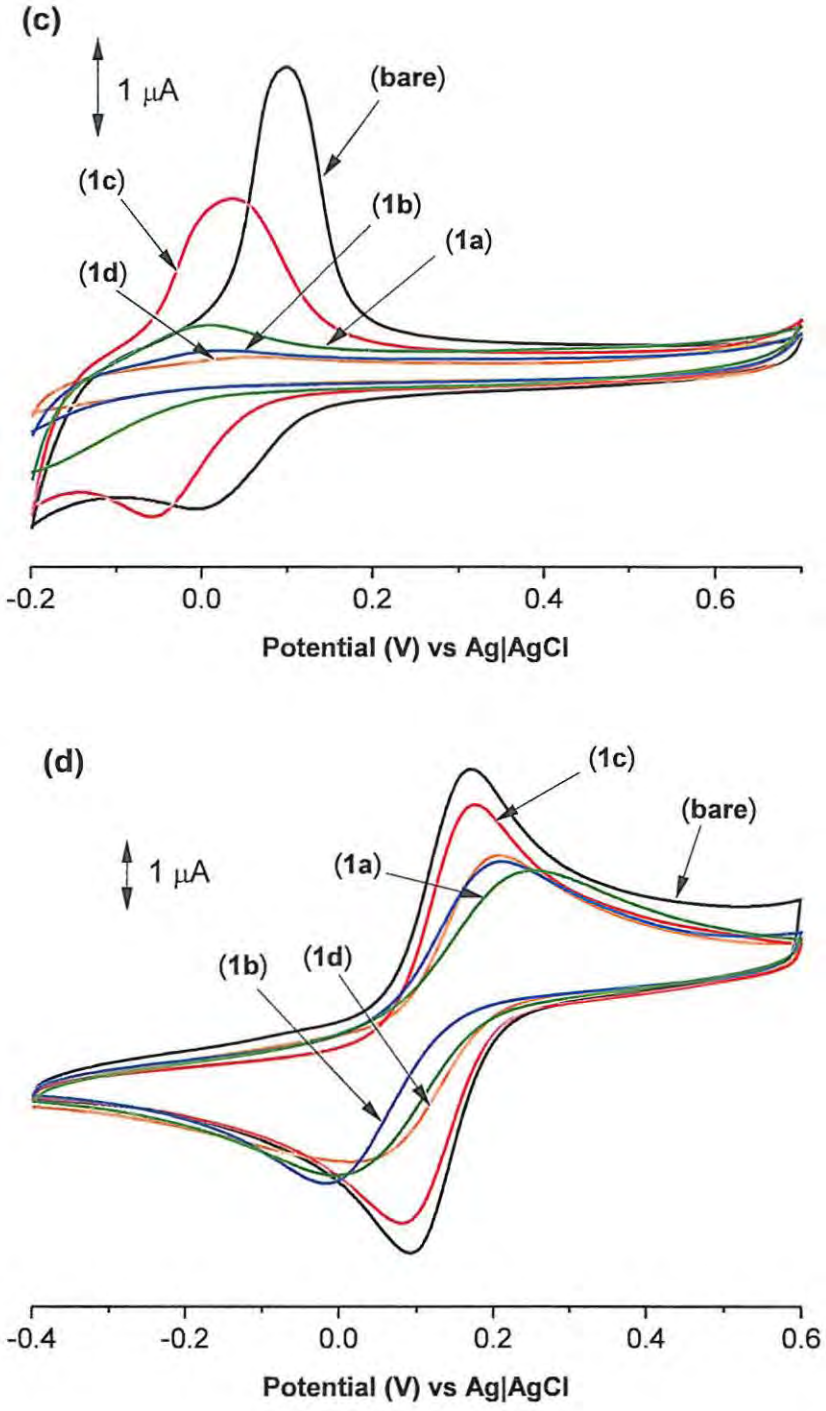

Figure 4.1. Cyclic voltammograms for bare Au, **1a**-SAM, **1b**-SAM, **1c**-SAM and **1d**-SAM in: (a) 1 M Na_2SO_4 in pH 4 buffer solution, (b) 1 mM $Fe(NH_4)(SO_4)_2$ in 1 M $HClO_4$, (c) 1 mM $CuSO_4$ in pH 4 buffer solution and (d) 1 mM $K_3[Fe(CN)_6]$ in 0.1 M KCl. Scan rate = 50 mV/s vs Ag|AgCl.

In general **1a** and **1b** showed particularly good blocking characteristics in all solutions, suggesting that the benzyl and phenyl groups for **1c** and **1d** prevent the formation of good SAMs, likely because the more bulky aryl groups do not act as a barrier to ion transport through the SAM layer, with steric effects preventing close packing of the MnPcs.

4.1.1.2. Surface coverage

Fig. 4.2 shows the cyclic voltammetry profiles obtained for the SAM-modified electrodes in 1 M $HClO_4$. The redox processes observed in Fig. 4.2 are associated with Mn^{3+}/Mn^{4+} ($E_{p1/2} \approx 0.23$ V vs. Ag|AgCl), Table 4.1, as compared to similar compounds [27,31,52].

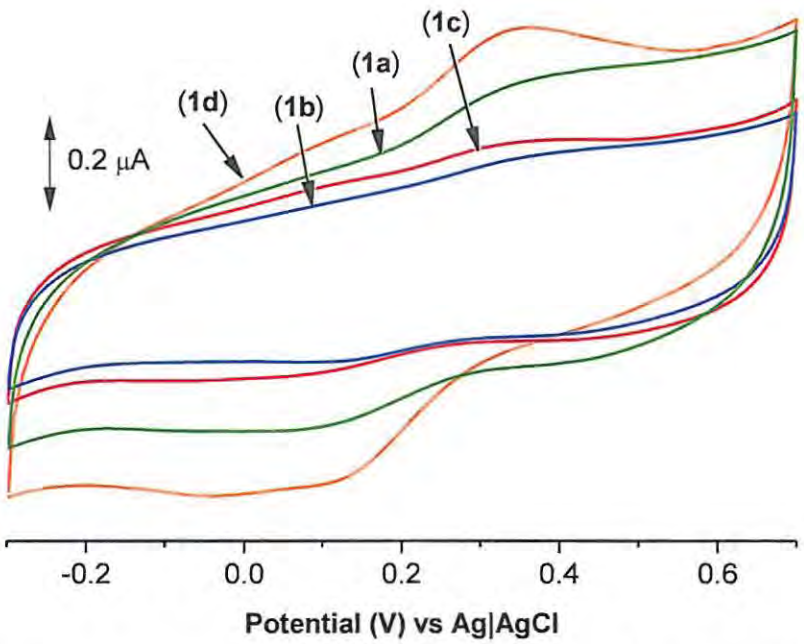

Figure 4.2. Cyclic voltammograms for **1a**-SAM, **1b**-SAM, **1c**-SAM and **1d**-SAM in 1 M $HClO_4$. Scan rate = 50 mV/s vs Ag|AgCl.

This process was not clearly observed for free MnPcs in solution, as there were no significant peaks in this potential range. It has been reported before for NiPc complexes that some metal processes are observed when the complexes are absorbed but not when in solution [22]. The difference between the free and bound MnPc is associated with the nature of the SAM and the different solution environments.

Surface coverage (Γ) for each SAM was estimated from the relevant redox process in Fig. 4.2 using equation 1.1, where I_{pa} is the anodic peak current in Fig. 4.2 for each SAM. The real surface area of the electrode was estimated using the well-established method [210] applying equation 1.3 (Randles-Sevcik equation). $[Fe(CN)_6]^{3-}$ was used as the redox active species because it has a known diffusion coefficient (7.6×10^{-6} cm²/s [210]). The roughness factor of the electrode was calculated to be 1.02 (ratio of I_{pa} (experimental)/I_{pa} (theoretical)), where I_{pa} (experimental) and I_{pa} (theoretical) are the experimental current and current calculated using equation 1.3 respectively. The geometrical area was used in the estimation of I_{pa} (theoretical). The product of the roughness factor and theoretical surface area gives the real surface area (0.0205 cm²).

Thus the values of surface coverage obtained on the gold electrode were 0.64×10^{-10} mol.cm^{-2} for **1a**, 0.30×10^{-10} mol.cm^{-2} for **1b**, 0.42×10^{-10} mol.cm^{-2} for **1c** and 1.45×10^{-10} mol.cm^{-2} for **1d** (Table 4.1). Except for **1d**, these values are slightly less than the values obtained for a monolayer coverage of an MPc molecule lying flat on the electrode [35], which is estimated at 1×10^{-10} mol.cm^{-2}. These values are, however, still within the range for monolayer coverage.

Table 4.1. Electrochemical parameters of SAMs of complexes **1a** – **1d** in 1 M $HClO_4$, (formation time = 48 h).

MnPc complex	Mn^{III}/Mn^{II} E (V)	Mn^{IV}/Mn^{III} E (V)	Surface coverage, Γ (10^{10} mol.cm^{-2})	Reference
1a	-	0.22	0.64	This work
1b	-	0.24	0.30	This work
1c	-	0.22	0.42	This work
1d	-	0.23	1.42	This work
5	-0.1	-	1.1	[81][a]
6	-	0.2	0.78 (18 h)[b]	[31][a]
7	-	0.35	0.69 (18 h)[b]	[31][a]
8	-0.2	0.30	1.1 (24 h)[b]	[27]

[a] In pH 4 phosphate buffer. [b] Numbers in brackets refer to the time allowed for SAM formation.

Complexes **5**-**8** showed higher (compared to **1a**-**1c**) surface coverage values in Table 4.1, even though shorter SAM formation times (18 h and 24 h, compared to 48 h used in this work) were employed, suggesting that the tetra-substitution may enhance SAM formation. Octa-substitution may allow fewer MnPcs to be attached to the surface due to steric hindrance.

The importance of allowing the monolayer to form completely and fully is shown by Fig. 4.3, where formation times of 0 h, 24 h, and 48 h for the **1d**-SAM on gold are tested by looking at the electrochemistry of the SAM in 1 mM $CuSO_4$ in pH 4 buffer solution. As seen in this figure, a formation time of 24 h was not enough to block the electrode, while after 48 h the monolayer was almost completely pinhole free.

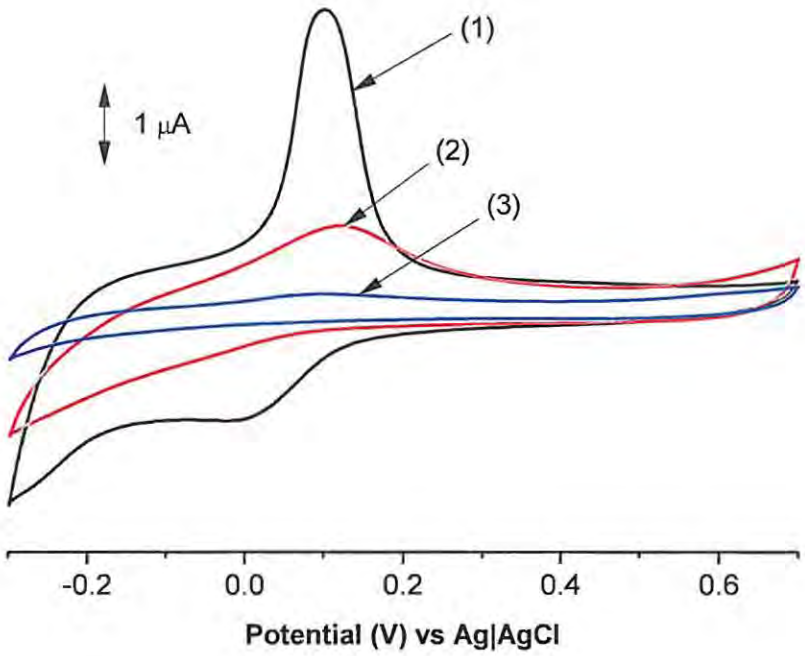

Figure 4.3. Cyclic voltammograms in 1 mM $CuSO_4$ in pH 4 buffer solution for AuE after: (1) 0 h, (2) 24 h and (3) 48 h SAM formation in 1 mM **1d** in $CHCl_3$. Scan rate = 50 mV/s vs Ag|AgCl.

Interestingly, the **1c**-SAM had an almost similar surface coverage to the **1b**-SAM despite the former SAM showing less inhibition of electrochemical processes at the electrode.

The 1c-SAM consistently displayed poor blocking of the gold surface in Fig. 4.1, but the surface coverage value indicates that this is not because of poor monolayer coverage. It is likely that the nature of the substituents, which are bulky and are also able to rotate more freely around the CH_2 group, create a layer that is more permeable to the small redox ions and so allowing them to reach the gold surface. The long alkyl chains, however, appear to prevent ions from reaching the surface so easily despite having a similar surface coverage value to **1c**, which could be also due to the more non-polar nature of the alkyl chains preventing diffusion of ions through the SAM layer. This indicates once again the importance of different substituents in the formation of these layers.

4.1.2. Raman, AFM, SEM and XPS characterisation

Gold-coated glass was employed, in place of a gold electrode, for probing surface properties of the **1b**- and **1d**-SAM films with Raman, AFM and SEM. For the XPS analysis, gold plate electrodes were used. The formation time was increased to 10 days to ensure complete coverage of the larger surfaces with the MnPcs.

4.1.2.1. Raman characterisation

Formation of a successful SAM is often confirmed by the appearance of the Au-S bond at a low wavenumber in Raman spectra, found between 250 and 340 cm^{-1} in most literature cases [35,80,211]. Often, surface enhanced Raman spectroscopy is required to detect this

very weak peak in SAMs [35]. In this work, the Au-S peak was detected at 345 cm^{-1} [35,212] (figure not shown).

4.1.2.2. *Microscopic characterisation*

Surface natures of the SAM films were probed using AFM (in the non-contact mode) and SEM. SEM and AFM are used to give information beyond the surface blocking characteristics (which are easily studied using electrochemical techniques), such as whether the MnPcs are aggregated on the gold surface or whether they form a uniform layer. As mentioned in the introduction, aggregation can inhibit the formation of a true SAM [39,170,172,213].

Fig. 4.4(a) shows the AFM 2D and 3D images of the gold-coated glass before the formation of SAMs, indicating that the bare gold surface was fairly smooth and uniform with the small bright areas being attributed to imperfections on the surface [80]. Fig. 4.4(b) shows the **1b**-SAM (alkylthio) and Fig. 4.4(c) shows the **1d**-SAM (arylthio) on gold. The most important data to take away from AFM are the values for mean thickness and roughness, and any clear indications of complete coverage or the formation of aggregates [171,172,213–215]. Fig. 4.4 indicates that there are significant differences in the topographies of the surfaces. The mean roughness and thickness of the gold-coated glass before SAM formation are 0.278 nm and 1.643 nm respectively. The mean roughness and thickness after the **1b**-SAM formation are 2.081 nm and 8.738 nm, while the mean roughness and thickness after **1d**-SAM formation are 1.870 nm and 8.666 nm

respectively. This increase in the roughness and thickness of the surface after SAM formation confirms the presence of a layer of the MnPcs on the surface. The images appear to show some nano-scale aggregation of the MnPcs, which can be expected as these peripherally substituted Pcs are more prone to aggregation than their non-peripherally substituted derivatives. The alkylthio-MnPc, **1b**, had higher roughness and thickness factors than the arylthio-MnPc, **1d**. This indicates that the layer was more densely packed because of the long chains, and is supported by the better blocking characteristics of the **1b**-SAM showed in Fig. 4.1(b) with regards to the $[Fe(H_2O)_6]^{3+}/[Fe(H_2O)_6]^{2+}$ redox process. For the non-peripheral tetra-substituted complex **8** (structure shown in Fig. 3.1), the inverse of the above behaviour was observed. AFM showed that the roughness of the surface decreased upon **8**-SAM formation, and this was explained to be a result of the complex filling in the grooves in the electrode [80]. In that case the bare gold had an initial roughness of 1.257 nm [80], which was far greater than the roughness of 0.278 nm observed in this work. This could explain the difference in the behaviour of the SAMs.

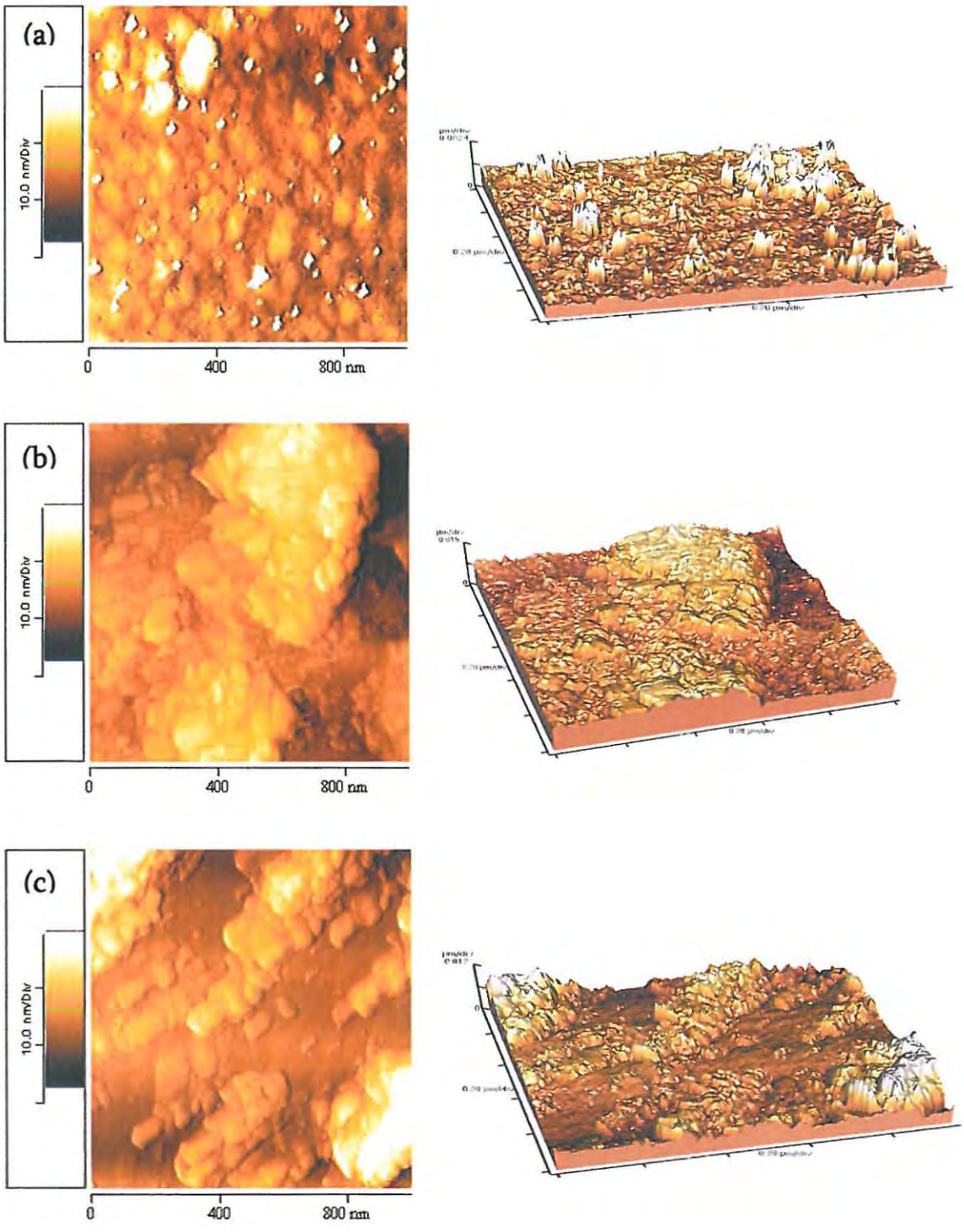

Figure 4.4. AFM images of (a) bare gold-coated glass, (b) **1b**-SAM modified gold-coated glass and (c) **1d**-SAM modified gold-coated glass.

SAMs of complexes **5**, **6** and **7** were not analyzed using AFM or SEM. However, octa- and tetra-substituted MPcs containing Sn as a central metal with non-peripherally substituted long alkylthio chains were shown to increase the roughness of the gold surface after SAM formation [216], as was observed in this work. Non-peripheral substituents also appeared to decrease the occurrence of surface aggregates.

Fig. 4.5 shows the SEM images of gold-coated glass alone (a), after **1b**-SAM formation (b), and after **1d**-SAM formation (c). Although detailed features are not visible because the scale does not permit resolution of distinct molecules [172], the bare gold-coated glass depicts a smoother surface than the SAM modified gold-coated glass which showed signs of aggregation. The SEM images indicate that there are areas with large clusters of aggregated MnPc molecules on the surface, as well as the smaller groups of aggregated molecules shown by the AFM results. As with the AFM images, the **1b**-SAM appeared to be rougher than the **1d**-SAM. Aggregation is known to be enhanced by the presence of long alkyl chains [205], which could account for the greater roughness of the **1b**-SAM in the AFM and the presence of larger surface clusters in the SEM image. SEM has not been used to analyze SAMs of complexes **5**-**8** on gold, but comparing the difference in topographies of the surfaces is another method that can be used to confirm SAM formation.

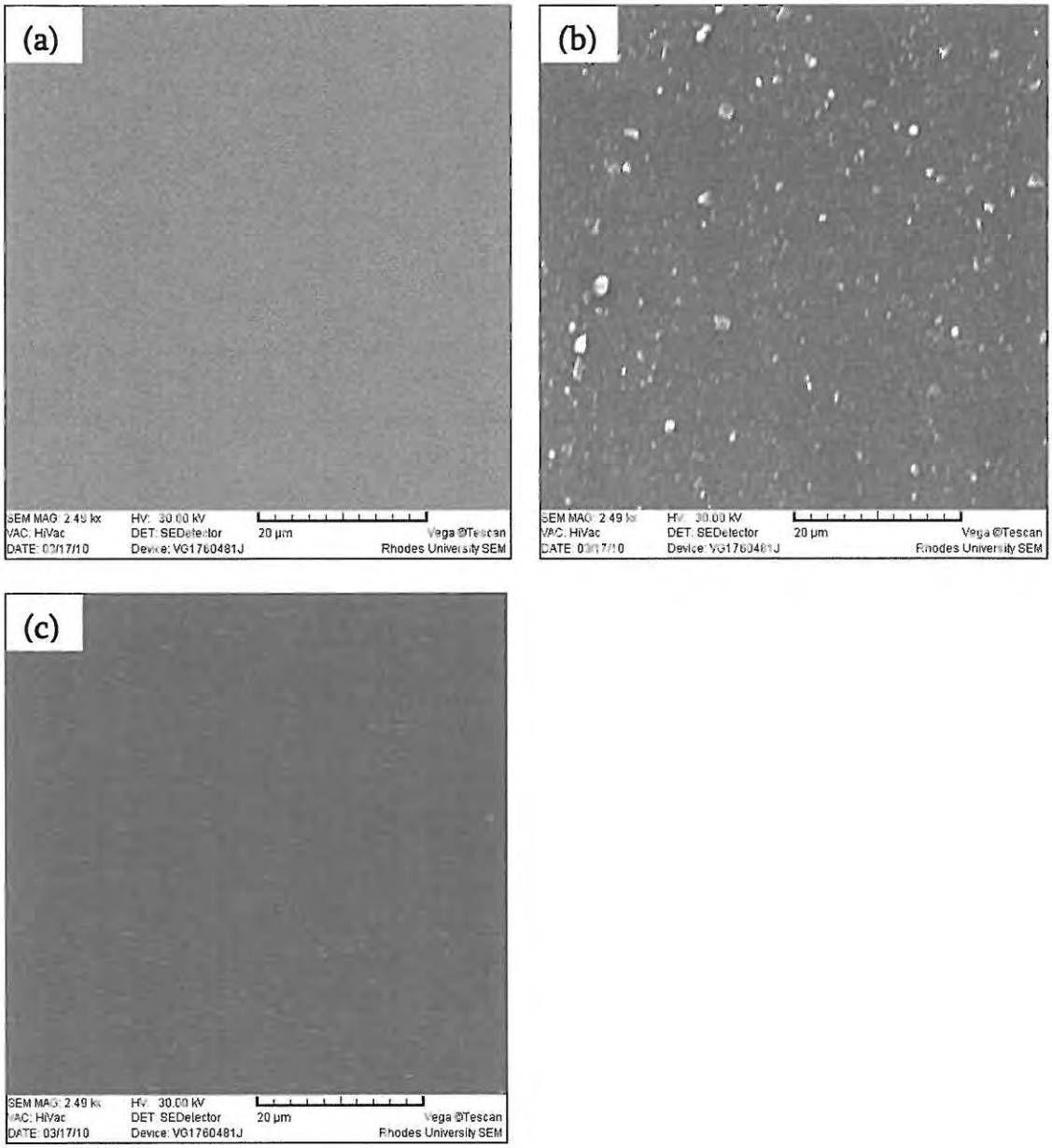

Figure 4.5. SEM images of (a) bare gold-coated glass, (b) **1b**-SAM modified gold-coated glass and (c) **1d**-SAM modified gold-coated glass.

4.1.2.3. XPS characterisation

Another useful technique for characterising SAMs is XPS, which can be used to do high resolution scans of the sulphur region S(2p) in order to show the formation of the Au-S bond, and also to determine whether any sulphur groups remain unbound [35,217–220].

For SAM formation using aryl- or alkylthio (SR) phthalocyanines, the question as to whether the R group remains intact following SAM formation remains unanswered, although retention of the R group was suggesting using electrochemical methods [221]. In this work we use XPS to examine in more detail the fate of the alkyl and aryl substituent following the formation of the SAM. The effect of the aryl versus alkyl substituent on the Au-S bond formation will also be discussed.

Fig. 4.6 shows the wide scans of both the free (Fig. 4.6(a)) and bound (Fig. 4.6(b)) MnPcs. The wide scans show the presence of sulphur as S(2s) and S(2p) for the free MnPcs. These are at 163 eV (2p) and 227 eV (2s) for **1d** and 166 eV (2p) and 229 eV (2s) for **1b**. The gold peaks are also very apparent in the MnPc-SAMs, Fig. 4.6(b), at 83 (Au($4f_7$)), 87 ($4f_5$), 335 ($4d_5$), 353 ($4d_3$), 546 ($4p_3$) and 642 eV ($4p_1$). Weak signals for Mn was seen in all four spectra at 643 and 653 eV (2p and $2p_1$). In Fig. 4.6(a), the higher intensity of carbon for **1b** can be attributed both to the greater proportion of carbon atoms in this MnPc, as well as to more residual solvent present as indicated by the higher intensity of the oxygen signal. The intensities of all of the MnPc peaks appear to decrease upon SAM formation, but this is likely only due to the much greater proportion of gold within the XPS analysis depth compared to the thin layer of attached MnPc.

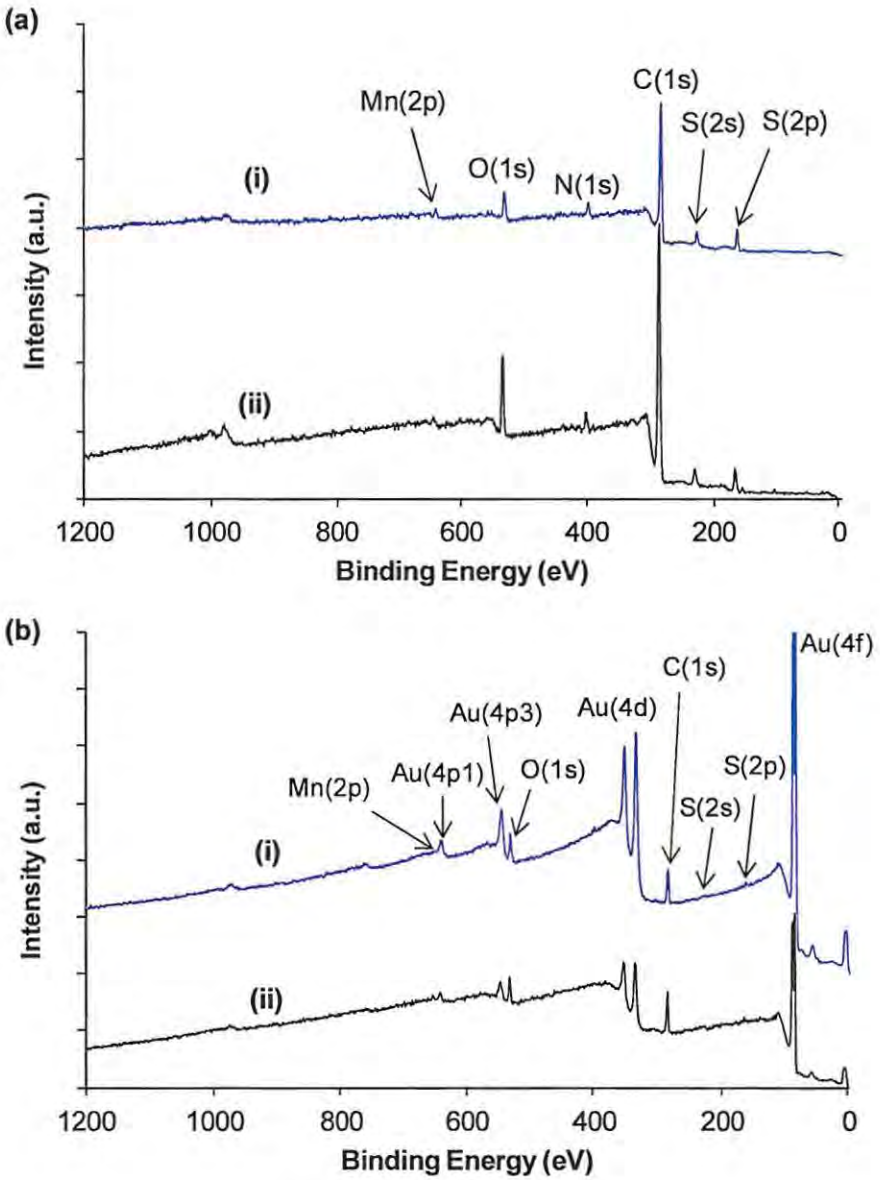

Figure 4.6. XPS spectra of (a) free MnPc and (b) MnPc-SAMs on gold for (i) **1d** and (ii) **1b**. Pass energy: 160 eV. Number of scans: 3.

High resolution scans of the sulphur 2p region were also done, Fig. 4.7, in an attempt to show the coordination between sulphur and gold. In this region, sulphur appears as a doublet in the XPS spectrum due to spin-orbit coupling, with the dominant peak being

the S($2p_{3/2}$) and the smaller peak S($2p_{1/2}$). The difference in binding energies between the peaks in the doublet are constrained to 1.2 eV with an area ratio of 2:1, with very little deviation [35,220,222]. Peak fitting was used to deconvolute the spectra into sets of doublets, to give an indication of the different sulphur groups present. This is shown in Fig. 4.7. For the free **1d**, Fig. 4.7(a), the S($2p_{3/2}$) peak is at a lower binding energy of 162.8 eV compared to the free **1b**, Fig. 4.7(b), at 164.6 eV. This is likely due to the phenyl ring substituents of **1d**, which contribute to the electron-rich environment and thus lowering the energy needed to remove an electron from this sulphur group. This is supported by the UV-vis spectra for these complexes, which showed a red-shifting of **1d** compared to the complexes with alkyl chains (Fig. 3.3).

In Fig. 4.7(c), the **1d**-SAM shows the presence of two overlapped doublet peaks, with the S($2p_{3/2}$) signals at (i) 161.5 eV and (ii) 163.4 eV. The second peak is at a similar binding energy to that seen for the free **1d** (at 162.8 eV) and indicates that not all of the sulphur groups are engaged with the gold surface, with shifts in the energies attributed to the changes in the electron density of the complex caused by some of the sulphur substituents binding to gold. MPcs octa-substituted with thio groups are believed to undergo attachment to the gold surface through an octopus arrangement. The same result has been seen for a silicon Pc with thioacetate substituents, where not all of the MPc "arms" were bound, and it was suggested that this is a consequence of the octopus strategy, rather than a lack in reactivity [35]. The peak at 161.5 eV is attributed to the formation of Au-S bonds as this is close to the values seen in studies of SAMs of thio-Pcs [35], and thiol-containing compounds [217–220,223–225]. Although some studies indicate evidence of gold-induced

deprotection of the sulphur and loss of the R group for MPc SAMs [35], the differences between the **1b**- and **1d**-SAM appeared to indicate otherwise.

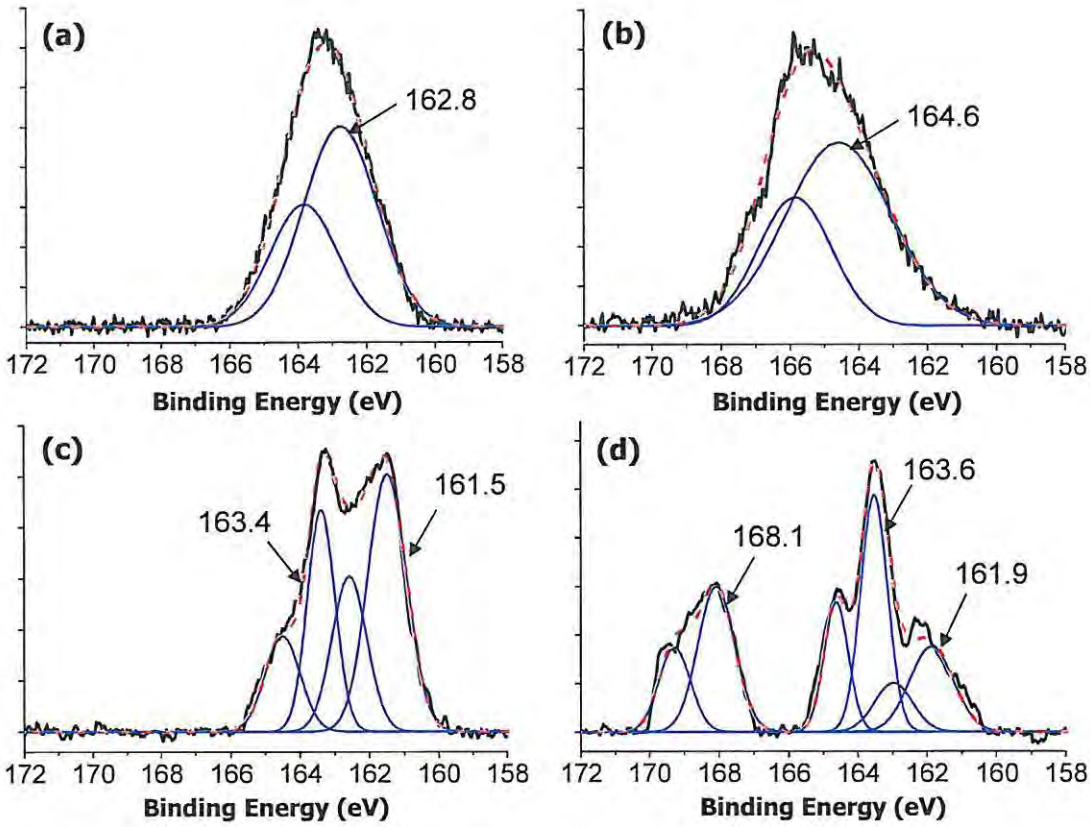

Figure 4.7. High resolution XPS spectra of the S(2p) region of (a) **1d**, (b) **1b**, (c) **1d**-SAM and (d) **1b**-SAM. Pass energy: 40 eV, number of scans: 5.

Fig. 4.7(d) shows the **1b**-SAM surface. The spectrum of this SAM before deconvolution is quite distinct from the phenylthio-derivative, and shows the presence of three sets of doublets with the dominant S($2p_{3/2}$) peaks at (i) 161.9, (ii) 163.6 and (iii) 168.1 eV. The lowest binding energy doublet is assigned to the Au-S groups of the SAM, as discussed

above, with a slightly higher binding energy compared to the **1d**-SAM (161.9 vs 161.5 eV for **1b**- and **1d**-SAM respectively). The differences in binding energies of peak (i) between the **1b**- and **1d**-SAM could indicate that there is retention of the R group upon SAM formation, because if the R groups were lost we would expect these peaks to be at the same energy. However, as we can attribute these differences to the effect of the lower electron density of the alkyl chain compared to the aryl substituent, this could indicate that the MnPcs in this work retain the R group upon SAM formation, with the lone pair of the sulphur engaged with the gold surface. The middle peak (ii) of the **1b**-SAM at 163.6 eV is closer in energy to the free **1b** at 164.6 eV, and is likely due to unbound sulphur. Peaks for sulphur that appear at high binding energies of ≈168 eV are assigned to oxidised sulphur groups [35,218,223]. In this case, peak (iii) may be due to decomposition of the **1b** through oxidation of sulphur. Both complexes appear to indicate retention of the R substituent following SAM formation, as was also observed using electrochemistry for similar complexes [221].

Looking at the relative areas of the (i) bound (161.9 and 161.5 eV for **1b**- and **1d**-SAM respectively) to (ii) unbound (163.6 and 163.4 eV for **1b**- and **1d**-SAM respectively) sulphur peaks, it appears that approximately 60 % of the sulphur groups in the **1d**-SAM surface were bound to gold, as opposed to only 37 % for the **1b**-SAM. These results show that the **1d**-SAM is closer to the "octopus" orientation than the **1b**-SAM. The fewer attachment sites of the latter could have been the cause of the poorer surface coverage of this MnPc on gold, indicating that the longer alkyl chain causes more steric hindrance to SAM formation than the aryl substituents. Surface coverage of the MnPcs on gold were

determined previously using electrochemistry, and found to be 1.42×10^{-10} mol.cm^{-2} for **1d**, compared to 0.30×10^{-10} mol.cm^{-2} for **1b**, Table 4.1.

4.2. Surface modification by grafting and click chemistry

This work studied the use of a combination of grafting and click chemistry in order to attach both ethynylferrocene and 4-ethynylpyridine to the electrode surfaces. The redox activity of ferrocene could be used to determine surface coverage of the attached species, allowing a comparison of this modification approach on the different surfaces to be made. Ferrocene was also used to compare a graft-then-click approach to a click-then-graft approach on the glassy carbon electrode (GCE). The first approach involves the introduction of azide groups to the surface through electrochemical grafting of 4-azidobenzenediazonium (**2b**), followed by click chemistry with ferrocene. The second approach involves the grafting of diazonium salt **2d** of the donated complex 4-(4-ferrocenyl-1H-1,2,3-triazol-1-yl)aniline (**2c**), which was produced through click chemistry, Fig. 1.6. Following the studies with ferrocene, pyridine was attached to the **2b**-grafted electrode through click chemistry and used to link iron phthalocyanine to the surfaces through axial ligation. The structures of the various complexes are given in Table 4.2.

First, the electrochemical grafting of **2b** on the various surfaces will be discussed, followed by the subsequent reactions using click chemistry.

Table 4.2. Complexes used for grafting and electropolymerisation.

Complex	Structure	Electrode Modification	Synthesis / Availability	Scheme
2a	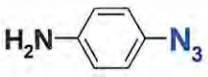	Polymerised then clicked [a]	Commercially available	4.4
2b		Grafted then clicked [b]	Pre-synthesised or *in situ* diazotised from **2a**	4.1, 4.2
2c	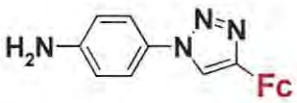	Polymerised	Pre-synthesised by clicking **2a** and ethynylferrocene	4.4
2d	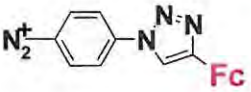	Grafted	*In situ* diazotised from **2c**	4.3

[a] Attached through click chemistry to ethynylferrocene. [b] Attached through click chemistry to ethynylferrocene and 4-ethynylpyridine.

4.2.1. *Electrochemical grafting of 4-azidobenzenediazonium (2b)*

Electrochemical grafting was used to modify GCEs through both direct grafting of synthesised **2b**, route B, as a reference route of modification [14], and through *in situ* diazotation of 4-azidoaniline (**2a**) to **2b** and grafting, route A. This versatile technique first demonstrated by the group of Savéant and Pinson [86] was also used for direct grafting of the synthesised **2b** on SWCNT adsorbed on GCEs (GC/SWCNT), route C, and on MWCNT-paper (route D). Scheme 4.1 shows the grafting approaches that were taken.

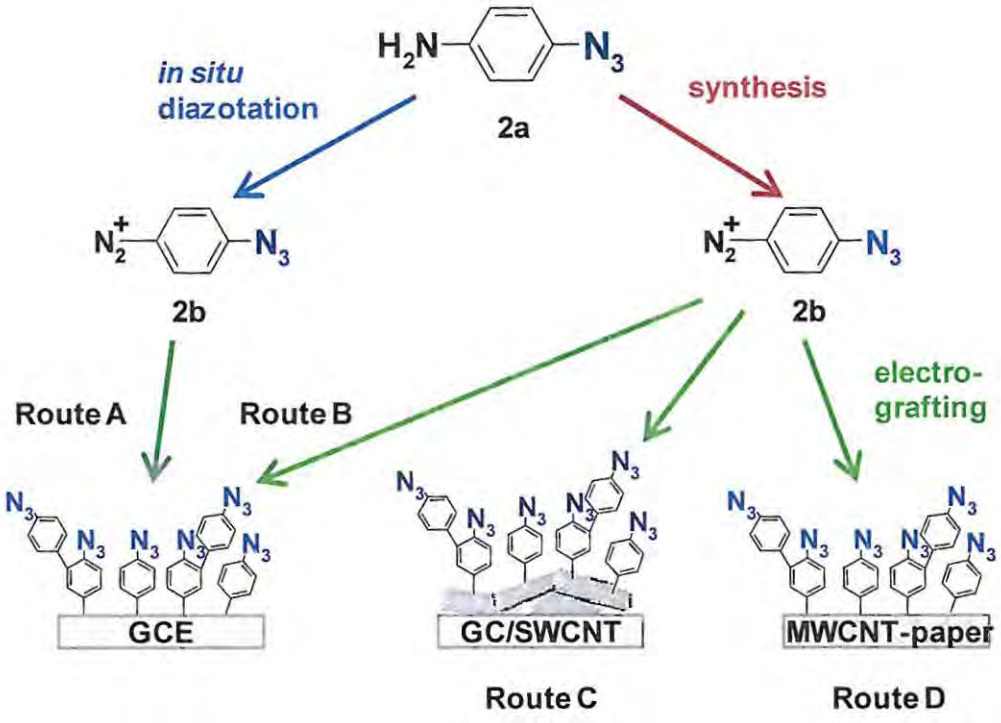

Scheme 4.1. Proposed electrochemical grafting approaches taken in this work.

For routes B, C and D, the grafting of the synthesised **2b** on to the GCE, GC/SWCNT and MWCNT-paper was accomplished by cyclic voltammetry in a solution of 1 mM **2b** in de-aerated acetonitrile with $TBABF_4$ as the electrolyte. The synthetic conversion of **2a** to the diazonium salt **2b** required for grafting was confirmed by ^1H NMR, with the signal at 10.05 ppm due to the NH_2 protons in the aniline not being present in the diazonium. The aromatic protons also shifted from 7.40 and 7.16 ppm in **2a** to 8.62 and 7.64 ppm in **2b** due to the change in the chemical environment, confirming that the reaction was successful. The GCE was also electrochemically modified through the use of *in situ* diazotation of **2a** and grafting of the resulting compound **2b** [226,227] (route A), to compare a one-pot grafting method. *In situ* diazotation was done through addition of sodium nitrite in aqueous acidic media [226,227].

Fig. 4.8 shows the grafting of these surfaces, with the broad reduction peak appearing in the first cycle but not in subsequent cycles due to the electrode blocking. This grafting process has been well studied, and involves reductive electron transfer to the diazonium salt followed by cleavage of the dinitrogen and production of aryl radicals, which then bind to the electrode surface by C-C bonding [14,87,94–97].

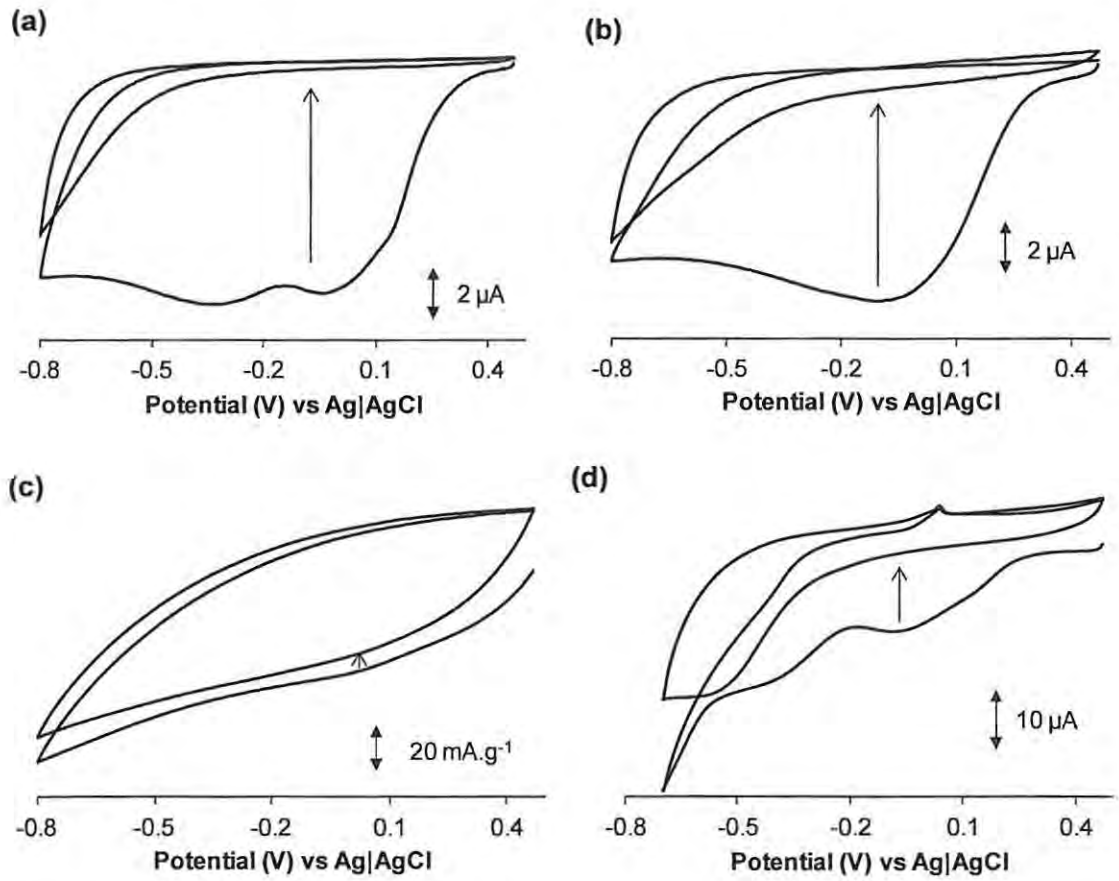

Figure 4.8. Electrochemical grafting of (a) GCE, (b) GC/SWCNT and (c) MWCNT-paper in 1 mM synthesised **2b** in 0.1 M $TBABF_4$ in ACN, and (d) GCE in 1 mM *in situ* diazotized **2a** to form **2b** in 96:4 ACN/1 M HCl in 0.1 M $TBABF_4$. Two cycles at 50 mV/s vs Ag|AgCl.

Fig. 4.8(a) and (d) compares grafting of the synthesised **2b** to *in situ* diazotation of **2a** and grafting of the resulting **2b**. Fig. 4.8(a) shows the cyclic voltammograms obtained during conventional grafting with the diazonium salt (route B, Scheme 4.1), and Fig. 4.8(d) shows two consecutive cyclic voltammograms obtained 15 min after *in situ* diazotation of **2a** (route A). Both of these CVs show the presence of three peaks at similar potentials: (a) -0.34, -0.02 and 0.14 V and (d) -0.38, -0.08 and 0.14 V. This has been seen with other

diazonium salts, as work by Baranton and Bélanger showed similar cyclic voltammetry behaviour for the *in situ* generated diazonium and the synthesised diazonium in organic media [226]. The shape is also similar to that reported in the literature with other diazonium species, with a decrease of the intensity of the peaks upon cycling [14,96,226,227]. Although one reduction peak is common for diazonium salts, the presence of multiple peaks with carbon electrodes is believed to be due to the graphitic planes and edges on the surface [92]. The origin of the first peak at the most positive potential is unknown, with the second peak attributed to reduction of the diazonium [96]. The peaks were more distinct when pure diazonium was used, rather than the *in situ*-generated species, indicating that the overlapped peaks are due to both the solvent and surface conditions.

Fig. 4.8(b) shows the grafting on the GC/SWCNT. The reduction of the diazonium salt on this surface shows the presence of one reduction peak at -0.07 V. The shape of the reduction peak was similar to that seen with grafting of synthesised **2b** on pyrolytic graphite electrodes (PGEs) [14].

Fig. 4.8(c) shows the electrochemical grafting of synthesised **2b** on MWCNT-paper. The electrochemical reduction of diazonium salts using an applied potential of -1.0 V for 30 min has been used to functionalize the side-walls of SWCNT-paper [89], and was shown to be successful. In this work, we attempted a similar process with MWCNT-paper using CV reduction of two and four cycles, taking care to coat the working electrode clip with colloidal silver paste in order to improve the connection between the paper electrode and the potentiostat, and also ensuring that the clip itself was not in solution [89]. Two

grafting cycles are shown in Fig. 4.8(c), with a very weak reduction peak seen at ≈ 0 V in the first cycle. The diazonium reduction peaks could not be more clearly seen due to the highly resistive nature of the MWCNT-paper.

4.2.1.1. Electrochemical characterisation

Grafting was confirmed by cyclic voltammetry in $K_4[Fe(CN)_6]$ where the grafted layer caused blocking of the electrode and thus this redox process. Fig. 4.9 shows the surfaces before and after grafting with **2b** in this redox probe, illustrating clearly the presence of a layer that blocked the electrochemical response of electrode towards ferrocyanide.

Fig. 4.9(a) shows complete suppression of the redox behaviour of ferrocyanide following grafting via route B (the synthesised **2b**). This indicates that the layer was compact and provided complete coverage of the electrode [94]. However, the *in situ* generated **2b**-grafted layer shows incomplete blocking of the electrode in Fig. 4.9(c), with a suppressed oxidation peak at 0.6 V. Different diazonium salts have varying barrier effects towards redox probes such as potassium ferrocyanide, and this blocking behaviour was found to be dependent on the applied overpotential, reduction time, and substituent effects on the compact nature of the layer [226,227]. It is clear that grafting of the *in situ* generated **2b** in this case did not form as compact a layer on the electrode, and this could be due to the solvent conditions or insufficient time allowed for diazotation to occur.

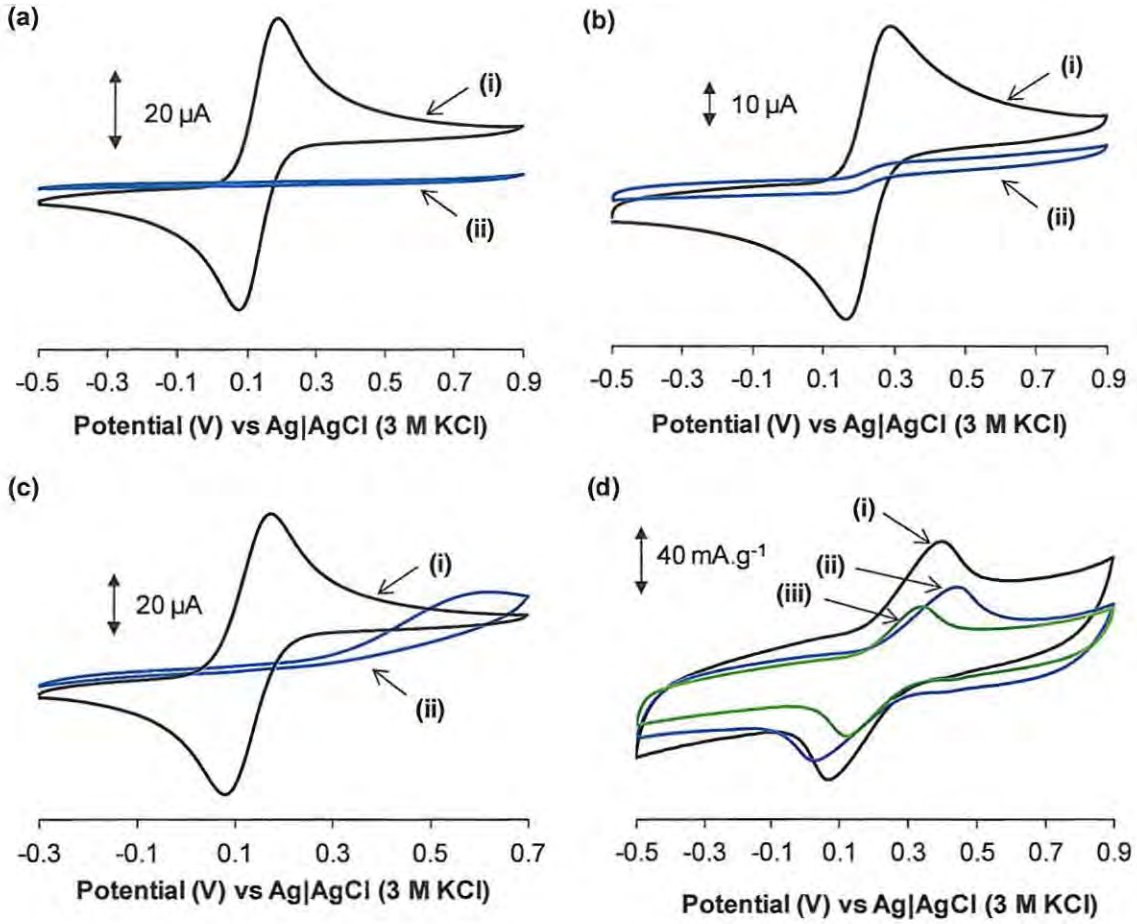

Figure 4.9. Cyclic voltammograms of (a) GCE and (b) GC/SWCNT before (i) and after (ii) grafting two cycles in synthesised **2b**, (c) GCE before (i) and after (ii) grafting two cycles in 1 mM *in situ* diazotized **2a** to form **2b** in 96:4 ACN/1 M HCl in 0.1 M $TBABF_4$, and (d) MWCNT-paper before (i) and after grafting two (ii) and four (iii) cycles in synthesised **2b**. In 5 mM $K_4[Fe(CN)_6]$ in 0.1 M KCl. Scan rates of (a)-(c) at 50 mV/s and (d) at 10 mV/s vs Ag|AgCl (3 M KCl).

Fig. 4.9(b) shows the blocking effect of the synthesised **2b**-grafted layer in ferrocyanide on the GC/SWCNT. There was a small reversible redox process at 0.25 V, the same

potential where ferrocyanide oxidation/reduction occurs. It is likely that the rough SWCNT layer and the resulting steric hindrance inhibited complete coverage of the conductive surface. This is expected, due to the non-homogeneous nature of the layer of SWCNTs, and a balance was needed between obtaining a well-covered surface, and the thickness of the grafted layer. A grafted layer that is too thick would result in an increased distance between the electrocatalyst (to be attached through click chemistry) and the electrode, and a reduction in efficiency. Electrografting on to SWCNTs has been described on carbon nanotube paper electrodes with other diazonium salts [89].

The bare MWCNT-paper electrode exhibited a large resistance to charge transfer in Fig. 4.9(d), as indicated by the ΔE of 330 mV at 10 mV/s, showing that the paper has poor conductivity – as expected since the manufacturer's measured resistivity was 0.1 ohm-cm. On the other hand, Fig. 4.9(b) shows the high conductivity of SWCNT with ΔE of 110 mV at 50 mV/s. However, the insulating effect following grafting indicates that the MWCNT-paper electrode was sufficiently conductive to allow reduction of the diazonium salt and functionalisation of the MWCNTs, resulting in a decrease in the current background and in the intensity of the ferrocyanide redox peaks. The current intensity (corrected for the mass of the MWCNT-paper, and shown as $mA.g^{-1}$) decreased by 25 % after two grafting cycles, and by 50 % after four grafting cycles – in Fig. 4.9(d)(ii) and (iii) respectively. There was very little decrease in current with a further increase in the number of grafting cycles. If the current intensity is roughly equated with the amount of grafted surface of the paper electrode, then it follows that although the signal for

ferrocyanide was not blocked completely, the current decrease indicated that the MWCNT-paper had been grafted successfully.

4.2.1.2. *Scanning electrochemical microscopy (SECM)*

SECM was also used to confirm the blocking of the electrode, and to give some indication of the electron transfer kinetics of the surfaces. For the SECM analyses of grafting the synthesised **2b** on GCEs and GC/SWCNT, glassy carbon plate electrodes were used, and modified in the same way as the conventional GCEs. The *in situ* grafted surface was not analysed using SECM or XPS due to the poorer blocking behaviour observed in Fig. 4.9(c) of this route A, compared to the modification route B. Upon grafting of these surfaces, the diazonium formed an insulating layer that was not electrochemically active, as has been noted previously with grafting of electrodes with aryl diazonium salts [87,88,92], and as was observed in Fig. 4.9 and discussed above.

For SECM approach curves, a constant potential was applied to the Pt ultramicroelectrode (UME) to oxidise the ferrocyanide in solution, and the current was monitored as the UME approached the un-biased substrate. Approach curves were plotted with both the current measured (I) and distance (d) normalised with respect to the limiting current, I_{lim}, and the radius of the probe (a) respectively. Fig. 4.10 shows the SECM approach curves to the grafted surfaces, and compares the response with approach curves to the bare surfaces and Teflon® as an almost ideal insulator. Deviations from total negative feedback for Teflon® was attributed to the substrate not being completely level.

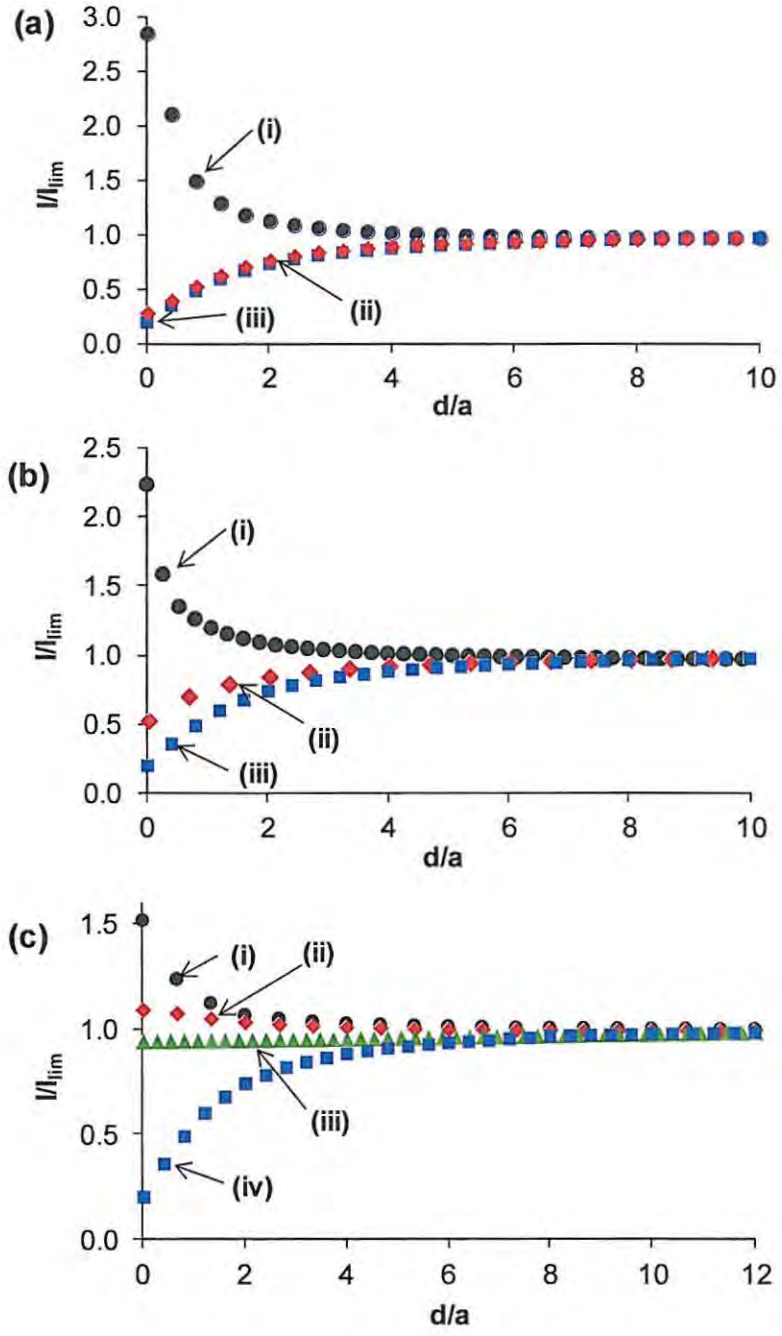

Figure 4.10. SECM approach curves using 15 μm Pt UME in 5 mM $K_4[Fe(CN)_6]$ in 0.1 M KCl. Approach to (a) GCE and (b) GC/SWCNT for (i) bare, (ii) after grafting two cycles in synthesised **2b**, and (iii) bare Teflon®. (c) Approach to (i) MWCNT-paper, (ii) after two grafting cycles, (iii) after four grafting cycles, (iv) bare Teflon®. At 0.5 V vs Ag|AgCl.

Two grafting cycles of the synthesised **2b** on the GCE were sufficient to completely block the electrode surface, as shown by the approach curves towards the grafted surface matching that seen with the approach to the purely insulating Teflon®, in Fig. 4.10(a)(ii) and (iii).

Fig. 4.10(b)(i) shows that the unmodified GC/SWCNT exhibited good conductivity with high electron transfer rates towards potassium ferrocyanide, which is a very surface-sensitive redox analyte [122,228,229]. The incomplete blocking of the grafted GC/SWCNT surface using synthesised **2b** was confirmed by the SECM approach curves in Fig. 4.10(b). Although the UME registered negative feedback on approach to the grafted surface, indicating insulating behaviour towards the redox species in solution, this substrate was slightly less insulating than the grafted GCE surface in Fig. 4.10(a)(ii) and the Teflon® as seen in Fig. 4.10(b)(iii).

Fig. 4.10(c) shows the response of the MWCNT-paper electrode. Although SECM could be used to analyze the MWCNT-paper, it must be noted that the conductivity – or electron transfer rates – of the surface as determined by approach curves in different places on the MWCNT-paper were not uniform, with some areas giving greater positive feedback than others. In no case did the synthesised **2b**-grafted surfaces exhibit pure insulating behaviour. This can be explained by an understanding of the structure of the MWCNT-paper, which is in essence a "mat" of branched nanotubes with pores and holes with only the outside nanotubes that have better electrical contact being grafted, while neighbouring nanotubes and areas more sterically hindered are likely free of the blocking

diazonium layer. Due to the small size of the nanotubes themselves, and the relatively large size of the SECM probe at 15 μm, adjacent nanotubes with differing electron transfer rates towards ferrocyanide oxidation (as well as holes in the paper) could cause the inconsistent feedback responses found at different points on the modified paper, similar to that seen with grafted layers containing defects and pores [179]. Thus, the approach curves shown in Fig. 4.10(d) were chosen as an "average" example of the results found.

The bare MWCNT-paper did not exhibit consistent electrochemical behaviour across its entire surface, with only some approach curves revealing good positive feedback, as seen in Fig. 4.10(d)(i). In all cases, however, the unmodified surface appeared to be conductive. The lower conductivity of this surface compared to the SWCNTs (as seen by the slower electron transfer kinetics) is likely due also to the nature of the branched MWCNTs used to make the paper, which do not have as good electrical conductivity properties as the SWCNTs, as well as the presence of holes and pores. However, a difference could be seen upon grafting of the synthesised **2b** on the MWCNT-paper. Grafting of two cycles was compared to four cycles, as electrochemical analysis has shown that two and even four grafting cycles did not block the detection of ferrocyanide completely, again as a result of the higher electrical resistance of this material and steric effects. Fig. 4.10(b)(ii) and (iii) shows the comparison between two and four grafting cycles, respectively, with the MWCNT-paper showing poorer electron transfer and less conductive behaviour after the greater number of grafting cycles.

Line scans across the surface of the electrodes modified with SWCNTs and the MWCNT-paper could also be used to give some indication of (i) the orientation of the SWCNTs on the surface, and (ii) the topography of the MWCNT-paper, Fig. 4.11. For line scans, the probe is brought close enough to the surface to detect the electrochemical behaviour and then scanned in either the x or y direction.

In Fig. 4.11(a)(i), the GC/SWCNT plate was scanned over the electrode surface for 800 μm and then off the edge of the electrode into bulk solution for 200 μm. Thus, the currents detected by the SECM probe show the conductive behaviour of the GC/SWCNT – with fluctuations in current showing that the surface is either not uniformly conductive, or more likely not uniform in topography due to the mixed vertical and horizontal alignment of the SWCNTs [65] – compared to the limiting current (I_{lim}) of 8.25 nA in bulk solution. In Fig. 4.11(a)(ii), the probe was once again scanned over the unmodified GC/SWCNT for 800 μm, and then over the grafted area of the electrode for 200 μm. The grafted area showed good insulating behaviour, with currents well below the I_{lim}. The unmodified area showed a slight decrease in conductivity compared to that in Fig. 4.11(a)(i), however this is most likely due to the greater distance between the probe and the substrate, or to some passivation by adsorbed material.

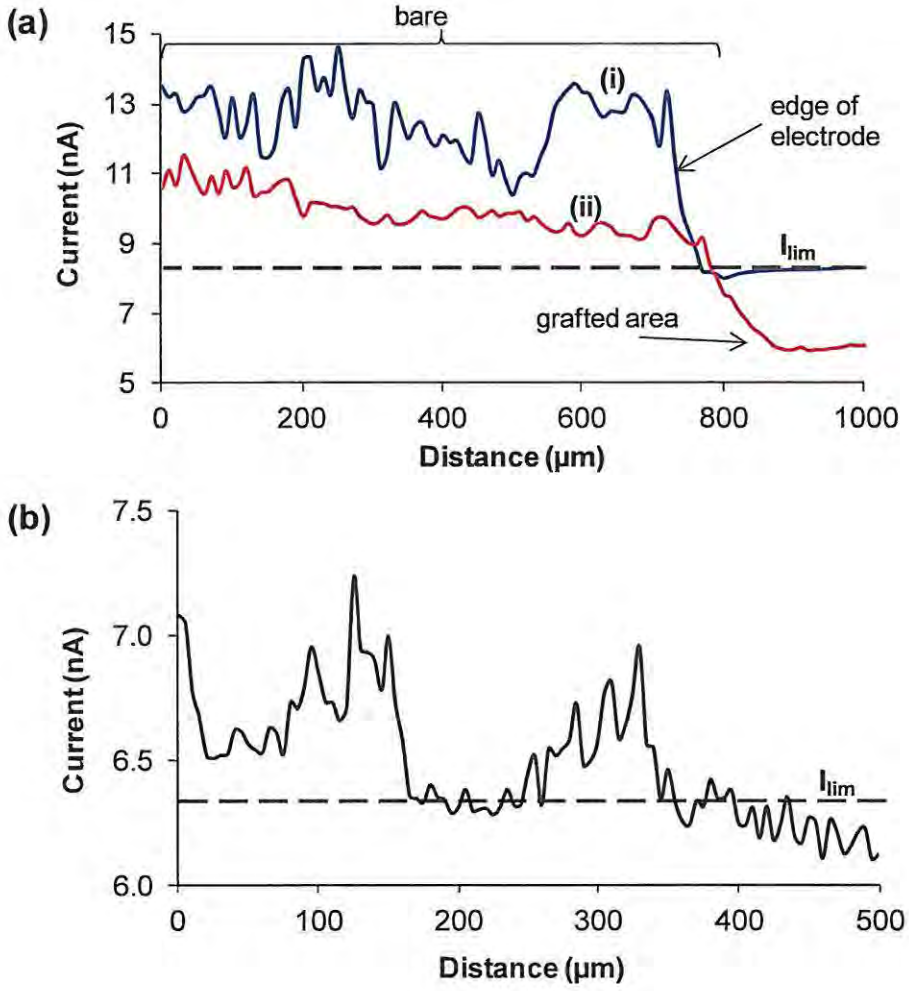

Figure 4.11. SECM line scans of (a) GC/SWCNT for (i) bare and (ii) after two cycles of grafting using synthesised **2b**, and (b) unmodified MWCNT. Both in 5 mM $K_4[Fe(CN)_6]$ in 0.1 M KCl. Probe = 15 μm Pt, E_{app} = 0.4 V vs Ag|AgCl, I_{lim} = 8.25 nA for (a) and 6.3 nA for (b).

The line scan in Fig. 4.11(b) of the unmodified MWCNT shows the fluctuating current response as the probe was scanned over the surface, due to the topography of the

branched nanotubes (and varying distance between the probe and the surface), the presence of holes in the paper, as well as the varying conductive behaviour.

For the SECM area scans, only the GCE and the GC/SWCNT were analyzed. For the GCE, a short GCE was placed in the SECM setup, and the image was done to show the contrast between the GC and the Teflon® casing. This electrode was used due to availability, however a GC plate electrode gave the same results. For the GC/SWCNT, the entire GC plate electrode was modified with SWCNTs to give the GC/SWCNT surface, and half of the plate was grafted with synthesised **2b** in order to obtain a clear interface between the bare and functionalized areas, giving a good current contrast. The roughness of the MWCNT-paper was much greater than the GC/SWCNT, resulting in the SECM probe being either too close or too far away from the surface to get a good image. Hence no SECM image is shown for MWCNT-paper.

Fig. 4.12 shows the SECM images of the (a) bare and (b) grafted GCE in 5 mM $K_4[Fe(CN)_6]$ in 0.1 M KCl. The grafting created a fairly uniform blocked layer of the synthesised **2b** on the surface, Fig. 4.12(b). The slight defects in the images in Fig. 4.12 were likely due to differences in height while scanning the electrode, as obtaining a perfectly flat surface at the micrometer scale is difficult. The constant height method that was used, while effective, can cause problems with crashing of the UME tip into the surface if it is not smooth or level [175]. However, it created a clear picture of the difference between the modified and unmodified electrode, and it was a fast and efficient method.

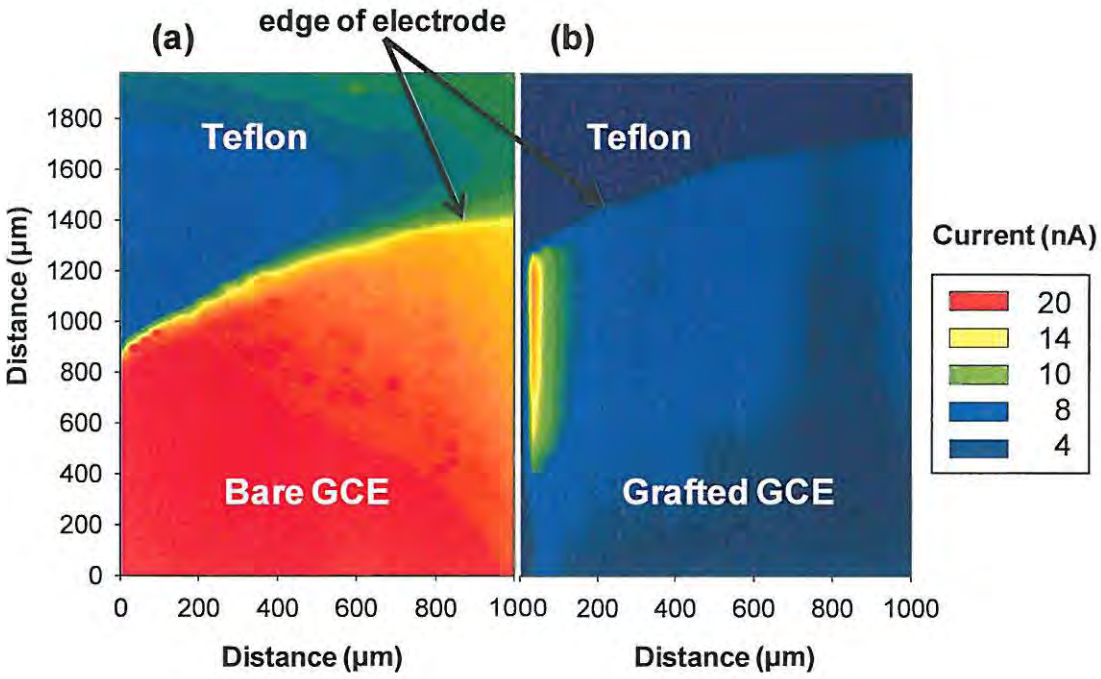

Figure 4.12. SECM images of (a) bare GCE and (b) synthesised **2b**-grafted GCE using 25 µm Pt UME in 5 mM $K_4[Fe(CN)_6]$ in 0.1 M KCl as the redox probe. The image was scanned from the GC disk towards the insulating Teflon® area. Scan area: 1000 µm x 2000 µm; applied potential: 0.5 V; I_{lim} = 9 nA.

Fig. 4.13 shows the three-dimensional area scans obtained from the SECM after each modification step for the GC/SWCNT. Fig. 4.13(a) shows the image obtained by scanning over the surface and off the edge of the electrode. The difference in conductivity of the GC/SWCNT section was due to a slight tilt in the surface, meaning that the probe was closer to the surface and detected higher currents in one area. The image shows clearly the rough alignment of SWCNTs on the surface, and indicates that it is likely that the

SWCNTs have a largely vertical arrangement from the spikes in current as the probe scanned over the surface.

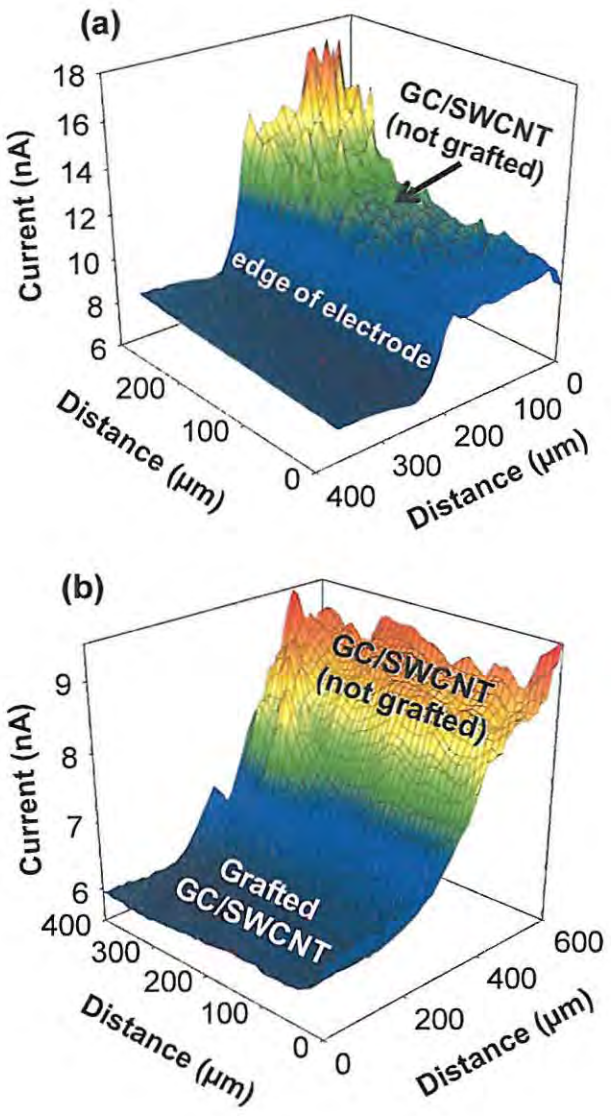

Figure 4.13. SECM images of (a) GC/SWCNT and (b) after grafting of synthesised **2b**. Imaged with a 15 μm diameter Pt UME in 5 mM $K_4[Fe(CN)_6]$ in 0.1 M KCl (E_{tip} = 0.5 V vs. Ag|AgCl; I_{lim} = 7.8 nA). The tip was scanned at 15 μm/s.

In Fig. 4.13(b), the probe was scanned over the electrode at the interface between the modified (grafted) and unmodified GC/SWCNT to show the contrast between the insulating modified surface and the conductive GC/SWCNT. Fig. 4.13(b) shows that the grafted area retained the rough surface from the underlying SWCNTs through the fluctuations in current, but was still uniformly insulating. As mentioned for the line scans in Fig. 4.11, the apparent variations between the unmodified GC/SWCNT areas of Fig. 4.13(a) and (b) are attributed to different distances between the UME tip and the substrate, which greatly affects the current intensities and surface detail as seen in Fig. 4.13(a) where the substrate was not completely level.

4.2.1.3. XPS characterisation

The final technique used to characterise the synthesised **2b**-grafted surfaces was XPS. High resolution XPS is very useful in showing the presence of the grafted azide, as the central nitrogen group of the azide has a distinctive peak at higher binding energy than the adjacent nitrogen groups [13,73,181,182,184]. The ratios of these peaks are expected to be 1:2 [181], however deviations from this ratio have been seen in certain cases [13,143,184], and are attributed to degradation of the azide following lengthy analysis under XPS conditions [182], and also to some residual nitrogen from the underlying surface or solvent.

The MWCNT-paper after four grafting cycles was used for these studies since it gave better blocking behaviour using cyclic voltammetry compared to that grafted with two

cycles. The GCE and GC/SWCNT following two grafting cycles (route B and C respectively) were also employed. High resolution XPS of the N(1s) region of the three surfaces is shown in Fig. 4.14. Each of the grafted electrodes had a peak at ≈404 eV, which is attributed to the central nitrogen of the azide, as explained above. The presence of this peak is indicative that grafting was successful for all three surfaces. The signal at 400.7 eV for the GCE and GC/SWCNT and 400.9 eV for the MWCNT-paper is due to the overlapped peaks of the adjacent nitrogen groups in the azide functionality [181,182]. A third peak was observed at 399.6 eV for the GCE, and at 399.4 eV as a weaker shoulder to the main signal for the MWCNT-paper and the GC/SWCNT, and most likely originates from the contribution of nitrogen groups found on the bare surfaces as well as residual solvent. The peaks for the azide groups at 404.3 eV on the MWCNT-paper were weaker than that seen for the grafted GCE and GC/SWCNT (at 404.1 eV). This is likely due both to the rougher surface of the MWCNT-paper, which results in more scattering of the photoelectrons in the XPS and thus weaker signals, as well as fewer grafted azide groups due to the resistivity of the MWCNT-paper.

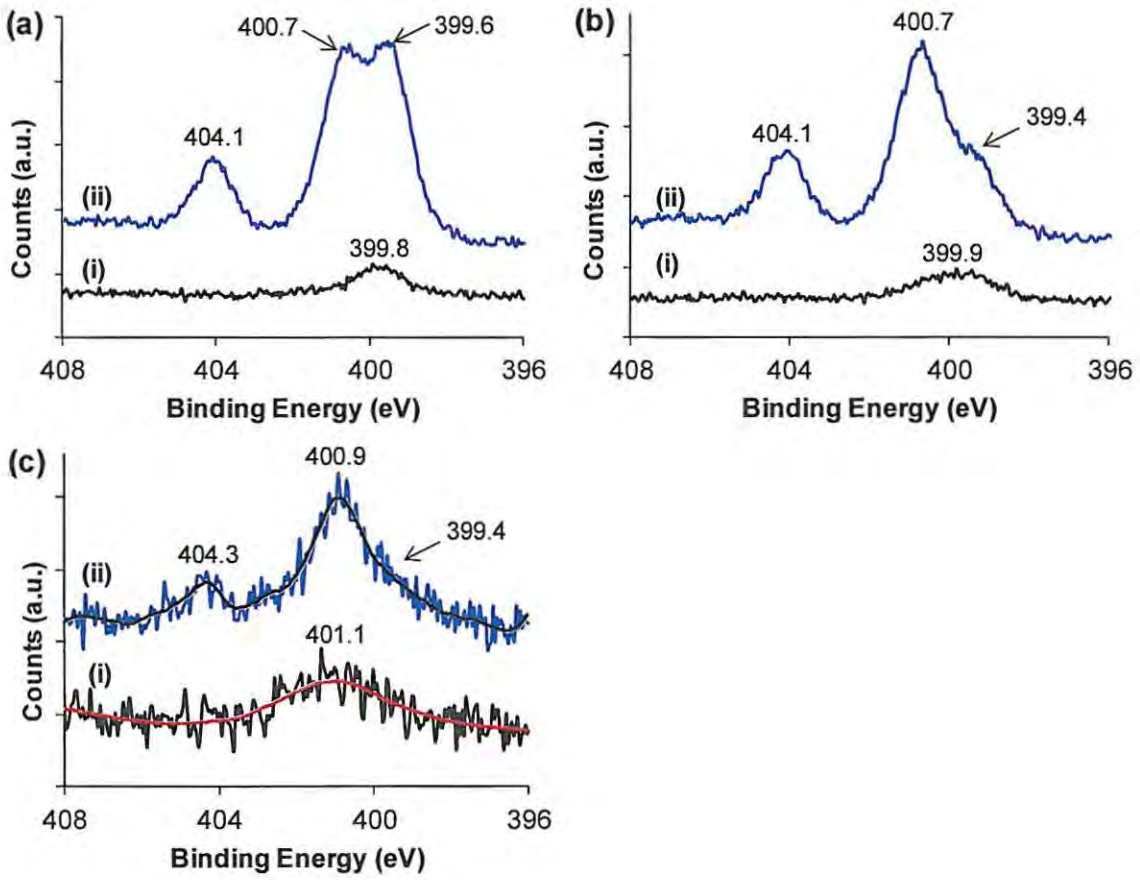

Figure 4.14. High resolution XPS of the N(1s) region of (a) GCE, (b) GC/SWCNT and (c) MWCNT-paper before (i) and after (ii) grafting for two cycles using synthesised **2b**. Pass energy = 40 eV, number of scans = 5.

4.2.2. *Click chemistry attachment of ferrocene*

Following electrochemical grafting with synthesised **2b**, the grafted GCE, GC/SWCNT and MWCNT-paper surfaces were further modified through click chemistry. The attachment of ferrocene through this approach is discussed first, through both a graft-then-click (Scheme 4.2) and click-then-graft (Scheme 4.3) approach, followed by graft-then-click attachment of pyridine to the GCE and GC/SWCNT and axial ligation to FePc (Scheme 4.2). These graft-then-click approaches are shown in Scheme 4.2.

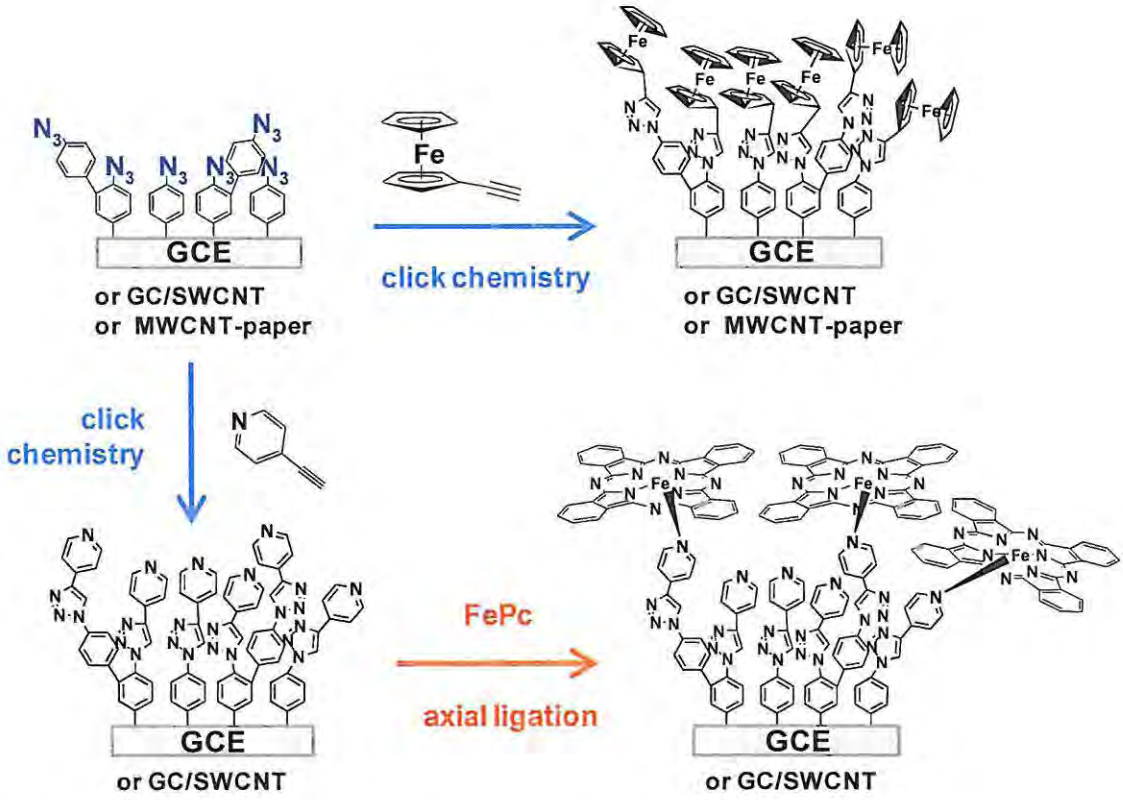

Scheme 4.2. Proposed click chemistry attachment of ethynylferrocene and 4-ethynylpyridine to the grafted surfaces, followed by axial ligation of FePc to the pyridine groups.

The graft-then-click chemistry approach to attaching ferrocene to the modified surfaces (Scheme 4.2) was compared to the click-then-graft approach (Scheme 4.3) through the use of the pre-clicked complex 4-(4-ferrocenyl-1H-1,2,3-triazol-1-yl)aniline (**2c**), which could be grafted through *in situ* diazotation to **2d** as demonstrated with **2a** above. This click-then-graft approach is discussed first, Scheme 4.3.

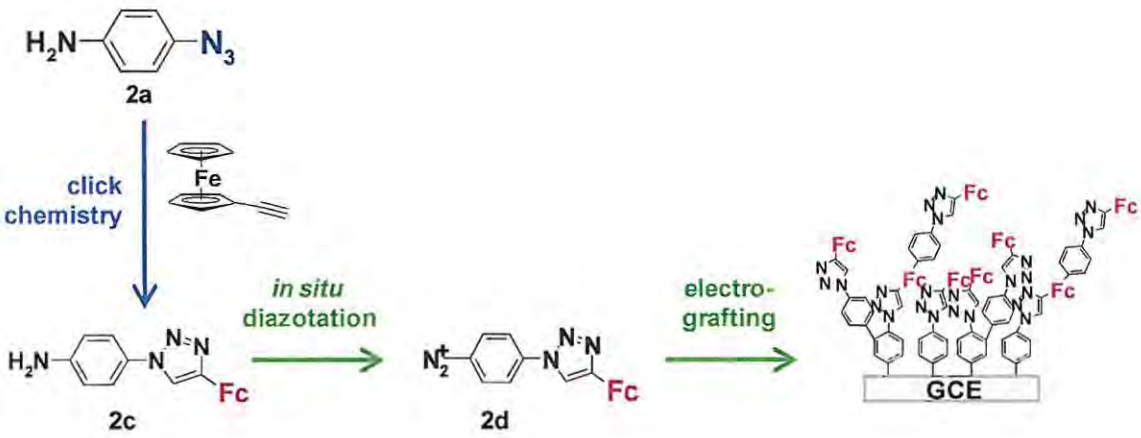

Scheme 4.3. Route for electrografting of the pre-clicked complex 4-(4-ferrocenyl-1H-1,2,3-triazol-1-yl)aniline (**2c**) through *in situ* diazotation to **2d**.

In order to characterise the surface layer by layer, electrochemistry, X-ray photoelectron spectroscopy (XPS) and scanning electrochemical microscopy (SECM) were used. XPS was particularly useful in monitoring the success of the click chemistry reaction by following the disappearance of the azide signal [8,13,73,143,184], while SECM proved useful in confirming the conductive or insulating behaviour of the surface [65,122].

4.2.2.1. *Click-then-graft approach using complex 2d*

The complex **2c** was converted to **2d** through *in situ* diazotation and **2d** was investigated for its potential in grafting of the GCE surface, for direct attachment of the pre-clicked ferrocene group, shown in Scheme 4.3. Grafting of species more complex than the simple *para*-substituted nitro, amino and alkyl diazonium salts has been done with ruthenium [115], nickel porphyrin [116] and osmium [117] complexes, with the importance of a spacer between the metal ligand and the N_2^+ group being stressed [115].

In situ diazotation of the aniline **2c** to form the diazonium complex **2d** was done in the same way as *in situ* diazotation of 4-azidoaniline (**2a**), in an acidic aqueous media with $NaNO_2$. Fig. 4.15 shows the CV of the grafting of **2d**.

The shape of the cyclic voltammogram observed during the electroreduction of **2d**, shown in Fig. 4.15, is similar to those reported in the literature obtained with other *in situ*-generated aryldiazoniums on GCEs with an intense reduction peak at ≈0.2 V [96,226,227], whose intensity decreases by successive cycling indicating the coupling of **2d** to the electrode surface [95,96,226,227]. The reduction peak is at more positive potentials than that seen for the reduction of **2b** in Fig. 4.8, indicating that the substituents on the diazonium salt have an effect on the reduction potential [87,96].

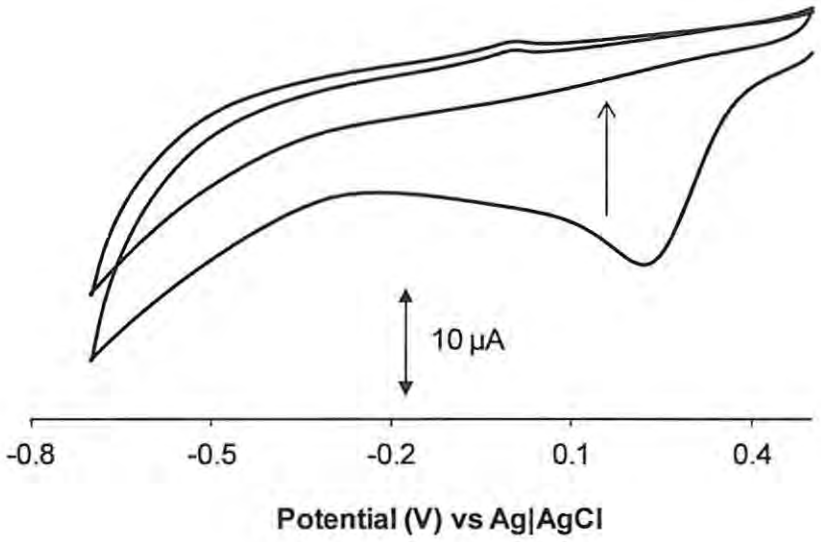

Figure 4.15. Electrochemical grafting of GCE in 1 mM *in situ* diazotized **2c** to form **2d** in 96:4 ACN/1 M HCl in 0.1 M $TBABF_4$. Two cycles at 50 mV/s vs Ag|AgCl.

4.2.2.1.1. Electrochemical characterisation

As with the surfaces grafted using **2b**, the **2d**-grafted GCE was characterised by analysis of the barrier effect in potassium ferrocyanide. This is shown in Fig. 4.16. The **2d**-grafted GCE showed complete suppression of the ferrocyanide redox process, indicating that grafting of **2d** was successful in forming a compact, pinhole-free layer.

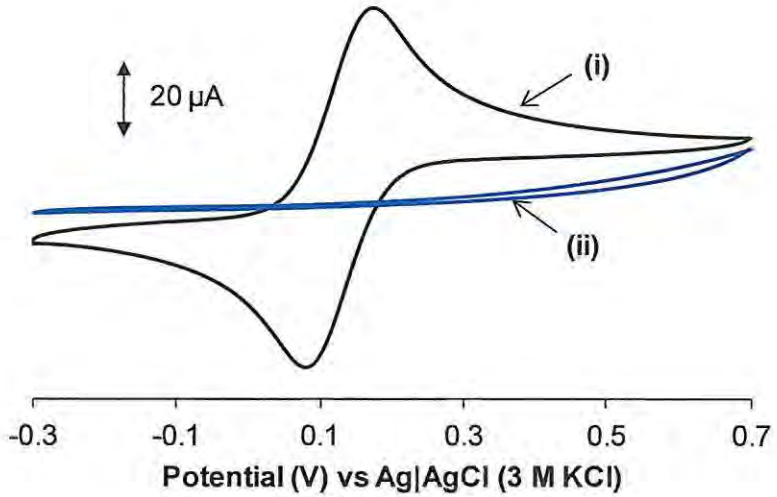

Figure 4.16. Cyclic voltammograms of (a) GCE before (i) and after (ii) grafting two cycles in 1 mM *in situ* diazotized **2c** to form **2d** in 96:4 ACN/1 M HCl in 0.1 M $TBABF_4$. In 5 mM $K_4[Fe(CN)_6]$ in 0.1 M KCl at 50 mV/s vs Ag|AgCl (3 M KCl).

Following grafting, the electrode was studied using CV in KPF_6, Fig. 4.17. A peak couple of weak intensity at $E_{p1/2}$ = 0.10 V was seen, which can tentatively be assigned to the presence of electroactive ferrocene groups inside the electrografted **2d**-layer. ΔE = 28 mV for this couple, which is indicative of fast electron transfer – as is expected for a species covalently attached to the electrode surface. However, the successful attachment of ferrocene could not be conclusively confirmed by this method, and XPS was needed to look at the system more closely.

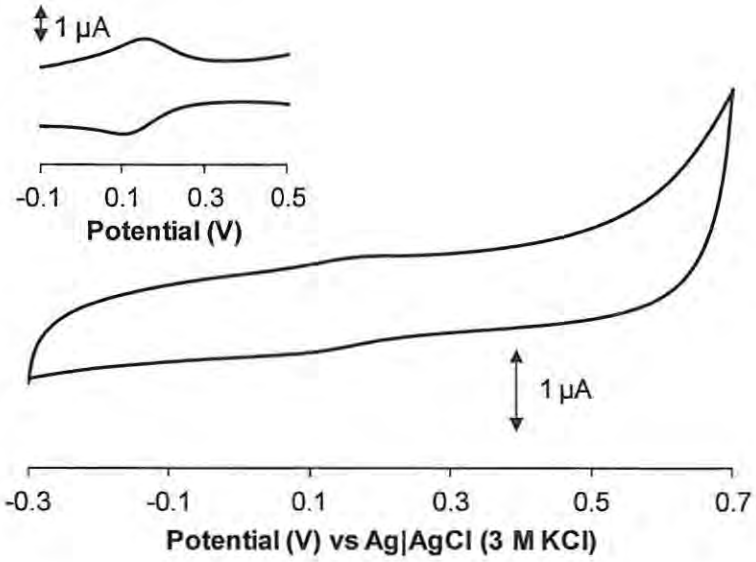

Figure 4.17. Cyclic voltammogram in 0.1 M KPF_6 of **2d**-grafted GCE. Scan rate 50 mV/s. Inset: square wave voltammogram.

The apparent surface coverage (Γ) in electroactive ferrocene sites was calculated for the **2d**-grafted GCE from the integration of the electrical charge Q of the anodic peak of the cyclic voltammogram in Fig. 4.17 and calculated as $\Gamma = Q/n$FA, eq. 1.2. The amount of electroactive ferrocene sites inside this layer was determined to be $0.7 \pm 0.2 \times 10^{-10}$ mol.cm^{-2}, Table 4.3.

Table 4.3. Surface coverage (Γ) of ferrocene on the modified surfaces following click chemistry. Grafting and click chemistry were done using 4-azidobenzenediazonium salt (**2b**) and ethynylferrocene respectively, unless stated otherwise.

Substrate	Electrode Modification	Γ [a] (10^{10} mol.cm^{-2})	Reference
GCE	grafting of synthesised **2b** followed by click chemistry	4.7 ± 0.2	This work
GCE	*in situ* diazotation of **2a** to form **2b**, grafting of **2b** and followed by click chemistry	4.9 ± 0.3	This work
GCE	electropolymerisation of **2a** followed by click chemistry	1.1 ± 0.4	This work
GCE	*in situ* diazotation of **2c** to form **2d**, followed by grafting of **2d**	0.7 ± 0.2	This work
GCE	electropolymerisation of **2c** (following click chemistry)	17.7 ± 2.8	This work
GC/SWCNT	grafting of synthesised **2b** followed by click chemistry	7.7 ± 0.9	This work
MWCNT-paper	grafting of synthesised **2b** followed by click chemistry	[b]	This work
GCE	grafting of **2b** then click chemistry	3.3 ± 0.9	[14]
GCE	grafting then click chemsitry [c]	0.9 ± 0.1	[14]
PGE	grafting of **2b** then click chemistry	14.3 ± 1.0	[14]
PGE	grafting then click chemistry [c]	2.7 ± 0.2	[14]

[a] Surface coverage of ferrocene determined by electrochemistry; [b] roughly calculated as 1.86 x 10^{-6} mol.g^{-1} from the anodic ferrocene peak at 0.59 V; [c] grafting of 4-ethynylbenzenediazonium and click chemistry with azidomethylferrocene.

Knowing that the surface coverage expected for a close-packed monolayer of ferrocene is 4.5×10^{-10} mol.cm^{-2} [7], the surface coverage calculated for this **2d**-modified electrode was less than a monolayer. The electrografted film may contain fewer ferrocene sites on the electrode surface due to steric hindrance between each monomer, leading to a lower number of grafted molecules, or all the ferrocene sites inside the film may not be accessible for electron transfer due to the non-conducting character of the electrografted layer. Another possibility is the elimination or displacement of ferrocene groups by the radicals generated during diazotization.

4.2.2.1.2. XPS characterisation

To complete the characterisation of the modified electrode, the sample was analysed by XPS, Fig. 4.18. However, only N(1s), O(1s) and C(1s) were visible in the spectrum. The lack of Fe(2p) signal with the **2d**-grafted GCE may be due to a very low concentration of ferrocene, confirming the weak electrochemical response observed in Fig. 4.17 and showing that with the experimental conditions used, this route was not an efficient method for modification of the electrode using this species.

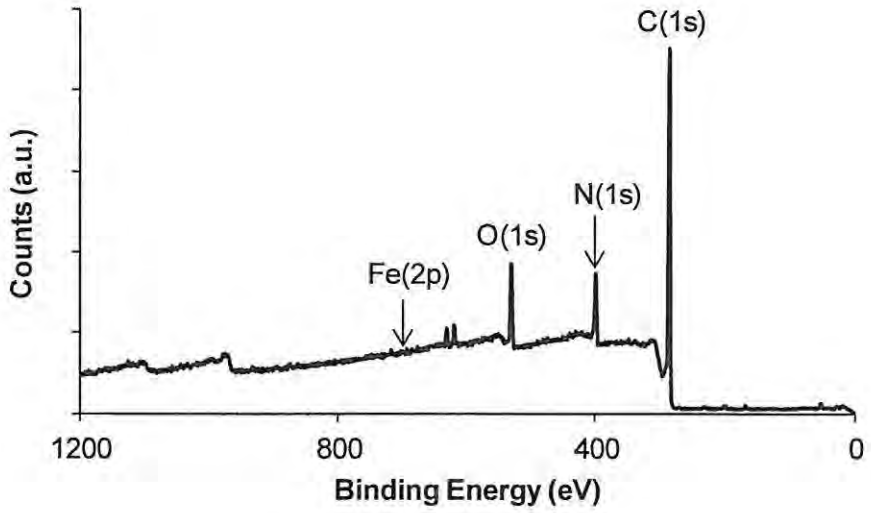

Figure 4.18. XPS spectrum for GCE after grafting complex **2d**. Pass energy = 160 eV, number of scans = 3.

4.2.2.2. *Graft-then-click approach using synthesised 2b*

The functionalisation of the GCE, GC/SWCNT and MWCNT-paper surfaces with azide groups through electrochemical grafting of **2b** was discussed in Section 4.2.1. No difference was seen in the ferrocene peaks when using *in situ* diazotation of **2a** and grafting of the resulting **2b** on the GCE followed by click chemistry of ethynylferrocene, and so only the results for the synthesised **2b**-grafted surfaces are shown here. In all of the click chemistry reactions discussed below, copper(II) sulphate was used and reduced to the catalytic Cu(I) *in situ* through addition of excess sodium ascorbate. These copper(II) salts are often purer and less costly than the copper(I) species [134]. The Cu(I) catalyst is responsible for the click chemistry reaction, through the production of a regiospecific 1,2,3-triazole link between the surface groups and the alkyne-bearing

compound [12,133,134,140,230]. In the case of click chemistry with ethynylferrocene, a 2:1 solvent mixture of ethanol/water was used due to the insolubility of ferrocene in pure aqueous media.

Global modification of a synthesised **2b**-grafted surface with ethynylferrocene has been accomplished before through click chemistry with the surface azide groups on PGEs and GCEs [14]. However, this is the first case of attachment of ferrocene to GC/SWCNT and MWCNT-paper through the use of this approach, as outlined in Scheme 4.2. This work also shows improved surface coverage of ferrocene on GCEs through the conventional grafting approach, compared to that seen in literature.

4.2.2.2.1. Electrochemical characterisation

Ferrocene was a particularly useful complex to attach to the modified surface as its strong redox activity means that, once covalently attached to the modified surfaces, electrochemical characterisation can be used to prove attachment and also to determine surface coverage of the ferrocene. The grafted electrodes retained their blocking characteristics towards ferrocyanide following click chemistry (figure not shown).

The CVs in 0.1 M KPF_6 of the surfaces following click chemistry with ethynylferrocene are shown in Fig. 4.19. Control experiments where ferrocene was used in the place of ethynylferrocene in the click chemistry step were used to ensure that the peaks were correctly assigned to linked ferrocene, rather than adsorbed species.

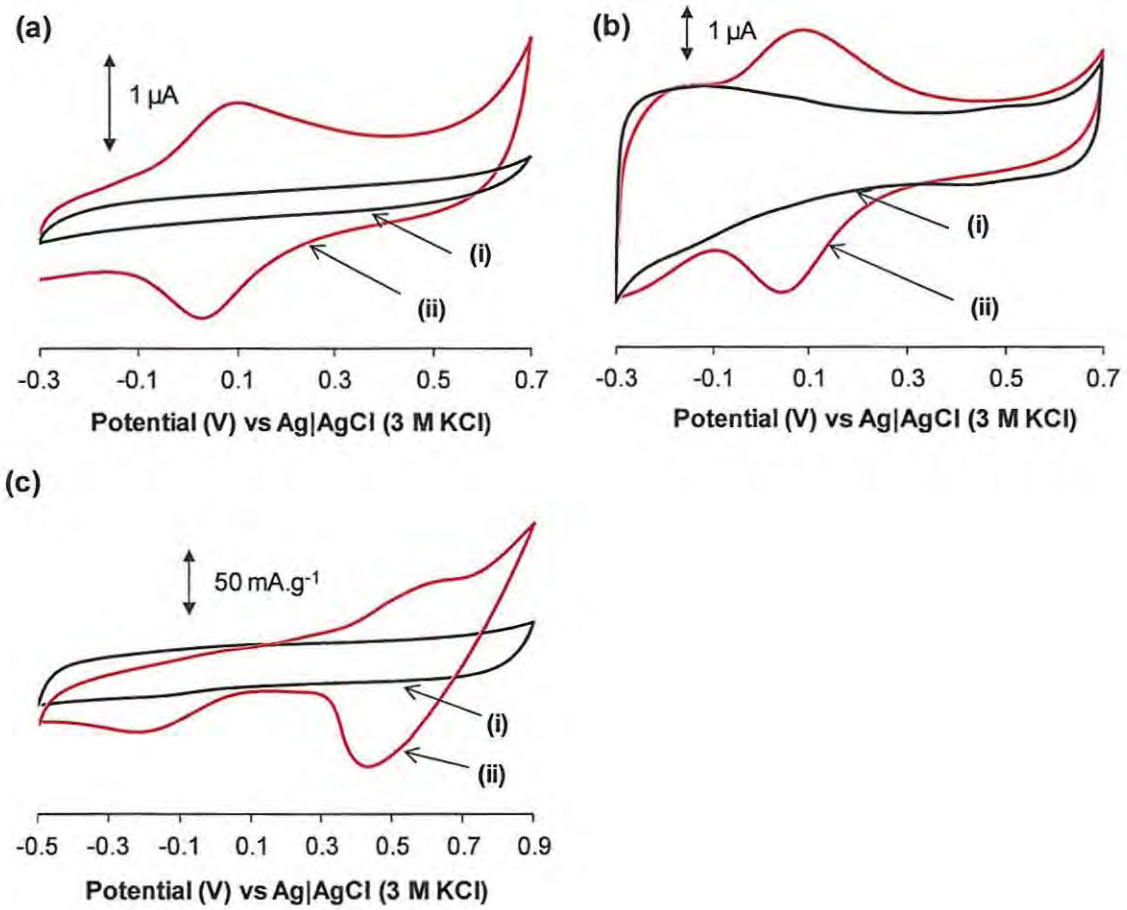

Figure 4.19. Cyclic voltammograms in 0.1 M KPF_6 of surfaces modified in 1 mM ethynylferrocene, 5 mM $CuSO_4$ and 40 mM sodium ascorbate for 18 h. (a) GCE, (b) GC/SWCNT and (c) MWCNT-paper after (i) grafting two cycles in **2b** and (ii) following click chemistry. Scan rate = 50 mV/s vs Ag|AgCl (3 M KCl).

A well-defined redox couple is visible for the GCE and GC/SWCNT electrodes in Fig. 4.19(a) and (b), with $E_{p1/2}$ = 70 mV for the GC/SWCNT, and $E_{p1/2}$ = 61 mV for the GCE. This redox couple is assigned to covalently attached ferrocene. The reversible redox process correspondes to that observed by others [14], and indicated a successful

modification of the electrode with the electroactive ferrocene. For the GC/SWCNT electrode, ΔE = 38 mV and for the GCE ΔE = 63 mV. This confirms that the SWCNTs also promote fast electron transfer at the electrode [21].

Fig. 4.19(c) shows the behaviour of the MWCNT-paper after grafting and click chemistry in 0.1 M KPF_6. The bare MWCNT-paper and the MWCNT-paper after two grafting cycles showed no peaks as expected in the electrolyte solution. However, after click chemistry attachment to ferrocene, Fig. 4.19(c)(ii), the MWCNT-paper electrode showed distinctive peaks due to ferrocene at 0.59 V (anodic) and 0.43 V (cathodic), with a ΔE of 161 mV and a half wave potential of $E_{p1/2}$ = 0.51 V vs Ag|AgCl (3 M KCl). These peaks were not observed in the control experiments without ethynylferrocene. The large ΔE shows the poor conductivity of MWCNT-paper compared to the other modified surfaces. The peak near -0.2 V was observed in the control without ethynylferrocene, and may be associated with reduction of the copper catalyst. No difference was seen in the intensity of these peaks when four grafting cycles were used.

The surface coverage of ferrocene (Γ) was determined using eq. 1.2 and the integration of the electrical charge of the ferrocene oxidation peak, Q, to calculate the number of electroactive ferrocene sites. This was compared to the surface coverage of ferrocene obtained with the GCEs grafted with the pre-clicked complex **2d**, Table 4.3.

As shown in the Table 4.3, the method for attachment of ferrocene to the GCE through click chemistry with electrografted synthesised **2b** gave 1.4 times higher values for surface coverage of ferrocene than that seen in literature on GCEs, at 4.7 ± 0.2 x 10^{-10}

mol.cm^{-2}, compared to 3.3 ± 0.9 x 10^{-10} mol.cm^{-2} [14]. This could be due to the different conditions used for grafting, where potential sweep was used for reduction of the diazonium in this work as opposed to potential step, or to the different conditions used during click chemistry, where a solvent mixture of 2:1 ethanol/water was used due to the insolubility of the ethynylferrocene, and the electrode was left to react for 18 h rather than 60 min [14]. The values obtained in this work for coverage of ferrocene on the grafted and clicked GCE are in very close agreement with the theoretical value of 4.5 x 10^{-10} mol.cm^{-2} for a close-packed monolayer of ferrocene moieties on a level surface [7]. Greater surface coverage values for ferrocene have been found on PGEs (14.3 ± 1.0 x 10^{-10} mol.cm^{-2}, Table 4.3) and were attributed to the porous nature of these electrode materials which lead to a larger real surface area than the geometric area [14]. It is also important to note the difference seen in literature between the surface coverage of ferrocene on both GCEs and PGEs for the acetylene-modified electrodes compared to the azide-modified electrodes, Table 4.3, which was attributed to the mechanism of the click chemistry reaction, which goes through a copper-acetylene complex intermediate and likely leads to steric effects with the surface-bound acetylene species and lower coverage [14]. This was another reason for the use of **2b** in this work, as opposed to the acetylene derivative.

The value for surface coverage of ferrocene on the GCE (4.7 ± 0.2 x 10^{-10} mol.cm^{-2}) could be used to compare this graft-then-click approach to the click-then-graft approach using **2d**. The surface coverage obtained from direct attachment of ferrocene through grafting of complex **2d** was 0.7 ± 0.2 x 10^{-10} mol.cm^{-2}. The 6.7 times improvement for surface coverage with the graft-then-click approach indicates that this stepwise method is more

effective in maximising the attachment of the ferrocene species to the surface, without a loss in electroactivity during the modification process.

The GC/SWCNT had greater surface coverage of ferrocene than the GCE at 1.6 times that seen on the GCE without SWCNTs. This indicates an increase in the surface area of the electrode due to the presence of the SWCNTs, as can also be seen by the increased capacitive current for this electrode in Figure 4.19(b). The GC/SWCNT proved to be fairly stable, suffering only a small decrease in the peak intensity (≈10 %) after one day in 0.1 M KPF_6.

The surface coverage of ferrocene on the MWCNT-paper was determined to be 1.86 $\mu mol.g^{-1}$ using the charge of the anodic peak at 0.59 V. This value was corrected for the weight of the paper, as correction for the area was not practical due to the morphology of the paper. This is given as a tentative value, as the highly resistive nature of the MWCNT-paper made absolute assignment of this peak as originating from ferrocene oxidation difficult, and the entire MWCNT-paper was not immersed in the grafting solution. This method can be compared to the chemoselective *in situ* diazotation of **2a** and chemical grafting of the resulting **2b** on SWCNTs, where the nanotubes were dispersed in a solution of acetonitrile with **2a** which was diazotised *in situ* through the addition of isopentylnitrite [105]. The SWCNTs were chemically grafted at 60 °C for 14 h before being washed, filtered, and then used for click chemistry attachment to ethynylferrocene [105]. For the SWCNTs, loading of ferrocene was calculated from cyclic voltammetry data to be 38 $\mu mol.g^{-1}$ using the $CuSO_4$/sodium ascorbate click chemistry

conditions [105]. The much greater loading determined by this method can be attributed to two main factors: (i) the poor conductivity of the MWCNT-paper used in this work, limiting electrochemical grafting compared to chemical grafting on the SWCNTs and (ii) steric hindrance preventing greater functionalisation of the MWCNT-paper, compared to the free SWCNTs. However, the potential of directly functionalising a paper electrode through the grafting and click chemistry approach used in this work could be useful for attachment of groups only at the outer areas of the paper, where they have the greatest use, and for applications in the production of flexible sensors, materials, capacitors and smart textiles. This is especially applicable due to the recent work being done on the improvement in conductivity and tensile strength of both SWCNT and MWCNT arrays, paper and nanomaterials [231–233].

Accurate determination of the thickness of the layers would require a technique such as AFM scratching, and these surface coverage values cannot be directly related to the thickness [234]. These results could not conclusively prove the attachment of ferrocene in themselves, but in conjunction with the XPS results do show that there is some reaction with the ferrocene after the click chemistry step.

4.2.2.2.2. SECM characterisation

Fig. 4.20 shows the approach curves to the GCE, GC/SWCNT and MWCNT-paper when bare and following grafting in synthesised **2b**, in order to compare the behaviour after click chemistry.

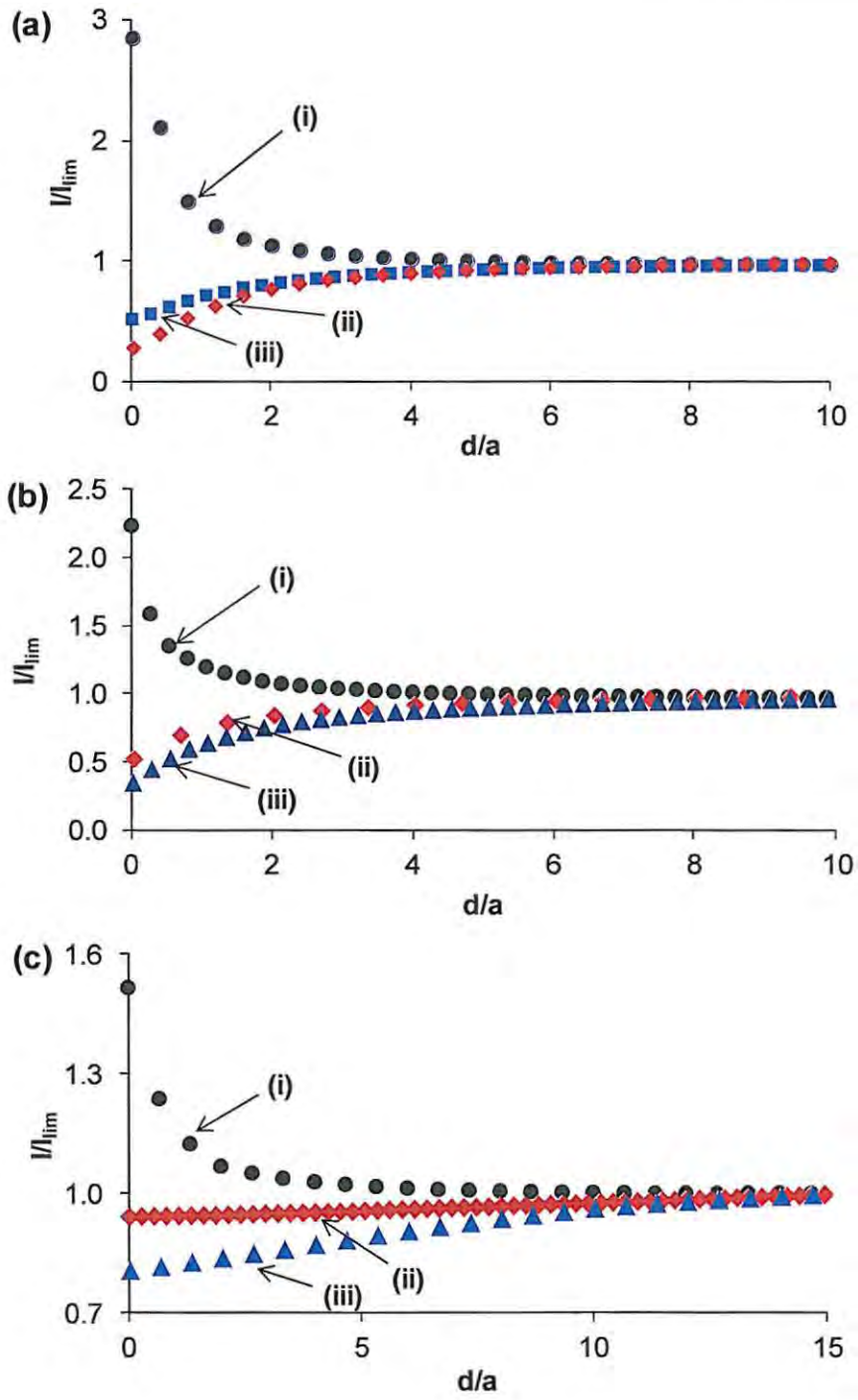

Figure 4.20. SECM approach curves using 15 μm Pt UME in 5 mM $K_4[Fe(CN)_6]$ in 0.1 M KCl. Approach to (a) GCE, (b) GC/SWCNT and (c) MWCNT-paper (i) bare, (ii) after two grafting cycles (four grafting cycles for the MWCNT-paper) in synthesised **2b** and (iii) following click chemistry with ethynylferrocene. At 0.5 V vs Ag|AgCl.

Fig. 4.20(a) shows the approach curve results for grafting and click chemistry on the GCE. Following click chemistry, the SECM probe still showed a negative feedback response upon approach to the modified surface, Fig. 4.20(a)(ii), indicating that the grafted layer was still present and the click chemistry conditions did not greatly affect the blocking capability of the electrode – although there was a slight decrease in the insulating characteristics. Ferrocene, although electrochemically active itself, did not catalyze the oxidation or reduction of the ferrocyanide and gave a negative feedback response.

SECM was used to study the MWCNT-paper as well as the GC/SWCNT after grafting and click chemistry, in order to compare the modification process on both a resistive and highly conductive electrode bearing carbon nanotubes. Thus, approach curves of the synthesised **2b**-grafted GC/SWCNT surface Fig. 4.20(b)(ii) and the surface after click chemistry Fig. 4.20(b)(iii) showed insulating behaviour through negative feedback. The slightly greater insulating behaviour showed by the clicked surface can be attributed to the formation of another layer on the substrate, which would further limit diffusion of the redox analyte to the GC surface and slow electron transfer. The MWCNT-paper after four grafting cycles and click chemistry with ferrocene is shown in Fig. 4.20(c). Following click chemistry, this surface also showed more insulating behaviour across more of the material, indicating that the formation of another layer on the MWCNT was successful.

As for the grafting results, SECM images of the MWCNT-paper could not be obtained. However, the GC/SWCNT plate was imaged using SECM following click chemistry, as shown in Fig. 4.21(b), in order to monitor changes in the topography of this surface.

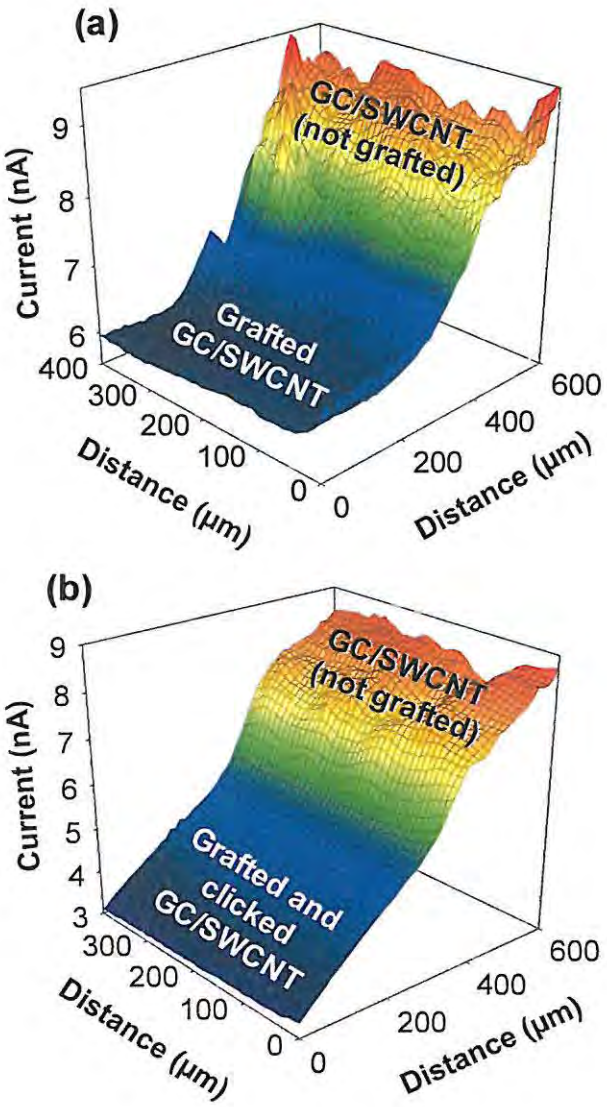

Figure 4.21. SECM images of the GC/SWCNT following (a) grafting of **2b** and (b) grafting followed by click chemistry with ethynylferrocene. Imaged with a 15 µm diameter Pt UME in 5 mM $K_4[Fe(CN)_6]$ in 0.1 M KCl (E_{tip} = 0.5 V vs. Ag|AgCl; I_{lim} = 7.8 nA). The tip was scanned at 15 µm/s.

This image appeared to show a decrease in surface roughness compared to the grafted surface shown in Fig. 4.21(a), again confirming the presence of an additional layer on the electrode. However, the un-grafted regions of the GC/SWCNT also appeared to have a decrease in roughness following the click chemistry step, Fig. 4.21(b). As the entire surface was immersed in the click chemistry solution containing ethynylferrocene in Fig. 4.21(b), it is likely that there was some adsorption of this species on the un-grafted GC/SWCNT, despite the washing steps used. Thus this apparent smoothness could be merely due to a greater distance of the tip from the surface, or it could be due to a decrease in surface roughness upon adsorption of the click chemistry species to un-grafted SWCNTs, and slower electron kinetics.

4.2.2.2.3. XPS characterisation

Fig. 4.22 shows the wide scan XPS spectra for the attachment of ferrocene – on GCE, GC/SWCNT and MWCNT-paper via grafting and click chemistry.

High resolution XPS scans of the N1s region following grafting of synthesised **2b** has been discussed in the previous section, however these wide scans of the GCE and GC/SWCNT following grafting (Fig. 4.22(a) and (b)(ii)) show very clearly an increase in the intensity of the N(1s) signal at ≈400 eV, as evidence of the successful grafting of the diazonium salt on these surfaces. The N(1s) signals also appear to decrease slightly after undergoing the click chemistry step (Fig. 4.22(a) and (b)(iii)), due to the formation of an additional layer on the surface. All of the modified surfaces following click chemistry showed the

presence of Fe at 708 ($2p_{3/2}$) and 720 ($2p_{1/2}$) eV in Fig. 4.22. The N(1s) and Fe(2p) signals after click chemistry demonstrate the formation of the triazole link and the immobilisation of ferrocene by these routes. The lesser intensity of the N(1s) signal for the grafted MWCNT-paper, Fig. 4.22(c), compared to (a) and (b), confirm what was already suggested by electrochemical analysis: fewer azide groups were available for bonding to ethynylferrocene on these surfaces, but they were present and click chemistry did occur.

For all of the modification routes, the presence of Cu was evidenced by two XPS peaks at 933 ($2p_{3/2}$) and 953 ($2p_{1/2}$) eV, showing some physical adsorption of copper catalyst used during the click reaction. XPS analysis of the grafted and clicked GCE before and after ultrasonic rinsing in a mixture of water and acetone evidenced the attenuation of the signal of copper of ≈40 %, without a loss of intensity of the N(1s) (data not shown). The use of another washing procedure, such as the rinsing of the modified electrode in a solution containing a ligand of copper such as EDTA, should promote the total removal of copper from the layer. The presence of residual copper catalyst was already reported in literature for the functionalisation of Si(100) by the click chemistry approach [235].

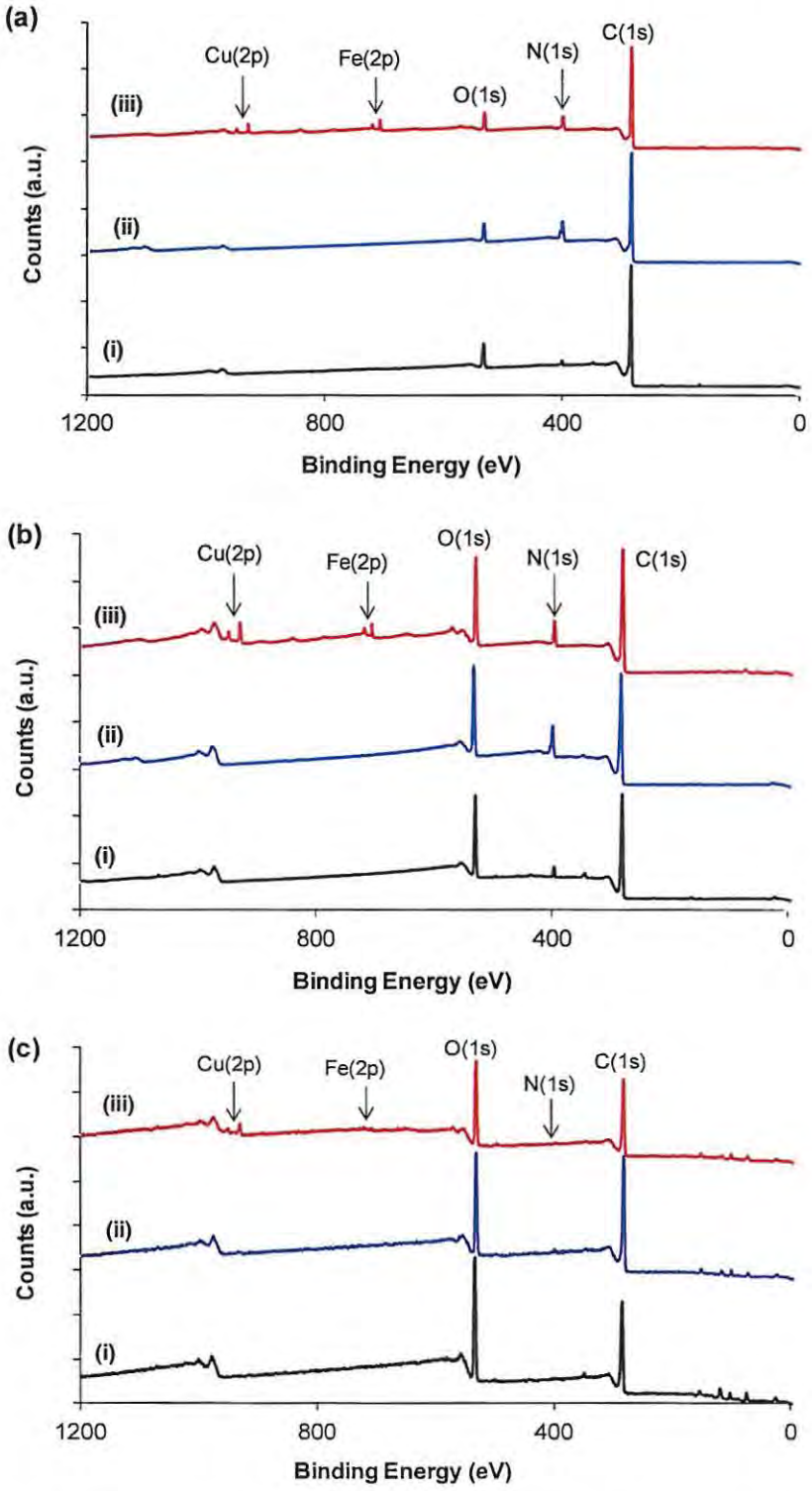

Figure 4.22. XPS spectra for: (a) GCE, (b) GC/SWCNT and (c) MWCNT-paper (i) unmodified, (ii) after grafting with synthesised **2b** and (iii) following click chemistry with ethynylferrocene. Pass energy = 160 eV, number of scans = 3.

The MWCNT-paper showed in Fig. 4.22(c) exhibited peaks for Al, Si, S and Na in the region 0 – 200 eV, which are expected from the manufacturer's specifications. It can also been seen that a higher percentage of oxygen was present on the nanotube-based surfaces. The high intensity of the O(1s) signal for the GC/SWCNT is attributed to the carboxylic acid functionalized SWCNTs, Fig. 4.22(b). For the MWCNT-paper, the O(1s) signal is likely due to residual solvent embedded in the paper, as well as functional groups on the nanotubes.

High resolution XPS was also used to analyse the N(1s) region, Fig. 4.23. As mentioned in the section discussing XPS peaks on grafted surfaces (Section 4.2.1.3), the presence of azide groups on the surface gave distinctive peaks in the XPS spectra. Most useful for click chemistry is that the disappearance of the peak at higher binding energy in the N(1s) region (at ≈404 eV, indicative of the presence of the azide) is considered to be evidence of successful click chemistry reaction to form the 1,2,3-triazole link, where all the nitrogen groups are in the same chemical environment [12,13,143,183,184].

Following the click chemistry step, Fig. 4.23(a)-(c) curves (iii) show the decrease in the peak at 404.1 eV at all surfaces (404.3 eV for the MWCNT-paper) and a shift in the largest peak (near 400.5 eV) to slightly lower energies compared to the grafted surfaces. This shift ranged from 0.1 eV to 0.6 eV for the various substrates. Shifts in binding energies in XPS are considered to be indicative of changes in the chemical environment [181], and can be assigned here to the changes in bonding following the click reaction to form the triazole ring.

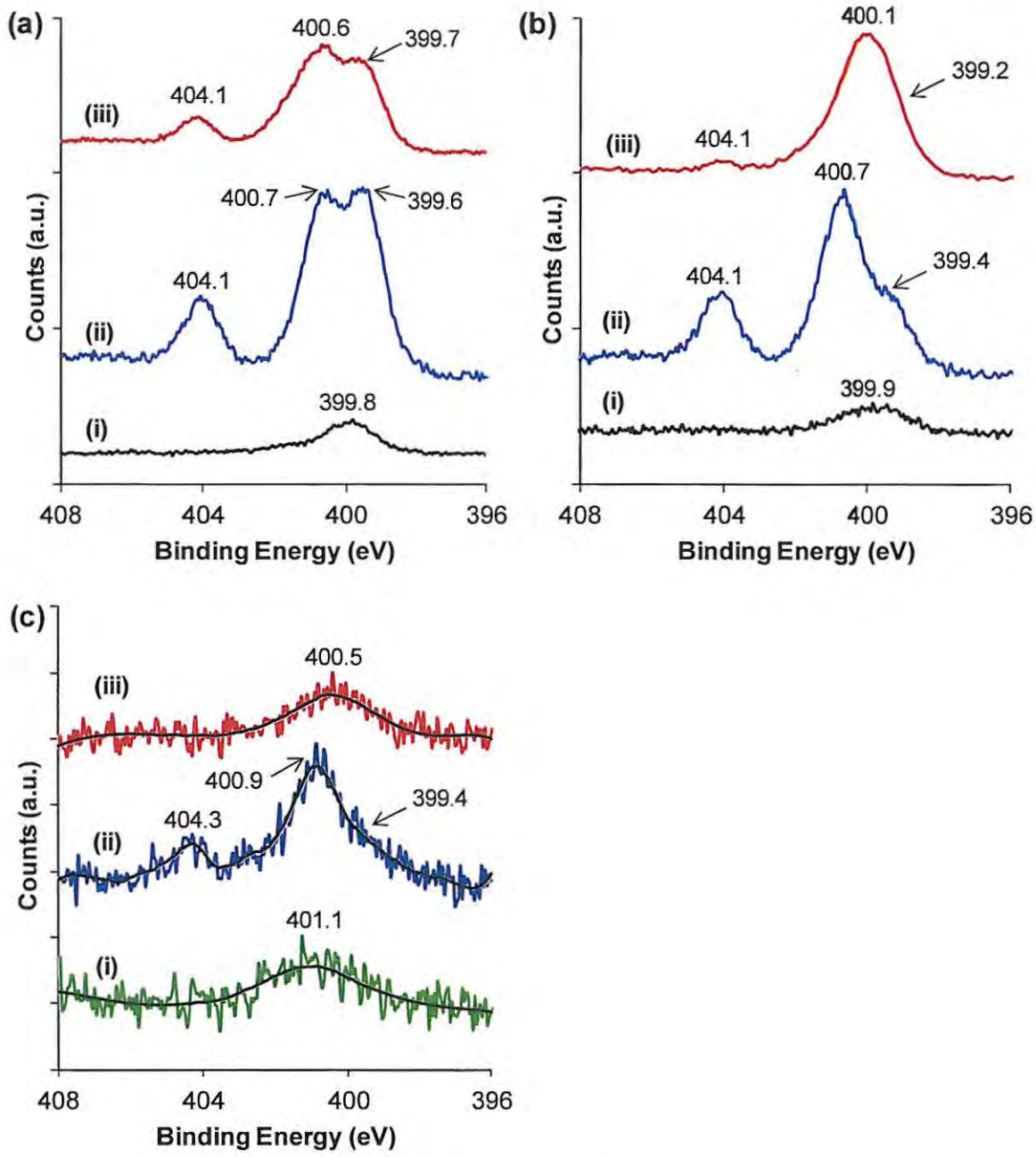

Figure 4.23. High resolution XPS spectra for: (a) GCE, (b) GC/SWCNT and (c) MWCNT-paper (i) unmodified, (ii) grafted using synthesised **2b** and (iii) following click chemistry with ethynylferrocene. Pass energy = 40 eV, number of scans = 5.

The N(1s) peak at 404.3 eV completely disappeared for the MWCNT-paper, Fig. 4.23(c)(iii), showing the completion of the click reaction on this surface. A small signal for the azide was still present after the click reaction for the GC/SWCNT (Fig. 4.23(b)(iii)), with a larger signal on the GCE (Fig. 4.23(a)(iii)), possibly due to steric hindrance preventing reaction of all the surface azide groups with ethynylferrocene. It appeared that more of the azide groups on the "rougher" surfaces were able to undergo reaction with ferrocene, supporting the effect of steric hindrance on limiting the extent of the reaction.

4.2.3. *Click chemistry attachment of pyridine and axial ligation to FePc*

The new proposed approach for click chemistry with 4-ethynylpyridine and axial ligation to iron phthalocyanine (FePc) is shown in Scheme 4.2. The graft-then-click method was used due to the greater effectiveness of this approach compared to click-then-graft, as shown by the studies with ferrocene in Section 4.2.2. This approach has been studied both on a GCE and on a GC/SWCNT substrate, but not on the MWCNT-paper because of the poorer electrochemical behaviour and resistivity of this surface. Previous studies with ferrocene showed that SWCNTs allowed the "loading" of 1.6 times the amount of ferrocene through click chemistry on to the synthesised **2b**-grafted electrode compared to the electrode without nanotubes, Table 4.3. Thus in this work as well, SWCNTs were adsorbed onto glassy carbon electrodes followed by grafting of the synthesised **2b** and then click chemistry with 4-ethynylpyridine – as a means to axially bind FePc. The benefits of this approach are the possibility of modifying a multitude of conductive surfaces – because of the versatility of the grafting step – and also the avoidance of the synthesis of complex, unstable, and expensive substituted-MPcs.

4.2.3.1. *Electrochemical characterisation*

The blocking capabilities of the grafted GCE and GC/SWCNT were discussed in the section on grafting above. The electrodes retained their barrier effects following click chemistry with pyridine and axial ligation with FePc, Fig. 4.24.

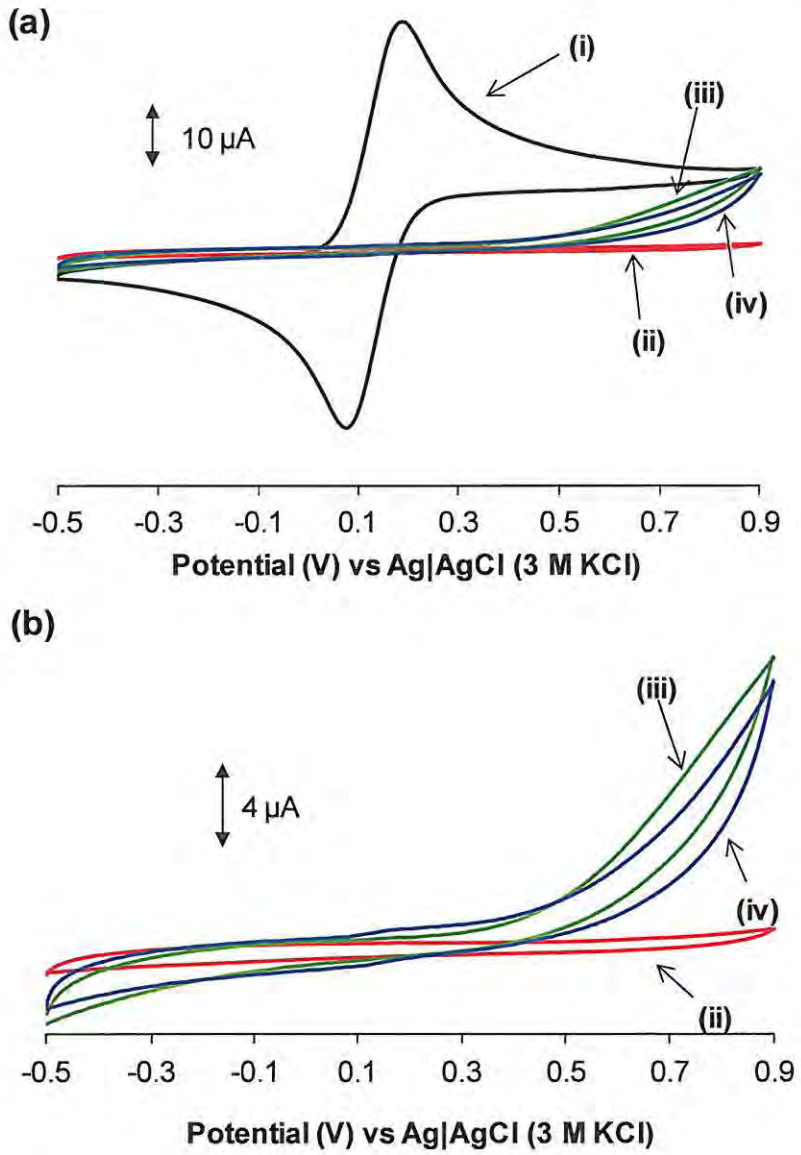

Figure 4.24. (a) Cyclic voltammograms of the GCE (i) bare, and after (ii) two grafting cycles in synthesised **2b**, (iii) grafting and then click chemistry in 4-ethynylpyridine, and (iv) grafting, click chemistry and then 3 h in 1 mM FePc in DMF. (b) Expansion of curves (ii) to (iv) from (a). Electrolyte = 5 mM $K_4[Fe(CN)_6]$ in 0.1 M KCl at 50 mV/s vs Ag|AgCl (3 M KCl).

Fig. 4.24 shows the blocking behaviour of the GCE electrode in potassium ferrocyanide after each step. The **2b**-grafted electrode in Fig. 4.24(a)(ii) showed good blocking behaviour towards the ferrocyanide, compared to the bare electrode Fig. 4.24(a)(i). During the click chemistry step, 4-ethynylpyridine was linked to the **2b**-grafted electrode through the formation of a 1,2,3-triazole ring with the azide in the presence of $CuSO_4$, which was reduced to Cu(I) *in situ* by sodium ascorbate. This surface was also blocked to ferrocyanide, shown in Fig. 4.24(a)(iii), although a weak redox process was visible at the potential of ferrocyanide oxidation/reduction at 0.15 V, Fig. 4.24(b). As the pyridine is not electroactive in itself, cyclic voltammetry could not be used to confirm the success of the click step. Following axial ligation to unsubstituted FePc, the electrode remained essentially blocked to the redox chemistry of ferrocyanide Fig. 4.24(b)(iv), with a weak ferrocyanide peak observed at 0.15 V.

The peak due to Fe(II)Pc/Fe(I)Pc was not very clear, however using square wave voltammetry a peak at -0.12 V vs Ag|AgCl (3 M KCl) was observed for the modified GCE in 0.1 M NaOH, Fig. 4.25(a). For the GC/SWCNT electrode, the couple due to the Fe(II)/Fe(I) process was most visible in 0.1 M pH 7.0 phosphate buffer solution (PBS), Fig. 4.25(b)(ii). Fig. 4.25(b) shows (i) the SWCNT oxidation/reduction process at -0.05 V and (ii) a redox couple that is attributed to Fe(II)/Fe(I) at 0.25 V in PBS. For the GCE $\Delta E_{Fe(II)/Fe(I)}$ = 28 mV, and for the GC/SWCNT ΔE_{SWCNT} = 36 mV and $\Delta E_{Fe(II)/Fe(I)}$ = 44 mV, which indicates very fast electron transfer as expected for species attached or closely linked to the electrode surface.

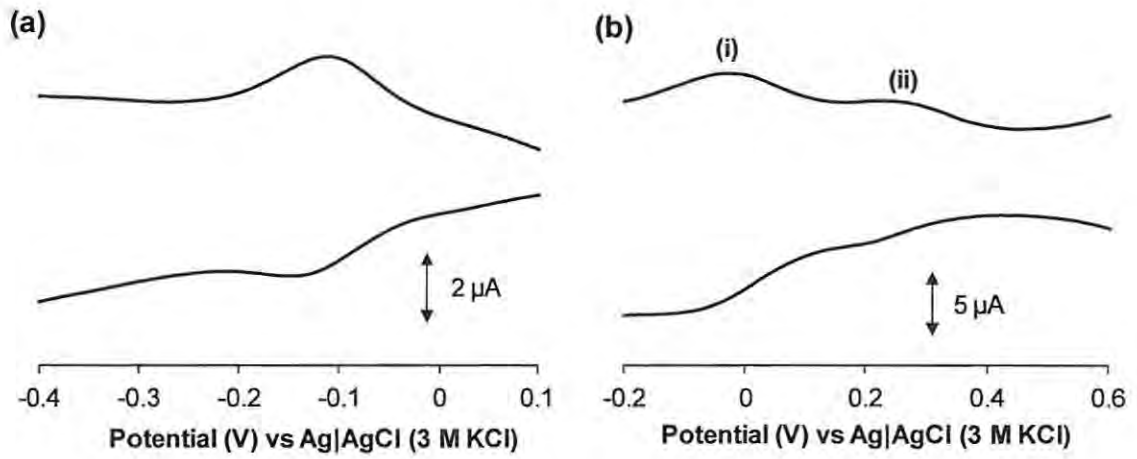

Figure 4.25. Square wave voltammograms of (a) GCE and (b) GC/SWCNT following grafting with synthesised **2b**, click chemistry with 4-ethynylpyridine, and axial ligation to FePc. (a) in 0.1 M NaOH, (b) in 0.1 M pH 7.0 PBS. At 60 mV/s vs Ag|AgCl (3 M KCl).

The electrochemical impedance spectroscopy measurements in 5 mM hydrazine as a test analyte (in 0.1 M NaOH) were also performed in order to assess the electron transfer properties of the modified GCE. Fig. 4.26 shows (a) the Nyquist plots and (b) their corresponding Bode plots for (i) the bare GCE, (ii) **2b**-grafted GCE, (iii) **2b**-grafted GCE after click chemistry in 4-ethynylpyridine, and (iv) **2b**-grafted GCE after click chemistry in ethynylpyridine and 3 h in 1 mM FePc in DMF.

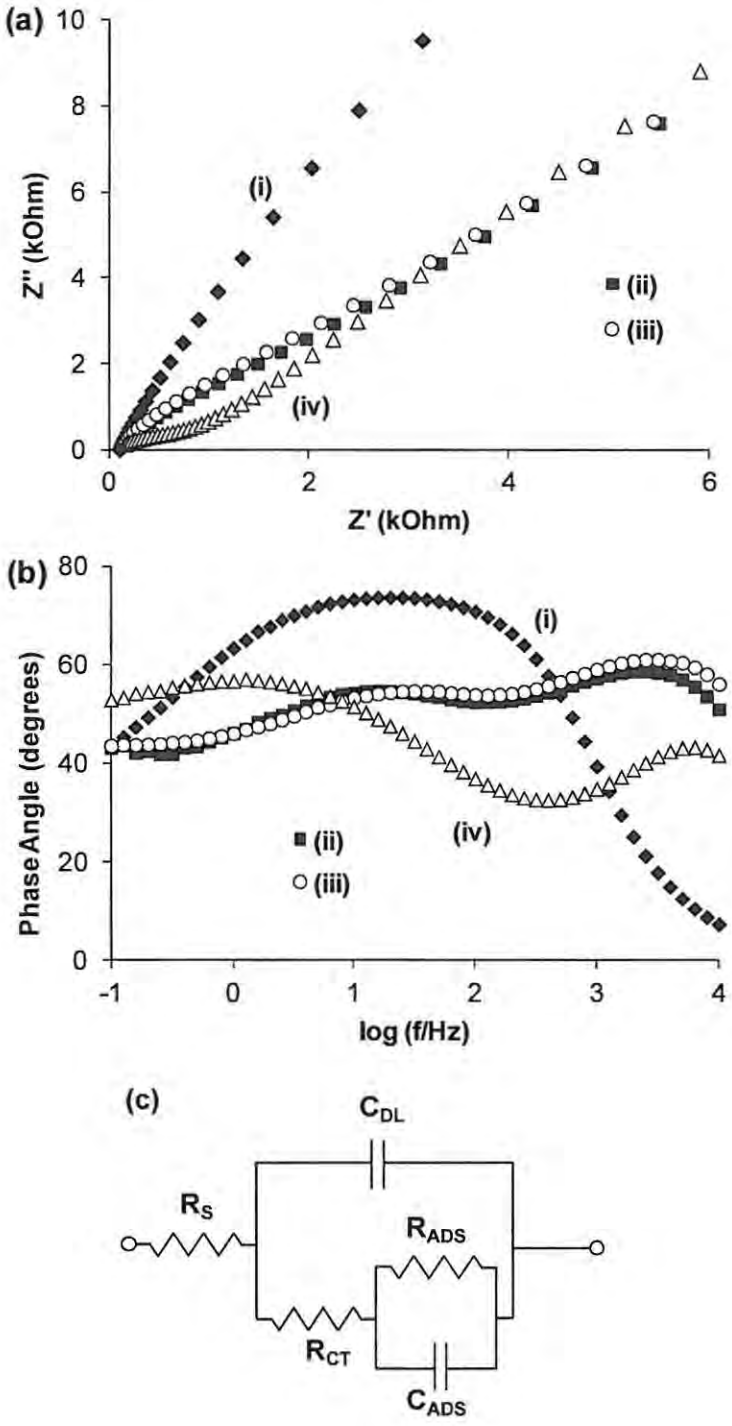

Figure 4.26. (a) Nyquist and (b) Bode plots for the GCE (i) bare, and after (ii) grafting synthesised **2b**, (iii) grafting **2b** and then click chemistry in 4-ethynylpyridine, and (iv) grafting **2b**, click chemistry, and then 3 h in 1 mM FePc in DMF. Recorded in 5 mM hydrazine sulphate in 0.1 M NaOH. (c) Randles equivalent circuit for (iv).

Fitting an appropriate Randles equivalent circuit (Fig. 4.26(c)) to the Nyquist data of (iv) gave a circuit similar to that which describes an electrochemical reaction with a strongly adsorbed intermediate [168], which is what we expect to see for this case. R_S is the solution resistance, R_{CT} is the charge transfer resistance, R_{ADS} and C_{ADS} are the contribution of the surface adsorbed species, and C_{DL} is the capacitance of the diffusion layer [168]. For this fit, it was necessary to replace the simple capacitance C_{ADS} with the constant phase element (CPE) capacitance Q. From the Nyquist plots in Fig. 4.26(a), the R_{CT} for each surface could be estimated. The R_{CT} increased from the bare GCE in (i) (0.107 kΩ) to the **2b**-grafted and pyridine-clicked electrode (ii) and (iii) (0.659 and 0.675 kΩ respectively), with both of the last two surfaces showing almost identical behaviour in both the Bode and Nyquist plots. This can be attributed to the inert or unreactive electrochemical nature of the grafted diazonium **2b** and the clicked pyridine groups, which form an insulating layer on the surface and do not interact with the electrolyte or the analyte – thus slowing the electron transfer kinetics. The surface with FePc, (iv), gave an R_{CT} value of 0.569 kΩ and showed a depressed semicircle followed by a diffusion-controlled response, which has in some cases been seen both with thin films [236] and with phthalocyanine-modified surfaces [74,100,237]. This decrease in the R_{CT} after modifying the electrode with FePc is attributed to the known catalytic properties of the metallophthalocyanines and hence the electron transfer is enhanced [22].

The Bode plots in Fig. 4.26(b) show two relaxation processes with capacitive features for surfaces (ii), (iii) and (iv). This has been seen in the same electrolyte (without hydrazine) for both metallated (cobalt) and unmetallated tetraaminophthalocyanine, and was

attributed to the changes in the double-layer capacitance as the metal oxidation state changes, and to the presence of different reactive sites on the ring, respectively [237]. This can explain the behaviour in the presence of FePc, Fig. 4.26(b)(iv), but in the case of the **2b**-grafted (Fig. 4.26(b)(ii)) and pyridine-clicked (Fig. 4.26(b)(iii)) surfaces it is more likely due to possible surface defects which do not completely block the electrolyte. The phase angle maxima of the high frequency peak in the grafted and clicked surfaces was approximately -60° (-58.66 and -61.07° respectively), with the low frequency peak at -54.28°. Upon the introduction of the FePc these peaks shift, with the high frequency peak maximum shifting to a higher frequency and lower phase angle (-42.30°) and the low frequency peak maximum shifting to a lower frequency and a higher phase angle (-57.11°). The shift of these peaks confirms the different surface properties introduced on the electrode after modifying with FePc.

The phase angle values for all of the electrodes studied in this work are less than the ideal -90° for a true capacitor leading to the conclusion that these electrodes have capacitive-like behaviour [238].

4.2.3.2. *SECM characterisation*

SECM characterisation of the GC/SWCNT surface was particularly important, due to the non-homogeneous nature of the adsorbed SWCNT layer. For the modification of the GC plates, SWCNTs were first adsorbed on to the whole surface of the plate. Half of the GC/SWCNT plate was then grafted in the **2b** diazonium solution, using two grafting

cycles as for the conventional electrodes. For the click chemistry step with 4-ethynylpyridine and for the FePc ligation, the whole plate was immersed in the relevant solutions. Thus half of the plate was "blank" (not grafted, hence not clicked, represented as the unmodified surface), and could be compared to the modified surface after each step. The modified surface was grafted, clicked and modified with FePc, and SECM was used to analyse the behaviour of the surface after each step. This was useful in confirming via SECM that the unmodified section remained conductive towards ferrocyanide, whereas the modified section was insulating towards this redox probe. $K_4[Fe(CN)_6]$ was chosen as the redox analyte for these experiments as it is highly surface-sensitive [122,228,229].

The approach curves in Fig. 4.27(a) show the insulating nature through negative feedback of the **2b**-grafted (modified) GC/SWCNT surface (ii), and also indicated that the surface remained the same following click chemistry with 4-ethynylpyridine (iii) and axial ligation to FePc (iv). This is expected, as the FePc was not conductive towards the redox probe and so appeared to be insulating despite its potential as an electrocatalyst.

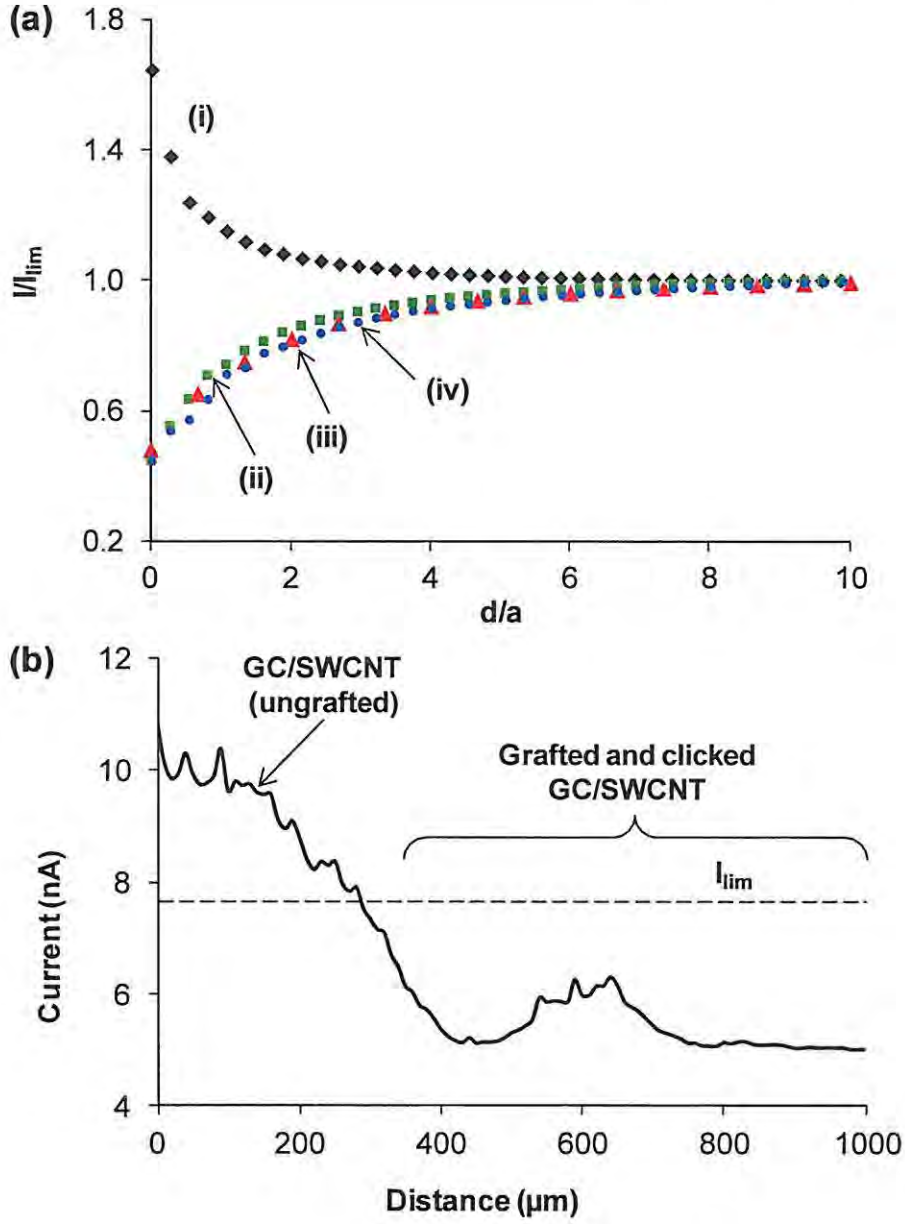

Figure 4.27. SECM results for (a) approach curves of (i) GC/SWCNT, (ii) synthesised **2b**-grafted GC/SWCNT, (iii) **2b**-grafted GC/SWCNT following click chemistry with 4-ethynylpyridine and (iv) **2b**-grafted GC/SWCNT after click and immersion in FePc and (b) the line scan for (iii) going from an unmodified GC/SWCNT area to the modified area (I_{lim} = 7.8 nA in 5 mM $K_4[Fe(CN)_6]$ in 0.1 M KCl at 0.4 V vs Ag|AgCl).

Fig. 4.27(b) shows a line scan curve where the tip travelled over the interface from the conductive (unmodified GC/SWCNT surface) to the insulating (grafted and clicked) surface. The conductive portion of the line scan appears to indicate that the SWCNTs are roughly arranged on the electrode surface, as stated previously, with some current spikes that could be due to vertically aligned nanotubes and a decrease in the tip-surface distance, or it could be due to the improved electron transfer kinetics of the SWCNTs [65]. However, the line scan in Fig. 4.27(b) still shows that the modified surface also has some rough topography and this is attributed to the presence of the SWCNTs under the modified layers. The slight differences in the conductive region of Fig. 4.27(b) and that seen in Fig. 4.11(a) are again attributed to differences in tip-substrate distance and possibly the presence of some adsorbed species following the click reaction.

The roughness of the surface is also indicated by the conductive region in Fig. 4.28(a). The surface following immersion in the FePc, however, did not have as sharp current deviations, Fig. 4.28(b). This could be merely due to a greater distance of the tip from the surface, or it could be due to a decrease in surface roughness upon adsorption of the FePc to un-grafted SWCNTs, and slower electron kinetics. Modification appears to bring some homogeneity to the electrochemical behaviour of the surface of the electrode, as indicated by the images in Fig. 4.28. A point to be noted as well is that the conductive region of Fig. 4.28(a) and (b) acted as a "blank", because while it was not grafted using synthesised **2b**, (a) was immersed in the click solution with 4-ethynylpyridine and (b) in the FePc as well. Both remained conductive, showing that the adsorbed species were not the cause of the insulating negative feedback seen in the grafted region.

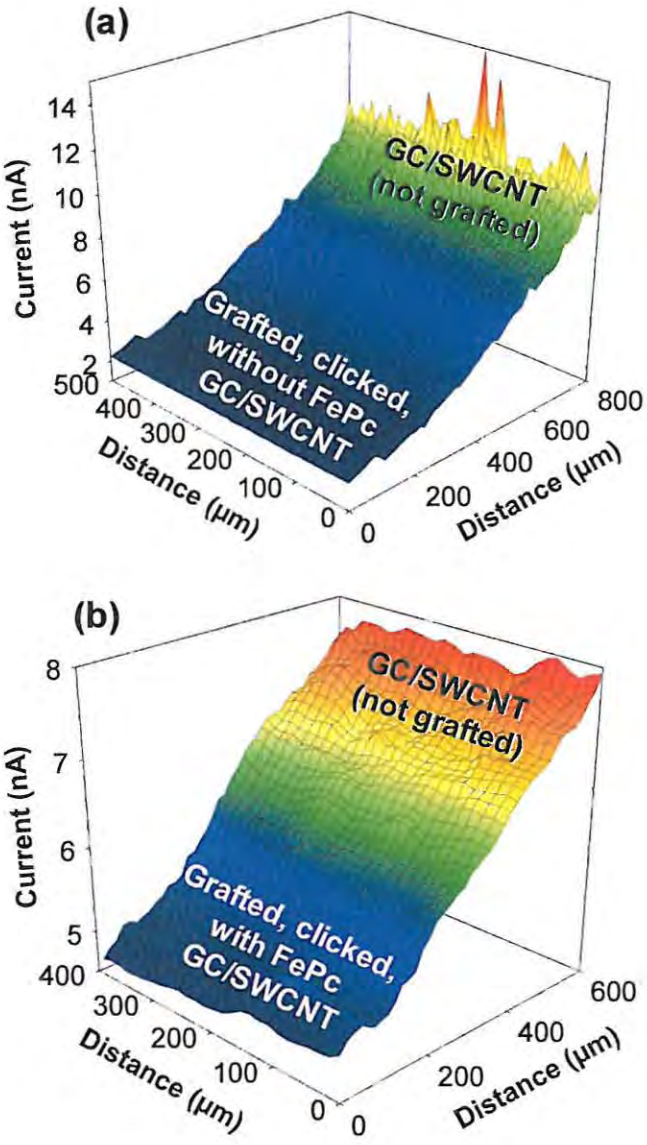

Figure 4.28. SECM images of GC/SWCNT without (a) and with (b) FePc, after grafting with synthesised **2b** and click chemistry attachment of 4-ethynylpyridine. Imaged with a 15 µm diameter Pt UME in 5 mM $K_4[Fe(CN)_6]$ in 0.1 M KCl (E_{tip} = 0.4 V vs. Ag|AgCl; I_{lim} = 7.8 nA). The tip was scanned at 15 µm/s.

4.2.3.3. *XPS characterisation*

XPS was used to analyse both the GCE and GC/SWCNT surfaces as shown in Figs. 4.29 and 4.30. Fig. 4.29 curves (iii) clearly shows the presence of iron in the form of the Fe(2p) peaks at 713 ($2p_{3/2}$) and 725 ($2p_{1/2}$) eV for the GCE and at 711 and 724 eV for the GC/SWCNT, which indicates that FePc was present and had undergone axial ligation to the pyridine groups. The slight decrease in binding energy at the GC/SWCNT is attributed to the high electron density of the nanotubes. The Fe signals from the FePc are at a higher binding energy compared to the Fe(2p) peaks found for ferrocene, which are at 708 and 725 eV.

There was a strong presence of copper on both surfaces following click chemistry, at 932 eV ($2p_{3/2}$) and 952 eV ($2p_{1/2}$), Fig. 4.29(a) and (b) curves (ii). This was likely due to the presence of weakly adsorbed copper following click chemistry, as had been observed for click chemistry with ferrocene, which showed that the copper could be removed by ultra-sonication. Following immersion of the surface in FePc for 3 h the intensity of this peak was greatly reduced, Fig. 4.29(a) and (b) curves (iii), indicating that the copper was merely weakly adsorbed on the surface. The atomic concentration of Fe in Fig. 4.29(a) and (b) curves (iii) were low, but this is to be expected due to the predominance of carbon from the phthalocyanine ring, the SWCNTs (for the GC/SWCNT), pyridine, and the GCE itself. The oxygen peak was likely due to the presence of residual solvent on the surface, and the carboxylic acid groups on the SWCNTs.

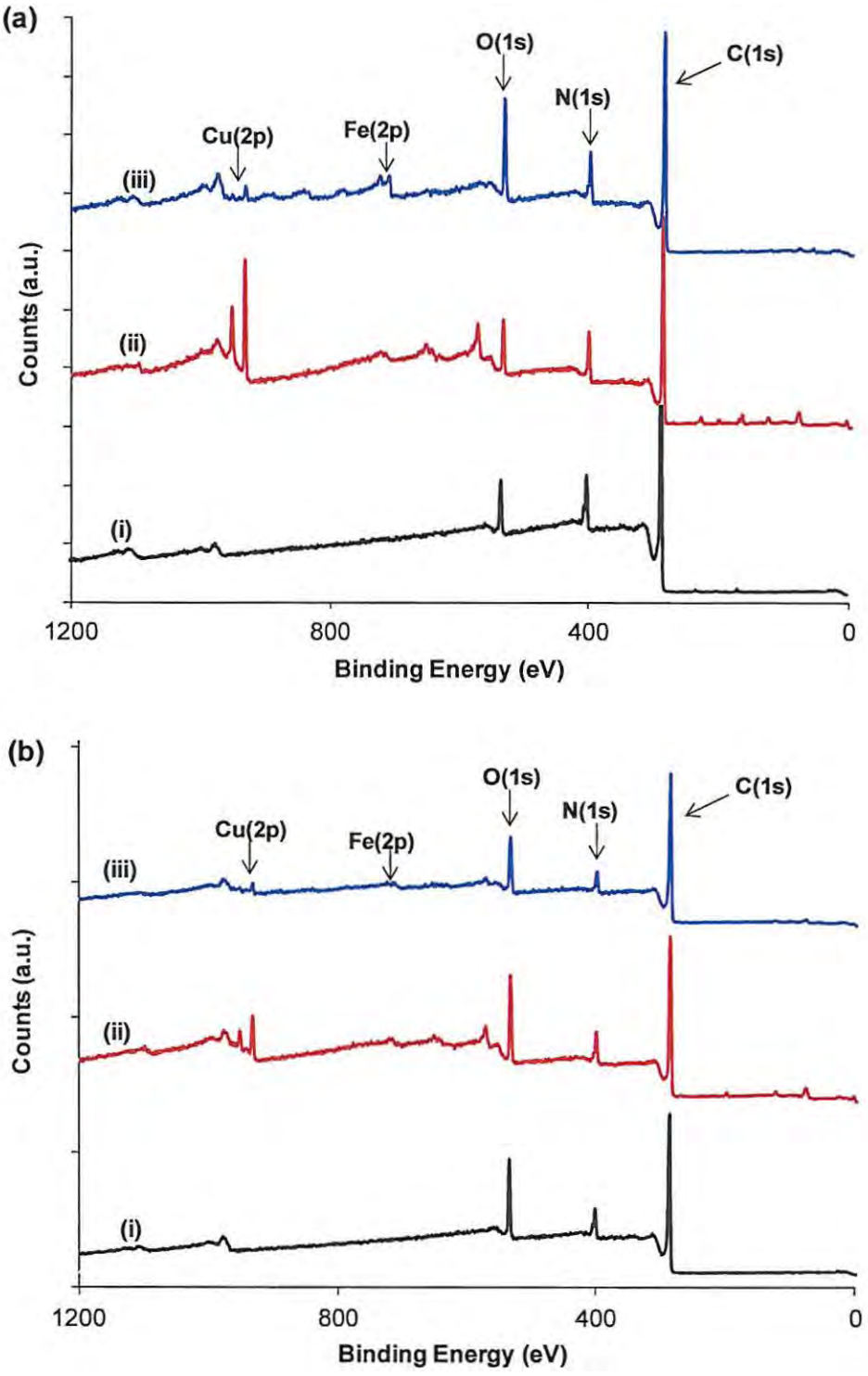

Figure 4.29. XPS spectra for: (a) GCE and (b) GC/SWCNT after (i) grafting with **2b**, (ii) grafting **2b** and click chemistry with 4-ethynylpyridine and (iii) grafting **2b**, click chemistry and immersion in FePc. Pass energy = 160 eV, number of scans = 3.

Fig. 4.30 shows the high resolution scans of the N(1s) region of the XPS spectrum. XPS was particularly useful in following the click chemistry process as the intensity of the characteristic peak for the central nitrogen of the azide group at 404.1 eV for the **2b**-grafted electrodes in Fig. 4.30(a) and (b) curves (ii) were greatly reduced after the click step, particularly for the GCE, showing that the majority of the azide groups reacted to form the triazole, as seen in Fig. 4.30(a) and (b) curves (iii) and (iv) for both surfaces [73]. Residual azide groups after click chemistry on both surfaces can be attributed to steric hindrance preventing some of the pyridine groups from reacting.

XPS analysis was also done on the free FePc and 4-ethynylpyridine species (figures not shown). The N(1s) region of the free FePc showed a sharp high intensity peak at 398.4 eV, which was attributed to the overlapped signals of the pyrrole and aza-nitrogens [239], while the 4-ethynylpyridine exhibited two broad, low intensity peaks for the pyridinic nitrogen at 398.7 and 401.6 eV. The broad nitrogen signals at 400.0 eV after click chemistry on the GCE and the two overlapped signals at 400.6 and 399.8 eV for the GC/SWCNT, shown in Fig. 4.30(a) and (b) curves (iii), was thus due to the contribution of both the pyridinic nitrogen of the clicked pyridine as well as the triazole ring and the remaining unreacted azide. For the GCE, upon ligation to FePc the nitrogen peak at lower binding energy appeared to shift from 400.0 to 399.4 eV in Fig. 4.30(a)(iv). This was in fact due to the contribution of the pyrrolic and aza-nitrogen groups from the FePc at 398.8 eV, shown more clearly at 398.5 eV for the GC/SWCNT. Fig. 4.30(b)(iv), the GC/SWCNT, shows the presence of the pyrrolic and aza-nitrogen groups of FePc at 398.5 eV, with a broad shoulder at 400.3 eV from the triazole ring and unreacted azide.

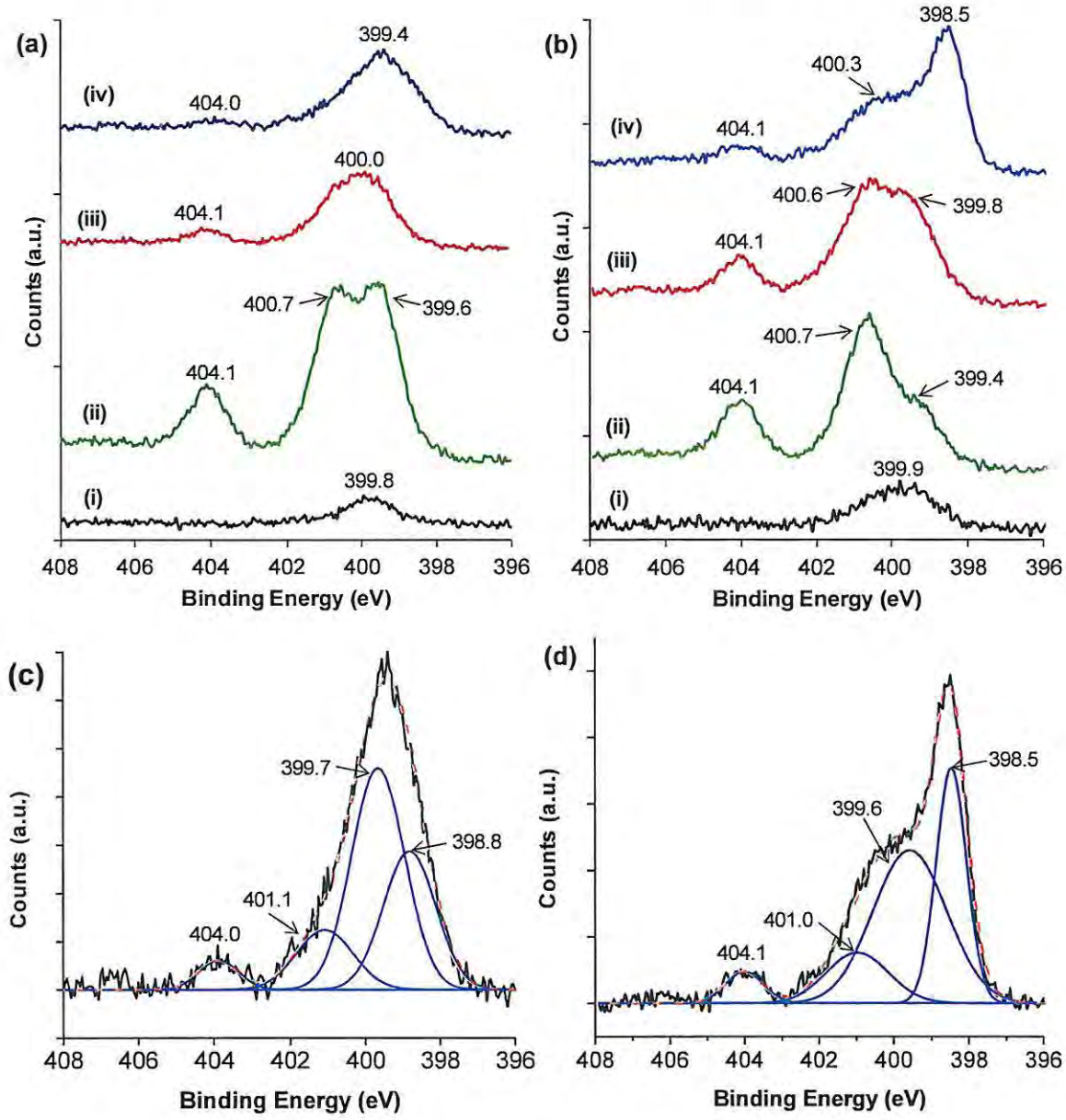

Figure 4.30. High resolution XPS spectra of the N(1s) region for (a) GCE and (b) GC/SWCNT (i) bare, (ii) after grafting **2b**, (iii) after grafting **2b** and click chemistry with 4-ethynylpyridine and (iv) after grafting **2b**, click chemistry and immersion in FePc. (c) and (d) the N(1s) peak fitting of (iv) for the GCE and GC/SWCNT, respectively. Pass energy = 40 eV, number of scans = 5.

Fig. 4.30(c) and (d) shows the deconvolution of the peak following click chemistry and axial ligation with FePc for the GCE and the GC/SWCNT, respectively, in order to better elucidate the presence of different species. For the GCE, the presence of the triazole was indicated by a peak at 399.7 eV, the pyrrole/aza FePc nitrogens at 398.8 eV and the pyridinic nitrogen groups contributing to the signal at 398.8 eV as well as the broad peak at 401.1 eV in Fig. 4.30(c). Unreacted azide groups on the GCE surface also contributed to the peaks at 401.1 eV and 404.0 eV. For the GC/SWCNT, Fig. 4.30(d) shows the presence of at least four nitrogen signals as well. The first, a sharp peak at 398.5 eV, was attributed to the FePc as discussed above. The second was a large, broad peak at 399.6 eV with a third at 401.0 eV and finally some residual unreacted azide-nitrogen at 404.1 eV. The signal at 399.6 eV, which was present in the clicked surface (iii) as well, was thus attributed to the overlapped peaks of the pyridinic nitrogen as well as the nitrogen groups on the triazole ring. The unreacted azide nitrogen groups adjacent to the electron-poor central nitrogen were most likely responsible for the weaker signal at 401.0 eV, as the ratio of the areas of the peak at 404.1 eV to this peak was approximately 1:2.6, indicating some contribution by the pyridinic nitrogen (which also has a weak, broad signal at 401.6 eV) as we expect a ratio of 1:2 for the azide nitrogen groups [181].

4.3. Surface modification by electropolymerisation and click chemistry

A combination of electropolymerisation and click chemistry was also investigated for the attachment of ferrocene to a GCE surface. As with the grafting and click chemistry approaches, both the polymerise-then-click and click-then-polymerise methods were investigated to determine which was the most effective for attachment of ferrocene to the GCE using this technique, Scheme 4.4. The direct electropolymerisation of **2a** and the newly synthesized **2c** are shown here for the first time through the possibility of electropolymerisation of its aniline group [126–128,130,131], as outlined in Scheme 1.5. A potential step method was used for the electrodeposition rather than potential sweep, as the former is believed to increase the rate of *ortho*-coupling [132].

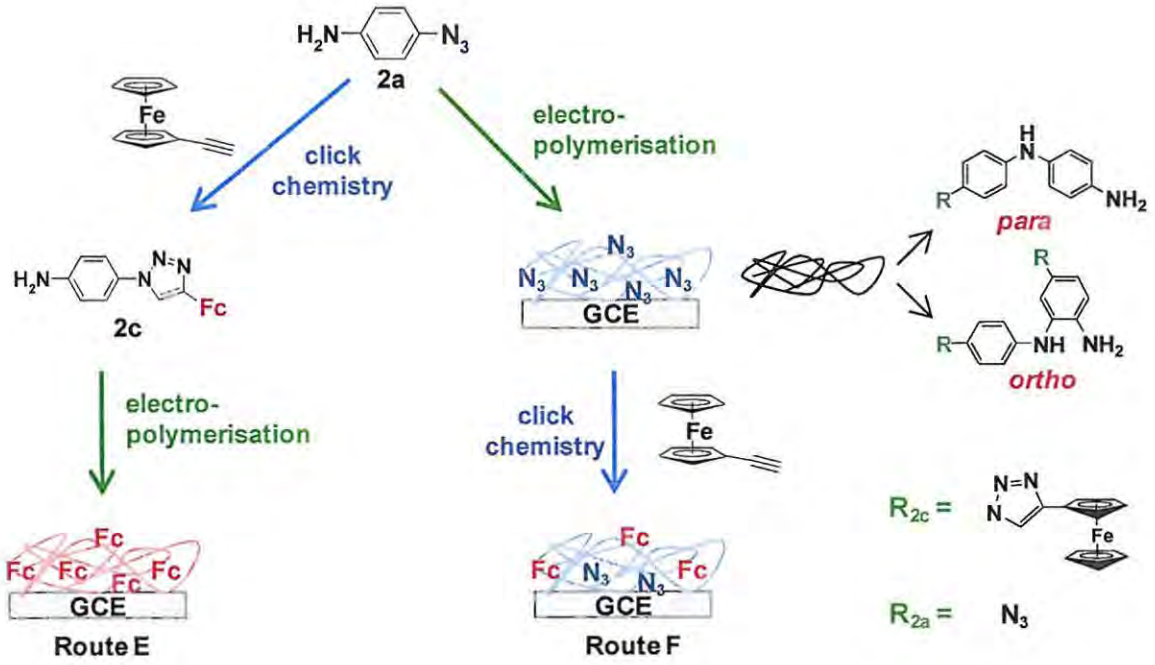

Scheme 4.4. Approaches for attaching ferrocene through click chemistry and electropolymerisation via *ortho*- or *para*-polymerisation of the aniline group.

Electropolymerisation of **2a** at the GC surface resulted in the visible formation of red polymer strands at the GC disk. Electrodeposition of **2a** was done in aqueous acidic media by potential step at 0.8 V for 10 min. Fig. 4.31(a) shows the cyclic voltammogram corresponding to the electropolymerisation of **2a**: on the second scan, a couple appeared at ≈0.6 V that could be attributed to electroactivity of the polymer formed at the electrode surface.

Electrodeposition of **2c** was conducted successfully in acetonitrile without a proton donor by potentiostatic method at 0.8 V for 10 minutes at the GCE [240]. Electrodeposition in acetonitrile/acid was also possible, however the poor solubility of **2c** in aqueous media made this method less effective. Fig. 4.31(b) shows the corresponding cyclic voltammograms obtained by successive cycling in a solution of **2c**, showing the increase of the intensity of anodic and cathodic peak located at ≈0.5 V indicating the increased deposition of ferrocene on the electrode surface. The process at 0.6 V could be attributed to the electropolymerisation of the aniline, as it was comparable to the peaks seen in Fig. 4.31(a) for **2a** at the same potential.

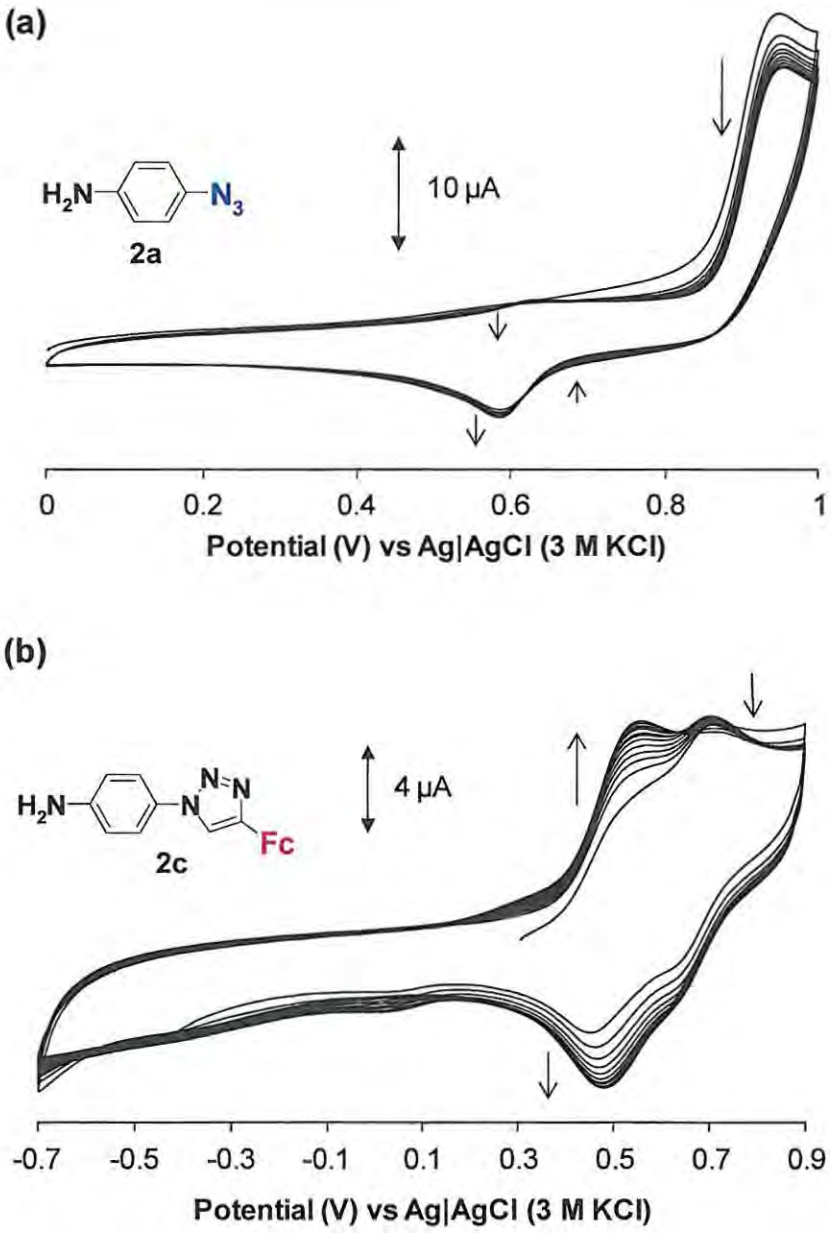

Figure 4.31. Cyclic voltammograms of the GCE showing electrodeposition in (a) 1 mM of **2a** in 96:4 ACN/1 M HCl with 0.1M $TBABF_4$ and (b) 1 mM **2c** in ACN with 0.1 M $TBABF_4$. Scan rate 50 mV/s.

4.3.1. *Electrochemical characterisation*

The electropolymerised layers were conductive, and as such did not suppress the redox peaks for ferrocyanide (figure not shown). There was no change in the potential for oxidation/reduction of this redox probe, indicating that the polymerised layers did not act as a barrier to charge transfer. However, the presence of ferrocene in complex **2c**, the click-then-polymerise approach (route E, Scheme 4.4), as well as on the **2a**-polymerised electrode following click chemistry with ferrocene (under the conditions described for click chemistry on the grafted GCE), the polymerise-then-click approach (route F, Scheme 4.4), could be used as a means to confirm attachment of the polymerised layer to the electrode, Fig. 4.32.

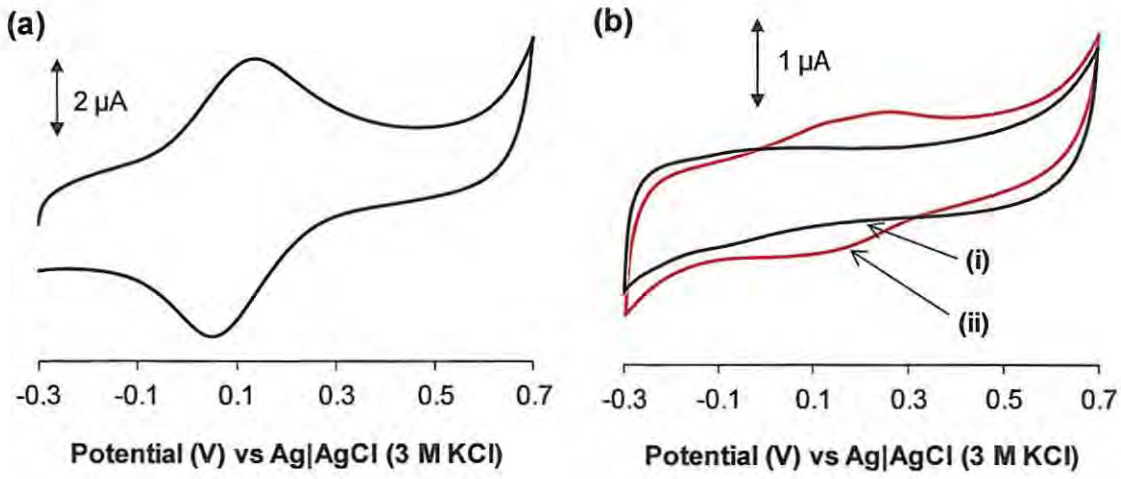

Figure 4.32. Cyclic voltammogram in 0.1 M KPF_6 of (a) **2c**-electropolymerised GCE and (b)(i) **2a**-electropolymerised GCE and (ii) after click chemistry with ethynylferrocene. Scan rate 50 mV/s vs Ag|AgCl (3 M KCl).

The **2c**-electropolymerised GCE (Fig. 4.32(a)) shows a well-defined couple of peaks at $E_{p1/2}$ = 0.10 V. The apparent potential value was close to that already reported for ferrocene immobilized at a synthesised **2b**-grafted carbon electrode by click chemistry [14]. This voltammetric feature could thus be assigned to the presence of immobilized ferrocene at the GCE. The variation of the log of the peak current intensity versus the log of the scan rate gave a slope of 0.82, close to the slope of 1 expected for attached redox species to electrode surface [241]. The surface coverage was determined as the amount of electroactive ferrocene sites inside the deposited layer, at 17.7 ± 2.8 x 10^{-10} mol.cm^{-2} for the **2c**-electropolymerised GCE, Table 4.3. This value corresponds to ≈4 layers, compared to the coverage of 4.5 x 10^{-10} mol.cm^{-2} for a close-packed monolayer of ferrocene [7]. This electropolymerisation strategy (route E, Scheme 4.4) using a pre-clicked molecule appears to be attractive to modulate the number of ferrocene groups immobilized at the electrode surface, although the coverage results indicated that some of the groups are embedded in a thick polymer multilayer.

Fig. 4.32(b)(ii) shows the GCE following electropolymerisation in **2a** and click chemistry with ferrocene, route F (Scheme 4.4). It exhibited a weak broad peak with maximum intensity at 0.26 V. A control experiment using ferrocene instead of ethynylferrocene for the second step revealed no voltammetric peak. In fact, this broad peak had two overlapped processes seen in Fig. 4.32(b)(ii) and more clearly observed by square wave voltammetry (figure not shown), one located at 0.10 V and attributed to the presence of immobilised ferrocene groups and the second at 0.26 V. The nature of this second peak was not fully understood but may be attributed to oxidation of adsorbed copper(I)

complex used during the click reaction that was not fully removed by rinsing. The surface coverage of ferrocene for this polymerise-then-click approach was calculated to be 1.1 x 10^{-10} mol.cm^{-2}, Table 4.3.

The 16 times improvement of the click-then-polymerise approach over the polymerise-then-click approach was opposite to that seen with grafting – where the graft-then-click approach showed a 7 times improvement to the click-then-graft approach. This shows that the poor behaviour of the grafted complex **2d** (formed by *in situ* diazotation of **2c**) was likely due to the insulating nature of the grafted layer and the possible loss of ferrocene groups through displacement by the radical. Whereas for electropolymerisation of **2c**, as the polymer remained conductive and *ortho*-direction growth appeared to be favoured, more of the ferrocene species were retained and they remained electroactive. However, surface coverage values for the electropolymerised **2a**-GCE after click chemistry showed that fewer ferrocene groups were attached via this route. This indicates that either fewer azide groups were initially attached in the first electropolymerisation step, or that the immobilised azide groups were less accessible for ethynylferrocene coupling in the polymer, Scheme 4.4. This reduction in the number of free surface azides for the polymer was supported by the XPS results, which are discussed below.

The electropolymerised **2c** had greater surface coverage of ferrocene than any of the grafting approaches on the GCE, Table 4.3, likely due to the ability of the polymer to form conductive multilayers while preserving the electroactivity of the attached species.

The electropolymerised surface remained conductive and so SECM could not be used to show the changes after layer formation.

4.3.2. *XPS characterisation*

To complete the characterization of the electropolymerised electrodes, the samples were analyzed by XPS, Fig. 4.33 and Fig. 4.34.

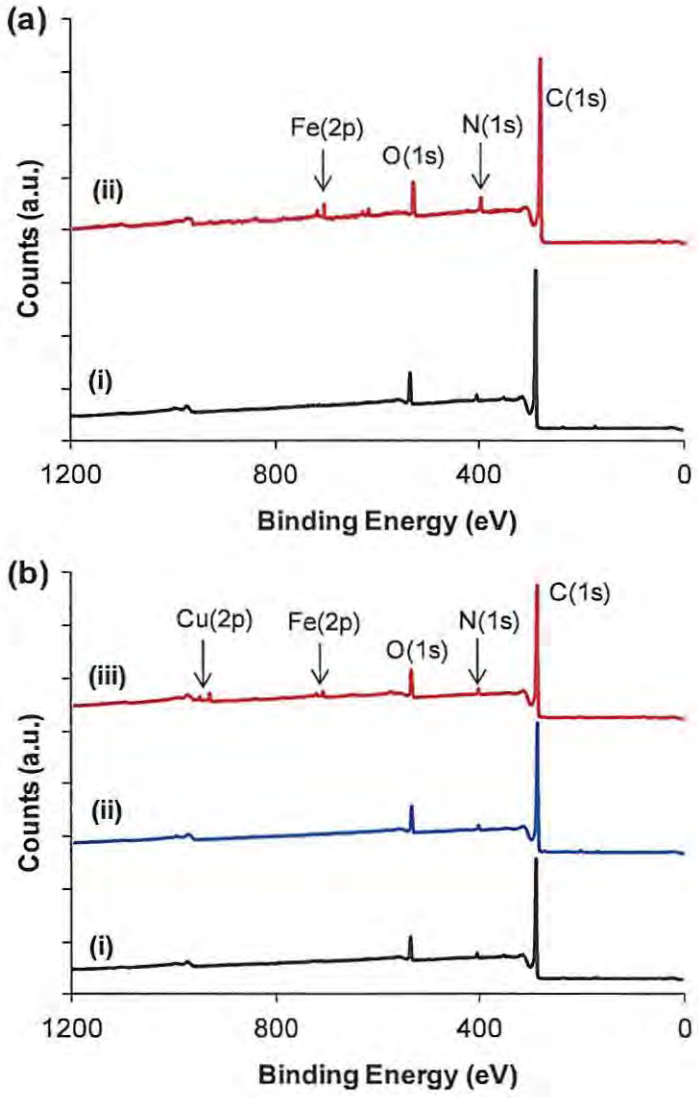

Figure 4.33. XPS spectra for: (a)(i) bare GCE and (ii) **2c**-polymerised GCE and (b)(i) bare GCE, (ii) **2a**-polymerised GCE and (iii) **2a**-polymerised GCE after click chemistry with ferrocene. Pass energy = 160 eV, number of scans = 3.

Both of the surfaces showed the presence of ferrocene through the Fe(2p) signals in Fig. 4.33(a)(ii) for the **2c**-polymerised GCE and in Fig. 4.33(b)(iii) for the **2a**-polymerised GCE following click chemistry. The lower intensity of the N(1s) signal for the **2a**-polymerised GCE both before and after click chemistry, Fig. 4.33(b) curves (ii) and (iii), compared to that seen with the **2b**-grafted GCE in Fig. 4.22(a), also indicated some confirmation of the low surface coverage of ferrocene, by the presence of few azide groups on the surface. The low amount of azide groups immobilized at the electropolymerised electrode could be explained by the fact that the electropolymerised films stop growing after a few cycles under the electropolymerisation conditions used; indeed the redox signal corresponding to the formation of the electrodeposited polymer stopped growing after three voltammetric cycles due to the fact that the *para*-position of the aniline was occupied by azide groups, thus limiting the electropolymerisation process to branching at the *ortho*-position [128,132]. The azide group could also be involved in the polymer growth at the *para*-position, and so limit the free azides to the ends of the polymer strands, or some of the azide groups may have been eliminated during *para*-direction polymerisation [126,242].

High resolution XPS of the **2a**-modified surface was used to analyse the N(1s) region for the presence of the high energy peak indicative of the presence of the azide, Fig. 4.34, to ensure that not all of these *para*-substituted groups were lost during electropolymerisation, as studies with halogen substituents gave elimination ratios of the *para*-group of up to 59 % [242].

Two peaks at 400.1 eV and 404.0 eV were observed for the electrode with electropolymerised **2a**, Fig. 4.34(ii). The peak at 404.0 eV was attributed to the presence of azide groups, as reported in the literature, confirming immobilization of azide groups at the GC surface [13,73,181,184]. The intensities of the N(1s) peaks were weaker than for the surface obtained after grafting **2b**, Fig. 4.23(a)(ii), indicating that fewer azide groups were present at the surface modified by electropolymerisation of **2a** compared to grafting of **2b**.

The N(1s) peak at 404.0 eV completely disappeared following click chemistry with ferrocene, Fig. 4.34(iii), showing the completion of the click reaction on this surface.

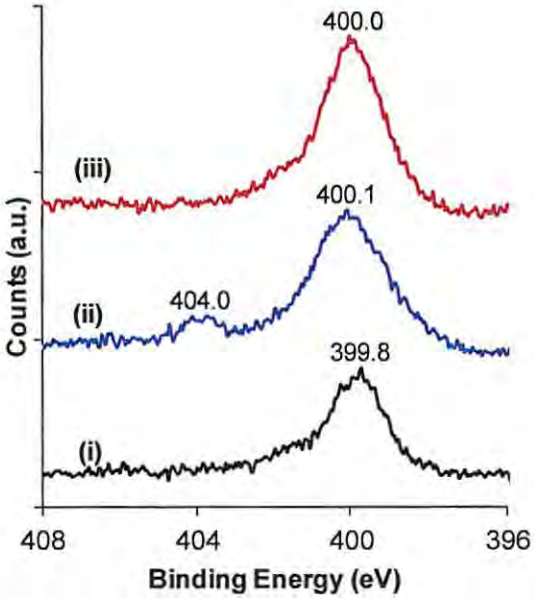

Figure 4.34. High resolution N(1s) XPS spectra obtained at GCE (i) bare, (ii) after electropolymerisation of **2a** and (iii) following click chemistry with ferrocene. Pass energy = 40 eV, number of scans = 5.

4.4. Micropatterning of gold surfaces

First, to perform local electrografting of **2b** by SECM, the Pt UME (12.5 μm diameter) was positioned at a desired close distance from the gold substrate surface using conventional approach curves in feedback mode in aqueous 0.1 M KCl with 5 mM $[Ru(NH_3)_6]Cl_3$. The calculated distance between the tip and the gold surface, by comparison with simulated pure positive feedback curve, was ≈1 μm. After rinsing with Milli-Q water and then acetonitrile, a solution of acetonitrile containing 5 mM **2b** and 0.1 M $TBABF_4$ was introduced. Preliminary experiments indicated that the electrochemical grafting of **2b** occurs on gold at potentials lower than -0.4 V, Fig. 4.35(a). The bare gold substrate was then polarized at -0.5 V while the SECM tip acted as a microanode (i.e. as a counter electrode in a three-electrode configuration). The positioning of the microanode (SECM tip) close to the gold surface allowed for the confining of the electric and diffusion fields [243] and restricted the reduction of the diazonium moieties to a local area beneath the tip. After reducing **2b** for 10 ms, the electrochemical set up was rinsed with acetonitrile and Milli-Q water, an aqueous solution of 5 mM $[Ru(NH_3)_6]Cl_3$ was introduced and the Pt microelectrode was used again as the SECM probe/working electrode, with no potential being applied to the gold substrate. The SECM tip was not passivated during the electrografting of the gold surface, and so it could be used directly to assess the characteristics of the grafted spot.

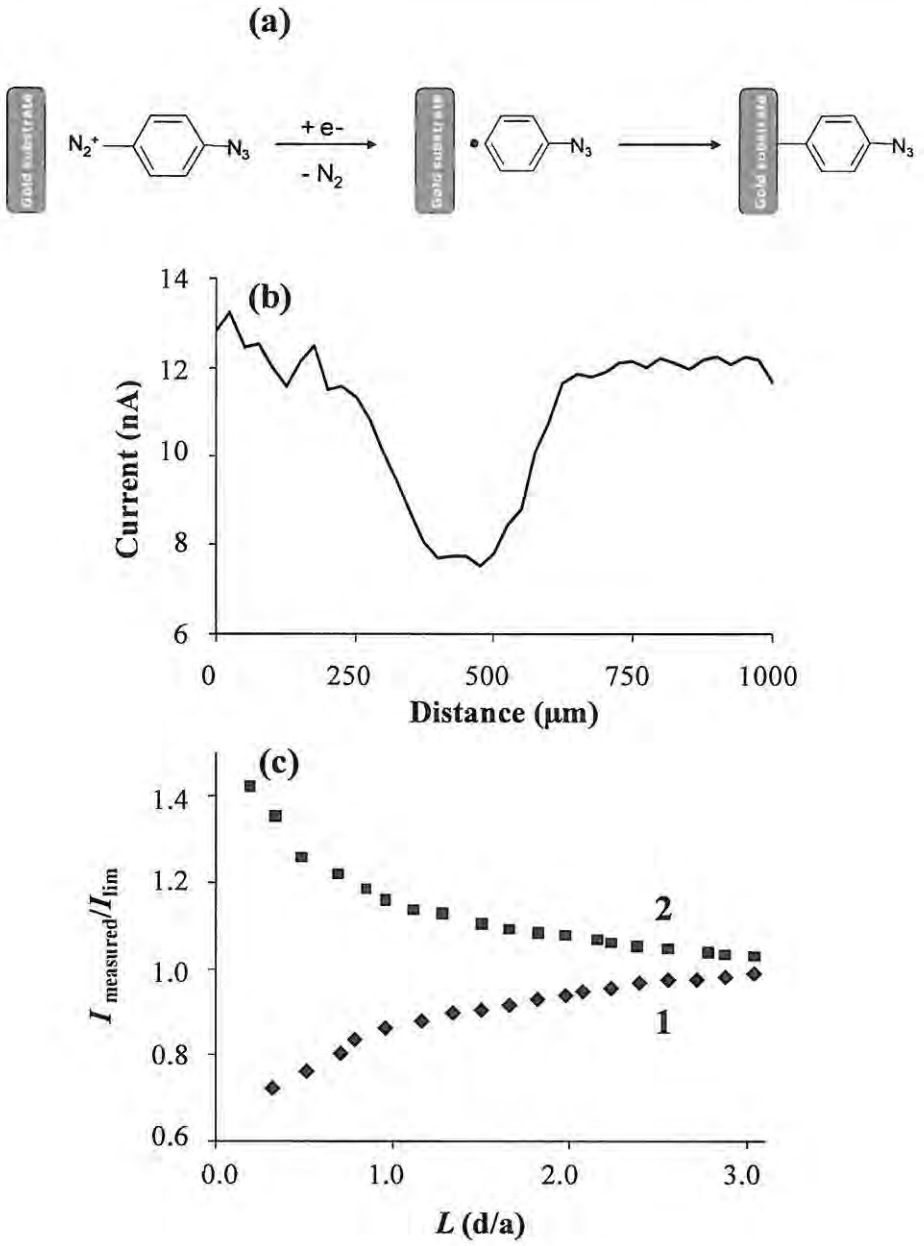

Figure 4.35. (a) Schematic electrografting reaction of **2b**, (b) SECM line scan above the gold substrate after its local electrografting and (c) SECM approach curves above the locally electrografted area of the gold substrate (curve 1) and 500 µm away (curve 2). (In 5 mM $[Ru(NH_3)_6]Cl_3$ in 0.1 M KCl, Pt UME = 12.5 µm diameter, E_{tip} = -0.45 V vs. Ag|AgCl; I_{lim} = 9.8 nA).

Fig. 4.35(b) shows the SECM line scan of the resulting pattern formed on the gold surface. The current decrease was consistent with a local derivatization and revealed the formation of a ≈300 μm wide passivating layer on the substrate. The electrografting was confined in a much larger region than the tip, indicating that, as expected for diazonium moieties, the reaction was very efficient. The area surrounding the micro-spotted electrografted zone remained apparently conducting as shown by a comparison of the approach curves performed on the spot (Fig. 4.35(c), curve 1) and at a distance of 500 μm from the centre of the spot (Fig. 4.35(c), curve 2). The approach curve performed on the spot clearly showed after simulation with theoretical curves that the grafted layer was affecting (decreasing) the electron transfer but it was not behaving as a pure insulator.

Fig. 4.36(a) shows the SECM image of the patterned spot by scanning the tip over the gold substrate laterally along the x and y axis within a square region of 1000 μm x 1000 μm centred on the position where the tip was placed for the electrografting. The electrografted spot was clearly visible with a good contrast due to the electron transfer features of $[Ru(NH_3)_6]Cl_3$. A similar image was obtained by using the well known surface sensitive $K_3[Fe(CN)_6]$ redox mediator [122], confirming that **2b** was not adsorbed at the gold in these experimental conditions (data not shown).

Pattern dimensions could be controlled by the concentration of the diazonium, the duration of the electrochemical reduction reaction, the presence or absence of supporting electrolyte and the dimensions of the cone of the electrolytic solution confined between the tip and the substrate [243,244]. In the latter case, the dimensions of the cone were

controlled by varying the distance between the UME tip and the gold substrate and/or the diameter of the tip. The use of a 50 μm diameter tip positioned at ≈3 μm above the gold substrate gave a very diffuse derivatised area (dimension larger than 500 μm, Fig. 4.36(b)), while a much smaller electrografted spot was obtained if the same tip was positioned at ≈1.5 μm (Fig. 4.36(c)). Reducing the tip diameter to 25 μm resulted a smaller electrografted spot as shown in Fig. 4.36(d). Thus, comparison of Figs. 4.36(a)-(d) shows how by moving the tip away from the gold substrate, the electrografting reaction was displaced to vicinal uncovered domains due to lesser radial diffusion restriction of the diazonium to enrich the surface of the substrate, and the very fast coupling reaction of the radical electro-generated at the base of the cone. It is important to note that in all cases the duration of the electrografting reaction was the same (10 ms). Finally, the spotted micro-zones were limited to a much smaller area (≈60 μm) by eliminating the supporting electrolyte, thus reducing the charge injected for the electrochemical transformation. This is exemplified in Fig. 4.36(e) and should be compared with Fig. 4.36(a), which had the same conditions except that the electrolyte was present.

The small conductive spots seen in Fig. 4.36(a) and (c) were attributed to a rough area on the UME or the substrate, where the probe and substrate were too close and the layer formation was inhibited.

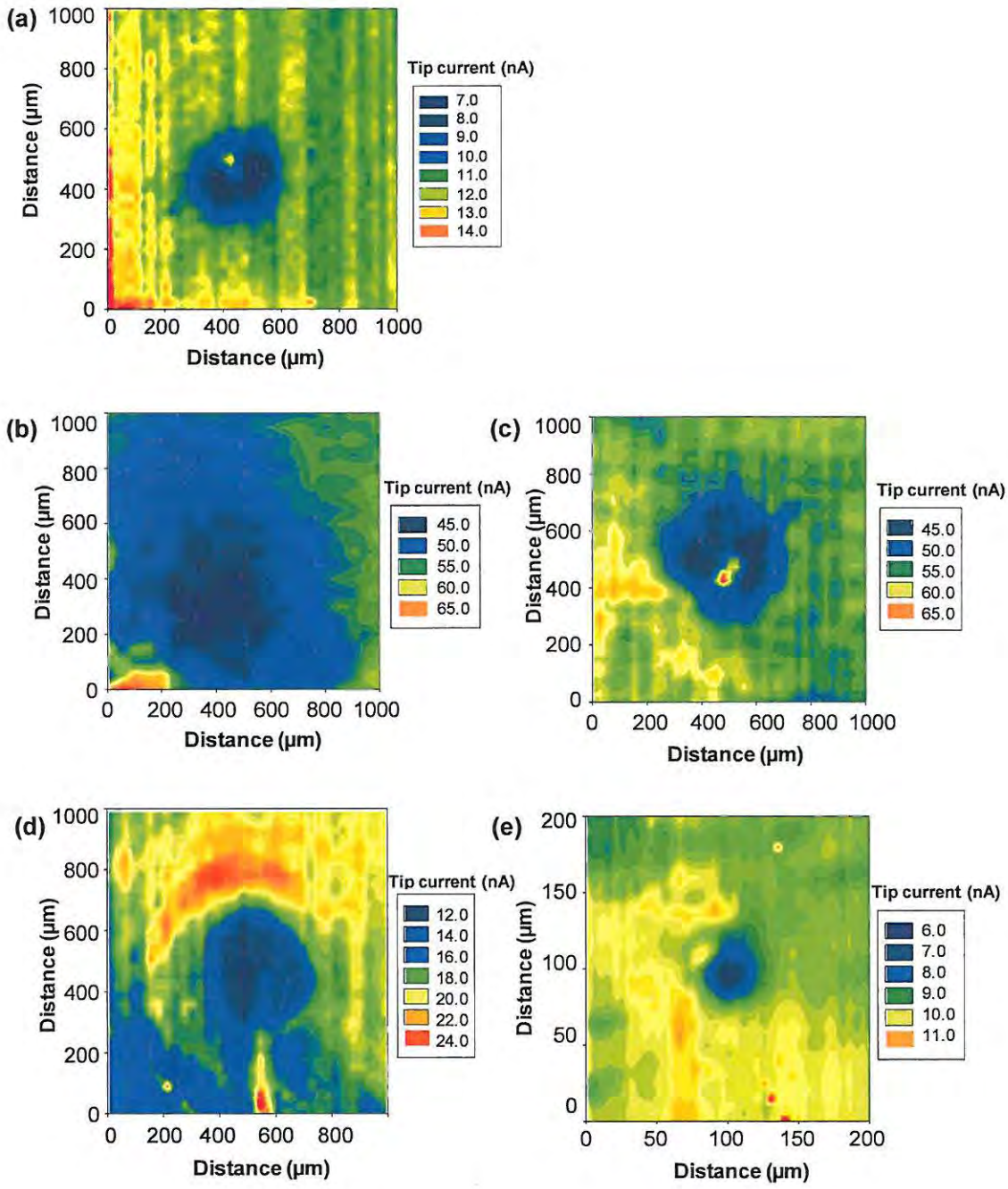

Figure 4.36. SECM images of locally electrografted gold substrate with a Pt tip in 5 mM $[Ru(NH_3)_6]Cl_3$ in 0.1 M KCl aqueous solution (E_{tip} = -0.45 V vs. Ag|AgCl; I_{lim} = 9.8, 19.6 and 48 nA for 12.5, 25 and 50 µm diameter). The tip was scanned at 50 µm/s. The electrografting was obtained by a Pt tip of (a) 12.5 µm diameter positioned 1 µm above the gold surface; (b) 50 µm diameter positioned 3 µm above the gold surface; (c) 50 µm

diameter positioned 1.5 μm above the gold surface; (d) 25 μm diameter positioned 1.5 μm above the gold surface and (e) 12.5 μm diameter positioned 1 μm above the gold surface. In all cases the electrografting reaction was performed in acetonitrile containing 5 mM **2b** and 0.1 M $TBABF_4$ during 10 ms except (e) where no supporting electrolyte was added.

It should also be pointed out that in all cases the SECM images were obtained by using the same Pt tip as the one used for the electrografting of the substrate, without any further polishing. This approach is thus a very appealing method to produce reduced size spots of electrografted aryldiazoniums, with the added benefit of the potential for the micro-spotted **2b**-layer on the surface to be used further for the click chemistry reactions as outlined in the previous sections.

CHAPTER 5

ELECTROCATALYTIC STUDIES

As mentioned in the previous sections, the focus of this work was on surface modification and characterisation. However, testing modified electrodes for electrocatalytic ability is used here as another form of characterisation. Thus a selection of the newly modified surfaces were tested in analyte solutions, and brief electrocatalytic studies were undertaken as an indication of the potential of these surfaces.

Tabulation and comparison of the following results was not useful, as all of the electrodes could not be used for detection of the same analyte.

5.1. MnPc-SAMs for electrocatalysis of thiocyanate

Self-assembled monolayers (SAMs) of MPcs containing sulphur groups on gold have in many cases shown good stability and electrocatalytic activity towards the detection of analytes such as hydrazine, L-cysteine and thiocyanate [72,80,188,221].

The **1d**-SAM (phenylthio) electrode was used to detect thiocyanate, because of its greater surface coverage and the higher ratio of bound sulphur groups compared to the **1b**-SAM, in order to determine the electrocatalytic properties of this SAM. Fig. 5.1 shows the CVs of the bare and modified electrodes in 1 mM potassium thiocyanate. The **1d**-SAM electrode showed the oxidation of thiocyanate at 0.84 V, with the oxidation on the bare electrode at 0.87 V. The modified electrode also showed a slight improvement in sensitivity, with a higher current detected for the thiocyanate. Both the lowering of the

oxidation potential and the greater sensitivity are indicative of electrocatalysis occurring on the modified electrode [196,221].

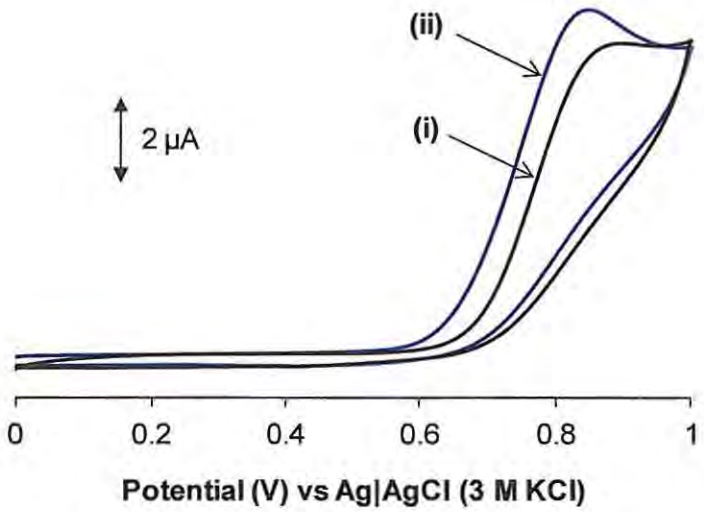

Figure 5.1. Cyclic voltammetry of (i) bare AuE and (ii) **1d**-SAM in 1 mM potassium thiocyanate in 0.1 M pH 4.0 acetate buffer. At 50 mV/s vs Ag|AgCl (3 M KCl).

Limits of detection (LoD) were obtained through the use of chronoamperometry in a vigorously stirred solution of the electrolyte, with the electrodes first being conditioned by cycling in the acetate buffer. Fig. 5.2 shows the chronoamperometry results for the modified electrode, with stepwise increases in current upon each addition of 0.01 mM of thiocyanate. The inset shows the plot of current vs concentration for one of the experiments, with a high linear coefficient. The LoD (using a signal to noise ratio of 3) for the **1d**-SAM was calculated to be 1.46 ± 0.11 µM, with an average sensitivity of 4.16

μA/mM, while for the bare electrode the LoD was 2.91 μM and the sensitivity was 3.22 μA/mM. The increase in sensitivity and better LoD values for the modified electrode correlates with the improved current intensity seen in Fig. 5.1, and was a result of electrocatalysis of the thiocyanate by complex **1d**. Gold electrodes modified with iron phthalocyanine have shown better LoD values of 0.10 μM at lower oxidation potentials [156], because of the greater catalytic ability of iron as a central metal [75]. However, the value for the **1d**-SAM is comparable and shows the successful formation of a SAM on gold using this phenylthio-MPc, with a linear detection range from 0.01 to 0.1 mM.

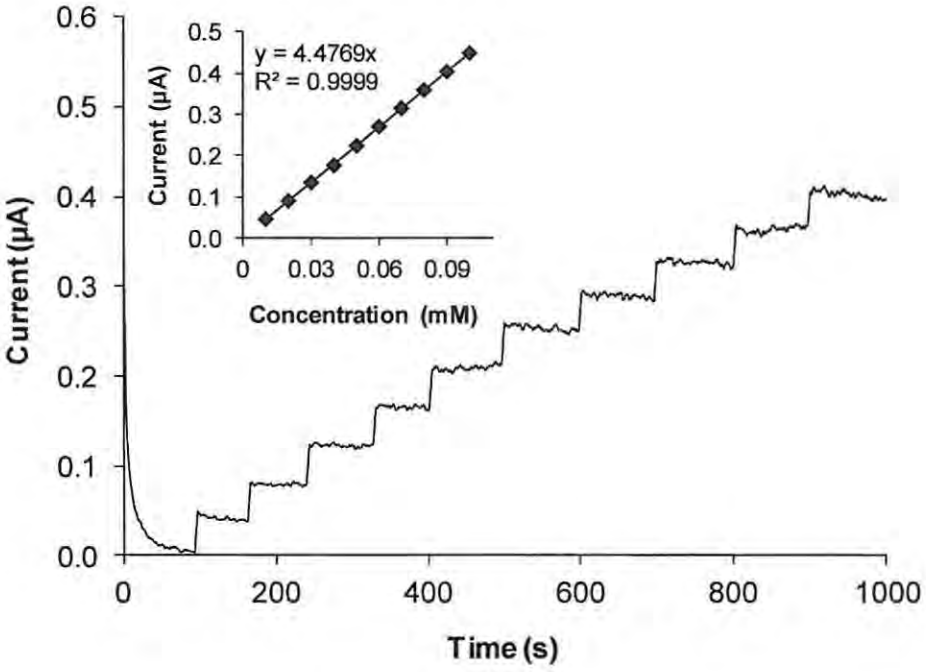

Figure 5.2. Chronoamperometry of **1d**-SAM in 0.1 M pH 4.0 acetate buffer with additions of 0.01 mM potassium thiocyanate. Inset: plot of current *vs* concentration of the analyte. Reference: Ag|AgCl (3 M KCl).

5.2. Ferrocene for electrocatalysis of sulphite

Although a number of electrodes were modified with ferrocene in this work, the GC/SWCNT electrode was tested for its ability to detect sulphite because it had the highest surface coverage of ferrocene of all of the grafted electrodes. The grafted electrodes were more interesting for electrocatalysis than the electropolymerised surfaces, because the grafted electrodes blocked or suppressed the redox activity of many analytes and the electrocatalytic effects of the clicked ferrocene could be more clearly observed.

Fig. 5.3 shows the typical chronoamperograms of the bare electrode (i), the **2b**-grafted GC/SWCNT (ii) and the same electrode after click chemistry with ethynylferrocene (iii), Scheme 4.2, at a fixed oxidative potential (0.3 V). The responses of the electrodes were investigated under stirring in PBS (pH 7.0) solution with successive additions of 0.25 mM sulphite. A well-defined and increasing current response due to sulphite oxidation was observed for GC/SWCNT (Fig. 5.3(iii)) after the clicking of ferrocene. The current response before clicking (Fig. 5.3(ii)) was much less than that observed in the presence of ferrocene. The slight decrease in current response at longer times signifies saturation in concentration. For the GC/SWCNT without grafting (figure not shown), the saturation was obtained at lower concentrations even though the current response was greater. This shows the suitability of the grafted and clicked electrode for analytical applications, and indicates its potential as an electrocatalytic surface. Fig. 5.3 inset displays the calibration curve (the plot of current response versus concentration of sulphite) in the presence of clicked ferrocene. A straight line within the studied concentration range (0.50 to 2.25

mM) with the correlation coefficient of 0.985 was obtained. The sensitivity was 0.42 μA/mM and the LoD was found to be 16.9 μM at a signal-to-noise ratio of 3. This was a poorer response than that seen with a MWCNT/ferrocene-chitosan composite, where the LoD was determined to be 2.8 μM [5], however it was sufficient to show the electrocatalytic potential of the surface.

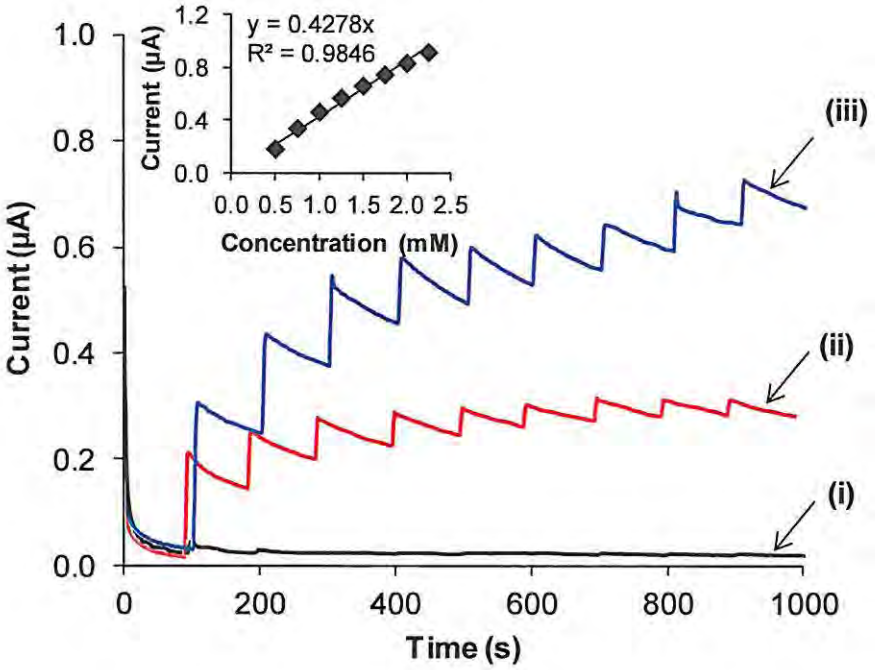

Figure 5.3. Chronoamperometry at 0.3 V with consecutive additions of sodium sulphite (0.25 mM). (i) Bare GCE, (ii) **2b**-grafted GC/SWCNT and (iii) **2b**-grafted and ferrocene-clicked GC/SWCNT. In 0.1M PBS, pH 7.0. Inset: Plot of current vs. concentration of sulphite for (iii).

5.3. FePc for electrocatalysis of hydrazine

As the newest approach used in this work, both the GCE and GC/SWCNT surfaces with axially ligated FePc were tested for their capability for electrocatalytic detection of hydrazine. Hydrazine was chosen as a test analyte as its behaviour is well known and the electrocatalysis of hydrazine by phthalocyanines is understood and has been studied in many cases [22,75,196,197,237,245,246]. This electrocatalysis was also used to confirm attachment of the FePc on these surfaces, because the unmodified GCE and GC/SWCNT did not detect hydrazine in the potential window used, Fig. 5.4(i). However, an electrocatalytic response was found after axial ligation with FePc on both the GCE and the GC/SWCNT, Fig. 5.4(a)(iv) and Fig. 5.4(b)(ii) respectively. A clear oxidation process was visible at -0.2 V, on both the anodic and cathodic scans. The electrocatalytic oxidation of hydrazine at or near this potential (-0.2 V) has been shown with CoPc [66,94,247], as well as FePc [245,248,249]. The electro-oxidation on both scans has been attributed in a similar study to the regeneration or reformation of the active catalyst that oxidises hydrazine [250] – the Fe(II)Pc species in this case. It has also been observed with substituted FePc sensors [248]. A number of studies confirming the relationship between the potential of the metal process and the potential of hydrazine electrocatalysis have been done, proving the involvement of the Fe(II)/Fe(I) couple of the FePc [75,196,197,245,248,249].

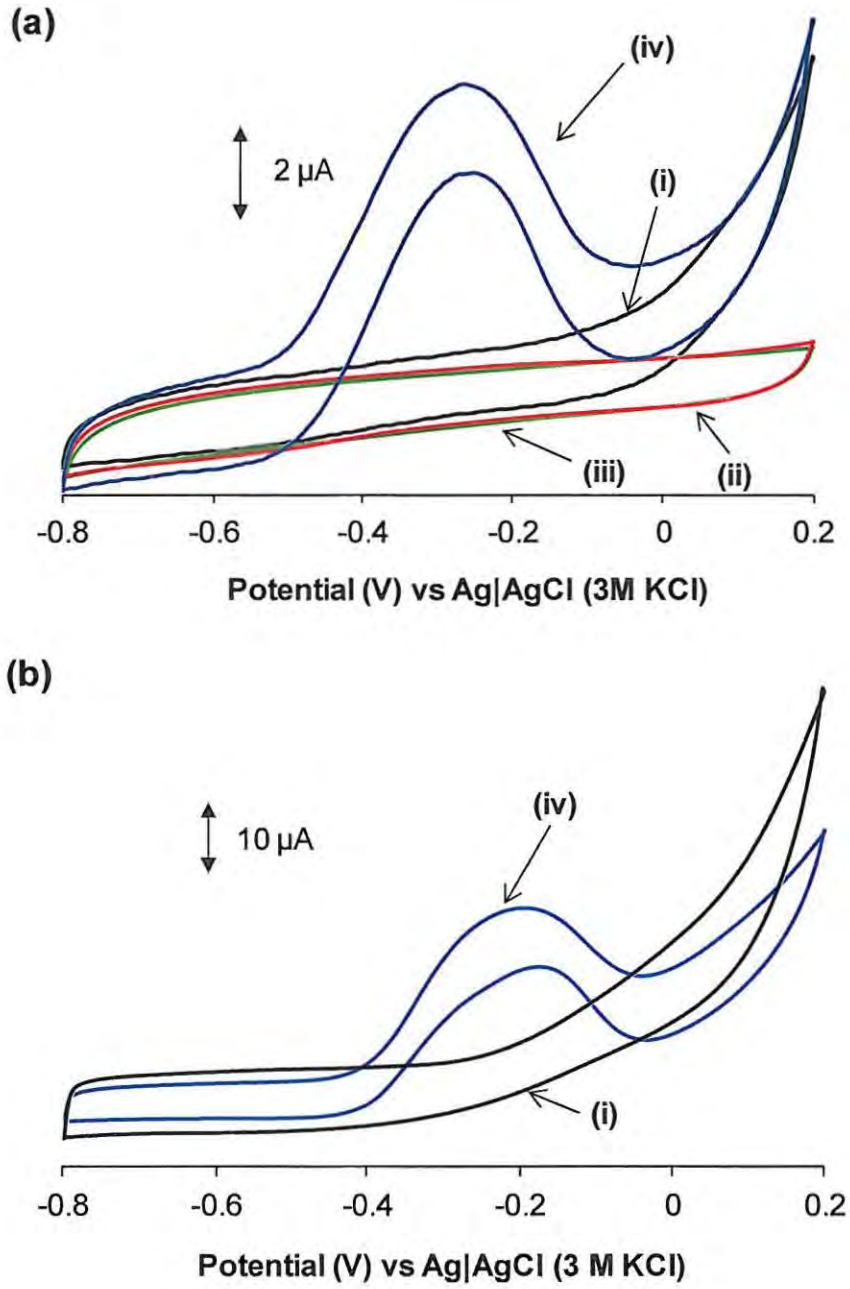

Figure 5.4. Cyclic voltammograms of (a) GCE and (b) GC/SWCNT (i) bare, after (ii) **2b**-grafting, (iii) **2b**-grafting and click chemistry in 4-ethynylpyridine, and (iv) **2b**-grafting, click chemistry and 3 h in 1mM FePc in DMF. In 5mM hydrazine sulphate in 0.1 M NaOH at 50 mV/s vs Ag|AgCl (3 M KCl).

Zagal and co-workers [75,196,197] have suggested the following mechanism for the oxidation of hydrazine on MPc modified electrodes (equations 5.1–5.3):

$$[Fe(I)Pc]^- \rightarrow Fe(II)Pc + e^- \qquad 5.1$$

$$Fe(II)Pc + N_2H_4 \rightarrow [Fe(I)Pc]^-(N_2H_4)^+] \qquad 5.2 \text{ (RDS)}$$

$$[Fe(I)Pc]^-(N_2H_4)^+ + OH^- \rightarrow Fe(II)Pc + N_2H_3^{\bullet} + H_2O + e^- \qquad 5.3$$

where RDS is the rate determining step. This mechanism is thought to occur in this work, and the rest of the equations are as listed in literature [75,196,197]. The involvement of the Fe(II)/Fe(I) couple was proved in this work by the observation of the Fe(II)/Fe(I) couple in the SWV for the GCE in Fig. 4.25(a). The Fe(II)/Fe(I) couple for the GC/SWCNT in 0.1 M NaOH was difficult to resolve due to the presence of the SWCNT peaks (data not shown). However, Fig. 4.25(b) showed the presence of this couple in the SWV in pH 7 buffer, and this couple would be shifted to more negative potentials in highly basic media. The potential for the oxidation of hydrazine is in the potential range of the Fe(II)/Fe(I) couple, hence this couple was involved in the catalysis.

Figs. 5.5 and 5.6 show the results of the scan rate studies in hydrazine.

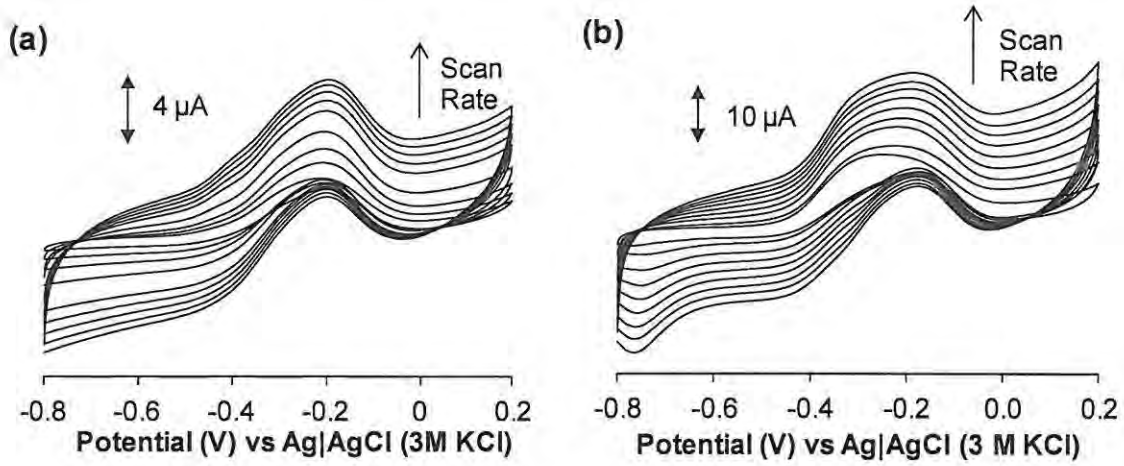

Figure 5.5. Scan rate studies of **2b**-grafted (a) GCE and (b) GC/SWCNT after click chemistry in 4-ethynylpyridine and 3 h in 1mM FePc in DMF. (a) In 5mM hydrazine sulphate in 0.1 M NaOH at 10, 25, 50, 100, 200, 250, 300, 350 and 400 mV/s. (b) In 1mM hydrazine sulphate in 0.1 M NaOH at 25, 50, 100, 150, 200, 250, 300, 350 and 400 mV/s.

Fig. 5.6 shows, very interestingly, that the hydrazine detection reached a limit at higher scan rates with a plateau from about 0.1 V/s for the GCE. This could most likely be due to the slow electron transfer from the surface of the electrode through the layers, limiting oxidation at high scan rates to those hydrazine species that are in direct contact with the FePc catalyst. This was shown by the EIS R_{CT} value for the GCE surface which, while improved compared to the grafted and clicked surfaces, was still greater than the bare electrode. The GC/SWCNT did not appear to reach an absolute limit, however the behaviour was very similar to that seen with the GCE. The RDS involved the formation

of a coordination complex between the catalyst and the analyte, and so the amount of FePc on the surface could also be a limiting factor.

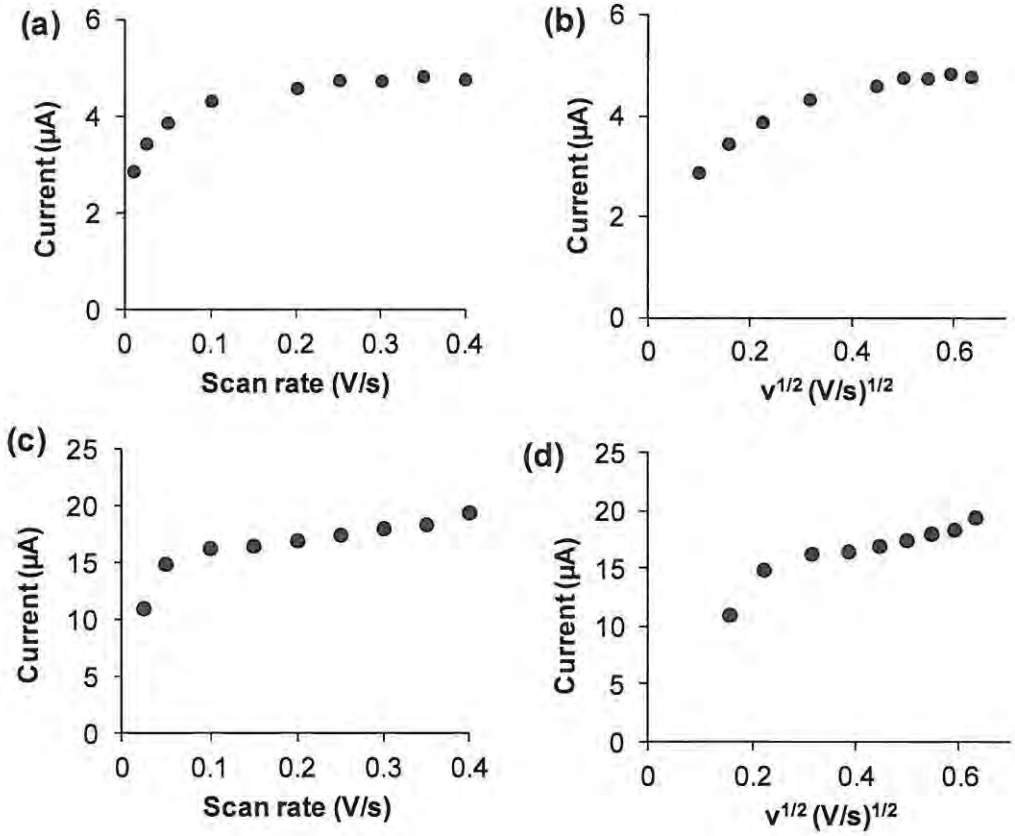

Figure 5.6. Plots of (a) current vs scan rate and (b) current vs the square root of the scan rate, from the scan rate studies of the GCE after grafting, click chemistry and immersion in FePc, in 5 mM hydrazine sulphate in 0.1 M NaOH. (c) current vs scan rate and (d) current vs the square root of the scan rate, from the GC/SWCNT after grafting, click chemistry and immersion in FePc, in 1 mM hydrazine sulphate in 0.1 M NaOH.

Fig. 5.7 shows the amperometric response of the modified electrodes at -0.2 V to successive additions of hydrazine sulphate to a stirred solution of 0.1 M NaOH. For the

GCE, the electrode showed good linearity over the range 1.0×10^{-5} to 3.4×10^{-4} M (R^2 = 0.9998). The sensitivity was 0.814 μA/mM, with a LoD of 10.0 ± 1.3 μM (based on a signal-to-noise ratio of 3). Although not as sensitive as some other sensors for hydrazine, such as that seen for a GCE modified with a Co-gluconate complex (LoD = 0.5 μM) [250] and a gold electrode bearing a SAM of mercaptopyridine and axially attached FePc (OSWV LoD = 5 μM) [188], the modified GCE showed good stability over successive additions of hydrazine and good reproducibility. The grafted electrode without pyridine was also left in FePc for 3 h, and tested by amperometry for detection of hydrazine. Interestingly, there did seem to be some interaction between the FePc and the grafted species, and some detection of hydrazine, however the response had poor stability and showed possible desorption of the FePc with time (data not shown).

The GC/SWCNT electrode response was linear over 1.0×10^{-5} to 1.0×10^{-4} M (R^2 = 0.9945), with an average sensitivity of 15.61 μA/mM and a LoD of 1.10 ± 0.06 μM (signal-to-noise ratio of 3). The electrode appeared to be stable during the chronoamperometry experiments, although the stability towards the detection of 1 mM hydrazine decreased by 10 % after one day (data not shown). The reproducibility was also good, with limited variation of the LoD over a number of electrodes.

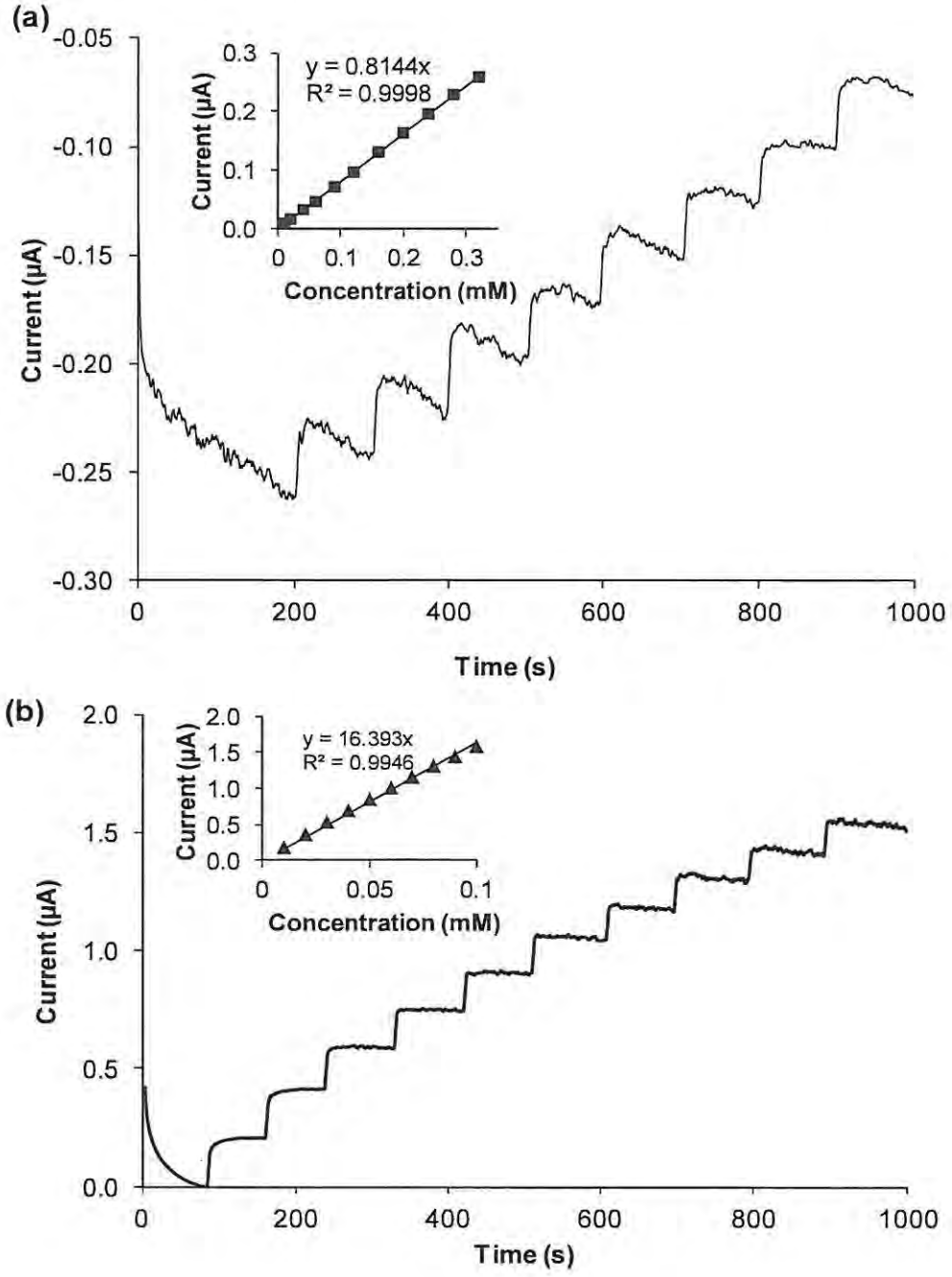

Figure 5.7. Amperometric response of the modified electrodes at -0.2 V during successive additions of (a) 0.04 mM hydrazine sulphate into continuously stirred 0.1 M NaOH for the GCE, and (b) 0.01 mM hydrazine for the GC/SWCNT. Insets: plots of peak current versus concentration of hydrazine.

Most interesting is the improvement of detection of hydrazine afforded by the SWCNTs, compared to the same surface without SWCNTs which has an LoD of 10.0 ± 1.3 μM. This ten times improvement of the detection of this test analyte must be compared to the study of a GC/SWCNT surface with clicked ferrocene, which showed that there were 1.6 times the amount of ferrocene on the surface with SWCNTs, compared to the bare electrode. This could be calculated due to the strong electrochemical activity of ferrocene, and if the same, or similar, increase in the amount of attached FePc occurred for this electrode compared to that without SWCNTs, then it follows that we could expect a 1.6 times improvement in the electrocatalysis. Thus, this ten-times improvement could not be due to the contribution of the FePc alone, but also to the good electron transfer kinetics of the SWCNTs as well which could increase the rate of reaction, and consequently the sensitivity of this electrode.

CONCLUSIONS

This work illustrated the use of a variety of techniques for surface modification purposes, in the attachment of electrocatalysts to gold and carbon substrates.

The octakis(pentylthio)-, (decylthio)-, (benzylthio)- and (phenylthio)phthalocyaninato manganese(III) acetate complexes (**1a–d**) were synthesised, and showed solvent-dependent conversion to the μ-oxo dimer, as well as a solvent-dependent shift in the Q band. The different substituents did not greatly affect the UV-vis spectra of the compounds, but did appear to have an effect on their electrochemical properties. Three main redox processes for the complexes were identified as $Mn^{III}Pc^{2-}/Mn^{II}Pc^{2-}$ (II), $Mn^{II}Pc^{2-}/Mn^{II}Pc^{3-}$ (III) and $Mn^{III}Pc^{1-}/Mn^{III}Pc^{2-}$ (I) and confirmed using spectroelectrochemistry. Self-assembled monolayers (SAMs) of these MnPcs were formed on gold, and showed good surface coverage in all cases. All of the MnPc-SAMs except **1c** showed good blocking characteristics for gold oxidation, copper underpotential deposition and the redox chemistry of $Fe(NH_4)_2(SO_4)_2$, and even some blocking for $K_3[Fe(CN)_6]$, with **1a** and **1b** being the most effective. Raman, XPS, AFM and SEM also confirmed SAM formation and good surface coverage, although the latter two did indicate that there was some aggregation of the Pcs. The specific behaviour of the SAM seemed again to be dependent on the nature of the substituents. The SAMs of MnPcs **1b** and **1d** showed a large proportion of unbound sulphur groups, as well as evidence of the formation of a gold-sulphur bond. The aryl substituent appeared to have a higher ratio of bound sulphur groups compared to the alkyl substituent, indicating that the alkyl chains inhibited SAM formation as confirmed by the poorer surface coverage of this MnPc. XPS also showed evidence of the retention of the R groups. Following characterisation, the **1d**-SAM was

used as a sensor for thiocyanate, and showed a two-fold improvement in the limit of detection compared to the bare electrode (1.46 *vs* 2.91 μM), as well as an increase in the sensitivity of the modified electrode.

This work also demonstrated the versatility of 4-azidoaniline (**2a**) as a precursor for the modification of many different conductive surfaces, taking notable advantages of its ability to be further modified through the Sharpless click chemistry reaction. Grafting of the diazonium derivative **2b** on to bare GCE, SWCNTs adsorbed on a GCE (GC/SWCNT), and on MWCNT-paper was achieved. Electropolymerisation of **2a** on to a GCE was also investigated here for the first time. Ferrocene was covalently linked to these electrodes using click chemistry, and the surface coverage (Γ) for ferrocene in each case could be determined using electrochemistry, due to the highly electroactive nature of this complex. Using this approach of introducing an azide group to the surface of the electrode through grafting or electropolymerisation followed by the click chemistry reaction was very successful for the grafted electrodes. The surface coverage of ferrocene on the synthesised **2b**-grafted GCE was equivalent to a tightly-packed monolayer on the surface, at $\Gamma = 4.7 \pm 0.2 \times 10^{-10}$ mol.cm^{-2}, with very little difference found in the coverage when *in situ* diazotation of **2a** and grafting of the resulting **2b** was used in the place of the synthesised diazonium salt ($\Gamma = 4.9 \pm 0.3 \times 10^{-10}$ mol.cm^{-2}). The amount of ferrocene on the electrode surface could be improved by 1.6 times by the addition of SWCNTs, at $7.7 \pm 0.9 \times 10^{-10}$ mol.cm^{-2} for the GC/SWCNT. Grafting and click chemistry of ferrocene on to highly resistive MWCNT-paper was also shown to be a possibility, with an approximate ferrocene coverage of 1.86 μmol.g^{-1}. XPS proved to be a useful technique in monitoring

the success of the click reaction, and the stability of the attached ferrocene to sonication. Although the drop-dry method of attaching the SWCNTs to the electrode was not the most efficient, the potential of directly electrografting diazonium salts on to the nanotubes has implications in the attachment of other appropriate molecules to electrodes containing nanomaterials, for the construction of efficient electrode materials. SECM was used to give both one-dimensional and two-dimensional figures of the conductivity of the MWCNT surface, as well as a three-dimensional figure of the orientation of the SWCNTs on the GCE surface. The potential for application of these methods on more conductive MWCNT-paper electrodes was thus shown, as well as a possibility for the modification of highly flexible paper electrodes, or in the production of "smart" textiles. Ferrocene was used as a test molecule for the click chemistry reaction, while the attachment of more specific complexes with fluorescent, electrocatalytic or biological applications could be easily done through the Sharpless click reaction.

The **2b**-grafted and ferrocene-clicked GC/SWCNT electrode was successfully employed to detect sulphite, showing the application of ferrocene as more than a test analyte, but an electrocatalyst as well.

The use of an approach involving the click chemistry reaction first, before surface modification (click-then-graft or click-then-polymerise), was also investigated using the donated complex 4-(4-ferrocenyl-1H-1,2,3-triazol-1-yl)aniline (**2c**). The surface coverage of ferrocene for the electropolymerised complex **2c** was the greatest of all the modification approaches, and was equivalent to ≈4 layers at $\Gamma = 17.7 \pm 2.8 \times 10^{-10}$ mol.cm^{-2}.

In situ diazotation of **2c** and grafting of the resulting complex **2d** was also achieved, although with a lower surface coverage of $0.7 \pm 0.2 \times 10^{-10}$ mol.cm^{-2}, indicating that this route is not optimal if maximal attachment is desired. This work showed the potential for click chemistry to be used in the synthesis of a family of compounds that are able to be electropolymerised or electrografted due to the presence of the aniline group, as well as the benefit of the click-then-polymerise approach versus the click-then-graft approach in retention of the electroactive species.

Axial ligation of FePc to pyridine which has been covalently attached to the GCE or GC/SWCNT surface through **2b**-grafting and click chemistry with 4-ethynylpyridine was another new, potentially useful method for electrode construction. The GCE was studied using electrochemistry, EIS, and XPS to confirm the modification steps, while the GC/SWCNT was analysed using SECM in place of EIS in order to get a better understanding of the electrochemical topography of this non-homogeneous surface. The electrodes were used as a sensor for hydrazine, and showed electrocatalytic oxidation of this analyte with a linear range over 1.0×10^{-5} to 3.4×10^{-4} M and a LoD of 10.0 ± 1.3 μM for the GCE, and a LoD of 1.10 ± 0.06 μM for the GC/SWCNT. These results showed a ten times improvement for the surface with nanotubes, exhibiting again the improved abilities that nanomaterials contribute to electrode construction.

Finally, this work shows for the first time the local micro-electrochemical grafting of a gold substrate by **2b** by SECM in a simple single-step procedure. The dimensions of the derivatised area were finely tuned by controlling different experimental conditions, such

as distance between the probe and the substrate, the size of the UME probe and the presence or absence of the electrolyte. The use of the azido-derivated diazonium molecule **2b** opens the gate to important applications and developments devoted to the micro-local functionalisation of electrodes and the implementation of the emerging interfacial click reaction.

REFERENCES

[1] J.H. Page, G. Wilkinson, J. Am. Chem. Soc. 74 (1952) 6149–6150.

[2] T. Kuwana, D.E. Bublitz, G. Hoh, J. Am. Chem. Soc. 82 (1960) 5811–5817.

[3] S.P. Gubin, S.A. Smirnova, L.I. Denisovich, A.A. Lubovich, J. Organomet. Chem. 30 (1971) 243–255.

[4] J.-C. Moutet, E. Saint-Aman, M. Ungureanu, T. Visan, J. Electroanal. Chem. 410 (1996) 79–85.

[5] H. Zhou, W. Yang, C. Sun, Talanta 77 (2008) 366–371.

[6] J.R. Lenhard, R.W. Murray, J. Am. Chem. Soc. 100 (1978) 7870–7875.

[7] C.E.D. Chidsey, C.R. Bertozzi, T.M. Putvinski, A.M. Mujsce, J. Am. Chem. Soc. 112 (1990) 4301–4306.

[8] E.W. Wollman, D. Kang, C.D. Frisbie, I.M. Lorkovic, M.S. Wrighton, J. Am. Chem. Soc. 116 (1994) 4395–4404.

[9] L.M. Goldenberg, M.R. Bryce, M.C. Petty, J. Mater. Chem. 9 (1999) 1957–1974.

[10] T.W. Lewis, G.G. Wallace, M.R. Smyth, Analyst 124 (1999) 213–219.

[11] J. Li, H.T. Ng, A. Cassell, W. Fan, H. Chen, Q. Ye, J. Koehne, J. Han, M. Meyyappan, Nano Lett. 3 (2003) 597–602.

[12] J.P. Collman, N.K. Devaraj, C.E.D. Chidsey, Langmuir 20 (2004) 1051–1053.

[13] A. Devadoss, C.E.D. Chidsey, J. Am. Chem. Soc. 129 (2007) 5370–5371.

[14] D. Evrard, F. Lambert, C. Policar, V. Balland, B. Limoges, Chem.-Eur. J. 14 (2008) 9286–9291.

[15] H.-B. Bu, G. Götz, E. Reinold, A. Vogt, S. Schmid, R. Blanco, J.L. Segura, P. Bäuerle, Chem. Comm. (2008) 1320–1322.

[16] S. Dong, B. Wang, B. Liu, Biosens. Bioelectron. 7 (1991) 215–222.

[17] J. Razumiene, A. Vilkanauskyte, V. Gureviciene, V. Laurinavicius, N. V Roznyatovskaya, Y. V Ageeva, M.D. Reshetova, A.D. Ryabov, J. Organomet. Chem. 668 (2003) 83–90.

[18] A. Chaubey, B.D. Malhotra, Biosens. Bioelectron. 17 (2002) 441–456.

[19] K. Wu, J. Fei, S. Hu, Anal. Biochem. 318 (2003) 100–106.

[20] G.A. Rivas, M.D. Rubianes, M.C. Rodríguez, N.F. Ferreyra, G.L. Luque, M.L. Pedano, S.A. Miscoria, C. Parrado, Talanta 74 (2007) 291–307.

[21] J. Zagal, S. Griveau, K.I. Ozoemena, T. Nyokong, F. Bedioui, J. Nanosci. Nanotech. 9 (2009) 2201–2214.

[22] T. Nyokong, in:, J.H. Zagal, F. Bedioui, J.-P. Dodelet (Eds.), N4-macrocyclic Metal Complexes, Springer, USA, 2006, pp. 315–362.

[23] E. Ben-Hur, W.S. Chan, in:, K.M. Kadish, K.M. Smith, R. Guilard (Eds.), The Porphyrin Handbook: Applications of Phthalocyanines, Volume 19, Academic Press, New York, 2003, pp. 1–36.

[24] D. Dini, M. Hanack, in:, K.M. Kadish, R. Guilard, K.M. Smith (Eds.), The Porphyrin Handbook: Phthalocyanines: Properties and Materials, Volume 17, Academic Press, New York, 2003, pp. 1–36.

[25] M. Gouterman, J. Mol. Spectrosc. 6 (1961) 138–163.

[26] M.J. Stillman, T. Nyokong, in:, C.C. Leznoff, A.B.P. Lever (Eds.), Phthalocyanines: Properties and Applications, Vol. 1, VCH, New York, 1989.

[27] F. Matemadombo, S. Griveau, F. Bedioui, T. Nyokong, Electroanal. 20 (2008) 1863–1872.

[28] O. Dolotova, N. Bundina, O. Kaliya, E. Lukyanets, J. Porphyr. Phthalocya. 1 (1997) 355–366.

[29] I.A. Akinbulu, T. Nyokong, Polyhedron 28 (2009) 2831–2838.

[30] N. Sehlotho, M. Durmuş, V. Ahsen, T. Nyokong, Inorg. Chem. Commun. 11 (2008) 479–483.

[31] B. Agboola, K.I. Ozoemena, P. Westbroek, T. Nyokong, Electrochim. Acta 52 (2007) 2520–2526.

[32] T.R.E. Simpson, D.A. Russell, I. Chambrier, M.J. Cook, A.B. Horn, S.C. Thorpe, Sensor. Actuat. B-Chem. 29 (1995) 353–357.

[33] M.J. Cook, Pure Appl. Chem. 71 (1999) 2145–2151.

[34] D.J. Revell, I. Chambrier, M.J. Cook, D.A. Russell, J. Mater. Chem. 10 (2000) 31–37.

[35] Z. Li, M. Lieberman, W. Hill, Langmuir 17 (2001) 4887–4894.

[36] A. de Haan, A. Decroly, Sensor. Actuat. B-Chem. 30 (1996) 143–150.

[37] N. Papageorgiou, E. Salomon, T. Angot, J. Layet, L. Giovanelli, G. Lay, Prog. Surf. Sci. 77 (2004) 139–170.

[38] P. Tau, T. Nyokong, J. Electroanal. Chem. 611 (2007) 10–18.

[39] M. Sánchez-Vergara, I. Islas-Bernal, M. Rivera, A. Ortíz-Rebollo, J. Alvarez-Bada, Thin Solid Films 515 (2007) 5374–5380.

[40] S. Vilakazi, T. Nyokong, Polyhedron 17 (1998) 4415–4423.

[41] D. Geraldo, C. Linares, Y. Chen, S. Ureta-Zanartu, J. Zagal, Electrochem. Commun. 4 (2002) 182–187.

[42] J. Obirai, T. Nyokong, Electrochim. Acta 50 (2005) 5427–5434.

[43] K.I. Ozoemena, T. Nyokong, J. Electroanal. Chem. 579 (2005) 283–289.

[44] F. Matemadombo, P. Westbroek, T. Nyokong, Electrochim. Acta 53 (2007) 480–486.

[45] K. Kasuga, M. Tsutsui, Coord. Chem. Rev. 32 (1980) 67–95.

[46] V.N. Nemykin, E. Lukyanets, in:, K. Kadish, K.M. Smith, R. Guilard (Eds.), Handbook of Porphyrin Science: Synthetic Methodology, Volume 3, World Scientific, Toh Tuck Link, Singapore, 2010, pp. 1–324.

[47] P. Mashazi, E. Antunes, T. Nyokong, J. Porphyr. Phthalocya. 14 (2010) 932–947.

[48] M.J. Stillman, in:, C.C. Leznoff, A.B.P. Lever (Eds.), Phthalocyanines: Properties and Applications, Vol. 3, VCH, New York, 1993.

[49] J. Wang, Analytical Electrochemistry, 2nd ed., Wiley-VCH, New York, 2000.

[50] C.M.A. Brett, A.M.O. Brett, Electrochemistry: Principles, Methods, and Applications, Oxford University Press, Oxford, 1993.

[51] A.J. Bard, L.R. Faulkner, Electrochemical Methods: Fundamentals and Applications, 2nd ed., Wiley, New York, 2001.

[52] G. Mbambisa, P. Tau, E. Antunes, T. Nyokong, Polyhedron 26 (2007) 5355–5364.

[53] J. Liu, A. Rinzler, H. Dai, J. Hafner, R. Bradley, P. Boul, A. Lu, T. Iverson, K. Shelimov, C. Huffman, F. Rodriguez-Macias, Y. Shon, T. Lee, D. Colbert, R. Smalley, Science 280 (1998) 1253–1256.

[54] P.M. Ajayan, Chem. Rev. 99 (1999) 1787–1800.

[55] L. Radushkevich, V. Lukyanovich, Zh. Phys. Khim. 26 (1952) 88–95.

[56] A. Oberlin, M. Endo, T. Koyama, J. Cryst. Growth 32 (1976) 335–349.

[57] S. Iijima, Nature 354 (1991) 56–58.

[58] S. Iijima, T. Ichihashi, Nature 363 (1993) 603–605.

[59] D.S. Bethune, C.H. Klang, M.S. de Vries, G. Gorman, R. Savoy, J. Vazquez, R. Beyers, Nature 363 (1993) 605–607.

[60] T.W. Odom, J.-L. Huang, P. Kim, C.M. Lieber, J. Phys. Chem. B 104 (2000) 2794–2809.

[61] S. Niyogi, M.A. Hamon, H. Hu, B. Zhao, P. Bhowmik, R. Sen, M.E. Itkis, R.C. Haddon, Acc. Chem. Res. 35 (2002) 1105–1113.

[62] S. Fan, M. Chapline, N. Franklin, T. Tombler, A. Cassell, H. Dai, Science 283 (1999) 512–514.

[63] D. Li, L. Dai, S. Huang, A. Mau, Z. Wang, Chem. Phys. Lett. 316 (2000) 349–355.

[64] B.E.K. Swamy, B.J. Venton, Analyst 132 (2007) 876–884.

[65] J. Silva, S. Griveau, C. Richard, J. Zagal, F. Bedioui, Electrochem. Commun. 9 (2007) 1629–1634.

[66] D. Geraldo, C. Togo, J. Limson, T. Nyokong, Electrochim. Acta 53 (2008) 8051–8057.

[67] M. Siswana, K.I. Ozoemena, T. Nyokong, Electrochim. Acta 52 (2006) 114–122.

[68] K.I. Ozoemena, T. Nyokong, D. Nkosi, I. Chambrier, M.J. Cook, Electrochim. Acta 52 (2007) 4132–4143.

[69] A. Merkoci, M. Pumera, X. Llopis, B. Perez, M. del Valle, S. Alegret, Trend. Anal. Chem. 24 (2005) 826–838.

[70] R.G. Nuzzo, D.L. Allara, J. Am. Chem. Soc. 105 (1983) 4481–4483.

[71] J.K. Lee, Y.S. Chi, I.S. Choi, Langmuir 20 (2004) 3844–3847.

[72] K.I. Ozoemena, P. Westbroek, T. Nyokong, Electrochem. Commun. 3 (2001) 529–534.

[73] J.P. Collman, N.K. Devaraj, T.P.A. Eberspacher, C.E.D. Chidsey, Langmuir 22 (2006) 2457–2464.

[74] P. Mashazi, P. Westbroek, K.I. Ozoemena, T. Nyokong, Electrochim. Acta 53 (2007) 1858–1869.

[75] J. Zagal, E. Muñoz, S. Ureta-Zañartu, Electrochim. Acta 27 (1982) 1373–1377.

[76] G. Engelsma, A. Yamamoto, E. Markham, M. Calvin, J. Phys. Chem. 2217 (1962).

[77] F. Matemadombo, M. Durmuş, V. Escriou, S. Griveau, D. Scherman, F. Bedioui, T. Nyokong, Curr. Anal. Chem. 5 (2009) 330–338.

[78] B. Agboola, T. Nyokong, Anal. Chim. Acta 587 (2007) 116–123.

[79] B. Agboola, T. Nyokong, Talanta 72 (2007) 691–698.

[80] F. Matemadombo, M. Durmuş, C. Togo, J. Limson, T. Nyokong, Electrochim. Acta 54 (2009) 5557–5565.

[81] G. Mbambisa, N. Nombona, T. Nyokong, Microchem. J. 93 (2009) 60–66.

[82] I.A. Akinbulu, K.I. Ozoemena, T. Nyokong, J. Solid State Electr. 15 (2010) 2239–2251.

[83] I.A. Akinbulu, S. Khene, T. Nyokong, Electrochim. Acta 55 (2010) 7085–7093.

[84] I. Booysen, F. Matemadombo, M. Durmuş, T. Nyokong, Dyes Pigments 89 (2011) 111–119.

[85] U. Siemeling, C. Schirrmacher, U. Glebe, C. Bruhn, J.E. Baio, L. Arnadóttir, D.G. Castner, T. Weidner, Inorg. Chim. Acta 374 (2011) 302–312.

[86] M. Delamar, R. Hitmi, J. Pinson, J.-M. Savéant, J. Am. Chem. Soc. 114 (1992) 5883–5884.

[87] P. Allongue, M. Delamar, B. Desbat, O. Fagebaume, R. Hitmi, J. Pinson, J.-M. Savéant, J. Am. Chem. Soc. 119 (1997) 201–207.

[88] C. Saby, B. Ortiz, G.Y. Champagne, D. Bélanger, Langmuir 13 (1997) 6805–6813.

[89] J.L. Bahr, J. Yang, D. V Kosynkin, M.J. Bronikowski, R. Smalley, J.M. Tour, J. Am. Chem. Soc. 123 (2001) 6536–6542.

[90] M.P. Stewart, F. Maya, D. V Kosynkin, S.M. Dirk, J.J. Stapleton, C.L. McGuiness, D.L. Allara, J.M. Tour, J. Am. Chem. Soc. 126 (2004) 370–378.

[91] M.G. Paulik, P.A. Brooksby, A.D. Abell, A. Downard, J. Phys. Chem. C 111 (2007) 7808–7815.

[92] D. Bélanger, J. Pinson, Chem. Soc. Rev. 40 (2011) 3995–4048.

[93] P. Doppelt, G. Hallais, J. Pinson, F. Podvorica, S. Verneyre, Chem. Mater. 19 (2007) 4570–4575.

[94] A. Adenier, N. Barre, E. Cabet-Deliry, A. Chaussé, S. Griveau, F. Mercier, J. Pinson, C. Vautrinul, Surf. Sci. 600 (2006) 4801–4812.

[95] S. Griveau, D. Mercier, C. Vautrinul, A. Chaussé, Electrochem. Commun. 9 (2007) 2768–2773.

[96] S. Baranton, D. Bélanger, Electrochim. Acta 53 (2008) 6961–6967.

[97] F. Le Floch, J.-P. Simonato, G. Bidan, Electrochim. Acta 54 (2009) 3078–3085.

[98] L. Fan, J. Chen, S. Zhu, M. Wang, G. Xu, Electrochem. Commun. 11 (2009) 1823–1825.

[99] J.K. Kariuki, M.T. McDermott, Langmuir 17 (2001) 5947–5951.

[100] P. Mashazi, T. Nyokong, Microchim. Acta 171 (2010) 321–332.

[101] Y.R. Leroux, H. Fei, J.-M. Noël, C. Roux, P. Hapiot, J. Am. Chem. Soc. 132 (2010) 14039–14041.

[102] S. Mahouche, N. Mekni, L. Abbassi, P. Lang, C. Perruchot, M. Jouini, F. Mammeri, M. Turmine, H. Ben Romdhane, M.M. Chehimi, Surf. Sci. 603 (2009) 3205–3211.

[103] S. Campidelli, B. Ballesteros, A. Filoramo, D.D. Díaz, G. de la Torre, T. Torres, G.M.A. Rahman, C. Ehli, D. Kiessling, F. Werner, V. Sgobba, D.M. Guldi, C. Cioffi, M. Prato, J.-P. Bourgoin, J. Am. Chem. Soc. 130 (2008) 11503–11509.

[104] T. Palacin, H. Le Khanh, B. Jousselme, P. Jegou, A. Filoramo, C. Ehli, D.M. Guldi, S. Campidelli, J. Am. Chem. Soc. 131 (2009) 15394–15402.

[105] G. Tuci, C. Vinattieri, L. Luconi, M. Ceppatelli, S. Cicchi, A. Brandi, J. Filippi, M. Melucci, G. Giambastiani, Chemistry 18 (2012) 8454–8463.

[106] H. Li, F. Cheng, A.M. Duft, A. Adronov, J. Am. Chem. Soc. 127 (2005) 14518–14524.

[107] J.L. Bahr, J.M. Tour, Chem. Mater. 13 (2001) 3823–3824.

[108] J.L. Bahr, J.M. Tour, J. Mater. Chem. 12 (2002) 1952–1958.

[109] C.A. Dyke, J.M. Tour, J. Am. Chem. Soc. 125 (2003) 1156–1157.

[110] C.A. Dyke, J.M. Tour, J. Phys. Chem. A 108 (2004) 11151–11159.

[111] M.E. Lipińska, S.L.H. Rebelo, M.F.R. Pereira, J.A.N.F. Gomes, C. Freire, J.L. Figueiredo, Carbon 50 (2012) 3280–3294.

[112] W. van Der Linden, J. Dieker, Anal. Chim. Acta 119 (1980) 1–24.

[113] J. Lennox, R.W. Murray, J. Electroanal. Chem. 78 (1977) 395–401.

[114] J. Lennox, R.W. Murray, J. Am. Chem. Soc. 100 (1978) 3710–3714.

[115] B. Jousselme, G. Bidan, M. Billon, C. Goyer, Y. Kervella, S. Guillerez, E.A. Hamad, C. Goze-Bac, J.-Y. Mevellec, S. Lefrant, J. Electroanal. Chem. 621 (2008) 277–285.

[116] A.J. Gross, C. Bucher, L. Coche-Guerente, P. Labbé, A. Downard, J.-C. Moutet, Electrochem. Commun. 13 (2011) 1236–1239.

[117] D.J. Garrett, P. Jenkins, M.I.J. Polson, D. Leech, K.H.R. Baronian, A. Downard, Electrochim. Acta 56 (2011) 2213–2220.

[118] C. Combellas, M. Delamar, F. Kanoufi, J. Pinson, F.I. Podvorica, Chem. Mater. 17 (2005) 3968–3975.

[119] F. Barrière, A. Downard, J. Solid State Electr. 12 (2008) 1231–1244.

[120] M. Toupin, D. Bélanger, Langmuir 24 (2008) 1910–1917.

[121] B.L. Hurley, R.L. McCreery, J. Electrochem. Soc. 151 (2004) B252–B259.

[122] S. Griveau, S. Aroua, D. Bediwy, R. Cornut, C. Lefrou, F. Bedioui, J. Electroanal. Chem. 647 (2010) 93–96.

[123] A. Adenier, E. Cabet-Deliry, A. Chaussé, S. Griveau, F. Mercier, J. Pinson, C. Vautrin-Ul, Chem. Mater. 17 (2005) 491–501.

[124] C. Cougnon, F. Gohier, D. Bélanger, J. Mauzeroll, Angew. Chem. Int. Ed. 48 (2009) 4006–4008.

[125] T. Matrab, C. Combellas, F. Kanoufi, Electrochem. Commun. 10 (2008) 1230–1234.

[126] J. Bacon, R.N. Adams, J. Am. Chem. Soc. 90 (1968) 6596–6599.

[127] L.H. Dao, M. Leclerc, J. Guay, J.W. Chevalier, Synthetic Met. 29 (1989) 377–382.

[128] A. Thyssen, A. Hochfeld, R. Kessel, A. Meyer, W. Schultze, Synthetic Met. 29 (1989) 357–362.

[129] A.A. Jbarah, R. Holze, J. Solid State Electr. 10 (2005) 360–372.

[130] S. Bhadra, D. Khastgir, N.K. Singha, J.H. Lee, Prog. Polym. Sci. 34 (2009) 783–810.

[131] Y. Oztekin, M. Tok, H. Nalvuran, S. Kiyak, T. Gover, Z. Yazicigil, A. Ramanaviciene, A. Ramanavicius, Electrochim. Acta 56 (2010) 387–395.

[132] E.M. Genies, C. Tsintavis, J. Electroanal. Chem. 195 (1985) 109–128.

[133] H.C. Kolb, M.G. Finn, K.B. Sharpless, Angew. Chem. Int. Ed. 40 (2001) 2004–2021.

[134] V. V Rostovtsev, L.G. Green, V. V Fokin, K.B. Sharpless, Angew. Chem. Int. Ed. 41 (2002) 2596–2599.

[135] J.-F. Lutz, Z. Zarafshani, Adv. Drug Deliv. Rev. 60 (2008) 958–970.

[136] H.A. Orgueira, D. Fokas, Y. Isome, P.C.-M. Chan, C.M. Baldino, Tetrahed. Lett. 46 (2005) 2911–2914.

[137] S. Hotha, R.I. Anegundi, A.A. Natu, Tetrahed. Lett. 46 (2005) 4585–4588.

[138] J.M. Casas-Solvas, A. Vargas-Berenguel, L.F. Capitán-Vallvey, F. Santoyo-González, Org. Lett. 6 (2004) 3687–3690.

[139] B.K. Yoo, S.-W. Joo, J. Colloid Interf. Sci. 311 (2007) 491–496.

[140] T. Lummerstorfer, H. Hoffmann, J. Phys. Chem. B 108 (2004) 3963–3966.

[141] N.K. Devaraj, G.P. Miller, W. Ebina, B. Kakaradov, J.P. Collman, E.T. Kool, C.E.D. Chidsey, J. Am. Chem. Soc. 127 (2005) 8600–8601.

[142] Y. Li, W. Zhang, J. Chang, J. Chen, G. Li, Y. Ju, Macromol. Chem. Phys. 209 (2008) 322–329.

[143] A.E. Daugaard, S. Hvilsted, T.S. Hansen, N.B. Larsen, Macromol. 41 (2008) 4321–4327.

[144] K. Hackethal, F. Herbst, W.H. Binder, J. Polym. Sci. Pol. Chem. 50 (2012) 4494–4506.

[145] L. Li, N. Zhao, S. Liu, Polymer 53 (2012) 67–78.

[146] A.M. Eissa, E. Khosravi, A.L. Cimecioglu, Carbohyd. Polym. 90 (2012) 859–869.

[147] B. Guillerm, V. Darcos, V. Lapinte, S. Monge, J. Coudane, J.-J. Robin, Chem. Comm. 48 (2012) 2879–2881.

[148] E.L. Foster, A. Bunha, R. Advincula, Polymer 53 (2012) 3124–3134.

[149] W.A. Amer, L. Wang, A.M. Amin, L. Ma, H. Yu, J. Inorg. Organomet. P. 20 (2010) 605–615.

[150] L.H. Vogt, A. Zalkin, D.H. Templeton, Inorg. Chem. 6 (1967) 1725–1730.

[151] T. Kobayashi, F. Kurokawa, T. Ashida, N. Uyeda, E. Suito, J. Chem. Soc. Chem. Comm. 19 (1971) 1631–1632.

[152] T. Kawai, M. Soma, Y. Matsumoto, T. Onishi, K. Tamaru, Chem. Phys. Lett. 37 (1976) 378–382.

[153] B. Stymne, F. Sauvage, G. Wettermark, Spectrochim. Acta A-M. 36A (1980) 397–402.

[154] J. Metz, O. Schneider, M. Hanack, Inorg. Chem. 23 (1984) 1065–1071.

[155] G. Kalyuzhny, A. Vaskevich, G. Ashkenasy, A. Shanzer, I. Rubinstein, J. Phys. Chem. B 104 (2000) 8238–8244.

[156] K.I. Ozoemena, T. Nyokong, Electrochim. Acta 51 (2006) 2669–2677.

[157] K. Ogura, S. Yamasaki, J. Appl. Electrochem. 15 (1985) 279–284.

[158] F.-H. Wu, G.-C. Zhao, X.-W. Wei, Electrochem. Commun. 4 (2002) 690–694.

[159] K. Wu, J. Fei, W. Bai, S. Hu, Anal. Bioanal. Chem. 376 (2003) 205–209.

[160] T. Mugadza, T. Nyokong, J. Colloid Interf. Sci. 354 (2011) 437–447.

[161] T. Mugadza, T. Nyokong, Electrochim. Acta 54 (2009) 6347–6353.

[162] T. Mugadza, T. Nyokong, Electrochim. Acta 55 (2010) 6049–6057.

[163] T. Mugadza, T. Nyokong, Electrochim. Acta 55 (2010) 2606–2613.

[164] S. Khene, T. Nyokong, Electroanal. 23 (2011) 1901–1911.

[165] T. Mugadza, Y. Arslanoğlu, T. Nyokong, Electrochim. Acta 68 (2012) 44–51.

[166] B.O. Agboola, S.L. Vilakazi, K.I. Ozoemena, J. Solid State Electr. 13 (2008) 1367–1379.

[167] J.R. Macdonald, W.B. Johnson, in:, E. Barsoukov, J.R. Macdonald (Eds.), Impedance Spectroscopy: Theory, Experiment, and Applications, 2nd ed., John Wiley & Sons, Inc, Hoboken, 2005, pp. 1–26.

[168] I.D. Raistrick, D.R. Franceschetti, J.R. Macdonald, in:, E. Barsoukov, J.R. Macdonald (Eds.), Impedance Spectroscopy: Theory, Experiment, and Applications, 2nd ed., John Wiley & Sons Ltd, Hoboken, 2005, pp. 27–128.

[169] N. Bonanos, B.C.H. Steele, E.P. Butler, J.R. Macdonald, W.B. Johnson, W.L. Worrel, M.C.H. McKubre, D.D. Macdonald, E. Barsoukov, in:, E. Barsoukov, J.R. Macdonald (Eds.), Impedance Spectroscopy: Theory, Experiment, and Applications, 2nd ed., John Wiley & Sons, Inc, Hoboken, 2005, pp. 205–538.

[170] L. Ottaviano, S. Di Nardo, L. Lozzi, M. Passacantando, P. Picozzi, S. Santucci, Surf. Sci. 373 (1997) 318–332.

[171] Y. Lee, Y. Chen, C. Chang, Y. Yang, J. Maa, Thin Solid Films 370 (2000) 278–284.

[172] R. Caminiti, A. Capobianchi, P. Marovino, A. Paoletti, G. Padeletti, G. Pennesi, G. Rossi, Thin Solid Films 382 (2001) 74–80.

[173] J. E, S. Kim, E. Lim, K. Lee, D. Cha, B. Friedman, Appl. Surf. Sci. 205 (2003) 274–279.

[174] G. Wittstock, M. Burchardt, S.E. Pust, in:, B. Bhushan, H. Fuchs (Eds.), Applied Scanning Probe Methods VII: Biomimetics and Industrial Applications, Springer, Berlin Heidelberg, 2007, pp. 259–299.

[175] M.V. Mirkin, B.R. Horrocks, Anal. Chim. Acta 406 (2000) 119–146.

[176] G. Nagy, L. Nagy, Fresen. J. Anal. Chem. 366 (2000) 735–744.

[177] S. Evans, K. Brakha, M. Billon, P. Mailley, G. Denuault, Electrochem. Commun. 7 (2005) 135–140.

[178] S.-Y. Ku, K.-T. Wong, A.J. Bard, J. Am. Chem. Soc. 130 (2008) 2392–2393.

[179] F. Hauquier, T. Matrab, F. Kanoufi, C. Combellas, Electrochim. Acta 54 (2009) 5127–5136.

[180] J.F. Watts, J. Wolstenholme, An Introduction to Surface Analysis by XPS and AES, John Wiley & Sons, Ltd, Chichester, UK, 2003.

[181] D.C. Boyd, R.T. Haasch, D.R. Mantell, R.K. Schulze, J.F. Evans, W.L. Gladfelter, Chem. Mater. 1 (1989) 119–124.

[182] R.K. Schulze, D.C. Boyd, J.F. Evans, W.L. Gladfelter, J. Vac. Sci. Technol. A 8 (1990) 2338–2343.

[183] E.C. Landis, R.J. Hamers, Chem. Mater. 21 (2009) 724–730.

[184] S. Prakash, T.M. Long, J.C. Selby, J.S. Moore, M.A. Shannon, Anal. Chem. 79 (2007) 1661–1667.

[185] W. Douglas Gould, M. King, B.R. Mohapatra, R.A. Cameron, A. Kapoor, D.W. Koren, Miner. Eng. 34 (2012) 38–47.

[186] E. Cookeas, C. Efstathiou, Analyst 119 (1994) 1607–1612.

[187] M.K. Amini, S. Shahrokhian, S. Tangestaninejad, Anal. Chim. Acta 402 (1999) 137–143.

[188] K.I. Ozoemena, T. Nyokong, Talanta 67 (2005) 162–168.

[189] H.P. Til, V.J. Feron, A.P. de Groot, Food Cosmet. Toxicol. 10 (1972) 291–310.

[190] H.P. Til, V.J. Feron, A.P. de Groot, P. van der Wal, Food Cosmet. Toxicol. 10 (1972) 463–473.

[191] A.F. Gunnison, Food Cosmet. Toxicol. 19 (1981) 667–682.

[192] M. Iammarino, A. Di Taranto, M. Muscarella, Meat Sci. 90 (2012) 304–308.

[193] F. Cardulla, J. Chem. Educ. 60 (1983) 505–508.

[194] J.R. Latendresse, G.B. Marit, E.H. Vernot, C.C. Haun, C.D. Flemming, Toxicol. Sci. 27 (1995) 33–48.

[195] K. Bando, T. Kunimatsu, J. Sakai, J. Kimura, H. Funabashi, T. Seki, T. Bamba, E. Fukusaki, J. Appl. Toxicol. 31 (2010) 524–535.

[196] J. Zagal, S. Ureta-Zanartu, J. Electrochem. Soc. 129 (1982) 2242–2247.

[197] J. Zagal, S. Lira, S. Ureta-Zañartu, J. Electroanal. Chem. 210 (1986) 95–110.

[198] A.G. Gürek, Ö. Bekaroğlu, J. Chem. Soc. Dalton Trans. (1994) 1419–1423.

[199] J.G. Young, W. Onyebuagu, J. Org. Chem. 55 (1990) 2155–2159.

[200] C. Girard, E. Onen, M. Aufort, S. Beauvière, E. Samson, J. Herscovici, Org. Lett. 8 (2006) 1689–1692.

[201] I. Jlalia, C. Beauvineau, S. Beauvière, E. Onen, M. Aufort, A. Beauvineau, E. Khaba, J. Herscovici, F. Meganem, C. Girard, Molecules 15 (2010) 3087–3120.

[202] P. Tau, T. Nyokong, Dalton Trans. 60 (2006) 4482–4490.

[203] A.B.P. Lever, J. Wilshire, S. Quan, Inorg. Chem. 20 (1981) 761–768.

[204] C. Leznoff, L. Black, A. Hiebert, P. Causey, D. Christendat, A.B.P. Lever, Inorg. Chim. Acta 359 (2006) 2690–2699.

[205] T.B. Ogunbayo, A. Ogunsipe, T. Nyokong, Dyes Pigments 82 (2009) 422–426.

[206] S. Khene, A.N. Cammidge, M.J. Cook, T. Nyokong, J. Porphyr. Phthalocya. 11 (2007) 761–770.

[207] D. Wohrle, V. Schmidt, J. Chem. Soc. Dalton Trans. 677 (1988) 549–551.

[208] A. Louati, M. El Meray, J.J. Andre, J. Simon, K.M. Kadish, M. Gross, A. Giraudeau, Inorg. Chem. 24 (1985) 1175–1179.

[209] S. Griveau, J. Pavez, J. Zagal, F. Bedioui, J. Electroanal. Chem. 497 (2001) 75–83.

[210] H.O. Finklea, in:, A.J. Bard, I. Rubenstein (Eds.), Electroanalytical Chemistry: a Series of Advances, Marcel Dekker, New York, 1996, pp. 109–335.

[211] T.G. Spiro, F.J. Farrell, Inorg. Chem. 10 (1971) 1606–1610.

[212] A. Sivanesan, S.A. John, Langmuir 24 (2008) 2186–2190.

[213] Y. Lee, H. Wu, C. Chang, Y. Yang, Thin Solid Films 423 (2003) 169–177.

[214] S. Kment, P. Kluson, M. Drobek, R. Kuzel, I. Gregora, M. Kohout, Z. Hubicka, Thin Solid Films 517 (2009) 5274–5279.

[215] R. Cao Jr., A.M. Díaz-García, Coord. Chem. Rev. 253 (2009) 1262–1275.

[216] S. Khene, D. Geraldo, C. Togo, J. Limson, T. Nyokong, Electrochim. Acta 54 (2008) 183–191.

[217] C.D. Bain, H.A. Biebuyck, G.M. Whitesides, Langmuir 5 (1989) 723–727.

[218] J. Zak, H. Yuan, M. Ho, L.K. Woo, M.D. Porter, Langmuir 9 (1993) 2772–2774.

[219] D.E. Weisshaar, M.M. Walczak, M.D. Porter, Langmuir 9 (1993) 323–329.

[220] C.-J. Zhong, J. Zak, M.D. Porter, J. Electroanal. Chem. 421 (1997) 9–13.

[221] K.I. Ozoemena, T. Nyokong, P. Westbroek, Electroanal. 15 (2003) 1762–1770.

[222] M. Beccari, A. Kanjilal, M.G. Betti, C. Mariani, L. Floreano, A. Cossaro, V. Di Castro, J. Electron Spectrosc. 172 (2009) 64–68.

[223] J.M. Tour, L. Jones, D.L. Pearson, J.J.S. Lamba, T.P. Burgin, G.M. Whitesides, D.L. Allara, A.N. Parikh, S. Atre, J. Am. Chem. Soc. 117 (1995) 9529–9534.

[224] W. Zhou, T. Baunach, V. Ivanova, D.M. Kolb, Langmuir 20 (2004) 4590–4595.

[225] Y.-H. Chan, A.E. Schuckman, L.M. Perez, M. Vinodu, C.M. Drain, J.D. Batteas, J. Phys. Chem. C 112 (2008) 6110–6118.

[226] S. Baranton, D. Bélanger, J. Phys. Chem. B 109 (2005) 24401–24410.

[227] J. Lyskawa, D. Bélanger, Chem. Mater. 18 (2006) 4755–4763.

[228] P. Chen, R.L. McCreery, Anal. Chem. 68 (1996) 3958–3965.

[229] R.L. McCreery, Chem. Rev. 108 (2008) 2646–2687.

[230] Z.P. Demko, K.B. Sharpless, Angew. Chem. Int. Ed. 41 (2002) 2113–2116.

[231] J. Di, D. Hu, H. Chen, Z. Yong, M. Chen, Z. Feng, Y. Zhu, Q. Li, ACS Nano 6 (2012) 5457–5464.

[232] Z. Li, J. Xu, J.P. O'Byrne, L. Chen, K. Wang, M. a. Morris, J.D. Holmes, Mater. Chem. Phys. 135 (2012) 921–927.

[233] L. Zhang, G. Zhang, C. Liu, S. Fan, Nano Lett. 12 (2012) 4848–4852.

[234] P.A. Brooksby, A. Downard, Langmuir 20 (2004) 5038–5045.

[235] S. Ciampi, T. Böcking, K.A. Kilian, M. James, J.B. Harper, J. Gooding, Langmuir 23 (2007) 9320–9329.

[236] Z. Gao, Y. Zhang, G. Wang, Anal. Sci. 14 (1998) 1053–1058.

[237] E. Trollund, P. Ardiles, M.J. Aguirre, S.R. Biaggio, R.C. Rocha-Filho, Polyhedron 19 (2000) 2303–2312.

[238] V. Lakshminarayanan, U.K. Sur, Pramana J. Phys. 61 (2003) 361–371.

[239] S. Kera, M. Casu, K. Bauchspies, D. Batchelor, T. Schmidt, E. Umbach, Surf. Sci. 600 (2006) 1077–1084.

[240] K. Yamada, K. Teshima, N. Kobayashi, R. Hirohashi, J. Electroanal. Chem. 394 (1995) 71–79.

[241] R.W. Murray, Molecular Design of Electrode Surfaces, Vol 22, Techniques of Chemistry, John Wiley & Sons Ltd, New York, 1992.

[242] P. Snauwaert, R. Lazzaroni, J. Riga, J.. Verbist, Synthetic Met. 18 (1987) 335–340.

[243] A.J. Bard, M. V. Mirkin, Scanning Electrochemical Microscopy, Marcel Dekker, New York, 2001.

[244] G. Wittstock, M. Burchardt, S.E. Pust, Y. Shen, C. Zhao, Angew. Chem. Int. Ed. 46 (2007) 1584–1617.

[245] C. Linares, D. Geraldo, M. Paez, J. Zagal, J. Solid State Electr. 7 (2003) 626–631.

[246] J. Zagal, S. Griveau, J. Silva, T. Nyokong, F. Bedioui, Coord. Chem. Rev. 254 (2010) 2755–2791.

[247] C. das D.C. Conceição, R.C. Faria, O. Fatibello-Filho, A.A. Tanaka, Anal. Lett. 41 (2008) 1010–1021.

[248] P. Ardiles, E. Trollund, M. Isaacs, F. Armijo, J.C. Canales, M.J. Aguirre, M.J. Canales, J. Mol. Catal. A-Chem. 165 (2001) 169–175.

[249] L.M.F. Dantas, A.P. Dos Reis, S.M.C.N. Tanaka, J. Zagal, Y.-Y. Chen, A.A. Tanaka, J. Brazil. Chem. Soc. 19 (2008) 720–726.

[250] I.G. Casella, M. Contursi, Electroanal. 24 (2012) 752–758.